

# **Surface Composition and Enrichment Effects in Mixtures of Functionalized and Non-Functionalized Ionic Liquids**

**Oberflächenzusammensetzung und Anreicherungseffekte  
in Mischungen funktionalisierter und  
nicht-funktionalisierter Ionischer Flüssigkeiten**

Der Naturwissenschaftlichen Fakultät  
der Friedrich-Alexander-Universität Erlangen-Nürnberg

zur Erlangung des Doktorgrades Dr. rer. nat.

vorgelegt von  
**BETTINA HELLER**  
aus Erlangen



Als Dissertation genehmigt von der Naturwissenschaftlichen Fakultät  
der Friedrich-Alexander-Universität Erlangen-Nürnberg

Tag der mündlichen Prüfung: 25.05.2020

Vorsitzender des Promotionsorgans: Prof. Dr. Georg Kreimer

Gutachter: Prof. Dr. Hans-Peter Steinrück  
Prof. Dr. Jürgen Schatz



## Table of Contents

1	Introduction.....	1
2	Angle-Resolved X-ray Photoelectron Spectroscopy .....	3
3	Materials, Instrumentation and Experimental Details.....	7
3.1	Chemicals and Sample Preparation.....	7
3.2	Dual Analyzer System for Surface Analysis.....	9
3.3	Data Evaluation .....	11
4	Results and Discussion .....	13
4.1	Surface Composition and Surface Tension of Homologue Ionic Liquids <sup>[P1]</sup> .....	13
4.2	Binary Mixtures Containing Functionalized Ionic Liquids.....	17
4.2.1	Equimolar Mixtures of Methoxy- and Non-Functionalized Ionic Liquids <sup>[P2]</sup> .....	18
4.2.2	Mixtures of Fluorinated and Non-Fluorinated Ionic Liquids <sup>[P3]</sup> .....	22
4.2.3	Mixtures of Methoxy-Functionalized and Fluorinated Ionic Liquids <sup>[P4]</sup> .....	29
4.3	Role of an Ionic Liquid Covering Graphene-Analogues <sup>[P5]</sup> .....	36
5	Summary.....	39
6	Zusammenfassung.....	42
7	Literature.....	45
8	Acknowledgment .....	56
9	Appendix.....	57
9.1	Publications [P1] – [P5] .....	57
	Publication [P1].....	59
	Publication [P2].....	68
	Publication [P3].....	97
	Publication [P4].....	111
	Publication [P5].....	130

9.2	Unpublished Results.....	144
9.2.1	(Pentafluorobutyl)thio-Functionalized Ionic Liquid and its Mixture with [C <sub>4</sub> C <sub>1</sub> Im][PF <sub>6</sub> ].....	146
9.2.2	Ether-Functionalized Phosphonium Ionic Liquids .....	152
9.2.3	Temperature-Dependent Measurements of Mixtures of [PFBMIm][PF <sub>6</sub> ] with [C <sub>2</sub> C <sub>1</sub> Im][PF <sub>6</sub> ] and [C <sub>8</sub> C <sub>1</sub> Im][PF <sub>6</sub> ].....	155

## Published Papers

**[P1] Probing the Surface Tension of Ionic Liquids Using the Langmuir Principle**

K. Shimizu, B. S. J. Heller, F. Maier, H.-P. Steinrück, J. N. Canongia Lopes

*Langmuir* **2018**, *34*, 4408–4416.

The author's contribution is the ARXPS data analysis and interpretation.

**[P2] Surface Enrichment in Equimolar Mixtures of Non-Functionalized and Functionalized Imidazolium-Based Ionic Liquids**

B. S. J. Heller, C. Kolbeck, I. Niedermaier, S. Dommer, J. Schatz, P. Hunt, F. Maier, H.-P. Steinrück

*ChemPhysChem* **2018**, *19*, 1733–1745.

The author's contribution is the sample preparation, ARXPS investigation, data analysis, data interpretation and manuscript preparation.

**[P3] Temperature-Dependent Surface Enrichment Effects in Binary Mixtures of Fluorinated and Non-Fluorinated Ionic Liquids**

B. S. J. Heller, M. Lexow, F. Greco, S. Shin, G. Partl, F. Maier, H.-P. Steinrück

*Chem. Eur. J.* **2020**, *26*, 1117–1126.

The author's contribution is the sample preparation, ARXPS investigation, data analysis, data interpretation and manuscript preparation.

**[P4] Pronounced surface enrichment of fluorinated ionic liquids in binary mixtures with methoxy-functionalized ionic liquids**

B. S. J. Heller, U. Paap, F. Maier, H.-P. Steinrück

*J. Mol. Liq.* **2020**, *305*, 112783.

The author's contribution is the sample preparation, ARXPS investigation, data analysis, data interpretation and manuscript preparation.

**[P5] Few layer 2D pnictogens catalyze the alkylation of soft nucleophiles with esters**

V. Lloret, M. Á. Rivero-Crespo, J. A. Vidal-Moya, S. Wild, A. Doménech-Carbó, B. S. J. Heller, S. Shin, H.-P. Steinrück, F. Maier, F. Hauke, M. Varela, A. Hirsch, A. Leyva-Pérez, G. Abellán

*Nat. Commun.* **2019**, *10*, 509.

The author's contribution is the XPS investigation, data analysis and interpretation.

---



## 1 Introduction

Ionic liquids (ILs) are salt melts with melting points typically below 100 °C, often even below room temperature. They are composed of organic cations and organic or inorganic anions, allowing for a wide structural variability including functional groups with heteroatoms, branched chains or aromatic groups.<sup>[1-4]</sup> The structural diversity results in a great tunability of physical and chemical properties like thermal stability, ionic conductivity, viscosity, solubility and electrochemical window, to name a few.<sup>[5-7]</sup> By mixing ILs in different compositions (note that the term “IL” is used throughout this thesis for neat ILs consisting of only one type of cation and anion), further fine tuning of properties is possible.<sup>[8-11]</sup> Thus, ILs and their mixtures are promising candidates for a range of applications in the field of *e.g.* electrochemistry,<sup>[5, 12-22]</sup> lubrication,<sup>[6, 23]</sup> extraction<sup>[5, 19, 24-30]</sup> and catalysis.<sup>[1, 7, 31-36]</sup>

In many of these applications, the outer surface representing the interface of the IL phase with the gas phase plays a major role. This is particularly true for large surface area systems like the Supported Ionic Liquid Phase (SILP)<sup>[36-39]</sup> catalysis. In SILP, a porous high surface area support is coated with a thin IL film, which contains the homogeneously dissolved catalyst. Gaseous reactants and the reaction products have to pass through the IL surface layer, which – in comparison to the isotropic bulk environment – can be very different in terms of composition and molecular orientation. Moreover, functionalized groups present in the IL can also have a profound impact on the composition of the topmost layer.<sup>[8, 9, 36, 40-57]</sup>

Therefore, a better understanding of the surface of neat ILs and of IL mixtures is of great interest. During the last two decades, the knowledge about the surface of ILs and IL mixtures has been extended using different surface-sensitive techniques such as small-angle X-ray and neutron scattering,<sup>[8]</sup> X-ray reflectivity,<sup>[58]</sup> low-energy ion scattering (LEIS),<sup>[46, 59]</sup> reactive-atom scattering with laser-induced fluorescence detection (RAS-LIF),<sup>[8, 60]</sup> time-of-flight secondary ion mass spectrometry (TOF-SIMS),<sup>[50, 61]</sup> metastable induced electron spectroscopy (MIES),<sup>[57, 62]</sup> Rutherford backscattering spectroscopy (RBS),<sup>[50, 51, 63, 64]</sup> X-ray photoelectron spectroscopy (XPS)<sup>[52-54, 62, 65-69]</sup> and simulations.<sup>[2, 8, 54-56, 60, 64, 70-72]</sup> The extremely low vapor pressure of most ILs makes them suitable for investigations under ultra-high vacuum (UHV) conditions, which is required for some of the aforementioned techniques.

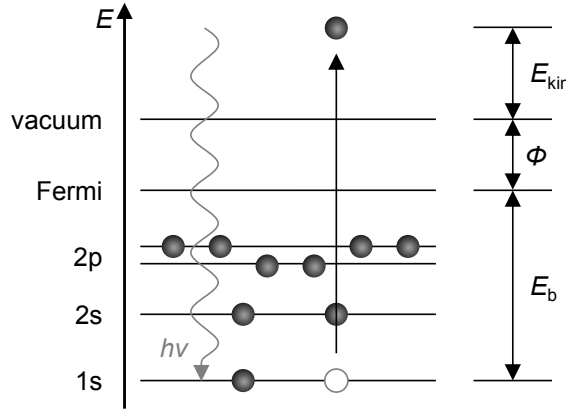
As will be demonstrated in this work, angle-resolved XPS (ARXPS) allows one to gain detailed information about the bulk and surface composition of IL systems by comparing spectra recorded under  $0^\circ$  and  $80^\circ$  emission (see Chapter 2). All ILs and their mixtures investigated here are based on imidazolium cations that contain alkyl chains or functional groups such as methoxy or fluorinated moieties (see Chapter 3). In Chapter 4.1, the surface enrichment of the alkyl chains of  $[C_nC_1\text{Im}][\text{Tf}_2\text{N}]$  (with  $n = 2, 4, 6, 8, 10$  and  $12$ ) with respect to the cationic head groups is correlated to the surface tension values of the ILs. The study of the IL/vacuum interface as well as the bulk composition of neat ILs and binary IL mixtures of a functionalized and a non-functionalized IL or two functionalized ILs are presented in Chapters 4.2.1 to 4.2.3: Surface enrichment and depletion effects in mixtures of  $[C_8C_1\text{Im}][\text{PF}_6]$  or  $[C_8C_1\text{Im}][\text{Tf}_2\text{N}]$  with  $[(\text{MeO})_2\text{Im}][\text{PF}_6]$  are investigated. Furthermore, mixtures containing  $[\text{PFBMIm}][\text{PF}_6]$  and  $[C_nC_1\text{Im}][\text{PF}_6]$  with  $n = 2, 4$  and  $8$  and mixtures of  $[(\text{MeO})_2\text{Im}][\text{PF}_6]$  and  $[\text{PFBMIm}][\text{PF}_6]$  are studied by temperature-dependent ARXPS from  $95^\circ\text{C}$  to their onset of solidification. This gives crucial information for SILP systems since the temperature of the process might have a major impact on the surface composition; for some reactions, *e.g.* the exothermal water-gas shift reaction, a lower temperature is desirable.<sup>[73]</sup>

Finally, in Chapter 4.3, the role of  $[C_4C_1\text{Im}][\text{BF}_4]$  as dispersing and stabilizing solvent to produce the catalytically active two-dimensional (2D) materials antimonene and phosphorene is discussed, particularly with respect to the protection of these pnictogens against oxidation under ambient conditions.

## 2 Angle-Resolved X-ray Photoelectron Spectroscopy

X-ray photoelectron spectroscopy (XPS) is an ultra-high vacuum (UHV)-based surface science technique, which was used to perform the experiments presented in this thesis. In this chapter, the basic aspects of XPS are highlighted. For more details, see *e.g.* the books of van der Heide,<sup>[74]</sup> Briggs and Seah<sup>[75]</sup> or Hüfner.<sup>[76]</sup>

XPS is based on the photoelectric effect which was first described by Hertz<sup>[77]</sup> and Hallwachs<sup>[78]</sup> in 1887 and 1888 and explained by Einstein in 1905.<sup>[79]</sup> A general scheme is shown in Figure 2.1.



**Figure 2.1:** General scheme of the photoelectric effect.

A sample is irradiated by photons of a fixed energy,  $h\nu$ , and photoelectrons with different kinetic energies are emitted from the core levels to above the sample vacuum level,  $E_{\text{vacuum}}$ . These photoelectrons are then detected by an electron analyzer. Their kinetic energy,  $E_{\text{kin}}$ , is measured with respect to the vacuum level of the analyzer,  $E_{\text{vacuum,an}}$ . Taking the work function of the analyzer,  $\Phi_{\text{an}}$ , into account, which is a constant derived by calibrating the analyzer to the Fermi level,  $E_{\text{Fermi}}$ , of a clean metal sample, the binding energy,  $E_{\text{b}}$ , of the excited orbital with respect to the common  $E_{\text{Fermi}}$ , can be obtained:

$$E_{\text{b}} = h\nu - E_{\text{kin}} - \Phi_{\text{an}} \quad (1)$$

Note that this relation holds only for conducting samples electrically connected to the electron analyzer ground to align  $E_{\text{Fermi}}$  of both sample and analyzer.

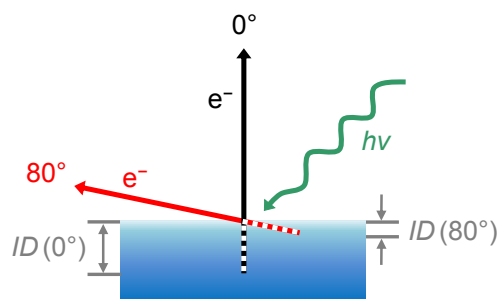
The binding energy of the detected electrons is element specific and allows for extracting information on the chemical environment and oxidation state of the probed atom by the so-called chemical shifts. XPS is thus also known as Electron Spectroscopy for

Chemical Analysis (ESCA). Moreover, XPS is a quantitative technique to extract the composition of a sample by the signal intensities (apart from hydrogen and helium).

XPS is a very surface-sensitive method resulting from the short inelastic mean free path,  $\lambda$ , of the excited photoelectrons in matter. This surface sensitivity is characterized by the so-called information depth,  $ID$ , which is also denoted as sample depth or escape depth. The  $ID$  depends on the emission angle,  $\vartheta$ , of the photoelectrons relative to the surface normal (see Figure 2.2), and is defined as:

$$ID(\vartheta) = 3\lambda \cdot \cos \vartheta \quad (2)$$

It corresponds to the depth, where 96% of the measured XP signal originates from.<sup>[74]</sup> For  $\vartheta = 0^\circ$ , the  $ID$  is 7 to 9 nm, depending on  $E_{\text{kin}}$ . Increasing  $\vartheta$  results in a decreased  $ID$  according to Equation 2: For measurements at  $\vartheta = 80^\circ$ , as performed in the course of this thesis,  $ID$  is only 1 to 1.5 nm, which limits the detected signal mostly to the topmost surface layer of the studied ILs.



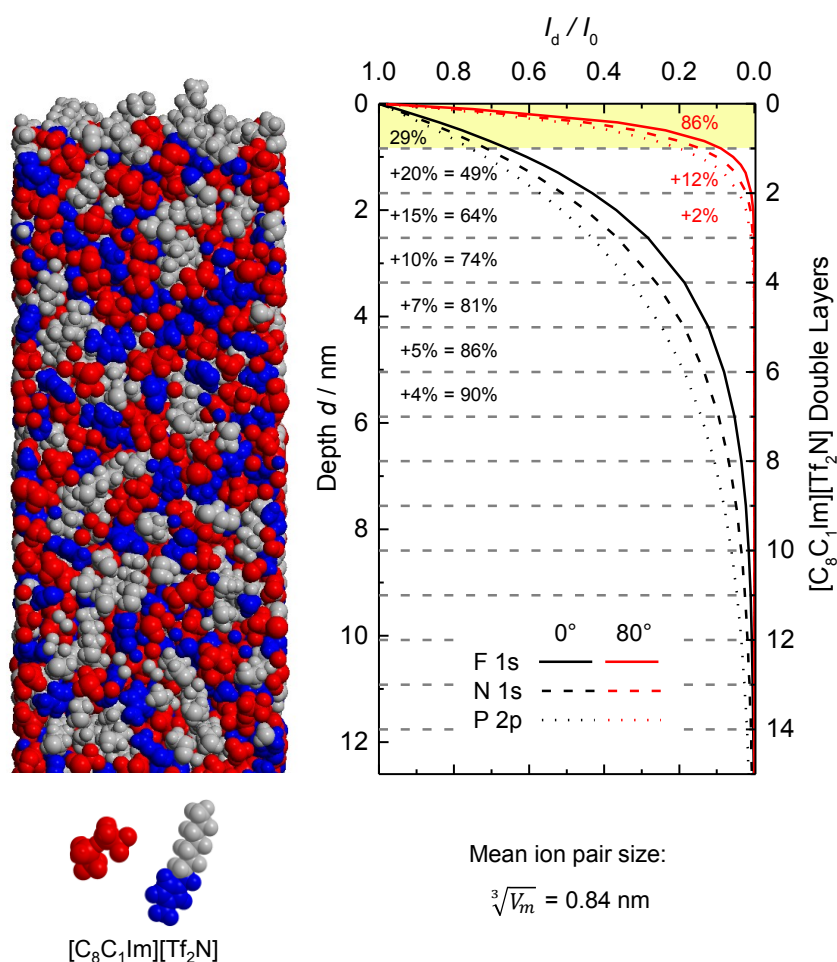
**Figure 2.2:** Scheme of ARXPS recorded under  $\vartheta = 0^\circ$  and  $80^\circ$  emission with respect to the surface normal of the sample. The dashed lines indicate the maximum “traveled” distance of  $3\lambda$  of electrons in matter at both emission angles; the resulting information depth,  $ID$ , is marked in gray.

At a given emission angle, the intensity,  $I_d$ , of a signal originating from a depth,  $d$ , relative to the intensity,  $I_0$ , at the IL/vacuum interface ( $d = 0$ ) decays exponentially according to:<sup>[80]</sup>

$$\frac{I_d}{I_0} = e^{-\frac{d}{\lambda \cdot \cos \vartheta}} \quad (3)$$

Figure 2.3 highlights the dependence of the surface sensitivity of angle-resolved XPS (ARXPS) on the emission angle. The exponential decay of the contribution to the measured XP signal is illustrated in Figure 2.3–right for  $0^\circ$  (black) and  $80^\circ$  (red) emission and a scaled molecular dynamics (MD) simulation of the near-surface region of  $[\text{C}_8\text{C}_1\text{Im}][\text{Tf}_2\text{N}]$  is shown in Figure 2.3–left. For both emission angles, the behavior is

shown for photoelectrons excited from distinct core levels (F 1s, N 1s and P 2p) with different  $E_b$  and thus different  $E_{kin}$  and  $\lambda$  values ( $\lambda_{F\ 1s} = 2.0$  nm,  $\lambda_{N\ 1s} = 2.5$  nm,  $\lambda_{P\ 2p} = 3.0$  nm; linearly<sup>[81]</sup> interpolated from previously published values<sup>[40, 80, 82-84]</sup>). In  $80^\circ$  emission, 86% of the signal of the N 1s core level originates from the first IL double layer ( $d = 0.84$  nm), whereas in  $0^\circ$  it is only 29%. These values differ depending on  $\lambda$  of the photoelectrons with different  $E_{kin}$  as indicated by the solid (F 1s), dashed (N 1s) and dotted (P 2p) lines in Figure 2.3–right.



**Figure 2.3:** Side view of a scaled MD simulation of [C<sub>8</sub>C<sub>1</sub>Im][Tf<sub>2</sub>N] (left).<sup>[85]</sup> Exponential decay of the contribution of individual [C<sub>8</sub>C<sub>1</sub>Im][Tf<sub>2</sub>N] double layers to the overall ARXPS signal in the F 1s (solid), N 1s (dashed) and P 2p (dotted) spectra under  $0^\circ$  (black) and  $80^\circ$  (red) emission (right). The mean ion pair size is estimated from the third root of the molecular volume,  $V_m$ .<sup>[80, 86]</sup>  $\lambda$  is 2.0, 2.5 and 3.0 nm for the F 1s, N 1s and P 2p photoelectrons, respectively. The small black ( $0^\circ$ ) and red ( $80^\circ$ ) numbers in the graph represent the contribution of each IL double layer to the N 1s signal, for clarity the first double layer is shaded in yellow.

From these considerations, it is evident that the surface sensitivity of ARXPS can be varied by changing the electron emission angle: Thereby, a higher peak intensity in  $80^\circ$  (surface-sensitive) compared to  $0^\circ$  (bulk-sensitive) indicates a higher concentration of this species in the topmost layer than in the bulk and vice versa.

## 3 Materials, Instrumentation and Experimental Details


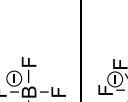
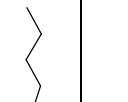


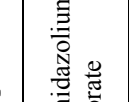
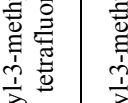
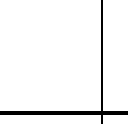
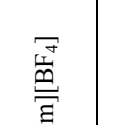
### 3.1 Chemicals and Sample Preparation

An overview of the ILs investigated in the course of this thesis is given in Table 3.1 including their formula, IUPAC name, molecular structure and the respective melting temperature,  $T_m$ , or glass transition temperature,  $T_g$ .

1-Ethyl-3-methylimidazolium hexafluorophosphate,  $[\text{C}_2\text{C}_1\text{Im}][\text{PF}_6]$ , and 1-butyl-3-methylimidazolium hexafluorophosphate,  $[\text{C}_4\text{C}_1\text{Im}][\text{PF}_6]$ , were purchased from Merck (purity for synthesis) and Iolitec (purity 99.5%), respectively. 1-Butyl-3-methylimidazolium tetrafluoroborate,  $[\text{C}_4\text{C}_1\text{Im}][\text{BF}_4]$ , and 1-methyl-3-octylimidazolium hexafluorophosphate,  $[\text{C}_8\text{C}_1\text{Im}][\text{PF}_6]$ , were purchased from Sigma-Aldrich (purities 99.9% and > 95%, respectively). 1-Methyl-3-octylimidazolium bis[(trifluoromethyl)sulfonyl]imide,  $[\text{C}_8\text{C}_1\text{Im}][\text{Tf}_2\text{N}]$ , was prepared by Dr. Nicola Taccardi according to literature.<sup>[87]</sup> 1,3-Di(methoxy)imidazolium hexafluorophosphate,  $[(\text{MeO})_2\text{Im}][\text{PF}_6]$ , was synthesized by Dr. Sabine Dommer according to previous publications.<sup>[88, 89]</sup> 1-[2-(2-Methoxy-ethoxy)-ethyl]-3-methylimidazolium bis[(trifluoromethyl)sulfonyl]imide,  $[\text{Me}(\text{EG})_2\text{C}_1\text{Im}][\text{Tf}_2\text{N}]$ , was synthesized by Wei Wei as published earlier.<sup>[86]</sup> 3-Methyl-1-(3,3,4,4,4-pentafluorobutyl)imidazolium hexafluorophosphate,  $[\text{PFBMIm}][\text{PF}_6]$ , was prepared by Dr. Gabriel Partl as reported in literature.<sup>[45]</sup> All ILs have been investigated as received without any further purification except for a minimum of four freeze-pump cycles for  $[\text{C}_4\text{C}_1\text{Im}][\text{BF}_4]$  prior to the preparation of the suspensions with phosphorene or antimonene.

To ensure proper mixing of the ILs in the investigated mixtures, acetonitrile (Sigma-Aldrich, purity 99.8%) was used as a co-solvent. For the ARXPS measurements, the respective IL or IL mixture was placed on a molybdenum reservoir with a depth of 0.5 mm with a Pasteur pipette or a spatula and afterwards spread over the whole sample holder. In the case of IL mixtures, the sample holder was sometimes heated up to ~65 °C to accelerate the vaporization of the solvent acetonitrile. In the case of the phosphorene and antimonene samples, a clean gold foil was used as support for the suspensions. After sample preparation, the sample is introduced into the load lock system of the UHV measuring apparatus.

**Table 3.1:** Overview of names, molecular structures and phase transition temperatures ( $T_m$  or  $T_g$ ) of the investigated ILs.

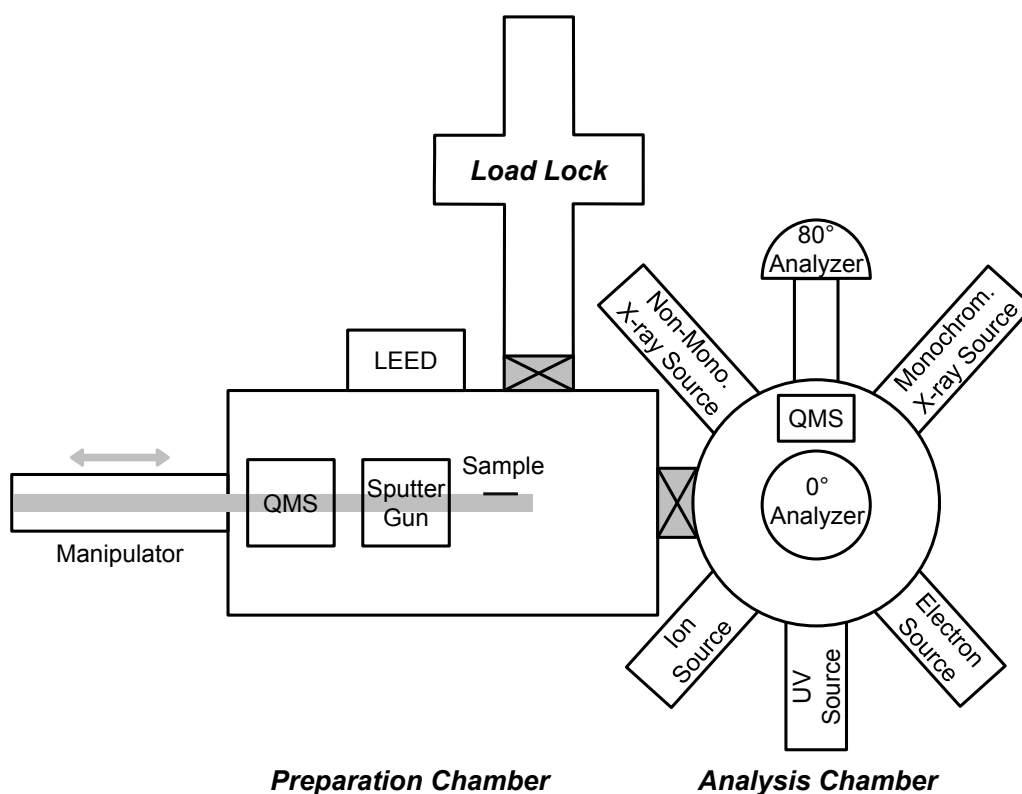
Short Name	IUPAC Name	Molecular Structure	$T_m$ or $T_g$ in °C <sup>a)</sup>
[C <sub>2</sub> C <sub>1</sub> Im][PF <sub>6</sub> ]	1-ethyl-3-methylimidazolium hexafluorophosphate		$T_m \sim 60$ <sup>[90, 91]</sup>
[C <sub>2</sub> C <sub>2</sub> Im][PF <sub>6</sub> ]	1,3-diethylimidazolium hexafluorophosphate		$T_m = 70$ <sup>[92]</sup>
[C <sub>4</sub> C <sub>1</sub> Im][BF <sub>4</sub> ]	1-butyl-3-methylimidazolium tetrafluoroborate		$T_g \sim -84$ <sup>[93, 94]</sup>
[C <sub>4</sub> C <sub>1</sub> Im][PF <sub>6</sub> ]	1-butyl-3-methylimidazolium hexafluorophosphate		$T_g \sim -77$ <sup>[90, 91, 93, 94]</sup>
[C <sub>8</sub> C <sub>1</sub> Im][Tf <sub>2</sub> N]	1-methyl-3-octylimidazolium bis[(trifluoromethyl)sulfonyl]imide		$T_g \sim -82$ <sup>[90, 95]</sup>
[C <sub>8</sub> C <sub>1</sub> Im][PF <sub>6</sub> ]	1-methyl-3-octylimidazolium hexafluorophosphate		$T_g \sim -71$ <sup>[90, 91]</sup>
[(MeO) <sub>2</sub> Im][PF <sub>6</sub> ]	1,3-di(methoxy)imidazolium hexafluorophosphate		$T_m = 83 - 84$ <sup>[96]</sup>
[Me(EG) <sub>2</sub> C <sub>1</sub> Im][Tf <sub>2</sub> N]	1-[2-(2-methoxy-ethoxy)ethyl]-3-methylimidazolium bis[(trifluoromethyl)sulfonyl]imide		n/a
[PFBMIm][PF <sub>6</sub> ]	3-methyl-1-(3,3,4,4-pentafluorobutyl)imidazolium hexafluorophosphate		$T_m = 66$ <sup>[45]</sup>

a) strongly depends on method, contamination level, etc.



### 3.2 Dual Analyzer System for Surface Analysis

Commonly ARXPS is performed by either tilting the sample to achieve grazing emission or by rotating the analyzer to gain the more surface-sensitive information as described in Chapter 2. In Figure 3.1, the UHV chamber, the so-called Dual Analyzer System for Surface Analysis (DASSA),<sup>[97]</sup> is sketched. This setup was developed in cooperation with Omicron NanoTechnology and was used for the acquisition of most ARXPS data presented in this thesis. It was built for investigating macroscopic amounts of liquid samples and has a base pressure below  $1 \cdot 10^{-10}$  mbar. The DASSA setup consists of three separated main parts: Preparation chamber, analysis chamber and load lock system. In the following, the equipment used throughout this thesis is described in more detail. Further details are provided in Ref. [97].



**Figure 3.1:** Scheme of the DASSA setup showing the three main parts: Preparation chamber (left), analysis chamber (right) and load lock system (top), as well as the components mounted to the respective chamber part.

Inside the UHV chamber, the samples typically are kept in horizontal position, so no dripping of the IL can occur. The samples are introduced into the load lock system and are degassed there for at least twelve hours. Afterwards, they are transferred onto the manipulator in the preparation chamber. The manipulator head has two sample stages

available: A low (equipped with liquid nitrogen cooling and radiative heating) and a high (with heating by electron bombardment) temperature stage. Throughout this thesis, mainly the low temperature stage with a temperature range between  $-123$  and  $1027$  °C is used. For cleaning the molybdenum reservoirs of the sample holders as well as for occasional surface cleaning of the investigated samples, a sputter gun (initially: Omicron NanoTechnology ISE 5; now: SPECS IQE 11/35) for  $\text{Ar}^+$  bombardment is mounted in the preparation chamber. Furthermore, a quadrupole mass spectrometer (QMS; HIDEN HAL 3F 511) and low energy electron diffraction (LEED; Omicron) optics are mounted at the preparation chamber.

Two identical hemispherical ARGUS electron analyzers from Omicron NanoTechnology are attached to the analysis chamber. They are mounted under an emission angle of  $0^\circ$  and  $80^\circ$  relative to the surface normal of a horizontally mounted sample holder on the manipulator. This configuration allows for simultaneous measurements of the same sample spot and therefore reduces the X-ray exposure time by about a factor of two compared to conventional ARXPS setups performing two consecutive measurements for both emission angles. The MATRIX T3.2 software was customized specifically for the DASSA setup for the simultaneous operation of both analyzers. A monochromated  $\text{Al K}_\alpha$  X-ray source (Omicron XM 1000;  $h\nu = 1486.6$  eV), operated at 238 W, is mounted in a magic angle configuration with respect to both analyzers. Survey scans are either recorded with 200 or 150 eV pass energy, whereas for region scans a pass energy of 35 eV is used resulting in an overall energy resolution of 0.4 eV. Moreover, a dual non-monochromated X-ray source (Omicron DAR 400) with  $\text{Mg K}_\alpha$  ( $h\nu = 1253.6$  eV) and  $\text{Al K}_\alpha$  ( $h\nu = 1486.6$  eV) radiation, an ion source (Omicron FIG 05), an electron source (Omicron CN 10), an ultraviolet source (UV source; Omicron HIS 13) and a QMS (Pfeiffer Vacuum PrismaPlus QMG 220) are mounted at the analysis chamber but have not been used in the course of this thesis.

### 3.3 Data Evaluation

In the following, the general procedure for the data evaluation is described. For more details, see the respective published peer-reviewed articles [P1] – [P5].

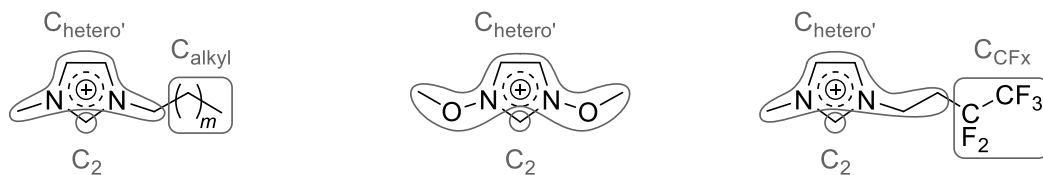
For the data evaluation, the CasaXPS (version 2.3.16Dev6) software is used for all spectra recorded at the DASSA setup. For the quantification, the atomic sensitivity factors (ASFs) are taken into account for each individual spectrum to correct *e.g.* different cross sections. A list of the ASFs used in this thesis is given in Table 3.2.<sup>[97]</sup>

**Table 3.2:** ASFs applied to the peak intensities for measurements carried out at the DASSA setup.

Core Level	ASF <sub>DASSA</sub>
F 1s	1.00
O 1s	0.67
N 1s	0.46
C 1s	0.30
S 2p	0.64
P 2p	0.46
B 1s	0.15

Commonly, a two point linear background is subtracted from the XP spectra, only when the IL contains a CF<sub>x</sub> group like in the [PFBMIm]<sup>+</sup> cation or the [Tf<sub>2</sub>N]<sup>-</sup> anion a three point linear background is subtracted from the C 1s spectrum. All peaks are fitted with a Gauss-Lorentz function with 30% Lorentzian contribution. The S 2p and P 2p spectra consist of the two spin-orbit-split components 2p<sub>1/2</sub> and 2p<sub>3/2</sub>. These two peaks are fitted with the same full width at half maximum (FWHM), a 1 : 2 area ratio and peak separations of 1.21 and 0.90 eV in the S 2p and P 2p spectra, respectively. For fitting the C 1s region different constraints are applied: For ILs consisting of the non-functionalized [C<sub>n</sub>C<sub>1</sub>Im]<sup>+</sup> cation, the area of the C<sub>hetero</sub>' peak is four times the area of the C<sub>2</sub> peak (for peak assignment see Figure 3.2) and both peaks are separated by 0.9 eV. The C<sub>hetero</sub>' peak is 1.1 times wider than the C<sub>2</sub> and the C<sub>alkyl</sub> peaks. For the [(MeO)<sub>2</sub>Im]<sup>+</sup> cation, the C<sub>hetero</sub>' peak is 1.02 times wider and four times more intense than the C<sub>2</sub> peak and both peaks are separated by 1.10 eV. For the [PFBMIm]<sup>+</sup> cation, the C<sub>hetero</sub>' peak is 1.33 times wider than the C<sub>2</sub> peak and both peaks are separated by 1.02 eV. Since the C<sub>CF3</sub> peak overlaps with the shake-up of the aromatic system of the imidazolium ring,<sup>[98]</sup> its intensity is set equal to the

intensity of the  $C_{CF_2}$  peak for quantification. All those constraints are applied to the spectra recorded in  $0^\circ$  and  $80^\circ$  emission.



**Figure 3.2:** Peak assignment for the C 1s species  $C_2$ ,  $C_{\text{hetero}'}$ ,  $C_{\text{alkyl}}$  and  $C_{CF_x}$  in different cations:  $[C_nC_1\text{Im}]^+$ ,  $[(\text{MeO})_2\text{Im}]^+$  and  $[\text{PFBMIm}]^+$ . Adapted from [P3] and [P4] under license CC BY 4.0.

Additional constraints are applied for the mixtures published in [P4]. The  $F_{PF_6}$  peak in the F 1s spectra is 0.79 times wider than the  $F_{CF_x}$  peak and in the N 1s region the  $N_{\text{MeO}}$  and  $N_{\text{PFB}}$  peaks are set to equal width. Due to only a very weak  $N_{\text{PFB}}$  signal in the 95 mol% mixture of  $[(\text{MeO})_2\text{Im}][\text{PF}_6]$  and  $[\text{PFBMIm}][\text{PF}_6]$ , the peak separation is constrained to  $1.40 \pm 0.04$  eV. For all mixtures in this paper, the  $C_2$  to  $C_{\text{hetero}'}$  ratio is set to the nominally expected ratio resulting from the molar ratio of the two ILs.

A lower intensity is detected for spectra recorded under an emission angle of  $80^\circ$  compared to  $0^\circ$  emission. To compensate for this, the  $80^\circ$  spectra are scaled up by a so-called geometry factor<sup>[97]</sup> to facilitate the visual comparison of both spectra showing enrichment and depletion effects directly.

## 4 Results and Discussion

Within this thesis, five peer-reviewed articles have been published and are summarized in this chapter. Some additional results, which are unpublished, are included to support the published results. For further experimental details see the respective publications [P1] – [P5].

### 4.1 Surface Composition and Surface Tension of Homologue Ionic Liquids<sup>[P1]</sup>

In contrast to all other data presented in this thesis, the XPS data shown in this chapter are measured in a different UHV setup equipped with a non-monochromated Al  $K_{\alpha}$  X-ray source and one analyzer attached, which requires a tilting of the sample for surface-sensitive  $80^{\circ}$  emission measurements. This UHV setup was described in detail earlier.<sup>[99-103]</sup> In contrast to the data recorded at the DASSA setup, the  $C_2$  and  $C_{\text{hetero}}$  peaks are combined in one  $C_{\text{hetero}}$  peak due to a lower energy resolution resulting from the non-monochromated X-ray source of this setup.

The aim of this study was to combine ARXPS measurements and MD simulations to determine the outer surface composition of the homologue series of  $[C_nC_1Im][Tf_2N]$  with  $n = 2, 4, 6, 8, 10$  and  $12$ , and to derive the surface tension values for these six ILs applying the so-called Langmuir principle. In 1917 and 1930, Langmuir stated that the surface free energy of a liquid as deduced by surface tension measurements is the result of “the structure of the surface layer of atoms”<sup>[104]</sup> and is thus influenced by the orientation of surface molecules as well as the intermolecular interaction not only at the surface but also “of the atoms underlying the surface”.<sup>[105]</sup> The ILs’ molecular orientation at the surface was probed by means of ARXPS<sup>[99]</sup> whereas the density profiles were recently simulated by MD performed by Dr. Karina Shimizu.<sup>[106]</sup> The density of groups at the outer surface determined by MD simulations (in particular, the number of surface aliphatic chains and ionic head groups) were then used to calculate the surface tension values for each of the  $[C_nC_1Im][Tf_2N]$  ILs according to the Langmuir principle and compared to the surface tension values experimentally determined for all six ILs under identical conditions.<sup>[86]</sup>

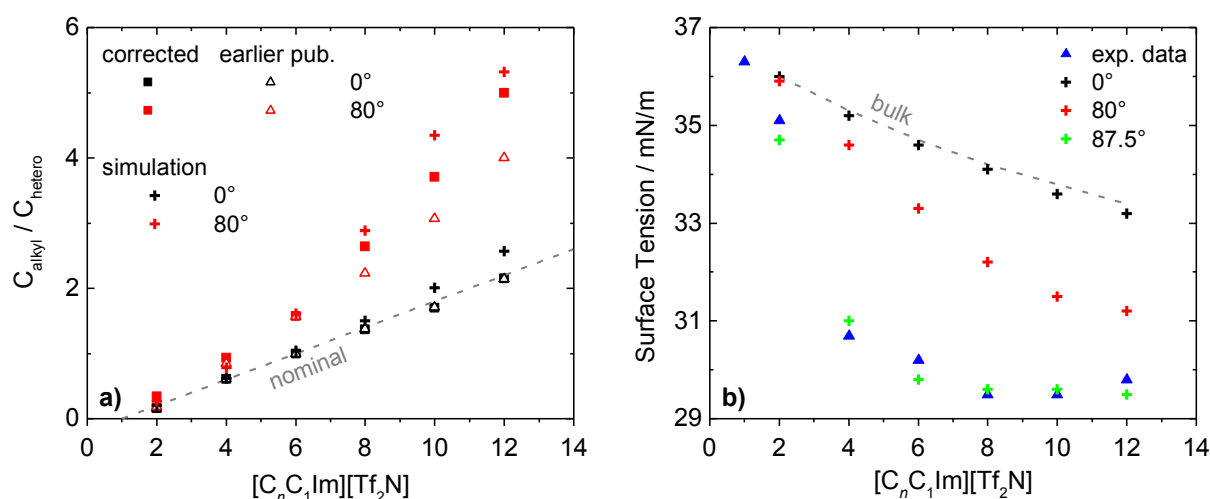
In the course of this thesis, a re-evaluation of the existing ARXPS data was necessary to allow for a more accurate quantitative comparison with the MD results. In previous publications,<sup>[42, 52, 86, 99]</sup> the surface enrichment of the alkyl chains relative to the cationic head groups in the  $[C_nC_1Im][Tf_2N]$  series was determined by the intensity ratios of the  $C_{alkyl}$  to  $C_{hetero}$  intensities as derived solely from fitting the C 1s ARXP spectra. However, the small peak separation between  $C_{alkyl}$  and  $C_{hetero}$  of  $\sim 1.5$  eV leads to rather high uncertainties of the  $I(C_{alkyl}) / I(C_{hetero})$  values in the  $80^\circ$  spectra, particularly for large  $n$  values with a strongly dominating  $C_{alkyl}$  signal next to a small  $C_{hetero}$  shoulder.

To overcome this difficulty and to obtain more accurate results, the N 1s spectra with the well-separated  $N_{Im}$  signals of the nitrogen atoms of the imidazolium ring in direct proximity to the  $C_{hetero}$  atoms are additionally taken into account as internal reference.<sup>[106]</sup> The intensity change of the  $N_{Im}$  peak is used to determine the corrected  $80^\circ$   $C_{hetero}$  intensity:  $I_{corr}(C_{hetero,80^\circ}) = [I(N_{Im,80^\circ}) / I(N_{Im,0^\circ})] \cdot I(C_{hetero,0^\circ})$ . This intensity is then subtracted from the combined  $C_{hetero}$  and  $C_{alkyl}$  signal in  $80^\circ$  to obtain the corrected  $C_{alkyl}$  intensity in  $80^\circ$  emission. This re-evaluation provides corrected  $I(C_{alkyl}) / I(C_{hetero})$  ratios in  $80^\circ$  with a higher accuracy (about  $\pm 8\%$ ), and reveals that the surface enrichment of the long alkyl chains was underestimated previously.<sup>[99]</sup> In Figure 4.1a, the corrected  $80^\circ$  ratios (full red squares) systematically lay above the previously published ratios (open red triangles).

For the comparison with the corrected ARXPS results, density profiles of the MD simulations, performed by Dr. Karina Shimizu, are analyzed assuming an exponential decay of the contribution as expected from the ARXPS signal attenuation depicted in Figure 2.3. From these surface profiles, the ratios of the terminal methyl carbon atom of the alkyl chain (representing  $C_{alkyl}$ ) and the  $C_2$  atom (representing  $C_{hetero}$ ), weighted by the respective nominal atom numbers of these atoms,  $(n-1) / 5$ , are shown in Figure 4.1a as crosses ( $0^\circ$  in black and  $80^\circ$  in red) to obtain the respective simulated  $C_{alkyl}$  to  $C_{hetero}$  ratio. Considering the assumptions made for the simulations, the corrected experimental and simulated ratios overall are in good agreement.

To derive the experimental surface tension values<sup>[86]</sup> from MD simulations using the Langmuir principle, the cationic head groups (represented by the  $C_2$  atom) and the  $[Tf_2N]^-$  anions (represented by the  $N_{Tf_2N}$  atom) are assumed to contribute equally to the surface tension of 36.3 mN/m for  $[C_1C_1Im][Tf_2N]$ . Furthermore, the nearly constant

surface tension of 29.5 mN/m for  $[C_nC_1Im][Tf_2N]$  with  $n = 8, 10$  and 12 (blue triangles in Figure 4.1b) is assumed to be built up only by the surface alkyl chains (represented by the terminal methyl carbon atom). Then, the surface tension for each of the  $[C_nC_1Im][Tf_2N]$  ILs is calculated by the sum over the contributions of the three different atoms being present at the MD simulated outer surface (note that the atoms are weighted by their respective molar volume). Comparing the values received from the simulations with the measured surface tension values, they are in good agreement assuming an outer surface layer thickness of 0.54 up to 0.93 nm for  $[C_nC_1Im][Tf_2N]$  with  $n = 2$  to 12, that would correspond to an emission angle of  $87.5^\circ$  in ARXPS (see Figure 4.1b). Note that such pronounced grazing emission conditions are impractical for our ARXPS setup due to sample holder shielding. In contrast, the employed  $80^\circ$  geometry probes between 0.91 and 1.31 nm for  $[C_2C_1Im][Tf_2N]$  and  $[C_{12}C_1Im][Tf_2N]$ , respectively, which is more than just the topmost surface layer of the ILs as it is evident from Figure 2.3.



**Figure 4.1:** a)  $C_{alkyl} / C_{hetero}$  ratios for varying alkyl chain length,  $n$ , in the  $[C_nC_1Im][Tf_2N]$  series. The corrected ARXP intensity ratios are given as full squares and the earlier published (earlier pub.) intensity ratios as open triangles for  $0^\circ$  (black) and  $80^\circ$  (red) emission, respectively. The ratios deduced from the density profile analysis (simulation) using an exponential decay are included as crosses. The nominally expected  $C_{alkyl} / C_{hetero}$  ratio is indicated by the dashed gray line. b) Surface tension values for varying alkyl chain length,  $n$ , in the  $[C_nC_1Im][Tf_2N]$  series. The blue triangles refer to the experimentally obtained surface tension values (exp. data)<sup>[86]</sup> and the crosses represent the values obtained from the density profile analysis assuming ARXP emission angles of  $0^\circ$  (black),  $80^\circ$  (red) and  $87.5^\circ$  (green). The surface tension of the bulk composition using the Langmuir principle is given as dashed gray line. Adapted from [P1] with permission from “Langmuir”.

In this investigation, the concept formulated by Langmuir about 100 years ago was most likely used in such explicit way for the first time to understand the surface tension data of highly structured fluids such as ILs. Combining ARXPS measurements and MD

simulations, the composition of the outer surface could be determined consistently, and a correct estimation of the complex surface tension trend within the  $[C_nC_1Im][Tf_2N]$  series could be derived applying the Langmuir principle of surface group contributions in a quantitative way.



## 4.2 Binary Mixtures Containing Functionalized Ionic Liquids

Over the last two decades, many surface science studies have been carried out revealing information about the surface composition and electronic structure of neat ILs containing a wide variety of cations and anions.<sup>[8, 42-53, 61-64, 67-72, 87, 99, 107-122]</sup> To extend this understanding, IL mixtures got more into the focus of research recently. Up to now, mainly mixtures of two non-functionalized imidazolium-based ILs<sup>[8, 9, 44, 50-52, 54-56, 58-61, 63-67]</sup> have been investigated and only few examples are found in literature discussing mixtures containing functionalized imidazolium-based cations.<sup>[45, 60, 70]</sup>

The aim of this chapter is to extend the knowledge about the surface composition of interesting methoxy-functionalized ( $[(\text{MeO})_2\text{Im}][\text{PF}_6]$ ) and fluorinated ( $[\text{PFBMIm}][\text{PF}_6]$ ) ILs. Oxygen atoms, like in the methoxy groups of  $[(\text{MeO})_2\text{Im}][\text{PF}_6]$ , are additional hydrogen bond acceptor sites in the ILs resulting in promising properties *e.g.* for the extraction of estrogens or analgesics from aqueous solutions and the dissolution of greenhouse gases like  $\text{N}_2\text{O}$  and  $\text{CO}_2$ .<sup>[27, 88, 123-126]</sup> Furthermore, the oxygen functionalization can decrease the toxicity as well as increase the biodegradability of the ILs.<sup>[127, 128]</sup> Fluorinated chains such as in  $[\text{PFBMIm}][\text{PF}_6]$  tend to agglomerate forming fluorine domains in addition to the well-known polar and non-polar domains in non-fluorinated ILs.<sup>[3, 70, 71, 129]</sup> Generally, properties and domain structures of ILs can be tuned by changing the chain length in neat ILs and the composition in IL mixtures.<sup>[4, 60, 70]</sup> Commonly, the surface tension of fluorinated ILs is lower compared to their alkylated analogues<sup>[60, 130, 131]</sup> and they are potential candidates to replace harmful fluorine-containing solvents like lubricants, coolants in refrigerators and others.<sup>[4, 129]</sup>

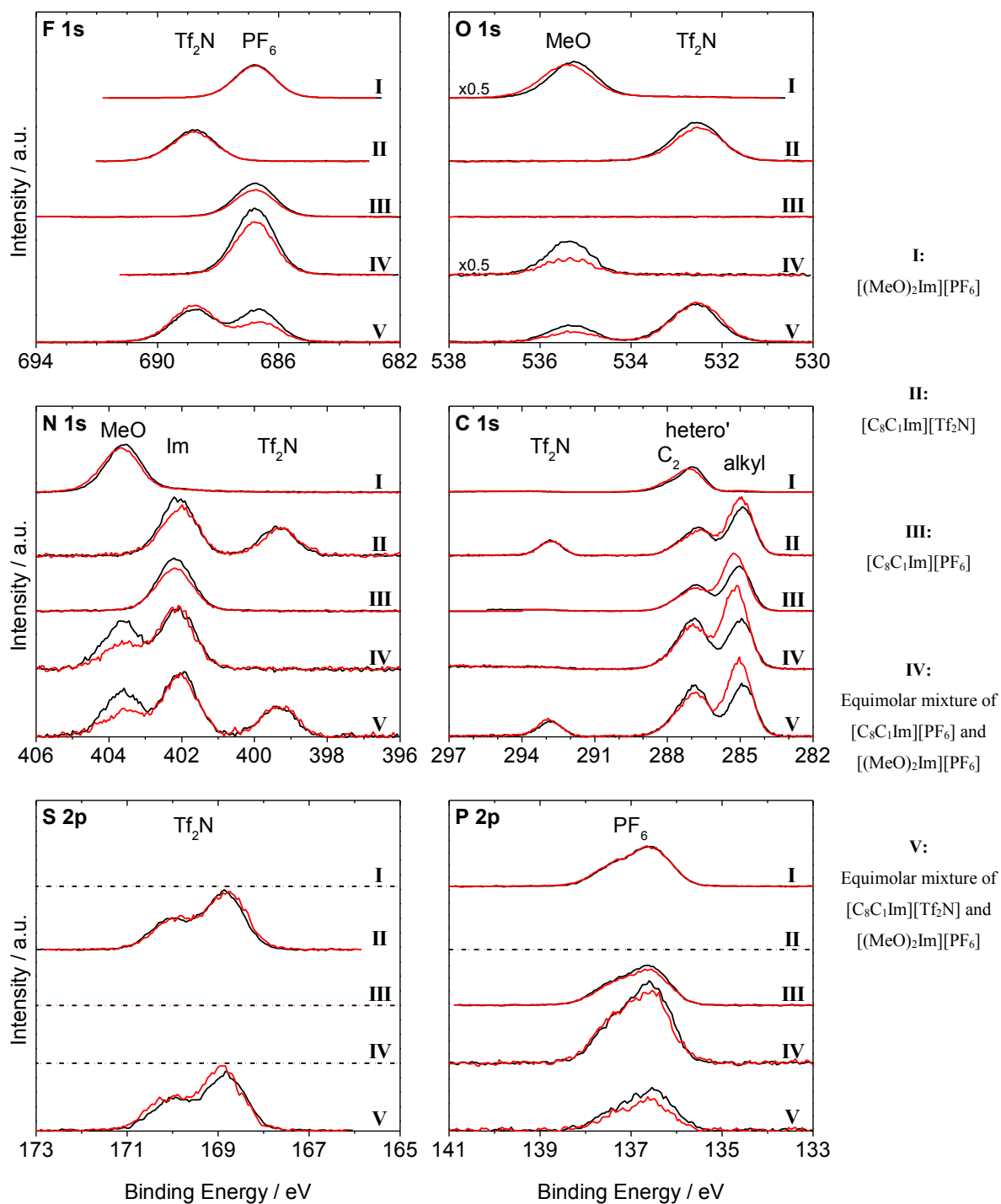
In this chapter, the knowledge about the surface enrichment and depletion effects is extended to binary IL mixtures containing both non-functionalized and functionalized cations as well as mixtures with methoxy-functionalized and fluorinated imidazolium-based cations. In addition, the effect of temperature on the surface enrichment and depletion is studied.

### 4.2.1 Equimolar Mixtures of Methoxy- and Non-Functionalized Ionic Liquids<sup>[P2]</sup>

Surface enrichment and depletion effects have been investigated in equimolar binary mixtures of a methoxy-functionalized IL, [(MeO)<sub>2</sub>Im][PF<sub>6</sub>], and two non-functionalized ILs, [C<sub>8</sub>C<sub>1</sub>Im][PF<sub>6</sub>] and [C<sub>8</sub>C<sub>1</sub>Im][Tf<sub>2</sub>N]. The neat ILs as well as the mixtures are all studied at 90 °C to ensure measurements in their liquid state. Both mixtures either consist of ILs with a common [PF<sub>6</sub>]<sup>-</sup> anion and two different cations, or are composed of four different ions.

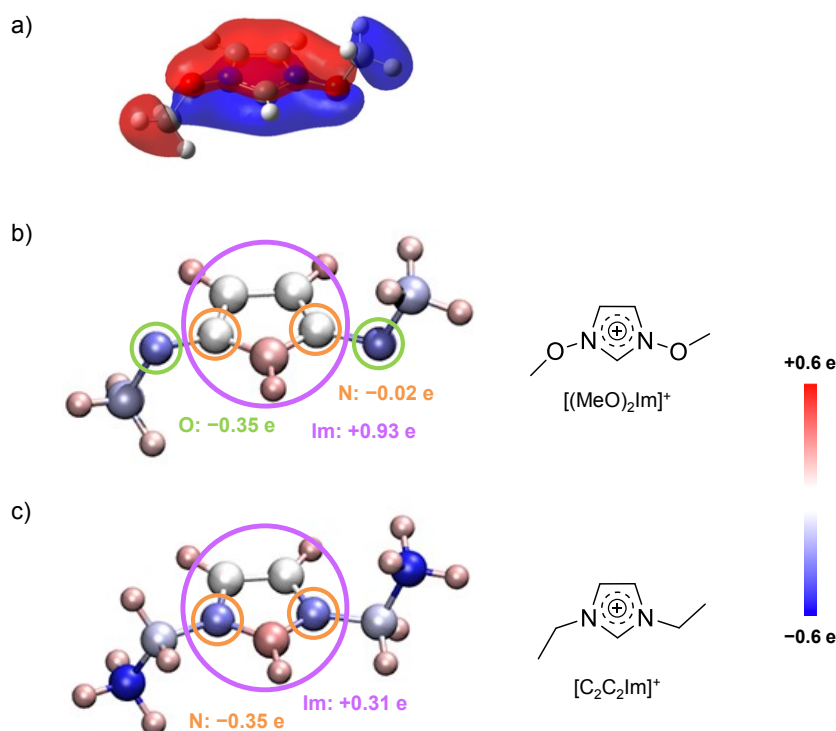
Due to unique core level signals and chemical shifts of the various ions in ARXPS, it is possible to distinguish between both cations, [(MeO)<sub>2</sub>Im]<sup>+</sup> and [C<sub>8</sub>C<sub>1</sub>Im]<sup>+</sup>, as well as between the two anions, [PF<sub>6</sub>]<sup>-</sup> and [Tf<sub>2</sub>N]<sup>-</sup>. In [(MeO)<sub>2</sub>Im][PF<sub>6</sub>], the two oxygen atoms, O<sub>MeO</sub>, directly bound to the nitrogen atoms of the imidazolium ring influence the electronic structure of the cation strongly, resulting in a binding energy of 403.6 eV for the N<sub>MeO</sub> signal of the cation. In contrast, the N<sub>Im</sub> signal of the [C<sub>8</sub>C<sub>1</sub>Im]<sup>+</sup> cation is located at 402.2 eV, corresponding to a shift of ~1.4 eV (see Figure 4.2–I, II and III). Furthermore, the carbon atoms of the imidazolium ring of the [(MeO)<sub>2</sub>Im]<sup>+</sup> cation are shifted to higher binding energy by 0.2 to 0.4 eV, compared to the C<sub>2</sub> and C<sub>hetero</sub> peaks of [C<sub>8</sub>C<sub>1</sub>Im]<sup>+</sup>. The O<sub>MeO</sub> signal is located at 535.3 eV, that is, ~2.7 eV higher compared to the O<sub>Tf2N</sub> peak of [C<sub>8</sub>C<sub>1</sub>Im][Tf<sub>2</sub>N] at 532.6 eV (see Figure 4.2–I and II).

These strong chemical shifts of the [(MeO)<sub>2</sub>Im]<sup>+</sup> cation are remarkable and will be discussed first. In literature, only very few examples of such high oxygen binding energies are reported, *e.g.* in peroxy-oxygen-functionalized polymers.<sup>[132]</sup> Typically, oxygen atoms located in the chains of IL cations, like in the polyethylene glycol-functionalized IL [Me(EG)<sub>2</sub>C<sub>1</sub>Im][Tf<sub>2</sub>N], exhibit binding energies of ~532.7 eV which is very similar to the binding energy position of the oxygen atoms in the [Tf<sub>2</sub>N]<sup>-</sup> anions.<sup>[96, 99]</sup> Moreover, the N 1s binding energy of the nitrogen atoms of the imidazolium ring of this IL and [C<sub>8</sub>C<sub>1</sub>Im][Tf<sub>2</sub>N] is about the same, excluding a pronounced impact of the oxygen functionality on the electronic structure of the [Me(EG)<sub>2</sub>C<sub>1</sub>Im]<sup>+</sup> head group. Very recently, other ether-functionalized ILs have been investigated by XPS revealing negligible binding energy shifts in the N 1s region and, compared to [(MeO)<sub>2</sub>Im][PF<sub>6</sub>], only small O 1s peak shifts.<sup>[68]</sup>



**Figure 4.2:** ARXP spectra of the neat ILs  $[(\text{MeO})_2\text{Im}][\text{PF}_6]$  (I),  $[\text{C}_8\text{C}_1\text{Im}][\text{Tf}_2\text{N}]$  (II) and  $[\text{C}_8\text{C}_1\text{Im}][\text{PF}_6]$  (III), and the equimolar mixture of  $[\text{C}_8\text{C}_1\text{Im}][\text{PF}_6]$  and  $[(\text{MeO})_2\text{Im}][\text{PF}_6]$  (IV) and the equimolar mixture of  $[\text{C}_8\text{C}_1\text{Im}][\text{Tf}_2\text{N}]$  and  $[(\text{MeO})_2\text{Im}][\text{PF}_6]$  (V) recorded under  $0^\circ$  (black) and  $80^\circ$  (red) emission. The sample temperature was  $90^\circ\text{C}$ . Adapted in part from [P2] under license CC BY-NC 4.0.

These particularly large chemical shifts of the XP signals of  $[(\text{MeO})_2\text{Im}][\text{PF}_6]$  are due to the extraordinary electronic structure of this cation. Density Functional Theory (DFT) calculations combined with charge distribution analysis using the natural bond orbital (NBO) methodology, performed in a collaboration by Prof. Dr. Patricia Hunt, showed that the positive charge in the cationic head group is distributed over the imidazolium ring and the adjacent oxygen atoms,  $\text{O}_{\text{MeO}}$ , resulting in an extended aromatic system (see Figure 4.3a). In contrast to the non-functionalized analogue cation,  $[\text{C}_2\text{C}_2\text{Im}]^+$ , the whole imidazolium ring of the  $[(\text{MeO})_2\text{Im}]^+$  cation (see Figure 4.3b) has a more positive charge of  $+0.93 \text{ e}$  (vs.  $+0.31 \text{ e}$  for  $[\text{C}_2\text{C}_2\text{Im}]^+$ ; see Figure 4.3c). As a consequence, the charge on the nitrogen atoms,  $\text{N}_{\text{MeO}}$ , of the  $[(\text{MeO})_2\text{Im}]^+$  cation shows a more positive value of  $-0.02 \text{ e}$  compared to  $-0.35 \text{ e}$  for the  $\text{N}_{\text{Im}}$  atoms of the  $[\text{C}_2\text{C}_2\text{Im}]^+$  cation.



**Figure 4.3:** a) Molecular orbital of  $[(\text{MeO})_2\text{Im}]^+$  showing the aromatic delocalization of the positive charge over the imidazolium ring and the  $\text{O}_{\text{MeO}}$  atoms. The NBO charge distribution at the atoms of the b)  $[(\text{MeO})_2\text{Im}]^+$  cation and c)  $[\text{C}_2\text{C}_2\text{Im}]^+$  cation. Red is positive and blue is negative. The charges localized in the imidazolium ring (purple) and on the nitrogen (orange) and oxygen (green) atoms are given. Adapted from [P2] under license CC BY-NC 4.0.

Next, the composition of the first 7 to 9 nm, as probed by the  $0^\circ$  XPS measurement, of the equimolar mixture of  $[\text{C}_8\text{C}_1\text{Im}][\text{PF}_6]$  and  $[(\text{MeO})_2\text{Im}][\text{PF}_6]$  will be discussed, *i.e.* the mixture with two different cations but the common  $[\text{PF}_6]^-$  anion. The cationic head groups of the ILs can be easily distinguished due to the well-separated  $\text{N}_{\text{MeO}}$  and  $\text{N}_{\text{Im}}$  peaks in the

N 1s region (see black spectrum in Figure 4.2–IV). Instead of the 1 : 1 ratio of the two nitrogen species expected for the equimolar bulk composition, the N 1s spectrum exhibits a  $N_{\text{Im}}$  to  $N_{\text{MeO}}$  ratio of 1 : 0.85 in  $0^\circ$  emission. This means that within the  $0^\circ$  XPS probing depth, a pronounced depletion of the  $[(\text{MeO})_2\text{Im}]^+$  cation from the topmost layers is found leaving the surface region enriched by the  $[\text{C}_8\text{C}_1\text{Im}]^+$  cation.

The depletion of the  $[(\text{MeO})_2\text{Im}]^+$  cation from the near-surface region is also found for the equimolar mixture of  $[\text{C}_8\text{C}_1\text{Im}][\text{Tf}_2\text{N}]$  and  $[(\text{MeO})_2\text{Im}][\text{PF}_6]$ , *i.e.* the mixture with two different cations and two different anions. The intensities of the  $N_{\text{Im}}$  and  $N_{\text{MeO}}$  peaks in  $0^\circ$  (black) emission (see Figure 4.2–V) reveals a 1 : 0.77 ratio instead of the expected 1 : 1 ratio. This indicates an even more pronounced depletion of the  $[(\text{MeO})_2\text{Im}]^+$  cation from the near-surface region in comparison to the previously discussed mixture with the common  $[\text{PF}_6]^-$  anion. This difference is possibly related to the slight surface enrichment of the  $[\text{Tf}_2\text{N}]^-$  anion in the second mixture. In the F 1s region with the two peaks corresponding to the six fluorine atoms of the  $[\text{Tf}_2\text{N}]^-$  anion at 688.8 eV and of the  $[\text{PF}_6]^-$  anion at 686.7 eV (see Figure 4.2–V) the  $F_{\text{Tf}_2\text{N}}$  signal is  $\sim 14\%$  larger than the  $F_{\text{PF}_6}$  peak instead of the expected 1 : 1 ratio.

The overall surface enrichment and depletion effects within the first 7 to 9 nm probed in  $0^\circ$  emission are much more pronounced when focusing on the outermost 1 to 1.5 nm investigated under  $80^\circ$  emission. In the following, surface enrichment and depletion effects of the neat ILs are briefly pointed out. Figure 4.2–I shows the ARXP spectra of  $[(\text{MeO})_2\text{Im}][\text{PF}_6]$  in  $0^\circ$  (black) and  $80^\circ$  (red) emission, revealing no changes in intensity ruling out strong preferential orientation in the surface layer. In contrast, the octyl chains of neat  $[\text{C}_8\text{C}_1\text{Im}][\text{Tf}_2\text{N}]$  and  $[\text{C}_8\text{C}_1\text{Im}][\text{PF}_6]$  are surface-enriched as indicated by a higher  $C_{\text{alkyl}}$  intensity in  $80^\circ$  compared to  $0^\circ$  (see Figure 4.2–II and III). The  $[\text{Tf}_2\text{N}]^-$  anion signals of  $[\text{C}_8\text{C}_1\text{Im}][\text{Tf}_2\text{N}]$  show a minor enrichment of the  $\text{CF}_3$  groups along with a slight depletion of the  $\text{SO}_2$  groups detected in the O 1s spectrum due to the lower kinetic energy (as compared to the S 2p signal). In the F 1s and P 2p spectra, a depletion of the  $[\text{PF}_6]^-$  anion is observed for  $[\text{C}_8\text{C}_1\text{Im}][\text{PF}_6]$  (see Figure 4.2–III).

For both IL mixtures, the surface enrichment of the  $[\text{C}_8\text{C}_1\text{Im}]^+$  cation at the expense of the  $[(\text{MeO})_2\text{Im}]^+$  cation is more obvious in the  $80^\circ$  spectra (red in Figure 4.2–IV and V) compared to  $0^\circ$ . The  $N_{\text{MeO}}$  signal is lower at  $80^\circ$  emission whereas the  $N_{\text{Im}}$  signal has almost identical signal intensities under both emission angles. The  $\text{O}_{\text{MeO}}$  peak in the O 1s

spectra decreases roughly by the same amount as the  $N_{\text{MeO}}$  signal validating the accuracy of the measurement as these two atoms are directly bound to each other. This is in line with the observations that the  $[\text{C}_8\text{C}_1\text{Im}]^+$  cation is surface-enriched at the IL/vacuum interface with its octyl chain pointing towards the vacuum as the  $C_{\text{alkyl}}$  signal gains intensity when going from  $0^\circ$  to  $80^\circ$  emission. Most likely, the driving force for the surface enrichment of the  $[\text{C}_8\text{C}_1\text{Im}]^+$  cation and the depletion of the  $[(\text{MeO})_2\text{Im}]^+$  cation is to obtain an overall low surface tension. Unfortunately, the surface tension value for  $[(\text{MeO})_2\text{Im}][\text{PF}_6]$  is not known but the surface tension for ILs with the same anion but different alkyl chain lengths are available in literature.<sup>[71, 86, 111, 133-135]</sup> In general, the IL containing the longer alkyl chain, in this case  $[\text{C}_8\text{C}_1\text{Im}][\text{X}]$ , possesses a lower surface tension compared to that with a short chain. Moreover, oxygen atoms in the side chain might increase the surface tension in addition.<sup>[86]</sup>

For the  $[\text{Tf}_2\text{N}]^-$  and  $[\text{PF}_6]^-$  anions in the equimolar mixture of  $[\text{C}_8\text{C}_1\text{Im}][\text{Tf}_2\text{N}]$  and  $[(\text{MeO})_2\text{Im}][\text{PF}_6]$ , the enrichment and depletion in the first 1 to 1.5 nm is directly visible in the F 1s spectrum recorded at  $80^\circ$  (see Figure 4.2–V). The  $F_{\text{Tf}_2\text{N}}$  peak is about two times higher than the  $F_{\text{PF}_6}$  peak. This pronounced surface enrichment of the  $[\text{Tf}_2\text{N}]^-$  anion on expense of the  $[\text{PF}_6]^-$  anion goes along with the surface tension values of ILs consisting of the respective anion and a common cation. The surface tension of  $[\text{C}_8\text{C}_1\text{Im}][\text{PF}_6]$  is 32.5 mN/m whereas  $[\text{C}_8\text{C}_1\text{Im}][\text{Tf}_2\text{N}]$  has a lower surface tension of 29.5 mN/m which supports the observed enrichment of the  $[\text{Tf}_2\text{N}]^-$  anion.<sup>[86]</sup>

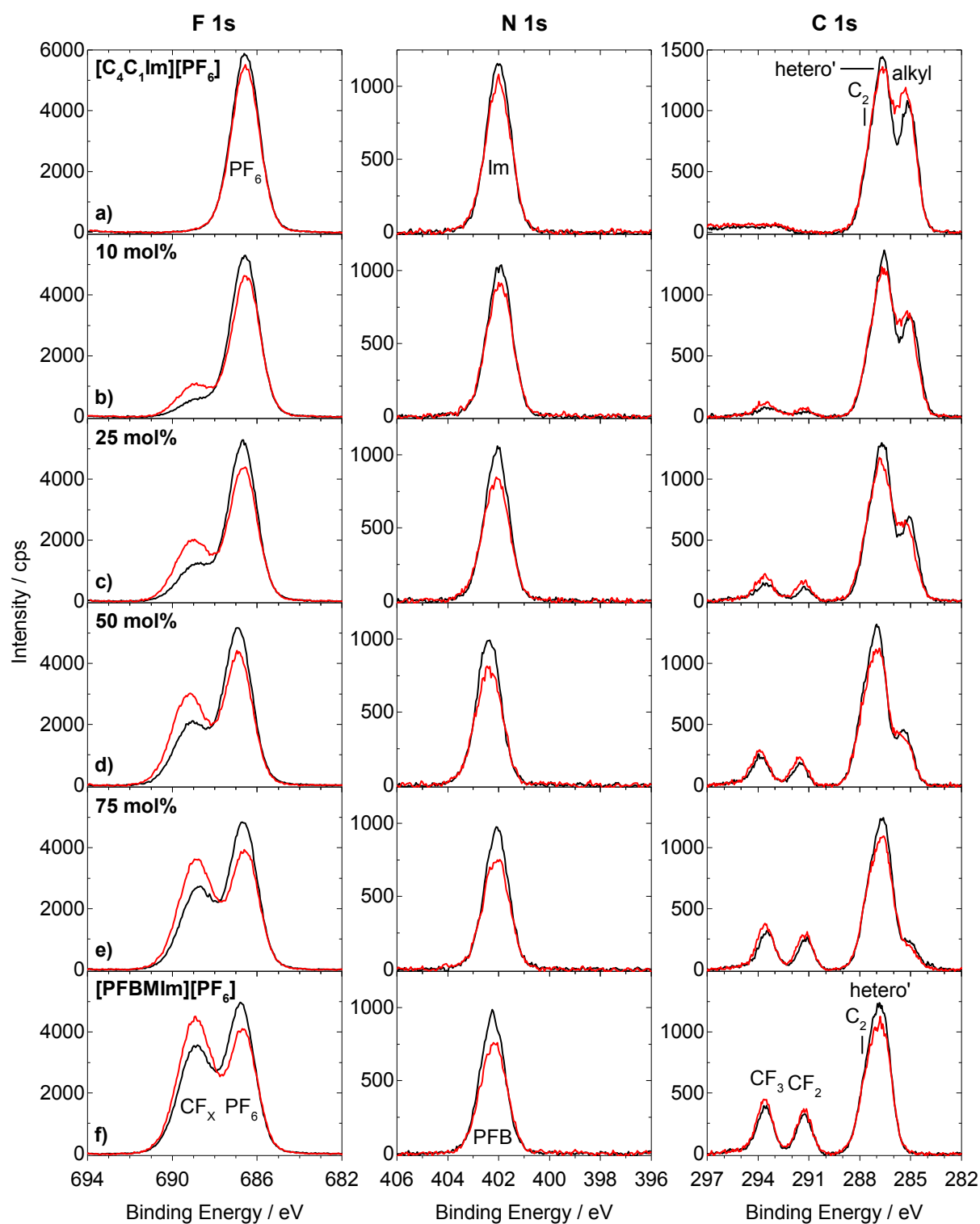
#### 4.2.2 Mixtures of Fluorinated and Non-Fluorinated Ionic Liquids<sup>[P3]</sup>

Mixtures of  $[\text{PFBMIm}][\text{PF}_6]$  and  $[\text{C}_4\text{C}_1\text{Im}][\text{PF}_6]$  have been investigated with different molar content of  $[\text{PFBMIm}][\text{PF}_6]$  by means of temperature-dependent ARXPS from  $95^\circ\text{C}$  to their onset of solidification. Both ILs consist of the same  $[\text{PF}_6]^-$  anion whereas the cation differs in the functionalization of the butyl chain. In contrast to the fully hydrogenated chain in the  $[\text{C}_4\text{C}_1\text{Im}]^+$  cation, the two terminal carbon atoms in the chain of the  $[\text{PFBMIm}]^+$  cation are fully fluorinated, resulting in a pentafluorobutyl (PFB) chain. Due to the differences in the chemical environment of the fluorine atoms in the  $[\text{PF}_6]^-$  anion compared to the ones in the  $[\text{PFBMIm}]^+$  cation, two distinct peaks are detected in the F 1s region. Also the carbon atoms in both butyl chains are in different chemical environments leading to chemical shifts in the C 1s spectrum.

Starting with the neat ILs at 95 °C, the  $C_{\text{alkyl}}$  peak in the C 1s spectrum of  $[\text{C}_4\text{C}_1\text{Im}][\text{PF}_6]$  (at  $\sim 285.1$  eV) is more intense in 80° (red) emission compared to 0° (black) (see Figure 4.4a–right panel), showing a slight surface enrichment of the butyl chain, as it is known from literature<sup>[53, 99]</sup> for  $[\text{C}_n\text{C}_1\text{Im}]^+$  cations with an alkyl chain with  $n \geq 4$ . In contrast, all the other IL signals are lower in intensity in 80° with respect to the 0° measurement as depicted for the F 1s (left panel) and N 1s (middle panel) spectra in Figure 4.4a.

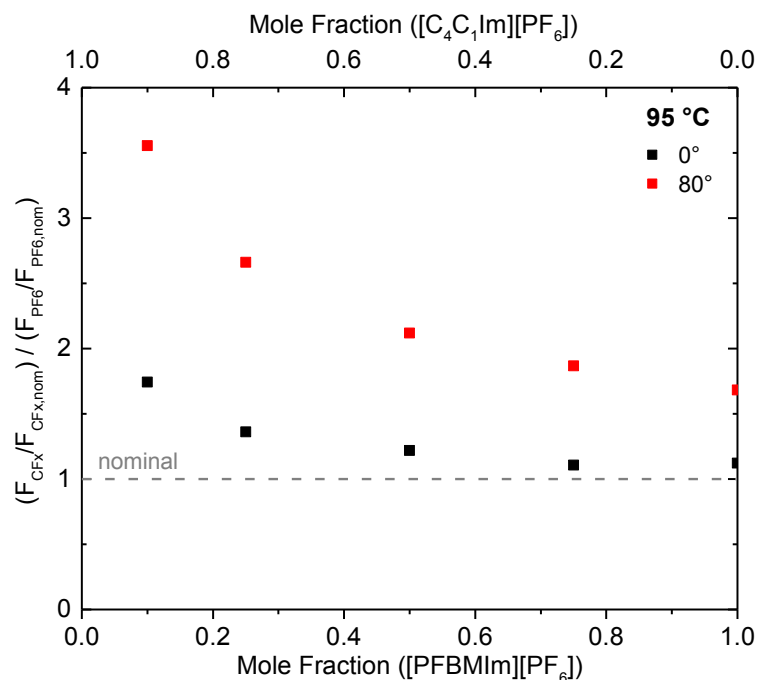
The ARXP spectra of  $[\text{PFBMIm}][\text{PF}_6]$  in Figure 4.4f show an increase of the 80° intensity of the  $F_{\text{CF}_x}$  ( $\text{CF}_x = \text{CF}_2 + \text{CF}_3$ ) peak at 688.9 eV in the F 1s spectrum and an increase of the  $C_{\text{CF}_3}$  and  $C_{\text{CF}_2}$  peaks at 293.6 and 291.3 eV, respectively, in the C 1s spectrum. The  $F_{\text{PF}_6}$  and  $P_{\text{PF}_6}$  signals of the anion at 686.8 and 137.0 eV, respectively, as well as the  $N_{\text{PFB}}$ ,  $C_2$  and  $C_{\text{hetero}}$  signals of the cationic head group at 402.2, 287.8 and 286.8 eV, respectively, are damped by the surface-enriched fluorinated chain.

Mixing  $[\text{PFBMIm}][\text{PF}_6]$  and  $[\text{C}_4\text{C}_1\text{Im}][\text{PF}_6]$  in molar ratios of 10, 25, 50 and 75 mol%  $[\text{PFBMIm}][\text{PF}_6]$  shows the same binding energy positions (within the margin of error) like in the neat ILs. Compared to neat  $[\text{PFBMIm}][\text{PF}_6]$ , a more pronounced surface enrichment of the fluorinated chain is observed in the ARXP spectra (see Figure 4.4b – e). In Figure 4.5, this is better visualized showing the normalized ratio of the  $F_{\text{CF}_x}$  and  $F_{\text{PF}_6}$  content with respect to the molar ratio of the two ILs. For the 80° measurements, a higher  $(F_{\text{CF}_x}/F_{\text{CF}_x,\text{nom}}) / (F_{\text{PF}_6}/F_{\text{PF}_6,\text{nom}})$  ratio is detected, the lower the amount of  $[\text{PFBMIm}][\text{PF}_6]$  in the mixture. This indicates a more pronounced surface enrichment of the fluorinated chain (compared to the nominal bulk composition) with decreasing  $[\text{PFBMIm}][\text{PF}_6]$  content. This enrichment is so pronounced that it is also detected in 0° emission for mixtures with 10 and 25 mol%  $[\text{PFBMIm}][\text{PF}_6]$ . A non-stoichiometric IL distribution in the near-surface region was recently also found for other IL systems by our group and others.<sup>[54, 96, 136]</sup> In contrast to the surface-enriched fluorinated chain, the alkyl chain of the  $[\text{C}_4\text{C}_1\text{Im}]^+$  cation shows no surface enrichment in the mixtures (see Figure 4.4b – e–right panel). This is attributed to a competing effect of the fluorinated and non-fluorinated chain most likely driven by the difference in surface tension of both ILs since it is known that non-functionalized ILs usually possess a higher surface tension compared to their fluorinated analogues.<sup>[60, 130, 131]</sup>



**Figure 4.4:** ARXP spectra recorded at  $0^\circ$  (black) and  $80^\circ$  (red) emission of a) neat  $[\text{C}_4\text{C}_1\text{Im}][\text{PF}_6]$ , b) – e) mixtures of  $[\text{PFBMIm}][\text{PF}_6]$  and  $[\text{C}_4\text{C}_1\text{Im}][\text{PF}_6]$  at molar ratios of b) 10 mol%  $[\text{PFBMIm}][\text{PF}_6]$ , c) 25 mol%  $[\text{PFBMIm}][\text{PF}_6]$ , d) 50 mol%  $[\text{PFBMIm}][\text{PF}_6]$  and e) 75 mol%  $[\text{PFBMIm}][\text{PF}_6]$ , and f) neat  $[\text{PFBMIm}][\text{PF}_6]$ : F 1s (left), N 1s (middle) and C 1s (right). The sample temperature was  $95^\circ\text{C}$ . Reproduced from [P3] under license CC BY 4.0.

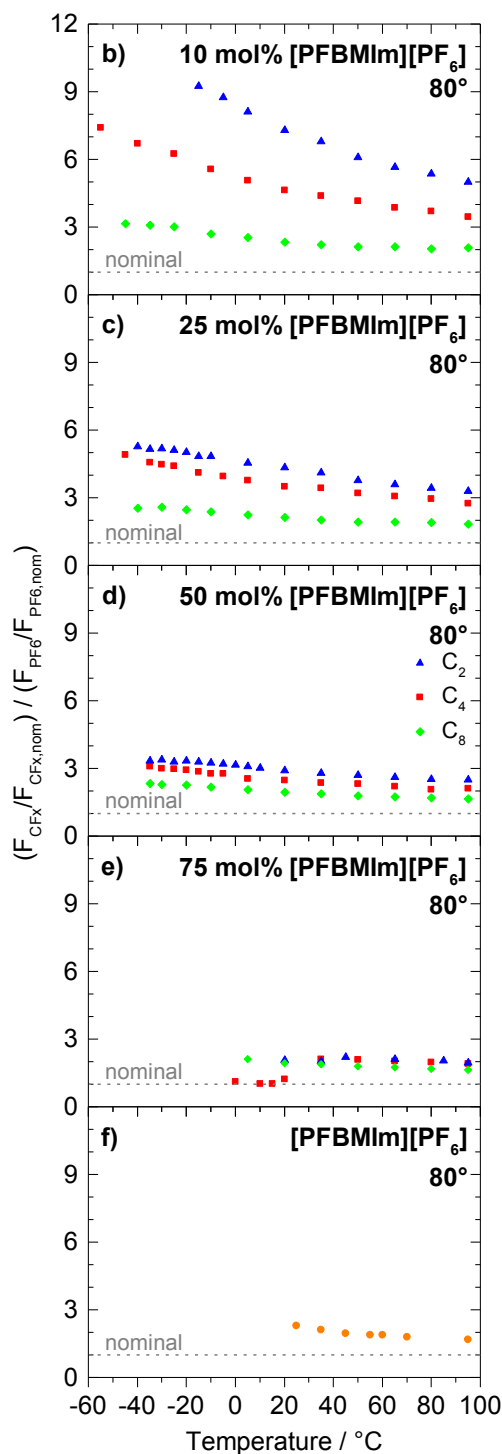




**Figure 4.5:** Normalized ratio of  $F_{\text{CFX}}$  and  $F_{\text{PF}_6}$  at  $0^\circ$  (black) and  $80^\circ$  (red) emission. The gray dashed line indicates the nominal composition. The sample temperature was  $95^\circ\text{C}$ . Adapted from [P3] under license CC BY 4.0.

In the following, temperature-dependent measurements are analyzed focusing on the  $80^\circ$  emission spectra, due to the higher surface sensitivity under this emission angle. By decreasing the temperature starting at  $95^\circ\text{C}$ , an increase of the  $C_{\text{alkyl}}$  signal in the C 1s spectrum of neat  $[\text{C}_4\text{C}_1\text{Im}][\text{PF}_6]$  is detected until  $-55^\circ\text{C}$ , indicating a more pronounced surface enrichment of the butyl chain. Concomitantly, the cationic head group and the  $[\text{PF}_6]^-$  anion are more surface-depleted, as indicated by the decrease of intensity of the  $\text{C}_2$ ,  $\text{C}_{\text{hetero}}$ , and  $F_{\text{PF}_6}$  peaks. In literature,<sup>[43]</sup> such intensity changes with decreasing temperature are assigned to an increase in preferential orientation of the IL ions at the outer surface. This is attributed to an increase in entropy with a more random distribution of the alkyl chains at higher temperature.

When cooling neat  $[\text{PFBMIm}][\text{PF}_6]$  from  $95$  to  $25^\circ\text{C}$ , a moderate decrease of the  $F_{\text{PF}_6}$  signal is detected in  $80^\circ$  without significant changes of the  $F_{\text{CFX}}$  peak intensity in the F 1s region. This shows a small increase of the surface enrichment of the fluorinated chain at the IL/vacuum interface compared to the surface depletion of the  $[\text{PF}_6]^-$  anion. In Figure 4.6f, this enrichment is depicted as an increase of the normalized ratio of  $F_{\text{CFX}}$  and  $F_{\text{PF}_6}$  when lowering the temperature. At  $20^\circ\text{C}$ , peak broadening due to solidification of  $[\text{PFBMIm}][\text{PF}_6]$  is detected.

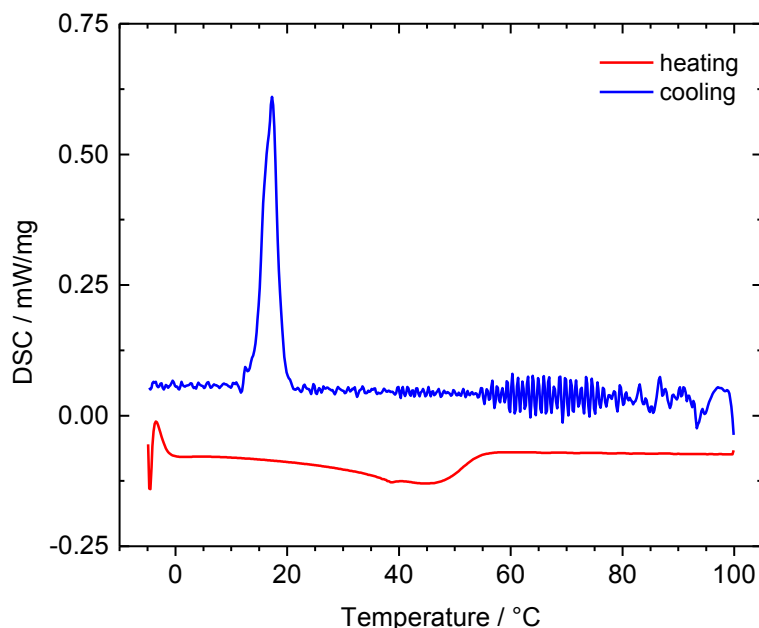


**Figure 4.6:** Normalized ratio of  $F_{\text{CFX}}$  and  $F_{\text{PF}_6}$  at  $80^\circ$  emission. The measurements were started at a sample temperature of  $95^\circ\text{C}$  and subsequently cooled. a) Neat  $[\text{C}_n\text{C}_1\text{Im}][\text{PF}_6]$ : Not shown due to the lack of a  $F_{\text{CFX}}$  signal of a fluorinated chain in the ILs, b) – e) mixtures of  $[\text{PFBMIm}][\text{PF}_6]$  with  $[\text{C}_n\text{C}_1\text{Im}][\text{PF}_6]$  ( $n = 2$ –blue triangles, 4–red squares, 8–green diamonds) at molar ratios of b) 10 mol%  $[\text{PFBMIm}][\text{PF}_6]$ , c) 25 mol%  $[\text{PFBMIm}][\text{PF}_6]$ , d) 50 mol%  $[\text{PFBMIm}][\text{PF}_6]$  and e) 75 mol%  $[\text{PFBMIm}][\text{PF}_6]$ , and f) neat  $[\text{PFBMIm}][\text{PF}_6]$ . The gray dashed lines indicate the nominal compositions. Adapted in part from [P3] under license CC BY 4.0.

As a next step, the 10, 25 and 50 mol% mixtures of [PFBMIm][PF<sub>6</sub>] and [C<sub>4</sub>C<sub>1</sub>Im][PF<sub>6</sub>] are cooled from 95 °C until their onset of solidification, indicated by peak broadening and/or peak shifts. Depending on the composition, differences in the temperature of solidification of the supercooled mixtures are observed, *i.e.* the lower the [PFBMIm][PF<sub>6</sub>] content, the lower is the onset of solidification. In general, during cooling the F<sub>CF<sub>x</sub></sub> peak gains intensity which leads to an increase of the normalized ratio of F<sub>CF<sub>x</sub></sub> and F<sub>PF<sub>6</sub></sub> as shown in Figure 4.6b – d (red squares) at 80° emission. The observed behavior is again attributed to an increase in order at low temperature. In accordance with the F<sub>CF<sub>x</sub></sub> signal, the surface enrichment of the fluorinated chain at the IL/vacuum interface is also observed in the C 1s region by an increase of the C<sub>CF<sub>3</sub></sub> and C<sub>CF<sub>2</sub></sub> intensities.

Cooling the 75 mol% [PFBMIm][PF<sub>6</sub>] mixture from 95 to 35 °C shows the same surface enrichment behavior of the fluorinated chain of the [PFBMIm]<sup>+</sup> cation as observed for the other three mixtures previously discussed. When cooling further to 20 °C, a drastic drop of the normalized ratio of F<sub>CF<sub>x</sub></sub> and F<sub>PF<sub>6</sub></sub> is detected (red squares in Figure 4.6e), resulting from a decrease of the F<sub>CF<sub>x</sub></sub> intensity by ~40% whereas the F<sub>PF<sub>6</sub></sub> intensity stays constant. In the C 1s spectrum, a simultaneous decrease of the C<sub>CF<sub>3</sub></sub> and C<sub>CF<sub>2</sub></sub> signals is observed while the C<sub>alkyl</sub> signal of the [C<sub>4</sub>C<sub>1</sub>Im]<sup>+</sup> cation gains intensity. Upon further cooling, no additional changes are observed in the XP spectra until at around –10 °C peak broadening due to solidification starts. The sudden intensity decrease of the signals of the fluorinated chain of the [PFBMIm]<sup>+</sup> cation is attributed to a partial depletion of this cation from the XPS detection volume, resulting in a [C<sub>4</sub>C<sub>1</sub>Im]<sup>+</sup>-rich mixture at the IL/vacuum interface. This is indicated by the increase of the signal of the butyl chain.

Indeed, the differential scanning calorimetry (DSC) measurement of the 75 mol% mixture (performed by Dr. Mikhail Gantman) in Figure 4.7 shows an exothermal peak at around 18 °C when cooling (blue) the sample which is attributed to the solidification of parts of the mixture. Subsequently, heating the 75 mol% [PFBMIm][PF<sub>6</sub>] mixture up to 95 °C shows the same ARXP spectra (within the margin of error) as before starting the cooling series. This indicates the reversibility of the experiment.



**Figure 4.7:** DSC measurement of a 75 mol% mixture of [PFBMIm][PF<sub>6</sub>] and [C<sub>4</sub>C<sub>1</sub>Im][PF<sub>6</sub>] showing the solidification of at least parts of this mixture around 18 °C. The heating and cooling rates were 2 K/min.

In the course of this experimental series, additional experiments with mixtures of [PFBMIm][PF<sub>6</sub>] and [C<sub>2</sub>C<sub>1</sub>Im][PF<sub>6</sub>] or [C<sub>8</sub>C<sub>1</sub>Im][PF<sub>6</sub>], respectively, have been performed to check the influence of different alkyl chain lengths,  $n$ , on the surface enrichment of the fluorinated chain in the [PFBMIm]<sup>+</sup> cation. In the following, only the temperature-dependent measurements are discussed and are included in Figure 4.6b – e as blue triangles for the mixtures of [PFBMIm][PF<sub>6</sub>] and [C<sub>2</sub>C<sub>1</sub>Im][PF<sub>6</sub>] and as green diamonds for the mixtures of [PFBMIm][PF<sub>6</sub>] and [C<sub>8</sub>C<sub>1</sub>Im][PF<sub>6</sub>], for more details see Chapter 9.2.3.

In Figure 4.6b – e, the normalized ratios of  $F_{\text{CF}_x}$  and  $F_{\text{PF}_6}$  of the mixtures of [PFBMIm][PF<sub>6</sub>] with [C <sub>$n$</sub> C<sub>1</sub>Im][PF<sub>6</sub>] with  $n = 2, 4$  and  $8$  are shown. When decreasing the temperature, an overall increase of the ratios is observed for all mixtures. Taking a closer look at the values of the ratio for the 10, 25, 50 and 75 mol% mixtures including different chain lengths, two trends are noticed: The lower the amount of [PFBMIm][PF<sub>6</sub>] in the mixture, the more pronounced is the surface enrichment of the fluorinated chain compared to the [PF<sub>6</sub>]<sup>-</sup> anion in the bulk. The second trend is that the shorter the alkyl chain, the higher is the normalized ratio of  $F_{\text{CF}_x}$  and  $F_{\text{PF}_6}$ , *i.e.* the mixtures containing [C<sub>2</sub>C<sub>1</sub>Im][PF<sub>6</sub>] give the highest ratios whereas the mixtures with [C<sub>8</sub>C<sub>1</sub>Im][PF<sub>6</sub>] show the lowest ratios. This difference is attributed to a competing effect of the alkyl chain of the [C <sub>$n$</sub> C<sub>1</sub>Im][PF<sub>6</sub>] with the fluorinated chain of the [PFBMIm][PF<sub>6</sub>]. Luís *et al.*<sup>[71]</sup> showed that in 1-alkyl-3-methylimidazolium perfluorobutanesulfonate, [C <sub>$n$</sub> C<sub>1</sub>Im][C<sub>4</sub>F<sub>9</sub>SO<sub>3</sub>] (with  $n = 2, 4, 6, 8, 10$

and 12), which contains fluorinated chains and alkyl chains, the fluorinated chain dominates the IL/vacuum interface for  $n \leq 4$ . Reaching  $n = 4$ , the alkyl chains also start pointing towards the surface. When further increasing the chain length, this competition becomes more pronounced with the alkyl chains dominating the surface. This is in line with the findings mentioned above that the most pronounced surface enrichment of the fluorinated chain is detected for the mixtures of [PFBMIm][PF<sub>6</sub>] and [C<sub>2</sub>C<sub>1</sub>Im][PF<sub>6</sub>] compared to the mixtures of [PFBMIm][PF<sub>6</sub>] with [C<sub>4</sub>C<sub>1</sub>Im][PF<sub>6</sub>] or [C<sub>8</sub>C<sub>1</sub>Im][PF<sub>6</sub>].

At the end of this chapter, it should be noted that another fluorinated IL was investigated in the course of these ARXPS binary mixture studies, namely the protic IL 3-methyl-2-((3,3,4,4,4-pentafluorobutyl)thio)imidazolium bis[(trifluoromethyl)sulfonyl]-imide, [C<sub>1</sub>S(PFB)HIm][Tf<sub>2</sub>N]. Due to decomposition during heating and X-ray exposure, this IL was not suitable for further investigations neither as neat IL nor in mixtures with [C<sub>4</sub>C<sub>1</sub>Im][PF<sub>6</sub>]. For details see Chapter 9.2.1.

### 4.2.3 Mixtures of Methoxy-Functionalized and Fluorinated Ionic Liquids<sup>[P4]</sup>

The two previous chapters discussed mixtures of two differently functionalized ILs with non-functionalized [C<sub>n</sub>C<sub>1</sub>Im][X] ILs. In the following, mixtures containing both functionalized imidazolium-based ILs, [(MeO)<sub>2</sub>Im][PF<sub>6</sub>] and [PFBMIm][PF<sub>6</sub>], will be presented.

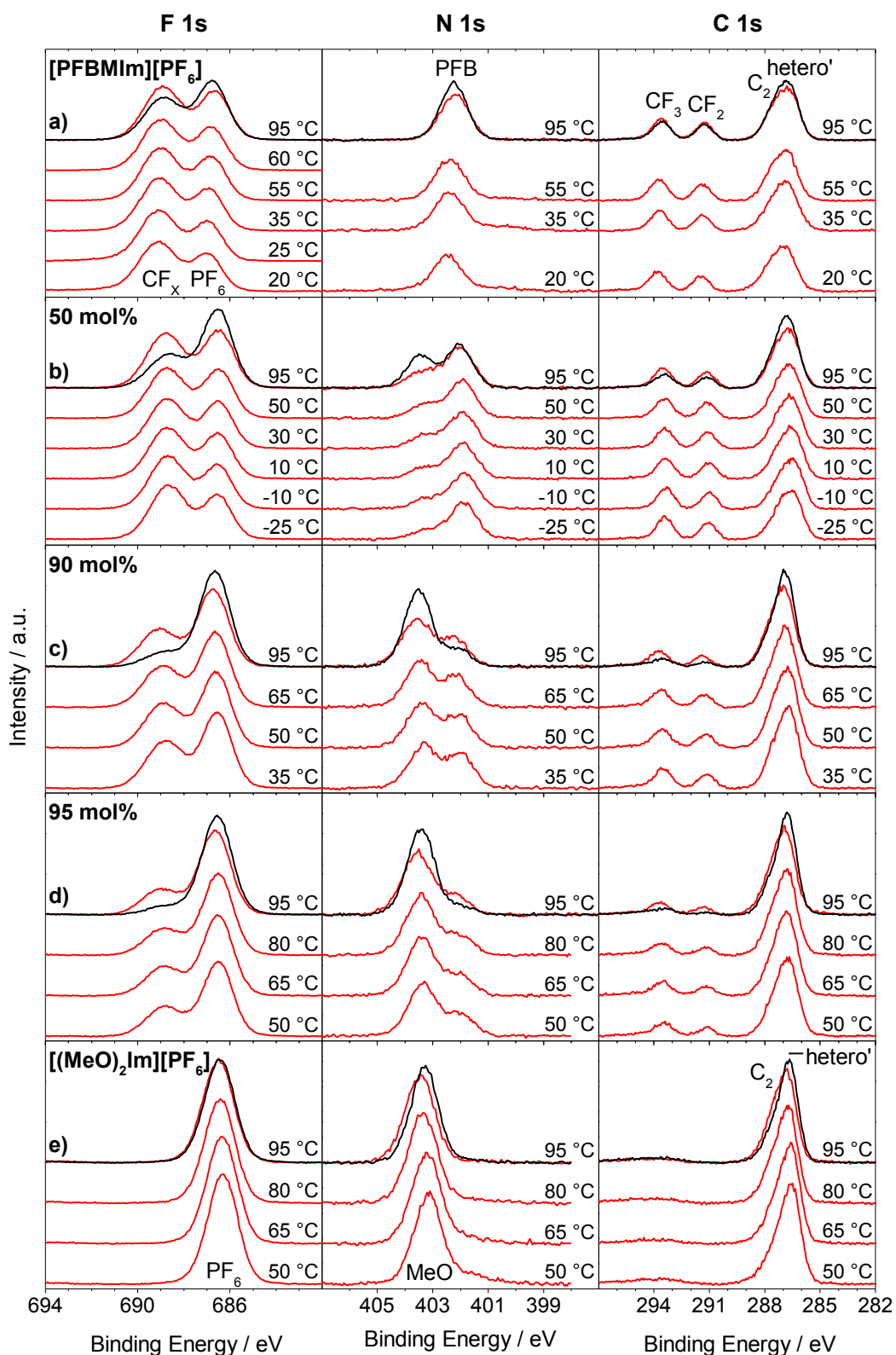
Temperature-dependent measurements from 95 °C to lower temperature of three mixtures of [(MeO)<sub>2</sub>Im][PF<sub>6</sub>] and [PFBMIm][PF<sub>6</sub>] with molar ratios of 50, 90 and 95 mol% [(MeO)<sub>2</sub>Im][PF<sub>6</sub>] have been performed. Both ILs consist of the same [PF<sub>6</sub>]<sup>-</sup> anion but differ in the functionalization of their cation either containing oxygen or fluorine atoms. In the ARXP spectra, a differentiation of the two cations is possible due to differences in the electronic structure of both head groups resulting in the aforementioned chemical shift in the N 1s spectra (see Chapter 4.2.1). Therefore, orientation, enrichment and depletion effects are possible to identify.

The ARXP spectra of [PFBMIm][PF<sub>6</sub>] as well as spectral changes by decreasing the temperature until solidification have already been discussed in Chapter 4.2.2 in detail. Briefly, the fluorinated chain is surface-enriched with respect to the [PF<sub>6</sub>]<sup>-</sup> anion which is

even more pronounced when lowering the temperature as can be seen by an increase in the  $F_{CF_x}$ ,  $C_{CF_3}$  and  $C_{CF_2}$  intensities in Figure 4.8a.

For  $[(MeO)_2Im][PF_6]$ , no preferential orientation is detected at  $95\text{ }^\circ\text{C}$ <sup>[136]</sup> in Figure 4.8e and the spectra are almost identical to the ones presented in Chapter 4.2.1 recorded at  $90\text{ }^\circ\text{C}$ .<sup>[96]</sup> When cooling  $[(MeO)_2Im][PF_6]$  from  $95$  to  $50\text{ }^\circ\text{C}$ , no changes occur in the ARXP spectra except for an additional peak arising around  $401.5\text{ eV}$  in the N 1s spectrum, which is attributed to beam damage due to a prolonged radiation time. Furthermore, the beam damage is also seen by a shift of about  $-0.3\text{ eV}$  of all core levels when comparing the spectra recorded at  $95$  and  $50\text{ }^\circ\text{C}$ . Heating the sample back to  $95\text{ }^\circ\text{C}$  gives the original peak positions (within the margin of error) and the shoulder in the N 1s region decreases significantly. Note that no beam damage effects are detected for any of the mixtures discussed below.

Gaining knowledge about the surface enrichment and depletion of the two distinct cations in the mixtures of  $[(MeO)_2Im][PF_6]$  and  $[PFBMIm][PF_6]$  was the main goal when investigating the mixtures with 50, 90 and 95 mol%  $[(MeO)_2Im][PF_6]$ . At  $95\text{ }^\circ\text{C}$ , the surface enrichment of the fluorinated chain of the  $[PFBMIm]^+$  cation is deduced from the increase in  $F_{CF_x}$ ,  $C_{CF_3}$  and  $C_{CF_2}$  intensity when going from  $0^\circ$  (black) to  $80^\circ$  (red) emission (see Figure 4.8b – d). In contrast, the  $F_{PF_6}$  and  $P_{PF_6}$  signals are lower in intensity in  $80^\circ$  compared to  $0^\circ$  revealing the surface depletion of the  $[PF_6]^-$  anion with respect to the other moieties of the cations. Due to two well-separated peaks in the N 1s region, it is possible to distinguish between the head groups of the  $[PFBMIm]^+$  and the  $[(MeO)_2Im]^+$  cations which are located at  $\sim 402.2$  and  $403.3\text{ eV}$ , respectively. Comparing the spectra recorded under  $0^\circ$  and  $80^\circ$  emission, a surface enrichment of the head group of the  $[PFBMIm]^+$  cation is deduced while the  $[(MeO)_2Im]^+$  cation is surface-depleted, resulting from a decrease of the  $80^\circ$  intensity of the  $N_{MeO}$  peak and a constant or even higher  $N_{PFB}$  signal. Combining the information of the F 1s, N 1s and C 1s spectra, an enrichment of the  $[PFBMIm]^+$  cation is observed in the 50, 90 and 95 mol%  $[(MeO)_2Im][PF_6]$  mixtures with the fluorinated chain pointing towards the vacuum whereas the  $[(MeO)_2Im]^+$  cation and the  $[PF_6]^-$  anion are surface-depleted.

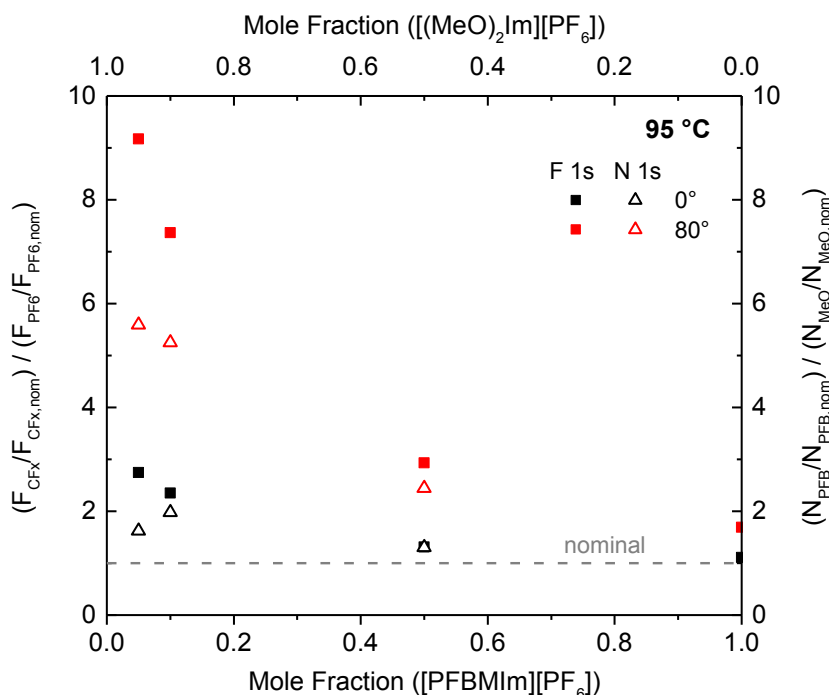


**Figure 4.8:** ARXP spectra recorded at 0° (black; only depicted for measurements at 95 °C) and 80° (red) emission of a) neat [PFBMIm][PF<sub>6</sub>], b) – d) mixtures of [(MeO)<sub>2</sub>Im][PF<sub>6</sub>] and [PFBMIm][PF<sub>6</sub>] at molar ratios of b) 50 mol% [(MeO)<sub>2</sub>Im][PF<sub>6</sub>], c) 90 mol% [(MeO)<sub>2</sub>Im][PF<sub>6</sub>] and d) 95 mol% [(MeO)<sub>2</sub>Im][PF<sub>6</sub>], and e) neat [(MeO)<sub>2</sub>Im][PF<sub>6</sub>]: F 1s (left), N 1s (middle) and C 1s (right). The samples were cooled from 95 °C to lower temperatures. Adapted in part from [P4] under license CC BY 4.0.

Again, this is attributed to a difference in surface tension related to the two different cations. Several structural features are known to influence the surface tension. From literature,<sup>[86]</sup> it is known that the surface tension of an oxygen-functionalized IL, [Me(EG)<sub>2</sub>C<sub>1</sub>Im][Tf<sub>2</sub>N], is higher compared to [C<sub>8</sub>C<sub>1</sub>Im][Tf<sub>2</sub>N] which has a comparable side chain length. In general, for homologous series of ILs with the same anion, the shorter the alkyl chain the larger the surface tension<sup>[71, 86, 111, 133-135]</sup> and an IL containing a fluorinated chain exhibits a lower surface tension compared to its respective alkylated IL.<sup>[60, 130, 131]</sup> Therefore, it is assumed that the surface tension value of [PFBMIm][PF<sub>6</sub>] is considerably lower than the one for [(MeO)<sub>2</sub>Im][PF<sub>6</sub>] resulting in the observed depletion of the [(MeO)<sub>2</sub>Im]<sup>+</sup> cation with respect to the surface-enriched [PFBMIm]<sup>+</sup> cation.

With increasing [(MeO)<sub>2</sub>Im][PF<sub>6</sub>] content in the mixtures, the normalized ratio of F<sub>CFx</sub> and F<sub>PF6</sub> (full squares in Figure 4.9) indicates a higher degree of surface enrichment of the fluorinated chain of the [PFBMIm]<sup>+</sup> cation relative to the [PF<sub>6</sub>]<sup>-</sup> anion bulk concentration. In 80° (red) emission, the ratio for neat [PFBMIm][PF<sub>6</sub>] is ~1.8 which represents solely the enrichment of the fluorinated chain. Values larger than this, like for the mixtures presented here, suggest an additional enrichment of the [PFBMIm]<sup>+</sup> head group. Furthermore, the open triangles in Figure 4.9 represent the normalized ratio of N<sub>PFB</sub> and N<sub>MeO</sub> in 80° (red) emission revealing the relative position of the two cationic head groups with respect to each other. The higher the [(MeO)<sub>2</sub>Im][PF<sub>6</sub>] content in the mixture, the higher is the normalized ratio of N<sub>PFB</sub> and N<sub>MeO</sub>, indicating a more pronounced depletion of the [(MeO)<sub>2</sub>Im]<sup>+</sup> cation with respect to the surface-enriched [PFBMIm]<sup>+</sup> head group. This trend coincides with the trend observed for the F<sub>CFx</sub> and F<sub>PF6</sub> ratio but is less pronounced for the nitrogen data. While the N 1s spectra only show the relative enrichment of the head groups damped by the surface-enriched fluorinated chain, the F<sub>CFx</sub> peaks in the F 1s spectra are not damped by any species. Remarkably, the trends of the normalized ratios of F<sub>CFx</sub> and F<sub>PF6</sub> as well as of N<sub>PFB</sub> and N<sub>MeO</sub> are also detected in 0° (black) emission for the mixtures with 90 and 95 mol% [(MeO)<sub>2</sub>Im][PF<sub>6</sub>], *i.e.* the depletion of the [PF<sub>6</sub>]<sup>-</sup> anion and the [(MeO)<sub>2</sub>Im]<sup>+</sup> cation is not only present in the topmost layer but also takes place in the near-surface region. Similar segregation effects have been detected for other IL systems earlier.<sup>[54, 96, 137]</sup>



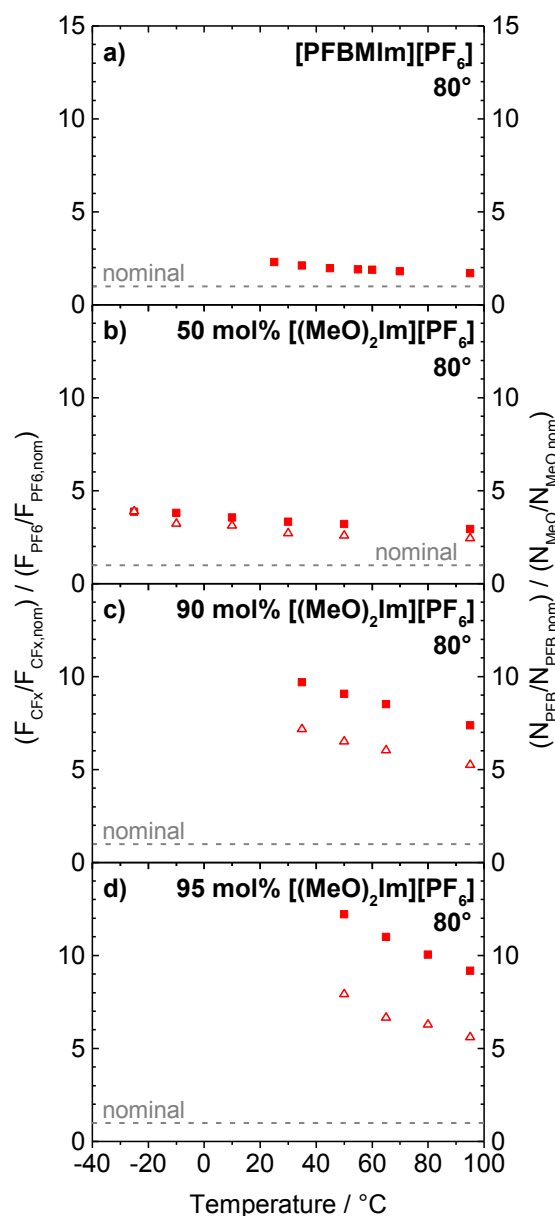


**Figure 4.9:** Normalized ratio of  $F_{\text{CFX}}$  and  $F_{\text{PF}_6}$  (full squares; left axis) and normalized ratio of  $N_{\text{PFB}}$  and  $N_{\text{MeO}}$  (open triangles; right axis) at  $0^\circ$  (black) and  $80^\circ$  (red) emission. The gray dashed line indicates the nominal composition. The sample temperature was  $95^\circ\text{C}$ . Adapted from [P4] under license CC BY 4.0.

Next, the 50, 90 and 95 mol% mixtures of  $[(\text{MeO})_2\text{Im}][\text{PF}_6]$  and  $[\text{PFBMIm}][\text{PF}_6]$  are cooled to check for an even stronger surface enrichment of the  $[\text{PFBMIm}]^+$  cation compared to the mixtures containing  $[\text{PFBMIm}][\text{PF}_6]$  and  $[\text{C}_n\text{C}_1\text{Im}][\text{PF}_6]$  described in Chapter 4.2.2. Since enrichment effects are most pronounced in  $80^\circ$  emission compared to  $0^\circ$ , only  $80^\circ$  spectra are discussed in the following. In Figure 4.8b – d, the F 1s, N 1s and C 1s spectra recorded at different temperatures are depicted and the normalized ratio of  $F_{\text{CFX}}$  and  $F_{\text{PF}_6}$  (full squares) and of  $N_{\text{PFB}}$  and  $N_{\text{MeO}}$  (open triangles) are given in Figure 4.10b – d.

The solidification temperature of the mixtures is decreasing with decreasing  $[(\text{MeO})_2\text{Im}][\text{PF}_6]$  content. In general, when lowering the temperature of the 50, 90 and 95 mol% mixtures, the  $C_{\text{CF}_3}$ ,  $C_{\text{CF}_2}$  and  $F_{\text{CFX}}$  peak intensities increase whereas the  $F_{\text{PF}_6}$  intensity decreases to a lower extent. These changes correspond to an increase in the normalized ratio of  $F_{\text{CFX}}$  and  $F_{\text{PF}_6}$  giving the highest value of  $\sim 12.2$  at  $50^\circ\text{C}$  for the mixture with 95 mol%  $[(\text{MeO})_2\text{Im}][\text{PF}_6]$ . Also when cooling, a decrease of the  $N_{\text{MeO}}$  peak and an increase of the  $N_{\text{PFB}}$  peak are detected, resulting in a higher normalized ratio of  $N_{\text{PFB}}$  and  $N_{\text{MeO}}$  at low temperature. These results clearly show that the surface depletion of the  $[\text{PF}_6]^-$

anion and the  $[(\text{MeO})_2\text{Im}]^+$  cation as well as the surface enrichment of the  $[\text{PFBMIm}]^+$  cation with its fluorinated chain pointing towards the vacuum side is more pronounced the lower the temperature is. In other words, in contrast to the more random distribution of the  $[\text{PFBMIm}]^+$  and  $[(\text{MeO})_2\text{Im}]^+$  cations at  $95^\circ\text{C}$ , a more ordered surface is detected at lower temperature resulting from changes in the entropic term  $-T\cdot\Delta S^\circ$ .



**Figure 4.10:** Ratio of the normalized  $F_{\text{CFX}}$  and  $F_{\text{PF}_6}$  content (full squares; left axis) and of the normalized  $N_{\text{PFB}}$  and  $N_{\text{MeO}}$  content (open triangles; right axis) at  $80^\circ$  emission. The measurements were started at a sample temperature of  $95^\circ\text{C}$  and subsequently cooled. a) Neat  $[\text{PFBMIm}][\text{PF}_6]$ , b) – d) mixtures of  $[(\text{MeO})_2\text{Im}][\text{PF}_6]$  and  $[\text{PFBMIm}][\text{PF}_6]$  at molar ratios of b) 50 mol%  $[(\text{MeO})_2\text{Im}][\text{PF}_6]$ , c) 90 mol%  $[(\text{MeO})_2\text{Im}][\text{PF}_6]$  and d) 95 mol%  $[(\text{MeO})_2\text{Im}][\text{PF}_6]$ , and e) neat  $[(\text{MeO})_2\text{Im}][\text{PF}_6]$ : Not shown due to the lack of  $F_{\text{CFX}}$  and  $N_{\text{PFB}}$  signals. The gray dashed lines indicate the nominal compositions. Adapted in part from [P4] under license CC BY 4.0.

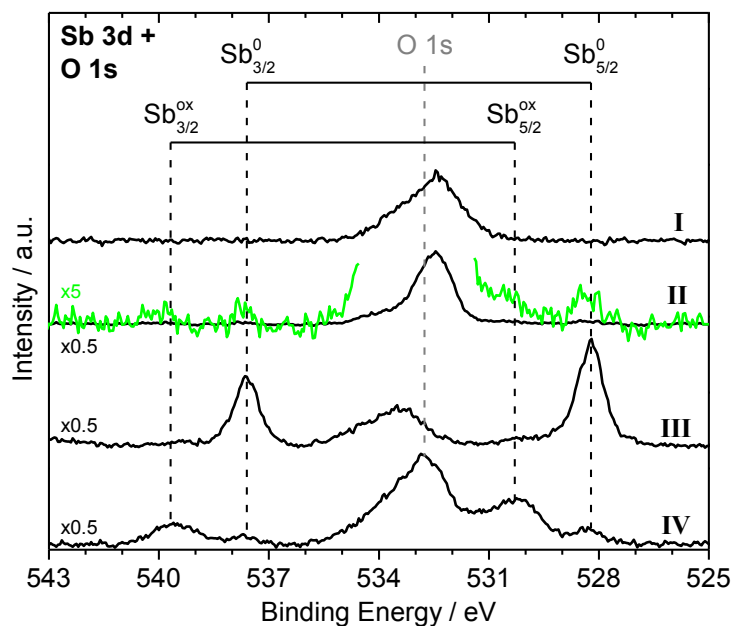
Compared to the mixtures of [PFBMIm][PF<sub>6</sub>] and [C<sub>4</sub>C<sub>1</sub>Im][PF<sub>6</sub>]<sup>[137]</sup> discussed in Chapter 4.2.2, a more pronounced enrichment of the fluorinated chain and the [PFBMIm]<sup>+</sup> head group is detected for the mixtures discussed in this chapter. For instance at 95 °C, the mixtures with 10 mol% [PFBMIm][PF<sub>6</sub>] have a normalized ratio of F<sub>CFx</sub> and F<sub>PF<sub>6</sub></sub> of ~7.4 or 3.5 when containing [(MeO)<sub>2</sub>Im][PF<sub>6</sub>] or [C<sub>4</sub>C<sub>1</sub>Im][PF<sub>6</sub>], respectively.

### 4.3 Role of an Ionic Liquid Covering Graphene-Analogues<sup>[P5]</sup>

Exfoliated few layer two-dimensional (2D) antimonene and phosphorene in zero oxidation state are promising catalysts for the alkylation of acid-sensitive nucleophiles with esters under mild conditions, resulting in excellent selectivity and good yield. Preparing these pnictogens in  $[\text{C}_4\text{C}_1\text{Im}][\text{BF}_4]$  results in suspended 2D materials. Moreover, catalytic reactions indicate that the IL efficiently protects these graphene-analogues from oxidation by air and water. To verify the zero oxidation state of antimonene and phosphorene and to confirm the protective effect of  $[\text{C}_4\text{C}_1\text{Im}][\text{BF}_4]$ , highly concentrated suspensions were prepared and spread on a clean gold foil by Vicent Lloret and Stefan Wild under inert glove box atmosphere. Subsequently, the suspensions were introduced into the DASSA setup after a short time period under ambient conditions. In this chapter, the XPS investigations will be discussed in detail. For further characterization and the catalytic activity studies performed by the co-authors, see the peer-reviewed article.<sup>[138]</sup>

In the following, only the  $0^\circ$  emission spectra of the antimonene (Sb 3d and O 1s region in Figure 4.11) and phosphorene (P 2p region in Figure 4.12) suspensions will be discussed. Starting with neat  $[\text{C}_4\text{C}_1\text{Im}][\text{BF}_4]$ , the survey spectrum shows the expected IL signals and additionally an O 1s (see also region spectrum in Figure 4.11–I) as well as a tiny Si 2p signal. Both most likely originate from a minor polysiloxane contamination of the glass ware used.<sup>[47, 114, 139]</sup> As expected, no signal is observed in the P 2p region shown in Figure 4.12–I.

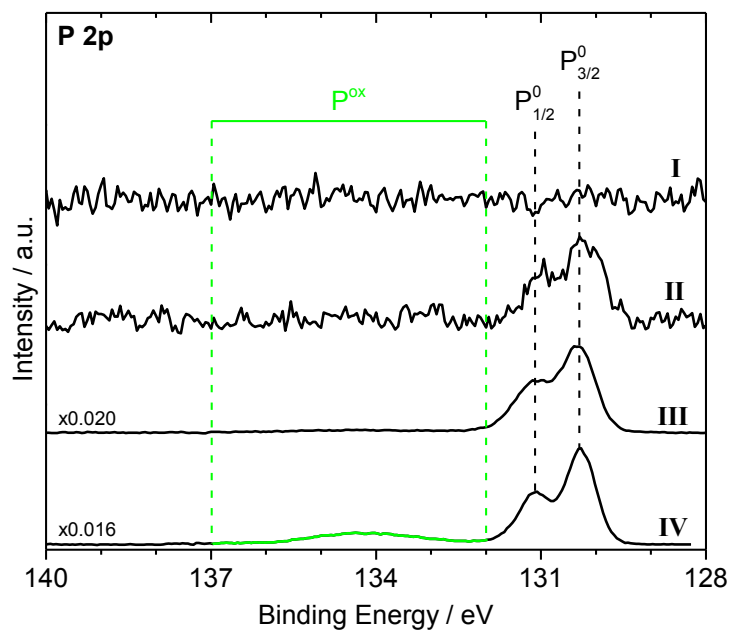
The Sb 3d signals of the highly concentrated antimonene suspension are weak compared to the strong O 1s contamination peak (note the scaling factors in Figures 4.11 and 4.12). Therefore, a magnified spectrum is shown in green for antimonene (see Figure 4.11–II) revealing small non-oxidized,  $\text{Sb}^0$ , and oxidized,  $\text{Sb}^{\text{ox}}$ , Sb 3d peaks with Sb 3d<sub>5/2</sub> peak positions of  $\sim 528.2$  and  $530.3$  eV, respectively. For the phosphorene suspension, only one phosphorus species is detected in the P 2p region as small peak at  $\sim 130.6$  eV in Figure 4.12–II, corresponding to non-oxidized phosphorus,  $\text{P}^0$ . The absence of a signal of oxidized phosphorus,  $\text{P}^{\text{ox}}$ , expected between 132 and 137 eV<sup>[140]</sup> confirms the protecting effect of  $[\text{C}_4\text{C}_1\text{Im}][\text{BF}_4]$  for this pnictogen.



**Figure 4.11:** Sb 3d spectra including the O 1s peak of neat  $[\text{C}_4\text{C}_1\text{Im}][\text{BF}_4]$  (I), a highly concentrated antimonene suspension (II) with a magnification (green) to see the small peaks of non-oxidized and oxidized antimony, after removal of most of the  $[\text{C}_4\text{C}_1\text{Im}][\text{BF}_4]$  by heating (III) and after exposure to air for about one day (IV). The spectra are offset for clarity. Adapted from [P5] under license CC BY 4.0.

Heating both suspensions above  $150\text{ }^\circ\text{C}$  for about one hour under UHV leads to a significant increase in the XP intensity of the non-oxidized antimonene and phosphorene signals in Figures 4.11–III and 4.12–III whereas the intensity of the IL related signals decreases drastically due to thermal IL desorption (and possibly some IL decomposition). This indicates that the majority of antimony and phosphorus in the 2D materials is in a zero oxidation state whereas the  $\text{Sb}^{\text{ox}}$  is indeed a minority species in the antimonene suspension.

The heated samples (with a considerably decreased IL content) are then removed from the UHV chamber and kept under ambient conditions for about one day. Subsequent XPS measurements revealed that due to the removal of most of the  $[\text{C}_4\text{C}_1\text{Im}][\text{BF}_4]$ , indeed its protective effect of the pnictogens against oxidation is lost: A considerable amount of oxidized antimony and phosphorus is detected in the respective sample after exposure to atmosphere. For the Sb  $3d_{5/2}$  peak of the non-oxidized  $\text{Sb}^0$  species at  $\sim 528.3\text{ eV}$  a pronounced decrease is detected while the peak of the oxidized  $\text{Sb}^{\text{ox}}$  species at  $\sim 530.2\text{ eV}$  has gained intensity (see Figure 4.11–IV). For the phosphorene sample, the non-oxidized  $\text{P}^0$  species is still detected at  $\sim 130.7\text{ eV}$ , however, at higher binding energy a broad peak between 132 and 137 eV is observed corresponding to oxidized phosphorus,  $\text{P}^{\text{ox}}$ , highlighted in green in Figure 4.12–IV.



**Figure 4.12:** P 2p spectra of neat [C<sub>4</sub>C<sub>1</sub>Im][BF<sub>4</sub>] (I), a highly concentrated phosphorene suspension (II), after removal of most of the [C<sub>4</sub>C<sub>1</sub>Im][BF<sub>4</sub>] by heating (III) and after exposure to air for about one day (IV). The spectra are offset for clarity. Adapted from [P5] under license CC BY 4.0.

## 5 Summary

This thesis focuses on the surface investigations of neat ionic liquids (ILs) and of binary IL mixtures, particularly mixtures involving functionalized imidazolium-based cations. The investigations are performed by means of angle-resolved X-ray photoelectron spectroscopy (ARXPS), a surface-sensitive ultra-high vacuum (UHV) technique, accessing the first 7 to 9 nm under  $0^\circ$  emission and the topmost 1 to 1.5 nm under  $80^\circ$  emission. Intensity changes of the IL signals with the emission angle directly reflect surface enrichment and depletion of ions as well as molecular orientation effects in the outermost surface layer.

The first part of this thesis is dedicated to the correlation of the surface composition with the surface tension according to the concept of molecular group contributions at the outer surface introduced by Langmuir.<sup>[104, 105]</sup> Combining ARXPS measurements and molecular dynamics (MD) simulations, the composition of  $[C_nC_1\text{Im}][\text{Tf}_2\text{N}]$  ILs (with  $n = 2, 4, 6, 8, 10$  and  $12$ ) close to the surface is investigated by comparing the surface enrichment of the alkyl chain with respect to the cationic head group along the IL series.<sup>[106]</sup> While an earlier fit model for ARXPS C 1s peaks worked well qualitatively, a correction involving the attenuation of the nitrogen signals of the imidazolium ring is crucial for the quantification of the  $C_{\text{hetero}}$  and  $C_{\text{alkyl}}$  signals at  $80^\circ$ . Taking the corresponding  $0^\circ$  and  $80^\circ$  information depth into account, a very good agreement between ARXPS measurements and MD simulations is obtained. Finally, the surface tension values are derived from the simulated outer surface composition allowing for the comparison with experimental data.<sup>[86]</sup> An emission angle of  $87.5^\circ$  might be surface-sensitive enough to limit ARXPS signals to the molecular groups at the outer surface.

As main topic of this thesis, enrichment and depletion effects at the IL/vacuum interface are investigated in various IL mixtures, containing functionalized imidazolium-based cations. The cation of neat  $[(\text{MeO})_2\text{Im}][\text{PF}_6]$ , a methoxy-functionalized IL containing oxygen atoms directly bound to each nitrogen atom of the imidazolium ring, reveals a different electronic structure induced by the oxygen atoms. The resulting more positively charged imidazolium ring exhibits characteristic XP peaks located at higher binding energy compared to  $[C_nC_1\text{Im}]^+$  cations, *e.g.* in the N 1s spectrum a shift of the  $N_{\text{MeO}}$  peak of  $\sim +1.4$  eV in contrast to the  $N_{\text{Im}}$  peak is detected.<sup>[96]</sup> The chemical shift of the nitrogen atoms of the  $[(\text{MeO})_2\text{Im}]^+$  cation facilitates the investigation of enrichment and depletion effects in IL mixtures. In the liquid state, no surface enrichment or depletion

effects are detected for neat  $[(\text{MeO})_2\text{Im}][\text{PF}_6]$ .<sup>[96, 136]</sup> The other investigated functionalized IL is  $[\text{PFBMIm}][\text{PF}_6]$ , possessing a butyl chain with its two terminal carbon atoms fluorinated. At 95 °C, a surface enrichment of the fluorinated chain with respect to the other IL moieties is observed.<sup>[136, 137]</sup>

Mixing the functionalized ILs with each other<sup>[136]</sup> and with non-functionalized  $[\text{C}_n\text{C}_1\text{Im}][\text{PF}_6]$  (with  $n = 2, 4$  and  $8$ ) or  $[\text{C}_8\text{C}_1\text{Im}][\text{Tf}_2\text{N}]$ <sup>[96, 137]</sup> results in distinct XP peaks for each ion, which allows for obtaining detailed information about the relative positions of the cation and the anion or the respective cations and anions to each other. It is proposed that the IL with the lower surface tension is preferentially enriched at the IL/vacuum interface. At 95 °C, one major result is that the fluorinated chain of mixtures containing  $[\text{PFBMIm}][\text{PF}_6]$  is surface-enriched. This is more pronounced the lower the  $[\text{PFBMIm}][\text{PF}_6]$  content in mixtures with  $[(\text{MeO})_2\text{Im}][\text{PF}_6]$  and  $[\text{C}_n\text{C}_1\text{Im}][\text{PF}_6]$  (with  $n = 2, 4$  and  $8$ ) is.<sup>[136, 137]</sup> Furthermore, the shorter the alkyl chain length,  $n$ , of  $[\text{C}_n\text{C}_1\text{Im}][\text{PF}_6]$  in the mixtures with  $[\text{PFBMIm}][\text{PF}_6]$ , the more pronounced is the enrichment of the fluorinated chain, which is attributed to a competing effect of the long alkyl chains with the shorter fluorinated chains at the surface. In contrast, the cationic head group of  $[(\text{MeO})_2\text{Im}][\text{PF}_6]$  is depleted from the topmost layers in mixtures with  $[\text{C}_8\text{C}_1\text{Im}][\text{PF}_6]$ ,  $[\text{C}_8\text{C}_1\text{Im}][\text{Tf}_2\text{N}]$  and  $[\text{PFBMIm}][\text{PF}_6]$ .<sup>[96, 136]</sup> A non-stoichiometric distribution of cations and anions of several mixtures is not only observed in 80° but also in the more bulk-sensitive 0° measurements revealing that in the near-surface region enrichment and depletion effects are present. In catalytic processes, *e.g.* Supported Ionic Liquid Phase (SILP) catalysis, a lower temperature can be desirable to achieve high equilibrium conversions.<sup>[73]</sup> To understand changes in the surface composition as a function of temperature, most of the aforementioned mixtures are investigated by means of temperature-dependent ARXPS from 95 °C to their onset of solidification. The surface enrichment of the fluorinated chain of the  $[\text{PFBMIm}]^+$  cation with respect to the  $[\text{PF}_6]^-$  anion is more pronounced, the lower the temperature resulting from a decrease in entropic contributions.

The last part of this thesis is dedicated to the investigation of the catalytically active two-dimensional (2D) materials antimonene and phosphorene dispersed in  $[\text{C}_4\text{C}_1\text{Im}][\text{BF}_4]$  with focus on the protection against oxidation by the IL.<sup>[138]</sup> In highly concentrated suspensions, XPS reveals that the majority of the synthesized antimonene and phosphorene is in a zero oxidation state. Thus, the IL protects the 2D materials from oxidation by air



and water. If the protective  $[\text{C}_4\text{C}_1\text{Im}][\text{BF}_4]$  film is removed and the samples are kept under ambient conditions for one day, pronounced oxidation of antimonene and phosphorene are observed.

## 6 Zusammenfassung

Diese Dissertation befasst sich mit der Oberflächenuntersuchung reiner Ionischer Flüssigkeiten (engl. ionic liquids, ILs) und deren binären Mischungen, die funktionalisierte Imidazolium-basierte Kationen enthalten. Die Untersuchungen werden mittels winkelaufgelöster Röntgenphotoelektronenspektroskopie (engl. angle-resolved X-ray photoelectron spectroscopy, ARXPS), einer oberflächenempfindlichen Messmethode im Ultrahochvakuum, durchgeführt. Dies ermöglicht unter einem Emissionswinkel von  $0^\circ$  die ersten 7 bis 9 nm sowie unter  $80^\circ$  die äußersten 1 bis 1,5 nm einer Probe zu untersuchen. Der Vergleich der unter  $0^\circ$  und  $80^\circ$  detektierten IL-Signalintensitäten lässt direkte Rückschlüsse auf Oberflächenanreicherung und -abreicherung von Ionen zu und gibt Informationen über molekulare Orientierungseffekte in der äußersten Oberflächenschicht.

Der erste Teil dieser Dissertation behandelt den Zusammenhang der IL-Oberflächenzusammensetzung und der Oberflächenspannung gemäß des Konzeptes nach Langmuir zum Beitrag der Molekülgruppen der äußersten Oberfläche zur Oberflächenspannung.<sup>[104, 105]</sup> Durch das Kombinieren von ARXPS-Messungen und Molekulardynamik-Simulationen (MD) wird die Oberflächenzusammensetzung der  $[C_nC_1Im][Tf_2N]$ -ILs (mit  $n = 2, 4, 6, 8, 10$  und  $12$ ) untersucht, indem entlang dieser IL-Reihe die Anreicherung der Alkylkette im Verhältnis zu den kationischen Kopfgruppen verglichen wird.<sup>[106]</sup> Da ein früheres Fitmodell der ARXPS C 1s-Signale nur qualitative Ergebnisse lieferte, wird für die Quantifizierung der  $C_{hetero}$ - und  $C_{alkyl}$ -Signale der  $80^\circ$ -Spektren eine Korrektur über die Dämpfung der Stickstoffsignale des Imidazoliumrings eingeführt. Unter Berücksichtigung der entsprechenden Informationstiefen unter  $0^\circ$  und  $80^\circ$ , ergibt sich eine gute Übereinstimmung zwischen den ARXPS-Messungen und den MD-Simulationen. Darüber hinaus wird die Oberflächenspannung mittels der simulierten Oberflächenzusammensetzung abgeleitet und mit experimentellen Werten verglichen.<sup>[86]</sup> Ein Emissionswinkel von  $87,5^\circ$  wäre wahrscheinlich ausreichend oberflächensensitiv, um mittels ARXPS nur die äußerste Oberfläche zu untersuchen.

Schwerpunkt dieser Dissertation sind Oberflächenanreicherungseffekte und -abreicherungseffekte an der IL/Vakuum-Grenzfläche in verschiedenen IL-Mischungen, die funktionalisierte Imidazolium-basierte Kationen enthalten.  $[(MeO)_2Im][PF_6]$  ist eine methoxy-funktionalisierte IL, deren Sauerstoffatome direkt an die beiden Stickstoffatome des Imidazoliumrings gebunden sind. Diese Sauerstoffatome verändern die elektronische

Struktur des Kations. Der Imidazoliumring des  $[(\text{MeO})_2\text{Im}]^+$ -Kations ist im Vergleich zu dem der  $[\text{C}_n\text{C}_1\text{Im}]^+$ -Kationen positiver geladen, woraus charakteristische XP-Peaks bei höheren Bindungsenergien resultieren. Im N 1s-Spektrum ist, im Vergleich zum  $\text{N}_{\text{im}}$ -Peak, das  $\text{N}_{\text{MeO}}$ -Signal beispielsweise um  $\sim +1,4$  eV verschoben.<sup>[96]</sup> Diese chemische Verschiebung der Stickstoffatome des  $[(\text{MeO})_2\text{Im}]^+$ -Kations erleichtert die Untersuchung von Oberflächenanreicherungseffekten und -abreicherungseffekten in IL-Mischungen. Die Spektren des reinen, flüssigen  $[(\text{MeO})_2\text{Im}][\text{PF}_6]$  zeigen keine Oberflächenaktivität.<sup>[96, 136]</sup> Des Weiteren wird die funktionalisierte  $[\text{PFBMIm}][\text{PF}_6]$ -IL untersucht, deren beide endständigen Kohlenstoffatome der Butylkette vollständig fluoriert sind. Im Vergleich zu den anderen IL-,Teilen“, ist die fluoriierte Kette bei 95 °C an der Oberfläche angereichert.<sup>[136, 137]</sup>

Mischungen der beiden funktionalisierten ILs miteinander<sup>[136]</sup> sowie von einer funktionalisierten IL mit den nicht-funktionalisierten ILs  $[\text{C}_n\text{C}_1\text{Im}][\text{PF}_6]$  (mit  $n = 2, 4$  und  $8$ ) oder mit  $[\text{C}_8\text{C}_1\text{Im}][\text{Tf}_2\text{N}]$ <sup>[96, 137]</sup> resultieren in charakteristischen XP-Signalen, welche die Unterscheidung der Ionen ermöglicht. Daraus können Schlussfolgerungen über die relative Position der jeweiligen Kationen und Anionen zueinander gezogen werden. Es wird angenommen, dass sich die IL mit der kleineren Oberflächenspannung bevorzugt an der IL/Vakuum-Grenzfläche befindet. Eines der Hauptergebnisse bei 95 °C ist, dass sich die fluoriierte Kette der  $[\text{PFBMIm}][\text{PF}_6]$ -Mischungen an der Oberfläche anreichert. In den Mischungen mit  $[(\text{MeO})_2\text{Im}][\text{PF}_6]$  und  $[\text{C}_n\text{C}_1\text{Im}][\text{PF}_6]$  (mit  $n = 2, 4$  und  $8$ ) ist dieser Anreicherungseffekt umso ausgeprägter, je kleiner der Anteil des  $[\text{PFBMIm}][\text{PF}_6]$  in der Mischung ist.<sup>[136, 137]</sup> Des Weiteren hat die Länge der Alkylkette,  $n$ , einen Einfluss auf die Anreicherung der fluoriierten Kette. Je kürzer die Alkylkette der  $[\text{C}_n\text{C}_1\text{Im}][\text{PF}_6]$ -IL in der Mischung mit  $[\text{PFBMIm}][\text{PF}_6]$ , desto stärker reichert sich die fluoriierte Kette an. Dies wird auf einen konkurrierenden Effekt der langen Alkylkette mit der kürzeren fluoriierten Kette an der Oberfläche zurückgeführt. Im Gegensatz dazu wird die Abreicherung der kationischen Kopfgruppe des  $[(\text{MeO})_2\text{Im}][\text{PF}_6]$  aus der obersten Lage der Mischungen mit  $[\text{C}_8\text{C}_1\text{Im}][\text{PF}_6]$ ,  $[\text{C}_8\text{C}_1\text{Im}][\text{Tf}_2\text{N}]$  und  $[\text{PFBMIm}][\text{PF}_6]$  detektiert.<sup>[96, 136]</sup> In einigen Mischungen werden nicht-stöchiometrische Verteilungen der Kationen und Anionen nicht nur an der Oberfläche unter  $80^\circ$ , sondern auch unter einem Emissionswinkel von  $0^\circ$  beobachtet. Dies zeigt, dass Anreicherungs- und Abreicherungseffekte im oberflächennahen Bereich vorliegen. Bei katalytischen Prozessen, wie beispielsweise SILP-Systemen (Supported Ionic Liquid Phase), kann eine niedrigere Prozesstemperatur erwünscht sein,

um einen höheren Gleichgewichtsumsatz zu erzielen.<sup>[73]</sup> Temperaturabhängige Änderungen der Oberflächensatzung einiger der zuvor genannten IL-Mischungen werden mittels temperaturabhängiger ARXPS-Messung von 95 °C bis zum Beginn der Verfestigung der Mischungen untersucht. Mit abnehmender Temperatur ist eine Zunahme der Oberflächenanreicherung der fluorierten Kette im Verhältnis zum  $[\text{PF}_6]^-$ -Anion zu beobachten, was durch die Abnahme des Entropiebeitrages erklärt werden kann.

Der letzte Teil dieser Dissertation widmet sich der Untersuchung der fein verteilten katalytisch aktiven zweidimensionalen (2D) Materialien Antimonen und Phosphoren in  $[\text{C}_4\text{C}_1\text{Im}][\text{BF}_4]$ .<sup>[138]</sup> Der Fokus dieser Untersuchung ist die schützende Wirkung der IL, um Oxidation zu verhindern. XPS zeigt, dass der größte Teil des synthetisierten Antimonens und Phosphorens in hoch konzentrierten Suspensionen im Oxidationszustand Null vorliegt. Das bedeutet, dass die IL die 2D-Materialien vor der Oxidation durch Luft und Wasser schützt. Wenn ein Großteil des schützenden  $[\text{C}_4\text{C}_1\text{Im}][\text{BF}_4]$ -Films entfernt wird, führt das eintägige Lagern der Proben unter Umgebungsbedingungen zur Oxidation des Antimonens und des Phosphorens.

## 7 Literature

- [1] H.-P. Steinrück, P. Wasserscheid, Ionic Liquids in Catalysis, *Catal. Lett.* **2015**, *145*, 380-397.
- [2] A. S. L. Gouveia, C. E. S. Bernardes, E. I. Lozinskaya, A. S. Shaplov, J. N. Canongia Lopes, I. M. Marrucho, Neat ionic liquids *versus* ionic liquid mixtures: a combination of experimental data and molecular simulation, *Phys. Chem. Chem. Phys.* **2019**, *21*, 23305-23309.
- [3] T. L. Greaves, D. F. Kennedy, Y. Shen, A. Hawley, G. Song, C. J. Drummond, Fluorous protic ionic liquids exhibit discrete segregated nano-scale solvent domains and form new populations of nano-scale objects upon primary alcohol addition, *Phys. Chem. Chem. Phys.* **2013**, *15*, 7592-7598.
- [4] M. L. Ferreira, M. J. Pastoriza-Gallego, J. M. M. Araújo, J. N. Canongia Lopes, L. P. N. Rebelo, M. M. Piñeiro, K. Shimizu, A. B. Pereiro, Influence of Nanosegregation on the Phase Behavior of Fluorinated Ionic Liquids, *J. Phys. Chem. C* **2017**, *121*, 5415-5427.
- [5] P. Sun, D. W. Armstrong, Ionic liquids in analytical chemistry, *Anal. Chim. Acta* **2010**, *661*, 1-16.
- [6] T. Torimoto, T. Tsuda, K.-i. Okazaki, S. Kuwabata, New Frontiers in Materials Science Opened by Ionic Liquids, *Adv. Mater.* **2010**, *22*, 1196-1221.
- [7] N. V. Plechkova, K. R. Seddon, Applications of ionic liquids in the chemical industry, *Chem. Soc. Rev.* **2008**, *37*, 123-150.
- [8] D. W. Bruce, C. P. Cabry, J. N. Canongia Lopes, M. L. Costen, L. D'Andrea, I. Grillo, B. C. Marshall, K. G. McKendrick, T. K. Minton, S. M. Purcell, S. Rogers, J. M. Slattery, K. Shimizu, E. Smoll, M. A. Tesa-Serrate, Nanosegregation and Structuring in the Bulk and at the Surface of Ionic-Liquid Mixtures, *J. Phys. Chem. B* **2017**, *121*, 6002-6020.
- [9] H. Niedermeyer, J. P. Hallett, I. J. Villar-Garcia, P. A. Hunt, T. Welton, Mixtures of ionic liquids, *Chem. Soc. Rev.* **2012**, *41*, 7780-7802.
- [10] M. T. Clough, C. R. Crick, J. Gräsvik, P. A. Hunt, H. Niedermeyer, T. Welton, O. P. Whitaker, A physicochemical investigation of ionic liquid mixtures, *Chem. Sci.* **2015**, *6*, 1101-1114.
- [11] G. Chatel, J. F. B. Pereira, V. Debbeti, H. Wang, R. D. Rogers, Mixing ionic liquids – “simple mixtures” or “double salts”?, *Green Chem.* **2014**, *16*, 2051-2083.
- [12] J. C. Forgie, S. El Khakani, D. D. MacNeil, D. Rochefort, Electrochemical characterisation of a lithium-ion battery electrolyte based on mixtures of carbonates with a ferrocene-functionalised imidazolium electroactive ionic liquid, *Phys. Chem. Chem. Phys.* **2013**, *15*, 7713-7721.
- [13] P. M. Bayley, A. S. Best, D. R. MacFarlane, M. Forsyth, The effect of coordinating and non-coordinating additives on the transport properties in ionic liquid electrolytes for lithium batteries, *Phys. Chem. Chem. Phys.* **2011**, *13*, 4632-4640.
- [14] S. Ferrari, E. Quartarone, C. Tomasi, D. Ravelli, S. Protti, M. Fagnoni, P. Mustarelli, Alkoxy substituted imidazolium-based ionic liquids as electrolytes for lithium batteries, *J. Power Sources* **2013**, *235*, 142-147.

- [15] D. S. Silvester, Recent advances in the use of ionic liquids for electrochemical sensing, *Analyst* **2011**, *136*, 4871-4882.
- [16] T. Yasuda, M. Watanabe, Protic ionic liquids: Fuel cell applications, *MRS Bull.* **2013**, *38*, 560-566.
- [17] M. Díaz, A. Ortiz, I. Ortiz, Progress in the use of ionic liquids as electrolyte membranes in fuel cells, *J. Membr. Sci.* **2014**, *469*, 379-396.
- [18] S. Tsuzuki, T. Umecky, H. Matsumoto, W. Shinoda, M. Mikami, Interactions of Perfluoroalkyltrifluoroborate Anions with Li Ion and Imidazolium Cation: Effects of Perfluoroalkyl Chain on Motion of Ions in Ionic Liquids, *J. Phys. Chem. B* **2010**, *114*, 11390-11396.
- [19] M. J. Trujillo-Rodríguez, H. Nan, M. Varona, M. N. Emaus, I. D. Souza, J. L. Anderson, Advances of Ionic Liquids in Analytical Chemistry, *Anal. Chem.* **2019**, *91*, 505-531.
- [20] M. S. Miran, T. Yasuda, M. A. B. H. Susan, K. Dokko, M. Watanabe, Binary Protic Ionic Liquid Mixtures as a Proton Conductor: High Fuel Cell Reaction Activity and Facile Proton Transport, *J. Phys. Chem. C* **2014**, *118*, 27631-27639.
- [21] S. Fang, L. Qu, D. Luo, S. Shen, L. Yang, S.-i. Hirano, Novel mixtures of ether-functionalized ionic liquids and non-flammable methylperfluorobutylether as safe electrolytes for lithium metal batteries, *RSC Adv.* **2015**, *5*, 33897-33904.
- [22] M. Watanabe, M. L. Thomas, S. Zhang, K. Ueno, T. Yasuda, K. Dokko, Application of Ionic Liquids to Energy Storage and Conversion Materials and Devices, *Chem. Rev.* **2017**, *117*, 7190-7239.
- [23] H. Xiao, Ionic Liquid Lubricants: Basics and Applications, *Tribol. Trans.* **2017**, *60*, 20-30.
- [24] Q. Q. Baltazar, S. K. Leininger, J. L. Anderson, Binary ionic liquid mixtures as gas chromatography stationary phases for improving the separation selectivity of alcohols and aromatic compounds, *J. Chromatogr. A* **2008**, *1182*, 119-127.
- [25] C. F. Poole, S. K. Poole, Ionic liquid stationary phases for gas chromatography, *J. Sep. Sci.* **2011**, *34*, 888-900.
- [26] L. Zhou, J. Fan, X. Shang, CO<sub>2</sub> Capture and Separation Properties in the Ionic Liquid 1-n-Butyl-3-Methylimidazolium Nonafluorobutylsulfonate, *Materials* **2014**, *7*, 3867-3880.
- [27] F. Meischl, M. Harder, C. G. Kirchler, J. Kremser, C. W. Huck, G. K. Bonn, M. Rainer, Novel asymmetric 1,3-di(alkyloxy)imidazolium based ionic liquids for liquid-phase microextraction of selected analgesics and estrogens from aqueous samples, *J. Mol. Liq.* **2019**, *289*, 111157.
- [28] R. I. Canales, J. F. Brennecke, Comparison of Ionic Liquids to Conventional Organic Solvents for Extraction of Aromatics from Aliphatics, *J. Chem. Eng. Data* **2016**, *61*, 1685-1699.
- [29] A. Bösmann, L. Datsevich, A. Jess, A. Lauter, C. Schmitz, P. Wasserscheid, Deep desulfurization of diesel fuel by extraction with ionic liquids, *Chem. Commun.* **2001**, 2494-2495.

- [30] R.-S. Zhao, X. Wang, F.-W. Li, S.-S. Wang, L.-L. Zhang, C.-G. Cheng, Ionic liquid/ionic liquid dispersive liquid–liquid microextraction, *J. Sep. Sci.* **2011**, *34*, 830-836.
- [31] U. Kernchen, B. Etzold, W. Korth, A. Jess, Solid Catalyst with Ionic Liquid Layer (SCILL) – A New Concept to Improve Selectivity Illustrated by Hydrogenation of Cyclooctadiene, *Chem. Eng. Technol.* **2007**, *30*, 985-994.
- [32] J. van den Broeke, F. Winter, B.-J. Deelman, G. van Koten, A Highly Fluorous Room-Temperature Ionic Liquid Exhibiting Fluorous Biphasic Behavior and Its Use in Catalyst Recycling, *Org. Lett.* **2002**, *4*, 3851-3854.
- [33] Y. Tsukada, K. Iwamoto, H. Furutani, Y. Matsushita, Y. Abe, K. Matsumoto, K. Monda, S. Hayase, M. Kawatsura, T. Itoh, Preparation of novel hydrophobic fluorine-substituted-alkyl sulfate ionic liquids and application as an efficient reaction medium for lipase-catalyzed reaction, *Tetrahedron Lett.* **2006**, *47*, 1801-1804.
- [34] S. Marullo, C. Rizzo, F. D'Anna, Task-Specific Organic Salts and Ionic Liquids Binary Mixtures: A Combination to Obtain 5-Hydroxymethylfurfural From Carbohydrates, *Front. Chem.* **2019**, *7*, 134.
- [35] S. Zhang, J. Zhang, Y. Zhang, Y. Deng, Nanoconfined Ionic Liquids, *Chem. Rev.* **2017**, *117*, 6755-6833.
- [36] H.-P. Steinrück, J. Libuda, P. Wasserscheid, T. Cremer, C. Kolbeck, M. Laurin, F. Maier, M. Sobota, P. S. Schulz, M. Stark, Surface Science and Model Catalysis with Ionic Liquid-Modified Materials, *Adv. Mater.* **2011**, *23*, 2571-2587.
- [37] C. P. Mehnert, E. J. Mozeleski, R. A. Cook, Supported ionic liquid catalysis investigated for hydrogenation reactions, *Chem. Commun.* **2002**, 3010-3011.
- [38] A. Riisager, R. Fehrmann, M. Haumann, B. S. K. Gorle, P. Wasserscheid, Stability and Kinetic Studies of Supported Ionic Liquid Phase Catalysts for Hydroformylation of Propene, *Ind. Eng. Chem. Res.* **2005**, *44*, 9853-9859.
- [39] J. M. Marinkovic, A. Riisager, R. Franke, P. Wasserscheid, M. Haumann, Fifteen Years of Supported Ionic Liquid Phase-Catalyzed Hydroformylation: Material and Process Developments, *Ind. Eng. Chem. Res.* **2019**, *58*, 2409-2420.
- [40] T. Cremer, L. Wibmer, S. Krick Calderón, A. Deyko, F. Maier, H.-P. Steinrück, Interfaces of ionic liquids and transition metal surfaces—adsorption, growth, and thermal reactions of ultrathin  $[C_1C_1Im][Tf_2N]$  films on metallic and oxidised Ni(111) surfaces, *Phys. Chem. Chem. Phys.* **2012**, *14*, 5153-5163.
- [41] M. B. Oliveira, M. Domínguez-Pérez, O. Cabeza, J. A. Lopes-da-Silva, M. G. Freire, J. A. P. Coutinho, Surface tensions of binary mixtures of ionic liquids with bis(trifluoromethylsulfonyl)imide as the common anion, *J. Chem. Thermodynamics* **2013**, *64*, 22-27.
- [42] H.-P. Steinrück, Recent developments in the study of ionic liquid interfaces using X-ray photoelectron spectroscopy and potential future directions, *Phys. Chem. Chem. Phys.* **2012**, *14*, 5010-5029.
- [43] C. Kolbeck, A. Deyko, T. Matsuda, F. T. U. Kohler, P. Wasserscheid, F. Maier, H.-P. Steinrück, Temperature-Dependent Surface-Enrichment Effects of Imidazolium-Based Ionic Liquids, *ChemPhysChem* **2013**, *14*, 3726-3730.

- [44] M. Lexow, B. S. J. Heller, F. Maier, H.-P. Steinrück, Anion Exchange at the Liquid/Solid Interface of Ultrathin Ionic Liquid Films on Ag(111), *ChemPhysChem* **2018**, *19*, 2978-2984.
- [45] M. Lexow, B. S. J. Heller, G. Partl, R. G. Bhui, F. Maier, H.-P. Steinrück, Cation Exchange at the Interfaces of Ultrathin Films of Fluorous Ionic Liquids on Ag(111), *Langmuir* **2019**, *35*, 398-405.
- [46] I. J. Villar-Garcia, S. Fearn, G. F. De Gregorio, N. L. Ismail, F. J. V. Gschwend, A. J. S. McIntosh, K. R. J. Lovelock, The ionic liquid–vacuum outer atomic surface: a low-energy ion scattering study, *Chem. Sci.* **2014**, *5*, 4404-4418.
- [47] J. M. Gottfried, F. Maier, J. Rossa, D. Gerhard, P. S. Schulz, P. Wasserscheid, H.-P. Steinrück, Surface Studies on the Ionic Liquid 1-Ethyl-3-Methylimidazolium Ethylsulfate Using X-ray Photoelectron Spectroscopy (XPS), *Z. Phys. Chem.* **2006**, *220*, 1439-1453.
- [48] J. J. Hettige, W. D. Amith, E. W. Castner, Jr., C. J. Margulis, Ionic Liquids with Symmetric Diether Tails: Bulk and Vacuum-Liquid Interfacial Structures, *J. Phys. Chem. B* **2017**, *121*, 174-179.
- [49] I. S. Martinez, S. Baldelli, On the Arrangement of Ions in Imidazolium-Based Room Temperature Ionic Liquids at the Gas–Liquid Interface, Using Sum Frequency Generation, Surface Potential, and Surface Tension Measurements, *J. Phys. Chem. C* **2010**, *114*, 11564-11575.
- [50] K. Nakajima, M. Miyashita, M. Suzuki, K. Kimura, Surface structures of binary mixtures of imidazolium-based ionic liquids using high-resolution Rutherford backscattering spectroscopy and time of flight secondary ion mass spectroscopy, *J. Chem. Phys.* **2013**, *139*, 224701.
- [51] K. Nakajima, S. Nakanishi, M. Lísal, K. Kimura, Surface structures of binary mixture of ionic liquids, *J. Mol. Liq.* **2017**, *230*, 542-549.
- [52] F. Maier, T. Cremer, C. Kolbeck, K. R. J. Lovelock, N. Paape, P. S. Schulz, P. Wasserscheid, H.-P. Steinrück, Insights into the surface composition and enrichment effects of ionic liquid mixtures, *Phys. Chem. Chem. Phys.* **2010**, *12*, 1905-1915.
- [53] C. Kolbeck, I. Niedermaier, A. Deyko, K. R. J. Lovelock, N. Taccardi, W. Wei, P. Wasserscheid, F. Maier, H.-P. Steinrück, Influence of Substituents and Functional Groups on the Surface Composition of Ionic Liquids, *Chem. Eur. J.* **2014**, *20*, 3954-3965.
- [54] Y. Zhang, Y. Khalifa, E. J. Maginn, J. T. Newberg, Anion Enhancement at the Liquid–Vacuum Interface of an Ionic Liquid Mixture, *J. Phys. Chem. C* **2018**, *122*, 27392-27401.
- [55] S. Palchowdhury, B. L. Bhargava, Segregation of ions at the interface: molecular dynamics studies of the bulk and liquid–vapor interface structure of equimolar binary mixtures of ionic liquids, *Phys. Chem. Chem. Phys.* **2015**, *17*, 19919-19928.
- [56] S. Palchowdhury, B. L. Bhargava, Surface Structure and Dynamics of Ions at the Liquid–Vapor Interface of Binary Ionic Liquid Mixtures: Molecular Dynamics Studies, *J. Phys. Chem. B* **2016**, *120*, 5430-5441.
- [57] C. Ridings, G. G. Warr, G. G. Andersson, Surface Ordering in Binary Mixtures of Protic Ionic Liquids, *J. Phys. Chem. Lett.* **2017**, *8*, 4264-4267.



- [58] F. Wu, W. V. Karunaratne, C. J. Margulis, Ionic Liquid Mixture at the Vacuum Interface and the Peaks and Antipeaks Analysis of X-ray Reflectivity, *J. Phys. Chem. C* **2019**, *123*, 4914-4925.
- [59] I. J. Villar-Garcia, S. Fearn, N. L. Ismail, A. J. S. McIntosh, K. R. J. Lovelock, Fine tuning the ionic liquid–vacuum outer atomic surface using ion mixtures, *Chem. Commun.* **2015**, *51*, 5367-5370.
- [60] E. J. Smoll, Jr., M. A. Tesa-Serrate, S. M. Purcell, L. D'Andrea, D. W. Bruce, J. M. Slattery, M. L. Costen, T. K. Minton, K. G. McKendrick, Determining the composition of the vacuum–liquid interface in ionic-liquid mixtures, *Faraday Discuss.* **2018**, *206*, 497-522.
- [61] R. Souda, Surface segregation in binary mixtures of imidazolium-based ionic liquids, *Surf. Sci.* **2010**, *604*, 1694-1697.
- [62] O. Höfft, S. Bahr, M. Himmerlich, S. Krischok, J. A. Schaefer, V. Kempter, Electronic Structure of the Surface of the Ionic Liquid [EMIM][Tf<sub>2</sub>N] Studied by Metastable Impact Electron Spectroscopy (MIES), UPS, and XPS, *Langmuir* **2006**, *22*, 7120-7123.
- [63] K. Nakajima, S. Oshima, M. Suzuki, K. Kimura, Surface structures of equimolar mixtures of imidazolium-based ionic liquids using high-resolution Rutherford backscattering spectroscopy, *Surf. Sci.* **2012**, *606*, 1693-1699.
- [64] K. Nakajima, S. Nakanishi, Z. Chval, M. Lísal, K. Kimura, Surface segregation in a binary mixture of ionic liquids: Comparison between high-resolution RBS measurements and molecular dynamics simulations, *J. Chem. Phys.* **2016**, *145*, 184704.
- [65] S. Men, P. Licence, Probing the electronic environment of binary and ternary ionic liquid mixtures by X-ray photoelectron spectroscopy, *Chem. Phys. Lett.* **2017**, *686*, 74-77.
- [66] I. J. Villar-Garcia, K. R. J. Lovelock, S. Men, P. Licence, Tuning the electronic environment of cations and anions using ionic liquid mixtures, *Chem. Sci.* **2014**, *5*, 2573-2579.
- [67] S. Men, P. Licence, Tuning the electronic environment of the anion by using binary ionic liquid mixtures, *Chem. Phys. Lett.* **2017**, *681*, 40-43.
- [68] E. J. Dick, A. E. A. Fouda, N. A. Besley, P. Licence, Probing the electronic structure of ether functionalised ionic liquids using X-ray photoelectron spectroscopy, *Phys. Chem. Chem. Phys.* **2020**, *22*, 1624-1631.
- [69] S. Men, K. R. J. Lovelock, P. Licence, X-ray photoelectron spectroscopy of pyrrolidinium-based ionic liquids: cation–anion interactions and a comparison to imidazolium-based analogues, *Phys. Chem. Chem. Phys.* **2011**, *13*, 15244-15255.
- [70] O. Hollóczki, M. Macchiagodena, H. Weber, M. Thomas, M. Brehm, A. Stark, O. Russina, A. Triolo, B. Kirchner, Triphilic Ionic-Liquid Mixtures: Fluorinated and Non-fluorinated Aprotic Ionic-Liquid Mixtures, *ChemPhysChem* **2015**, *16*, 3325-3333.
- [71] A. Luís, K. Shimizu, J. M. M. Araújo, P. J. Carvalho, J. A. Lopes-da-Silva, J. N. Canongia Lopes, L. P. N. Rebelo, J. A. P. Coutinho, M. G. Freire, A. B. Pereiro, Influence of Nanosegregation on the Surface Tension of Fluorinated Ionic Liquids, *Langmuir* **2016**, *32*, 6130-6139.

- [72] D. Yang, F. Fu, L. Li, Z. Yang, Z. Wan, Y. Luo, N. Hu, X. Chen, G. Zeng, Unique orientations and rotational dynamics of a 1-butyl-3-methyl-imidazolium hexafluorophosphate ionic liquid at the gas–liquid interface: the effects of the hydrogen bond and hydrophobic interactions, *Phys. Chem. Chem. Phys.* **2018**, *20*, 12043-12052.
- [73] P. Wolf, M. Aubermann, M. Wolf, T. Bauer, D. Blaumeiser, R. Stepic, C. R. Wick, D. M. Smith, A.-S. Smith, P. Wasserscheid, J. Libuda, M. Haumann, Improving the performance of supported ionic liquid phase (SILP) catalysts for the ultra-low-temperature water–gas shift reaction using metal salt additives, *Green Chem.* **2019**, *21*, 5008-5018.
- [74] P. van der Heide, X-ray Photoelectron Spectroscopy: An Introduction to Principles and Practices, John Wiley & Sons, Inc., Hoboken, NJ, **2012**.
- [75] D. Briggs, M. P. Seah, Practical Surface Analysis: Volume 1 – Auger and X-ray Photoelectron Spectroscopy, 2nd Edition, John Wiley & Sons Ltd, Chichester, **1990**.
- [76] S. Hüfner, Photoelectron Spectroscopy: Principles and Applications, Third Edition, Springer-Verlag, Berlin, **2003**.
- [77] H. Hertz, Ueber einen Einfluss des ultravioletten Lichtes auf die elektrische Entladung, *Ann. Phys.* **1887**, *267*, 983-1000.
- [78] W. Hallwachs, Ueber den Einfluss des Lichtes auf electrostatisch geladene Körper, *Ann. Phys.* **1888**, *269*, 301-312.
- [79] A. Einstein, Über einen die Erzeugung und Verwandlung des Lichtes betreffenden heuristischen Gesichtspunkt, *Ann. Phys.* **1905**, *322*, 132-148.
- [80] T. Cremer, M. Stark, A. Deyko, H.-P. Steinrück, F. Maier, Liquid/Solid Interface of Ultrathin Ionic Liquid Films: [C<sub>1</sub>C<sub>1</sub>Im][Tf<sub>2</sub>N] and [C<sub>8</sub>C<sub>1</sub>Im][Tf<sub>2</sub>N] on Au(111), *Langmuir* **2011**, *27*, 3662-3671.
- [81] S. Tanuma, C. J. Powell, D. R. Penn, Calculations of Electron Inelastic Mean Free Paths. V. Data for 14 Organic Compounds over the 50–2000 eV Range, *Surf. Interface Anal.* **1994**, *21*, 165-176.
- [82] T. Cremer, M. Killian, J. M. Gottfried, N. Paape, P. Wasserscheid, F. Maier, H.-P. Steinrück, Physical Vapor Deposition of [EMIM][Tf<sub>2</sub>N]: A New Approach to the Modification of Surface Properties with Ultrathin Ionic Liquid Films, *ChemPhysChem* **2008**, *9*, 2185-2190.
- [83] F. Rietzler, J. Nagengast, H.-P. Steinrück, F. Maier, Interface of Ionic Liquids and Carbon: Ultrathin [C<sub>1</sub>C<sub>1</sub>Im][Tf<sub>2</sub>N] Films on Graphite and Graphene, *J. Phys. Chem. C* **2015**, *119*, 28068-28076.
- [84] A. Deyko, T. Cremer, F. Rietzler, S. Perkin, L. Crowhurst, T. Welton, H.-P. Steinrück, F. Maier, Interfacial Behavior of Thin Ionic Liquid Films on Mica, *J. Phys. Chem. C* **2013**, *117*, 5101-5111.
- [85] Personal communication with J. N. Canongia Lopes and K. Shimizu, **2016**.
- [86] C. Kolbeck, J. Lehmann, K. R. J. Lovelock, T. Cremer, N. Paape, P. Wasserscheid, A. P. Fröba, F. Maier, H.-P. Steinrück, Density and Surface Tension of Ionic Liquids, *J. Phys. Chem. B* **2010**, *114*, 17025-17036.

- [87] C. Kolbeck, T. Cremer, K. R. J. Lovelock, N. Paape, P. S. Schulz, P. Wasserscheid, F. Maier, H.-P. Steinrück, Influence of Different Anions on the Surface Composition of Ionic Liquids Studied Using ARXPS, *J. Phys. Chem. B* **2009**, *113*, 8682-8688.
- [88] G. Laus, A. Schwärzler, P. Schuster, G. Bentivoglio, M. Hummel, K. Wurst, V. Kahlenberg, T. Lörting, J. Schütz, P. Peringer, G. Bonn, G. Nauer, H. Schottenberger, *N,N'*-Di(alkyloxy)imidazolium Salts: New Patent-free Ionic Liquids and NHC Precatalysts, *Z. Naturforsch.* **2007**, *62b*, 295-308.
- [89] S. Bartz, B. Blumenröder, A. Kern, J. Fleckenstein, S. Frohnäpfel, J. Schatz, A. Wagner, Hydroxy-1*H*-imidazole-3-oxides – Synthesis, Kinetic Acidity, and Application in Catalysis and Supramolecular Anion Recognition, *Z. Naturforsch.* **2009**, *64b*, 629-638.
- [90] S. V. Dzyuba, R. A. Bartsch, Influence of Structural Variations in 1-Alkyl(aralkyl)-3-Methylimidazolium Hexafluorophosphates and Bis(trifluoromethylsulfonyl)-imides on Physical Properties of the Ionic Liquids, *ChemPhysChem* **2002**, *3*, 161-166.
- [91] P. B. P. Serra, F. M. S. Ribeiro, M. A. A. Rocha, M. Fulem, K. Růžička, J. A. P. Coutinho, L. M. N. B. F. Santos, Solid-liquid equilibrium and heat capacity trend in the alkylimidazolium PF<sub>6</sub> series, *J. Mol. Liq.* **2017**, *248*, 678-687.
- [92] S. V. Dzyuba, R. A. Bartsch, New room-temperature ionic liquids with C<sub>2</sub>-symmetrical imidazolium cations, *Chem. Commun.* **2001**, 1466-1467.
- [93] C. P. Fredlake, J. M. Crosthwaite, D. G. Hert, S. N. V. K. Aki, J. F. Brennecke, Thermophysical Properties of Imidazolium-Based Ionic Liquids, *J. Chem. Eng. Data* **2004**, *49*, 954-964.
- [94] H. Tokuda, K. Hayamizu, K. Ishii, M. A. B. H. Susan, M. Watanabe, Physicochemical Properties and Structures of Room Temperature Ionic Liquids. 1. Variation of Anionic Species, *J. Phys. Chem. B* **2004**, *108*, 16593-16600.
- [95] H. Tokuda, K. Hayamizu, K. Ishii, M. A. B. H. Susan, M. Watanabe, Physicochemical Properties and Structures of Room Temperature Ionic Liquids. 2. Variation of Alkyl Chain Length in Imidazolium Cation, *J. Phys. Chem. B* **2005**, *109*, 6103-6110.
- [96] B. S. J. Heller, C. Kolbeck, I. Niedermaier, S. Dommer, J. Schatz, P. Hunt, F. Maier, H.-P. Steinrück, Surface Enrichment in Equimolar Mixtures of Non-Functionalized and Functionalized Imidazolium-Based Ionic Liquids, *ChemPhysChem* **2018**, *19*, 1733-1745.
- [97] I. Niedermaier, C. Kolbeck, H.-P. Steinrück, F. Maier, Dual analyzer system for surface analysis dedicated for angle-resolved photoelectron spectroscopy at liquid surfaces and interfaces, *Rev. Sci. Instrum.* **2016**, *87*, 045105.
- [98] I. J. Villar-Garcia, E. F. Smith, A. W. Taylor, F. Qiu, K. R. J. Lovelock, R. G. Jones, P. Licence, Charging of ionic liquid surfaces under X-ray irradiation: the measurement of absolute binding energies by XPS, *Phys. Chem. Chem. Phys.* **2011**, *13*, 2797-2808.
- [99] K. R. J. Lovelock, C. Kolbeck, T. Cremer, N. Paape, P. S. Schulz, P. Wasserscheid, F. Maier, H.-P. Steinrück, Influence of Different Substituents on the Surface

- Composition of Ionic Liquids Studied Using ARXPS, *J. Phys. Chem. B* **2009**, *113*, 2854-2864.
- [100] T. Cremer, Ionic Liquid Bulk and Interface Properties: Electronic Interaction, Molecular Orientation and Growth Characteristics, Doctoral Thesis, Friedrich-Alexander-Universität Erlangen-Nürnberg, **2012**.
- [101] C. Kolbeck, Surface Characterisation of Ionic Liquid Systems and *in situ* Monitoring of Liquid-Phase Reactions by X-ray Photoelectron Spectroscopy, Doctoral Thesis, Friedrich-Alexander-Universität Erlangen-Nürnberg, **2012**.
- [102] I. Niedermaier, Surface Enrichment Effects, CO<sub>2</sub> Capture, and Acid-Base Reactions in Ionic Liquids Studied by Conventional and Dual Analyser X-ray Photoelectron Spectroscopy, Doctoral Thesis, Friedrich-Alexander-Universität Erlangen-Nürnberg, **2016**.
- [103] F. Rietzler, Interfaces of Ionic Liquids and of Liquid Metals Studied by X-Ray Photoelectron Spectroscopy, Doctoral Thesis, Friedrich-Alexander-Universität Erlangen-Nürnberg, **2016**.
- [104] I. Langmuir, The constitution and fundamental properties of solids and liquids. II. Liquids, *J. Am. Chem. Soc.* **1917**, *39*, 1848-1906.
- [105] I. Langmuir, Forces Near the Surfaces of Molecules, *Chem. Rev.* **1930**, *6*, 451-479.
- [106] K. Shimizu, B. S. J. Heller, F. Maier, H.-P. Steinrück, J. N. Canongia Lopes, Probing the Surface Tension of Ionic Liquids Using the Langmuir Principle, *Langmuir* **2018**, *34*, 4408-4416.
- [107] C. Waring, P. A. J. Bagot, J. M. Slattery, M. L. Costen, K. G. McKendrick, O(<sup>3</sup>P) Atoms as a Probe of Surface Ordering in 1-Alkyl-3-methylimidazolium-Based Ionic Liquids, *J. Phys. Chem. Lett.* **2010**, *1*, 429-433.
- [108] C. Waring, P. A. J. Bagot, J. M. Slattery, M. L. Costen, K. G. McKendrick, O(<sup>3</sup>P) Atoms as a Chemical Probe of Surface Ordering in Ionic Liquids, *J. Phys. Chem. A* **2010**, *114*, 4896-4904.
- [109] M. A. Tesa-Serrate, B. C. Marshall, E. J. Smoll, Jr., S. M. Purcell, M. L. Costen, J. M. Slattery, T. K. Minton, K. G. McKendrick, Ionic Liquid–Vacuum Interfaces Probed by Reactive Atom Scattering: Influence of Alkyl Chain Length and Anion Volume, *J. Phys. Chem. C* **2015**, *119*, 5491-5505.
- [110] S. Rivera-Rubero, S. Baldelli, Surface Characterization of 1-Butyl-3-methylimidazolium Br<sup>-</sup>, I<sup>-</sup>, PF<sub>6</sub><sup>-</sup>, BF<sub>4</sub><sup>-</sup>, (CF<sub>3</sub>SO<sub>2</sub>)<sub>2</sub>N<sup>-</sup>, SCN<sup>-</sup>, CH<sub>3</sub>SO<sub>3</sub><sup>-</sup>, CH<sub>3</sub>SO<sub>4</sub><sup>-</sup>, and (CN)<sub>2</sub>N<sup>-</sup> Ionic Liquids by Sum Frequency Generation, *J. Phys. Chem. B* **2006**, *110*, 4756-4765.
- [111] C. S. Santos, S. Baldelli, Alkyl Chain Interaction at the Surface of Room Temperature Ionic Liquids: Systematic Variation of Alkyl Chain Length (R = C<sub>1</sub>–C<sub>4</sub>, C<sub>8</sub>) in both Cation and Anion of [RMIM][R–OSO<sub>3</sub>] by Sum Frequency Generation and Surface Tension, *J. Phys. Chem. B* **2009**, *113*, 923-933.
- [112] S. Men, K. R. J. Lovelock, P. Licence, X-ray photoelectron spectroscopy of trihalide ionic liquids: Comparison to halide-based analogues, anion basicity and beam damage, *Chem. Phys. Lett.* **2017**, *679*, 207-211.

- [113] B. May, M. Hönle, B. Heller, F. Greco, R. Bhui, H.-P. Steinrück, F. Maier, Surface-Induced Changes in the Thermochemical Transformation of an Ionic Liquid Cobalt Thiocyanate Complex, *J. Phys. Chem. Lett.* **2017**, *8*, 1137-1141.
- [114] C. Kolbeck, M. Killian, F. Maier, N. Paape, P. Wasserscheid, H.-P. Steinrück, Surface Characterization of Functionalized Imidazolium-Based Ionic Liquids, *Langmuir* **2008**, *24*, 9500-9507.
- [115] C. J. Clarke, S. Maxwell-Hogg, E. F. Smith, R. R. Hawker, J. B. Harper, P. Licence, Resolving X-ray photoelectron spectra of ionic liquids with difference spectroscopy, *Phys. Chem. Chem. Phys.* **2019**, *21*, 114-123.
- [116] T. Cremer, C. Kolbeck, K. R. J. Lovelock, N. Paape, R. Wölfel, P. S. Schulz, P. Wasserscheid, H. Weber, J. Thar, B. Kirchner, F. Maier, H.-P. Steinrück, Towards a Molecular Understanding of Cation–Anion Interactions—Probing the Electronic Structure of Imidazolium Ionic Liquids by NMR Spectroscopy, X-ray Photoelectron Spectroscopy and Theoretical Calculations, *Chem. Eur. J.* **2010**, *16*, 9018-9033.
- [117] T. Hammer, M. Reichelt, H. Morgner, Influence of the aliphatic chain length of imidazolium based ionic liquids on the surface structure, *Phys. Chem. Chem. Phys.* **2010**, *12*, 11070-11080.
- [118] R. M. Lynden-Bell, M. Del Pópolo, Simulation of the surface structure of butylmethylimidazolium ionic liquids, *Phys. Chem. Chem. Phys.* **2006**, *8*, 949-954.
- [119] X. Paredes, J. Fernández, A. A. H. Pádua, P. Malfreyt, F. Malberg, B. Kirchner, A. S. Pensado, Using Molecular Simulation to Understand the Structure of  $[C_2C_{1im}]^+$ -Alkylsulfate Ionic Liquids: Bulk and Liquid–Vapor Interfaces, *J. Phys. Chem. B* **2012**, *116*, 14159-14170.
- [120] A. S. Pensado, M. F. Costa Gomes, J. N. Canongia Lopes, P. Malfreyt, A. A. H. Pádua, Effect of alkyl chain length and hydroxyl group functionalization on the surface properties of imidazolium ionic liquids, *Phys. Chem. Chem. Phys.* **2011**, *13*, 13518-13526.
- [121] A. S. Pensado, P. Malfreyt, A. A. H. Pádua, Molecular Dynamics Simulations of the Liquid Surface of the Ionic Liquid 1-Hexyl-3-methylimidazolium Bis(trifluoromethanesulfonyl)amide: Structure and Surface Tension, *J. Phys. Chem. B* **2009**, *113*, 14708-14718.
- [122] R. M. Fogarty, R. Rowe, R. P. Matthews, M. T. Clough, C. R. Ashworth, A. Brandt, P. J. Corbett, R. G. Palgrave, E. F. Smith, R. A. Bourne, T. W. Chamberlain, P. B. J. Thompson, P. A. Hunt, K. R. J. Lovelock, Atomic charges of sulfur in ionic liquids: experiments and calculations, *Faraday Discuss.* **2018**, *206*, 183-201.
- [123] G. Laus, A. Schwärzler, G. Bentivoglio, M. Hummel, V. Kahlenberg, K. Wurst, E. Kristeva, J. Schütz, H. Kopacka, C. Kreutz, G. Bonn, Y. Andriyko, G. Nauer, H. Schottenberger, Synthesis and Crystal Structures of 1-Alkoxy-3-alkylimidazolium Salts Including Ionic Liquids, 1-Alkylimidazole 3-oxides and 1-Alkylimidazole Perhydrates, *Z. Naturforsch.* **2008**, *63b*, 447-464.
- [124] G. Laus, K. Wurst, V. Kahlenberg, H. Kopacka, C. Kreutz, H. Schottenberger, *N*-Heterocyclic Carbene (NHC) Derivatives of 1,3-Di(benzyloxy)imidazolium Salts, *Z. Naturforsch.* **2010**, *65b*, 776-782.

- [125] A.-L. Revelli, F. Mutelet, J.-N. Jaubert, High Carbon Dioxide Solubilities in Imidazolium-Based Ionic Liquids and in Poly(ethylene glycol) Dimethyl Ether, *J. Phys. Chem. B* **2010**, *114*, 12908-12913.
- [126] A.-L. Revelli, F. Mutelet, J.-N. Jaubert, Reducing of Nitrous Oxide Emissions Using Ionic Liquids, *J. Phys. Chem. B* **2010**, *114*, 8199-8206.
- [127] Y. Deng, P. Besse-Hoggan, M. Sancelme, A.-M. Delort, P. Husson, M. F. Costa Gomes, Influence of oxygen functionalities on the environmental impact of imidazolium based ionic liquids, *J. Hazard. Mater.* **2011**, *198*, 165-174.
- [128] C. Froschauer, R. Salchner, G. Laus, H. K. Weber, R. Tessadri, U. Griesser, K. Wurst, V. Kahlenberg, H. Schottenberger, 1,3-Di(alkoxy)imidazolium-based Ionic Liquids: Improved Synthesis and Crystal Structures, *Aust. J. Chem.* **2013**, *66*, 391-395.
- [129] A. B. Pereiro, M. J. Pastoriza-Gallego, K. Shimizu, I. M. Marrucho, J. N. Canongia Lopes, M. M. Piñeiro, L. P. N. Rebelo, On the Formation of a Third, Nanostructured Domain in Ionic Liquids, *J. Phys. Chem. B* **2013**, *117*, 10826-10833.
- [130] T. L. Merrigan, E. D. Bates, S. C. Dorman, J. H. Davis, Jr., New fluorous ionic liquids function as surfactants in conventional room-temperature ionic liquids, *Chem. Commun.* **2000**, 2051-2052.
- [131] M. Tariq, M. G. Freire, B. Saramago, J. A. P. Coutinho, J. N. Canongia Lopes, L. P. N. Rebelo, Surface tension of ionic liquids and ionic liquid solutions, *Chem. Soc. Rev.* **2012**, *41*, 829-868.
- [132] A. Dilks, The Identification of Peroxy-Features at Polymer Surfaces by ESCA, *J. Polym. Sci. Polym. Chem. Ed.* **1981**, *19*, 1319-1327.
- [133] P. J. Carvalho, M. G. Freire, I. M. Marrucho, A. J. Queimada, J. A. P. Coutinho, Surface Tensions for the 1-Alkyl-3-methylimidazolium Bis(trifluoromethylsulfonyl)imide Ionic Liquids, *J. Chem. Eng. Data* **2008**, *53*, 1346-1350.
- [134] T. M. Koller, M. H. Rausch, K. Pohako-Esko, P. Wasserscheid, A. P. Fröba, Surface Tension of Tricyanomethanide- and Tetracyanoborate-Based Imidazolium Ionic Liquids by Using the Pendant Drop Method, *J. Chem. Eng. Data* **2015**, *60*, 2665-2673.
- [135] H. F. D. Almeida, M. G. Freire, A. M. Fernandes, J. A. Lopes-da-Silva, P. Morgado, K. Shimizu, E. J. M. Filipe, J. N. Canongia Lopes, L. M. N. B. F. Santos, J. A. P. Coutinho, Cation Alkyl Side Chain Length and Symmetry Effects on the Surface Tension of Ionic Liquids, *Langmuir* **2014**, *30*, 6408-6418.
- [136] B. S. J. Heller, U. Paap, F. Maier, H.-P. Steinrück, Pronounced surface enrichment of fluorinated ionic liquids in binary mixtures with methoxy-functionalized ionic liquids, *J. Mol. Liq.* **2020**, *305*, 112783.
- [137] B. S. J. Heller, M. Lexow, F. Greco, S. Shin, G. Partl, F. Maier, H.-P. Steinrück, Temperature-Dependent Surface Enrichment Effects in Binary Mixtures of Fluorinated and Non-Fluorinated Ionic Liquids, *Chem. Eur. J.* **2020**, *26*, 1117-1126.
- [138] V. Lloret, M. Á. Rivero-Crespo, J. A. Vidal-Moya, S. Wild, A. Doménech-Carbó, B. S. J. Heller, S. Shin, H.-P. Steinrück, F. Maier, F. Hauke, M. Varela, A. Hirsch,

- A. Leyva-Pérez, G. Abellán, Few layer 2D pnictogens catalyze the alkylation of soft nucleophiles with esters, *Nat. Commun.* **2019**, *10*, 509.
- [139] E. F. Smith, I. J. Villar Garcia, D. Briggs, P. Licence, Ionic liquids *in vacuo*; solution-phase X-ray photoelectron spectroscopy, *Chem. Commun.* **2005**, 5633-5635.
- [140] K. L. Kuntz, R. A. Wells, J. Hu, T. Yang, B. Dong, H. Guo, A. H. Woomer, D. L. Druffel, A. Alabanza, D. Tománek, S. C. Warren, Control of Surface and Edge Oxidation on Phosphorene, *ACS Appl. Mater. Interfaces* **2017**, *9*, 9126-9135.

## 8 Acknowledgment

An dieser Stelle möchte ich mich bei folgenden Personen herzlich bedanken:

- Bei Prof. Dr. Hans-Peter Steinrück für die Möglichkeit meine Dissertation am Lehrstuhl für Physikalische Chemie II anzufertigen, insbesondere für die Weitergabe seiner langjährigen Erfahrung im Bereich der Oberflächenforschung und für viele konstruktive Diskussionen.
- Bei Dr. Florian Maier für seine Betreuung als Leiter der IL-Gruppe, seine umfassende Unterstützung und die zahlreichen Diskussionen über gemessene Daten.
- Bei allen ehemaligen und jetzigen IL-Gruppenmitgliedern Dr. Inga Niedermaier, Dr. Claudia Kolbeck, Dr. Florian Rietzler, Dr. Radha Bhui, Dr. Sunghwan Shin, Dr. Benjamin May, Dr. Matthias Lexow, Francesco Greco, Manuel Meusel, Ulrike Paap, Stephen Massicot, Leonhard Winter und Patrick Schreiber für die tolle Arbeitsatmosphäre.
- Besonders bei Francesco Greco für das unkomplizierte Zusammenarbeiten an der DASSA, auch während der vielen gemeinsamen Reparaturen. Das machte die Arbeit im Labor sehr angenehm.
- Bei Hans-Peter Bäumler und Bernd Kreß für ihre Unterstützung bei Problemen an der DASSA. Ohne sie hätte die Problembehebung oftmals ewig gedauert. Außerdem bei Friedhold Wölfel und dem gesamten Werkstattteam für alle gefertigten Bauteile.
- Bei meinen Kooperationspartnern: Prof. Dr. Patricia Hunt, Dr. Karina Shimizu, Dr. Sabine Dommer, Dr. Gabriel Partl, Dr. Nicola Taccardi, Dr. Mikhail Gantman, Dr. Marlene Scheuermeyer, Wei Wei, Vicent Lloret und Stefan Wild für die Simulationen, die (IL-)Synthesen und die DSC-Messungen.
- Bei Andrea Meixner-Wolf und Susana Kreß, die bei allen administrativen Fragen mit Rat und Tat behilflich waren und bei Norman Anja Schmidt für die IT-Unterstützung.
- Bei Sofia Korenko für Messdaten im Rahmen ihrer Bachelorarbeit.
- Bei allen Mitgliedern des Lehrstuhls für Physikalische Chemie II für die tolle Zeit.
- Abschließend auch bei meiner Familie und meinen Freunden für ihre Unterstützung.



## 9 Appendix

### 9.1 Publications [P1] – [P5]

**[P1] Probing the Surface Tension of Ionic Liquids Using the Langmuir Principle**

K. Shimizu, B. S. J. Heller, F. Maier, H.-P. Steinrück, J. N. Canongia Lopes

*Langmuir* **2018**, *34*, 4408–4416.

DOI: [10.1021/acs.langmuir.7b04237](https://doi.org/10.1021/acs.langmuir.7b04237)

Reprinted with permission from "Langmuir". Copyright © 2018 American Chemical Society. Further permissions related to this article should be directed to the American Chemical Society.

**[P2] Surface Enrichment in Equimolar Mixtures of Non-Functionalized and Functionalized Imidazolium-Based Ionic Liquids**

B. S. J. Heller, C. Kolbeck, I. Niedermaier, S. Dommer, J. Schatz, P. Hunt, F. Maier, H.-P. Steinrück

*ChemPhysChem* **2018**, *19*, 1733–1745.

DOI: [10.1002/cphc.201800216](https://doi.org/10.1002/cphc.201800216)

This article is licensed under the Creative Commons Attribution Non-Commercial License (CC BY-NC 4.0). To view a copy of the license, visit <https://creativecommons.org/licenses/by-nc/4.0/>. Copyright © 2018 The Authors. Published by Wiley-VCH Verlag GmbH & Co. KGaA.

**[P3] Temperature-Dependent Surface Enrichment Effects in Binary Mixtures of Fluorinated and Non-Fluorinated Ionic Liquids**

B. S. J. Heller, M. Lexow, F. Greco, S. Shin, G. Partl, F. Maier, H.-P. Steinrück

*Chem. Eur. J.* **2020**, *26*, 1117–1126.

DOI: [10.1002/chem.201904438](https://doi.org/10.1002/chem.201904438)

This article is licensed under the Creative Commons Attribution License (CC BY 4.0). To view a copy of the license, visit <https://creativecommons.org/licenses/by/4.0/>. Copyright © 2019 The Authors. Published by Wiley-VCH Verlag GmbH & Co. KGaA, Weinheim.

**[P4] Pronounced surface enrichment of fluorinated ionic liquids in binary mixtures with methoxy-functionalized ionic liquids**

B. S. J. Heller, U. Paap, F. Maier, H.-P. Steinrück

*J. Mol. Liq.* **2020**, *305*, 112783.

DOI: [10.1016/j.molliq.2020.112783](https://doi.org/10.1016/j.molliq.2020.112783)

This article is licensed under the Creative Commons CC BY 4.0 license. To view a copy of the license, visit <https://creativecommons.org/licenses/by/4.0/>. Copyright © 2020 The Authors. Published by Elsevier B.V.

**[P5] Few layer 2D pnictogens catalyze the alkylation of soft nucleophiles with esters**

V. Lloret, M. Á. Rivero-Crespo, J. A. Vidal-Moya, S. Wild, A. Doménech-Carbó, B. S. J. Heller, S. Shin, H.-P. Steinrück, F. Maier, F. Hauke, M. Varela, A. Hirsch, A. Leyva-Pérez, G. Abellán

*Nat. Commun.* **2019**, *10*, 509.

DOI: [10.1038/s41467-018-08063-3](https://doi.org/10.1038/s41467-018-08063-3)

This article is licensed under the Creative Commons CC BY 4.0 license. To view a copy of this license, visit <https://creativecommons.org/licenses/by/4.0/>. Copyright © 2019, Springer Nature.

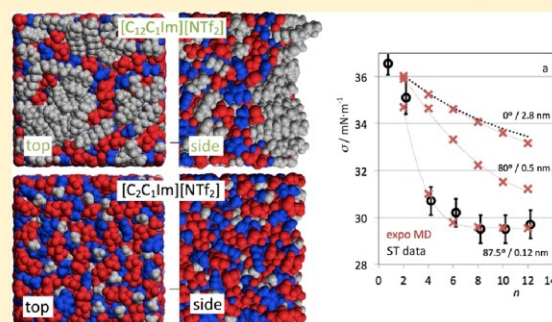
## Probing the Surface Tension of Ionic Liquids Using the Langmuir Principle

Karina Shimizu,<sup>†</sup> Bettina S. J. Heller,<sup>‡</sup> Florian Maier,<sup>\*,‡</sup> Hans-Peter Steinrück,<sup>‡</sup> and José N. Canongia Lopes<sup>\*,†</sup>

<sup>†</sup>Centro de Química Estrutural, Instituto Superior Técnico, Universidade de Lisboa, 1049-001 Lisboa, Portugal

<sup>‡</sup>Lehrstuhl für Physikalische Chemie II, Universität Erlangen-Nürnberg, 91054 Erlangen, Germany

**ABSTRACT:** At 298 K, the surface tension of ionic liquids (ILs) of the 1-alkyl-3-methylimidazolium bis-(trifluoromethylsulfonyl)imide series,  $[C_nC_1\text{Im}][\text{NTf}_2]$ , ranges from around  $35 \text{ mN}\cdot\text{m}^{-1}$  for  $[C_2C_1\text{Im}][\text{NTf}_2]$  to just below  $30 \text{ mN}\cdot\text{m}^{-1}$  for  $[C_{12}C_1\text{Im}][\text{NTf}_2]$ . However, the decrease rate along the series is not constant: a large decrease from  $[C_2C_1\text{Im}][\text{NTf}_2]$  to  $[C_8C_1\text{Im}][\text{NTf}_2]$  is followed by almost constant values from  $[C_8C_1\text{Im}][\text{NTf}_2]$  to  $[C_{12}C_1\text{Im}][\text{NTf}_2]$ . Such behavior is hard to interpret from a molecular point of view without suitable information about the free-surface structure of the different ILs. In this work, we have successfully used the Langmuir principle in combination with structural data obtained from angle-resolved X-ray photoelectron spectroscopy experiments and molecular dynamics simulations, to predict the correct surface tension trend along the IL series. The concepts unveiled for this particular homologous IL family can be easily extended to other systems.



### INTRODUCTION

Ionic liquids (ILs), salts that melt at temperatures not far from room temperature, are a relatively recent class of fluids with several unique structural properties.<sup>1–6</sup> Due to their extremely low vapor pressure, large electrochemical window, high thermal stability, and structural variability, ILs are promising candidates for applications in multiphase catalysis, electrochemistry, separation technology, and many other areas.<sup>7</sup> The nature of the IL surface layer, that is, the interface between an IL and a gas phase, becomes an important factor particularly when high surface area systems are involved. In the case of ILs, the composition of the surface layer and the structure of its gas (or vacuum) boundary is a result of different types of short- and long-range interactions related to the ILs' complex molecular structure; the IL's tendency to minimize its surface free energy results in its experimentally observable surface tension values.

Different ILs can exhibit quite diverse surface tension values. For instance, at 298 K, 1,3-dimethylimidazolium methylsulfate,  $[C_1C_1\text{Im}][\text{C}_1\text{SO}_4]$ , exhibits a surface tension of  $65.1 \text{ mN}\cdot\text{m}^{-1}$ , whereas 1-butyl-3-methylimidazolium octylsulfate,  $[C_4C_1\text{Im}][\text{C}_8\text{SO}_4]$ , exhibits a surface tension of only  $25.2 \text{ mN}\cdot\text{m}^{-1}$  at the same temperature.<sup>8</sup>

Interestingly, many ILs fill the  $40\text{--}70 \text{ mN}\cdot\text{m}^{-1}$  surface tension gap that exists between most molecular solvents (with values up to  $40 \text{ mN}\cdot\text{m}^{-1}$  at 298 K) and water ( $72 \text{ mN}\cdot\text{m}^{-1}$  at the same temperature).<sup>9</sup> Molecular fluids that are exceptions to this trend and exhibit surface tensions within the  $40\text{--}70 \text{ mN}\cdot\text{m}^{-1}$  interval generally have a large tendency to form multiple hydrogen bonds (e.g., glycols, alkanesulfonic acids). In fact,

water can be regarded as the fluid with the highest hydrogen bonding density, thus explaining its anomalous surface tension values. Conversely, in the case of ILs, the relatively high surface tension values can be rationalized in terms of electrostatic interactions between ions.

Several attempts have been made to correlate in an empirical or semiempirical way the surface tension of different ionic liquids with the characteristics of their constituting ions. Those works range from the use of quantitative structure–property relationship (QSPR) methods, to the definition of the so-called Parachor and ionic Parachor (surface-tension-weighted molar volumes) and their use in group-contribution methods.<sup>10–14</sup> However, the development of a general framework for explaining and predicting surface tension trends across a large number of different ILs seems to be difficult, which could be related to the complex structural nature of ILs.<sup>15</sup>

As pointed out by Irving Langmuir more than 80 years ago,<sup>16</sup> the surface tension of a fluid is related on one hand to the intermolecular interactions in the bulk (cohesive energy) and on the other to the molecular orientation at the surface. In general, high cohesive energies contribute to high surface tension values. However, this correlation is only a good approximation for liquids where surface ordering effects are negligible.

Received: December 14, 2017

Revised: February 27, 2018

Published: February 27, 2018

Thus, within the framework of the so-called “Langmuir principle”, the surface tension is given by “the result of superposition over the molecule parts present at outer surface”.<sup>16</sup>

Even as isotropic bulk liquids, ILs are known to exhibit complex structuration and nanosegregated domains which are a consequence of the balance that has to be achieved between local electroneutrality conditions among ions of opposite charge and the competition between electrostatics and other van der Waals forces that are present in different moieties of the IL ions.<sup>17,18</sup> Such local structural anisotropy is further modified (and exacerbated) at the surface of the liquid: the 2D liquid-vacuum boundary imposes limiting conditions that induce the structural rearrangement of the ILs ions into layered arrangements parallel to the surface with different local composition.<sup>19,20</sup>

In the present work, we will use an IL homologous series, 1-alkyl-3-methylimidazolium bis(trifluoromethylsulfonyl)imide,  $[C_nC_1Im][NTf_2]$  ( $2 \leq \text{even } n \leq 12$ ), to discuss the bulk cohesive energy and surface molecular orientation. These two issues are, according to the Langmuir principle, paramount to the correct evaluation and understanding of the surface tension from a molecular perspective. We have chosen this series because the experimental values for the surface tension and surface composition have been derived by the same group under identical experimental conditions.<sup>15</sup> Despite the fact that absolute surface tension values of neat ILs deviate considerably in literature even for this series,<sup>21</sup> in all cases the same general trend is found: surface tension of  $[C_nC_1Im][NTf_2]$  ILs steeply decreases from the highest value for  $n = 2$ , and with increasing chain length this decrease is reduced reaching a plateau at around  $n = 8-12$ .

Nowadays, the surface molecular orientation, or as stated originally by Langmuir, the “molecule parts present at outer surface”, can be probed by surface-sensitive experimental methods such as angle-resolved X-ray photoelectron spectroscopy (ARXPS).<sup>15</sup> In the present work, we will match such type of data to density profiles calculated from Molecular Dynamic simulation trajectories.

## ■ SIMULATION DETAILS

The interfacial structure of all ILs studied experimentally was probed using molecular dynamics (MD) simulations. The ILs were modeled using the CL&P atomistic force field,<sup>22</sup> which is an extension of the AMBER and OPLS force fields<sup>23</sup> specially designed to study ILs and their homologous series. MD simulations were carried out using the DL\_POLY 2.20 package.<sup>24</sup> The runs were performed with a 2 fs time step and a 1.6 nm cutoff distance. Ewald summation corrections were performed beyond the cutoffs. Due to the slow dynamics of this type of systems, special care was taken to ensure the attainment of true equilibrium conditions (we have performed equilibration runs under harsh temperature and charge annealing conditions). The number of ion pairs and the size of the simulation box for all studied ILs are presented in Table 1.

All simulations started from low-density configurations that were subjected to 3 ns equilibration runs under isobaric isothermal ensemble conditions at  $p = 0.1$  MPa and  $T = 298$  K, with Nosé–Hoover thermostats and barostats with relaxation time constants of 1 and 4 ps, respectively. The bulk density of each system reached constant and consistent values, indicating that equilibrium had been attained and possible ergodicity problems had been overcome. Finally, several (at least six) consecutive production stages of 1.0 ns each were performed and the combined results were used for the evaluation of relevant structural data in bulk conditions.

**Table 1. Simulation Conditions and Size of the Equilibrated Boxes**

system	$N$ ion pairs	slab dimensions (nm $\times$ nm $\times$ nm)
$[C_2C_1Im][NTf_2]$	600	$4.0 \times 4.0 \times 16.0$
$[C_4C_1Im][NTf_2]$	600	$4.0 \times 4.0 \times 18.0$
$[C_6C_1Im][NTf_2]$	600	$4.0 \times 4.0 \times 20.0$
$[C_8C_1Im][NTf_2]$	600	$4.0 \times 4.0 \times 23.5$
$[C_{10}C_1Im][NTf_2]$	450	$4.0 \times 4.0 \times 18.0$
$[C_{12}C_1Im][NTf_2]$	450	$4.0 \times 4.0 \times 20.0$

To model the IL–vacuum interface, each cubic simulation box containing a pure IL was expanded to a value three times its initial size by elongating the sides of the cube along the  $z$ -axis. This generated an IL slab with two explicit liquid–vacuum interfaces and tetragonal simulation boxes with approximately  $4.5 \times 4.5 \times 35.0$  nm<sup>3</sup> dimensions. A simulation run was then conducted under  $NVT$  ensemble conditions ( $T = 298$  K), with 0.5 and 2 ns equilibration and production stages, respectively; no drift in the studied properties was found from block analysis of the production stage. In order to obtain a thicker IL slab, the system was then subjected to a lateral compression (in the  $x$ - and  $y$ -axes) by running a  $NpT$  ensemble simulation for around 150 ps. This process leads to a tetragonal box with a  $4.0 \times 4.0$  nm<sup>2</sup> base and a liquid layer about 16 nm thick. This configuration was then subjected to new (3 ns equilibration + 6 ns production) processes under  $NVT$  conditions that conducted to the results discussed below. Possible ergodicity problems were tested by calculating the system properties at different stages of the production runs, including comparisons between slabs of different thickness or between processes interspersed by temperature-annealing cycles.

## ■ EXPERIMENTAL DETAILS

Surface orientation effects within the  $[C_nC_1Im][NTf_2]$  ( $n = 2, 4, 6, 8, 10, 12$ ) IL series of this work was already investigated and published before;<sup>25</sup> now, a re-evaluation of these data was applied to obtain more accurate values for the composition within the outermost surface layers (for more details, see Results). In particular, the absence of surface-active contaminations such as polysiloxanes or additional hydrocarbon compounds<sup>26</sup> has been proven by angle-resolved X-ray photoelectron spectroscopy (ARXPS) as will be discussed below. It should be noted that the identical ILs have been used not only for ARXPS but for surface tension measurements as well, employing the pendant drop method.<sup>15</sup> Experimental details of our ARXPS setup and spectra analysis are extensively described in earlier publications.<sup>25</sup> In short, IL films with thicknesses of about 0.1 mm were spread on a planar Au foil ( $20 \times 15 \times 0.1$  mm<sup>3</sup>) forming a smooth coating layer and then introduced into the ultra high vacuum (UHV) system via a loadlock. The rather large sample size was chosen to avoid signal contributions from the foil edges where deviations from flat film morphology occur, particularly at the bottom part of the tilted sample holder. After at least 6 h of pumping, a base pressure of  $\sim 5 \times 10^{-10}$  mbar was eventually achieved, confirming the absence of volatile impurities such as water or nonreacted imidazole. Detailed spectra were recorded with an ESCALAB 200 VG system using nonmonochromated Al  $K\alpha$  radiation ( $h\nu = 1486.6$  eV) with an overall energy resolution of 0.9 eV. Due to the small layer thickness, the good wetting characteristics, and the relatively high viscosity of the ILs, the IL-coated Au foil could be tilted from horizontal to vertical position in order to change the polar electron detection angle for ARXPS without affecting the IL film morphology (recently, we remeasured some of the ILs of this series using a unique UHV setup with two analyzers mounted for simultaneous  $0^\circ$  and  $80^\circ$  electron detection with the IL sample holder fixed in horizontal geometry;<sup>27</sup> the resulting ARXP spectra do not differ significantly from the ones obtained by sample tilting, which is a clear indication that the morphology in the center of the sample holder is not affected by sample tilting). ARXPS makes use of the dependence of XPS information depth (ID) on the electron emission angle  $\theta$  (relative to the surface normal) due to the small inelastic mean free path  $\lambda$  of the excited photoelectrons in matter;  $\lambda$  depends on kinetic

**Table 2. Quantitative Analysis of the XP Spectra of  $[C_nC_1Im][NTf_2]$ , for  $n = 2-12$  (Approximate Binding Energy Positions and Atomic Sensitivity Factors, ASF, of the Core Levels Used Are Given in the First Row)<sup>a</sup>**

		C 1s (hetero)	C 1s (alkyl)	N 1s (cation)	C 1s (anion)	N 1s (anion)	O 1s (anion)	S 2p (anion)	F 1s (anion)	
	approx. position (eV)	286.5	285.0	401.9	292.8	399.2	532.5	167.7	688.8	
	ASF	0.205	0.205	0.350	0.205	0.350	0.540	0.400	1.000	ratio $C_{alkyl}/C_{hetero}$
$[C_2C_1Im][NTf_2]$	nominal	5.0	1.0	2.0	2.0	1.0	4.0	2.0	6.0	0.20
	0°	5.1	0.8	2.1	2.1	1.0	4.0	2.0	5.9	0.16
	80°	4.4	1.5	1.8	2.1	1.0	3.3	1.8	7.0	0.34
$[C_4C_1Im][NTf_2]$	nominal	5.0	3.0	2.0	2.0	1.0	4.0	2.0	6.0	0.60
	0°	5.1	3.1	2.1	2.1	1.0	3.9	2.1	5.8	0.61
	80°	4.4	4.1	1.8	2.0	0.9	3.3	1.9	6.6	0.93
$[C_6C_1Im][NTf_2]$	nominal	5.0	5.0	2.0	2.0	1.0	4.0	2.0	6.0	1.00
	0°	5.2	5.2	2.0	2.0	1.0	3.8	2.0	5.8	1.00
	80°	4.4	6.9	1.7	1.9	0.9	3.2	1.8	6.2	1.57
$[C_8C_1Im][NTf_2]$	nominal	5.0	7.0	2.0	2.0	1.0	4.0	2.0	6.0	1.40
	0°	5.1	7.0	2.1	2.0	1.0	3.9	2.0	5.9	1.37
	80°	3.9	10.3	1.6	1.7	0.9	3.1	1.8	5.8	2.64
$[C_{10}C_1Im][NTf_2]$	nominal	5.0	9.0	2.0	2.0	1.0	4.0	2.0	6.0	1.80
	0°	5.4	9.2	2.0	2.0	1.0	3.8	2.0	5.7	1.70
	80°	3.8	14.1	1.4	1.6	0.8	2.9	1.7	4.8	3.71
$[C_{12}C_1Im][NTf_2]$	nominal	5.0	11.0	2.0	2.0	1.0	4.0	2.0	6.0	2.20
	0°	5.5	11.8	2.0	1.9	1.0	3.9	1.9	5.5	2.15
	80°	3.5	17.5	1.3	1.4	0.8	2.7	1.4	4.3	5.00

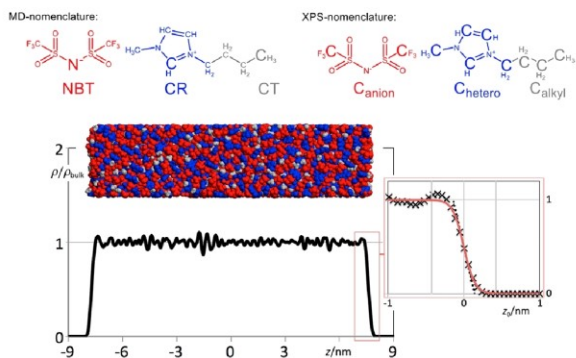
<sup>a</sup>The nominal and the experimentally determined composition in number of atoms (bold numbers; for nomenclature, see Figure 3 “XPS nomenclature”) are measured at 0° (bulk-sensitive) and 80° (surface-sensitive) electron emission angle as has been presented earlier;<sup>25</sup> in addition to ref 25,  $C_{alkyl}$  and  $C_{hetero}$  content was corrected as described in the text taking the N 1s (cation) intensity of the imidazolium ring into account, which leads to more accurate values for the ratio  $C_{alkyl}/C_{hetero}$  (last column).

energy, that is, the core level studied, with values between 2 and 3 nm for organic materials.<sup>28</sup> Due to the small acceptance angle of our electron analyzer, measurements at  $\theta = 0^\circ$  probe the near-surface region with an ID of 7–9 nm (ID is the depth where 95% of the detected signal originates from, which is three times  $\lambda$ ). This corresponds to 10–15 IL layers, estimating the mean ion pair size from the cubic root of the molecular volume for the different ILs. In contrast, measurements at 80° ( $ID(80^\circ) \approx ID(0^\circ)\cos\theta \approx ID(0^\circ)/6$ ; 1–1.5 nm) predominately probe the outermost surface layers.<sup>27</sup> To give an example, for the C 1s level with  $\lambda = 2.8$  nm of  $[C_8C_1Im][NTf_2]$  with an estimated size of 0.84 nm,<sup>15</sup> 82% of the total signal originates from the outermost layer at 80° and only 26% at 0°. Note that our positioning in absolute tilt angle is estimated to be accurate within  $\pm 1^\circ$ ; whereas at 0°, this uncertainty has no impact on  $ID(0^\circ)$ , the  $\pm 1^\circ$  uncertainty in 80° grazing emission translates into a uncertainty in  $ID(80^\circ)$  of  $\pm 10\%$ . The high surface sensitivity in 80° allows us to derive information on the outermost surface composition and on the arrangement and orientation of the molecules in this outermost layer. For the quantitative analysis, a three-point linear background subtraction was used for the C 1s spectra; for all other core-level spectra a two-point linear background subtraction was applied. All peaks were fitted using a Gaussian-Lorentz profile with 30% Lorentz contribution employing fitting constraints described somewhere else.<sup>29</sup> Quantitative composition from the obtained peak areas was derived using carefully calibrated atomic sensitivity factor (ASF) values, which take into account the specific experimental setup such as the electron analyzer transmission function.<sup>27</sup> ASF values for the individual core levels are given in Table 2. In contrast to earlier publications,<sup>25</sup> the evaluation of C 1s spectra for quantifying aliphatic and nonaliphatic carbon atoms at the surface has been corrected for the first time using the N 1s signals of the imidazolium ring, as will be

detailed later, leading to the more accurate surface composition values shown in Table 2.

## RESULTS AND DISCUSSION

Figure 1 shows a snapshot of a simulation box containing 600  $[C_2C_1Im][NTf_2]$  ion pairs. The box is a quadrangular prism with  $4 \times 4 \times 35$  nm<sup>3</sup> dimensions and periodic boundary conditions in the  $x$  and  $y$  directions. The equilibrated system is a slab of IL with two explicit liquid–vacuum interfaces and a thickness of around 18 nm. The figure also shows a representation of the total numerical density profile along the normal to the interfaces ( $z$  axis) using the same scale of the snapshot. It was calculated taking into account equilibrated MD trajectories ca. 10 ns long. The numerical density data at a given  $z$  value was calculated considering all atoms within a  $4 \times 4 \times \Delta z$  nm<sup>3</sup> layer ( $\Delta z = 0.058$  nm) of the simulation box, with the hydrogen atoms weighted by a 0.5 factor, and was normalized taking into account the average numerical density at the center of the slab (the 10 nm-thick central layer further away from either interface). The profiles at the interfaces have shapes which can be fitted to sigmoid functions,  $S(z) = \rho(z)/\rho_{bulk} = 1/(1 + \exp((z - z_{1/2})/k))$ , where  $z_{1/2}$  is the depth where  $\rho(z)/\rho_{bulk} = 1/2$  (interface midpoint), and  $k$  is the decay length. The  $z_{1/2}$  values were used to define the origin of the  $z$ -axes in internal coordinates,  $z_0$ , relative to each interface (inset of Figure 1). The decay length of the sigmoid function,  $k$ , is an indication of the width of the interface: the positions of the density profile liftoff,  $\rho(z)/\rho_{bulk} = 0.002$ , is at approximately  $+6k$  and of those



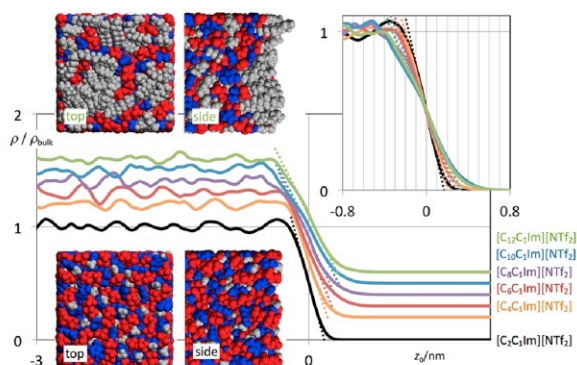
**Figure 1.** Simulation snapshot of the  $[\text{C}_2\text{C}_1\text{Im}][\text{NTf}_2]$  system. The equilibrated system is a 18 nm thick slab of IL with two explicit IL-vacuum interfaces contained in a  $4 \times 4 \times 35 \text{ nm}^3$  prism. The main graph in the bottom shows the corresponding total reduced numerical density profile,  $\rho/\rho_{\text{bulk}}$ , along the direction normal to the interfaces,  $z$ . It was plotted using the same length scale of the snapshot and normalized taking into account the average numerical density at the center of the slab ( $-5 < z/\text{nm} < 5$ ). The inset graph is a zoom of the interface on the right and shows the fitting of a sigmoid function,  $S(z) = \rho(z)/\rho_{\text{bulk}}$  (red line), to the reduced numerical density data (black crosses). The  $x$ -axis in the inset graph is rescaled such that  $z_0 = 0$  at  $S(z) = 0.5$ . The three vertical lines correspond to  $z_0 = -6k$ ,  $0$ , and  $+6k$ , where  $k$  is the decay length of the sigmoid function. In the snapshot, anions are depicted as red space-filled atoms, the charged parts of the cations as blue space-filled atoms and the alkyl side chains of the cations as gray space-filled atoms. The coloring and nomenclature of the different atoms used in the MD and XPS studies are given in the structural formulas at the top of the figure.

of the attainment of the liquid density,  $\rho(z)/\rho_{\text{bulk}} = 0.998$ , at approximately  $-6k$ .

The other five systems,  $[\text{C}_n\text{C}_1\text{Im}][\text{NTf}_2]$  ( $n = 4, 6, 8, 10, 12$ ), were simulated using similar conditions. Since we were interested in the comparison of the liquid-vacuum interfaces, we have decided to keep all quadrangular prisms with  $4 \times 4 \text{ nm}^2$  cross sections, thus minimizing any difference arising from finite-size effects related to the use of periodic boundary conditions in the directions parallel to the interfaces. This means that the overall width of the IL slabs increases as the corresponding molar volume of the ILs also increases along the homologous series. In the case of  $[\text{C}_{10}\text{C}_1\text{Im}][\text{NTf}_2]$  and  $[\text{C}_{12}\text{C}_1\text{Im}][\text{NTf}_2]$ , we reduced the number ion pairs present in the system from 600 to 450 to avoid unnecessarily thick slabs.

**Figure 2** compares the total number density profiles of the six systems in the region close to one of the interfaces. The graph is given in internal  $z_0$  coordinates relative to that interface, with positive  $z_0$  values pointing toward the vacuum region. The  $\rho(z_0)/\rho_{\text{bulk}}$  values of the different profiles were offset in the graph in order to avoid superimposition of the plots. The inset shows the superimposed sigmoid functions without the offset of the profiles. The figure also shows top-view and side-view snapshots of the  $[\text{C}_2\text{C}_1\text{Im}][\text{NTf}_2]$  and  $[\text{C}_{12}\text{C}_1\text{Im}][\text{NTf}_2]$  interfaces.

The sigmoid profiles show that the liquid-vacuum interfaces get broader and somewhat less well-defined along the homologous series. The corresponding decay lengths of the sigmoid functions,  $k$ , for the six  $[\text{C}_n\text{C}_1\text{Im}][\text{NTf}_2]$ -ILs range from 0.071 nm for  $[\text{C}_2\text{C}_1\text{Im}][\text{NTf}_2]$  over 0.087 nm ( $n = 4$ ), 0.101 nm (6), 0.115 nm (8), 0.129 nm (10) to 0.134 nm for  $[\text{C}_{12}\text{C}_1\text{Im}][\text{NTf}_2]$ . This can be appreciated qualitatively by the

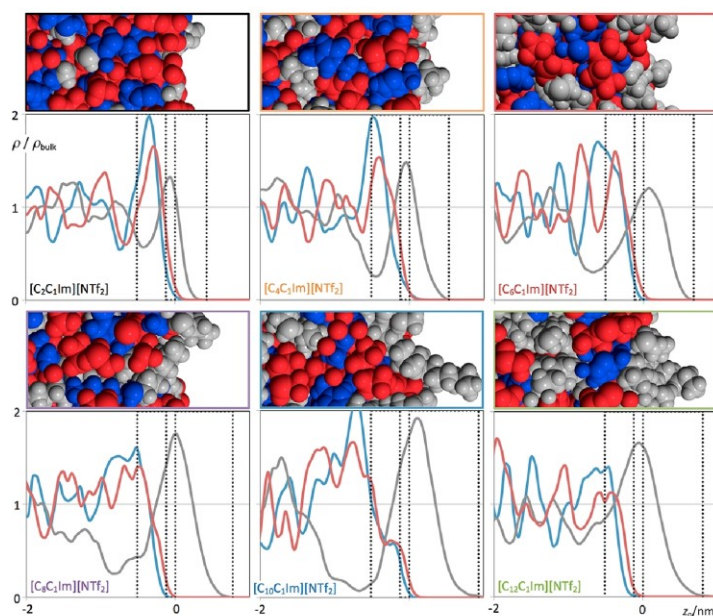


**Figure 2.** Total reduced numerical density profiles,  $\rho/\rho_{\text{bulk}}$ , along the direction normal to the interfaces,  $z$ , for the  $[\text{C}_n\text{C}_1\text{Im}][\text{NTf}_2]$  systems. Traces other than that for  $[\text{C}_2\text{C}_1\text{Im}][\text{NTf}_2]$  were vertically offset for clarity. Simulation snapshots of the  $[\text{C}_2\text{C}_1\text{Im}][\text{NTf}_2]$  (bottom) and  $[\text{C}_{12}\text{C}_1\text{Im}][\text{NTf}_2]$  (top) systems showing top (left) and side views (right) of the surface. The inset shows the superimposed sigmoid density profiles near the interface (gray vertical lines indicate 0.1 nm steps). The dotted lines represent the slope,  $s_0$ , of the sigmoid curve at  $z_0 = 0$ . Color-coding of the MD snapshots as in Figure 1.

side-view snapshots: shorter alkyl-chain ILs such as  $[\text{C}_2\text{C}_1\text{Im}][\text{NTf}_2]$  exhibit a sharper, more homogeneous interface than longer ones such as  $[\text{C}_{12}\text{C}_1\text{Im}][\text{NTf}_2]$ . In the latter case, the long alkyl chains do not cover the entire surface (one can still observe patches of the charged moieties of the IL in the top view in the upper left corner of **Figure 2**) and tend to form clusters, thus producing a more irregular surface. Nevertheless, by defining the zero of each interface at the sigmoid function midpoint and considering in-plane averages while calculating the numerical density profiles of the different species present in the system, it is possible to compare the different interfaces in a meaningful way, indirectly taking into account their intrinsic thickness and roughness. The definition of an origin for each interface of the slabs also allowed us to combine the simulation results from the two interfaces of each IL simulation run in order to improve the corresponding statistics. The following analyses have been performed considering such averaged data.

**Figure 3** shows the numerical density profiles for all studied ILs of three selected atoms that are used as proxies for different moieties of the IL: the  $[\text{NTf}_2]^-$  anions are represented in red by their nitrogen atom, NBT; the charged headgroups of the  $[\text{C}_n\text{C}_1\text{Im}]^+$  cations are represented in blue by the carbon atom, CR, of the imidazolium ring that lies between its two nitrogen atoms; the alkyl side chains of the cations are represented in gray by their terminal carbon atom, CT.

The profiles show the stratification of fluid at the IL-vacuum interface even for the IL with the shortest alkyl side chain: the  $[\text{C}_2\text{C}_1\text{Im}][\text{NTf}_2]$  profiles show CT atoms at the outermost surface forming a thin alkyl layer, followed by a charged layer (containing the charged moieties of both ions, NBT/CR lines) which is depleted of CT atoms. The profiles show that the anions (red profile) tend to be slightly closer to the surface than the charged headgroup of the cations, blue profile). It must be stressed that the graphs are averages over each  $4 \times 4 \times \Delta z_0$  slice used to calculate the numerical density profiles. The peaks do not represent homogeneous layers but rather the relative probability of finding an atom of a specific type at a given distance from the surface.

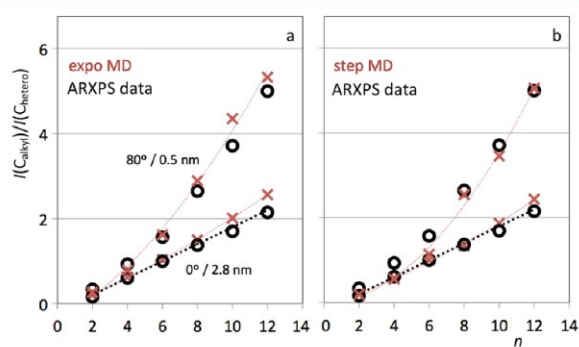


**Figure 3.** Reduced numerical density profiles of selected atoms,  $\rho/\rho_{\text{bulk}}$ , along the direction normal to the interfaces,  $z_0$ , for the  $[\text{C}_n\text{C}_1\text{Im}][\text{NTf}_2]$  systems. Each graph is accompanied by a snapshot of the corresponding MD simulated surface depicted using the same length scale. Red lines, anion NBT atoms; blue lines, cation CR atom; gray lines, cation CT atom. The vertical dotted lines in each graph are, from right to left: the lift-off of density profiles (at  $+6k$ ), the origin of the surfaces (at  $S(z_0) = 0.5$ ), the limit of the “outer surface” (at  $-0.12$  nm), and the limit (at  $-0.5$  nm) corresponding to 95% of the signal of an  $80^\circ$  ARXPS experiment. Color-coding of the MD snapshots as in Figure 1.

As the alkyl chains increase in length along the series, the profiles show a broadening of the first CT peak, and the shift of the first CR/NBT maxima further away from the surface. This broadening of the first layers is complemented by a more obvious separation of the alkyl layer and the accompanying charged layer. It also goes along with a more pronounced dip of the CT curve after the first peak, at least up to  $[\text{C}_{10}\text{C}_1\text{Im}][\text{NTf}_2]$ . The profiles also show less defined NBT/CR curves (double peaks, shoulders) near the surface as the series progresses toward longer alkyl side chains. Such a behavior suggests less ordered charged layers for the ILs with longer alkyl side chains.

The “molecule parts present at outer surface” issue can now be addressed by taking into account the different numerical density profiles and establishing a boundary for the “outer surface”. In order to validate the simulation results and check possible definitions for the outer surface, we have decided to match ARXPS results for the  $[\text{C}_n\text{C}_1\text{Im}][\text{NTf}_2]$  series with the present simulation data.

Figure 4 shows the ARXPS results as black circles. The surface enrichment of the alkyl chains is quantified by the intensity ratio of XPS signal of the alkyl carbon atoms,  $C_{\text{alkyl}}$ , and of the carbon atoms with hetero atom (nitrogen) neighbors  $C_{\text{hetero}}$ . The data show how the ratio  $I(C_{\text{alkyl}})/I(C_{\text{hetero}})$  varies along the  $[\text{C}_n\text{C}_1\text{Im}][\text{NTf}_2]$  IL series. For measurements at an angle of  $\theta = 0^\circ$  to the surface normal, the ratio is similar to the nominal  $(n-1)/5$  ratio (in a  $[\text{C}_n\text{C}_1\text{Im}]$  cation there are 5 hetero C atoms and  $n-1$  alkyl C atoms, cf. Figure 1) observed for the bulk IL, cf. dotted black line in Figure 4. For measurements at  $\theta = 80^\circ$ , that is, in the surface-sensitive geometry, the ratio starts to be significantly larger at  $n = 4$  than the nominal value (dotted black line); with increasing chain length ( $n > 4$ ) this difference increases, as is evident from Figure 4. In other words, the



**Figure 4.**  $I(C_{\text{alkyl}})/I(C_{\text{hetero}})$ , the ratio between the probability of finding a carbon atom belonging to the alkyl chain ( $C_{\text{alkyl}}$ ) and the probability of finding a carbon atom attached to the imidazolium ring ( $C_{\text{hetero}}$ ), versus the size of the alkyl chain,  $n$ , in the  $[\text{C}_n\text{C}_1\text{Im}][\text{NTf}_2]$  series. The black circles refer to ratios found for the  $0^\circ$  (bulk-sensitive) and the  $80^\circ$  (surface-sensitive) measurements. The bulk nominal ratio is given by the dotted line. The red crosses refer to MD simulations taking into account similar layers and using exponential decay (a) or step (b) contributions (for details, see text).

surplus presence of the alkyl chains in the surface layers progressively increases along the  $[\text{C}_n\text{C}_1\text{Im}][\text{NTf}_2]$  series.

The observed enrichment of the longer alkyl chains as derived from ARXPS has been published before.<sup>25</sup> For the quantitative comparison performed here, these results have been carefully reanalyzed with a modified procedure, which yields an even more pronounced surface enrichment as the original analysis, in particular for chain lengths with  $n = 10$  and  $12$ . This is due to the fact that the  $C_{\text{alkyl}}$  and  $C_{\text{hetero}}$  peaks are separated only by  $\sim 1.5$  eV (285.0 and 286.5 eV, respectively),

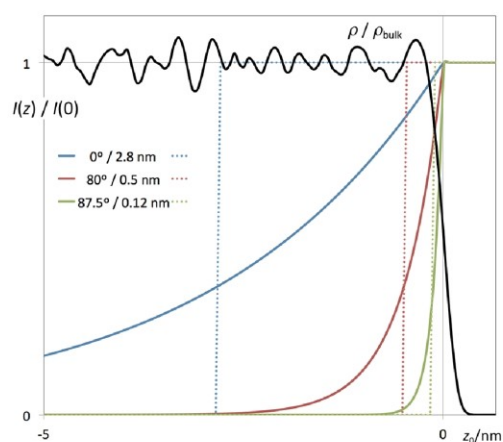
which is just 1.7 times larger than our overall energy resolution. For long alkyl chains, the  $C_{\text{alkyl}}$  signal is strongly dominating the peak shape. Additionally, the  $C_{\text{hetero}}$  signal is strongly attenuated in the surface-sensitive geometry due to the surface enrichment of the alkyl chains. Both effects impose an increasing uncertainty in the fitting of both, the small  $C_{\text{hetero}}$  and the large  $C_{\text{alkyl}}$  signal. To overcome this difficulty and to obtain more accurate results, we have now used the  $N_{\text{cation}}$  signal of the imidazolium ring nitrogen atoms as internal reference. Due to the small diameter of the imidazolium ring and the direct vicinity of the two imidazolium nitrogen atoms to the surrounding  $C_{\text{hetero}}$  atoms, and due to the very similar inelastic mean free path, their intensities should change in parallel. The well-separated  $N_{\text{cation}}$  signal can easily be quantified even without peak fitting. Its decrease from  $0^\circ$  to  $80^\circ$  ( $N_{1s(\text{cation})_{80^\circ}}/N_{1s(\text{cation})_{0^\circ}}$ ) was used to constrain the decrease of the  $C_{\text{hetero}}$  signal in  $80^\circ$  accordingly; the number of  $C_{\text{alkyl}}$  atoms in  $80^\circ$  was then derived by subtracting the obtained  $C_{\text{hetero}}$  atoms from the total carbon signal in  $80^\circ$ . By this simple procedure, improved numbers for the surface composition in  $80^\circ$  were obtained. Table 2 provides the results for the ILs' composition in  $0^\circ$  and  $80^\circ$  in number of atoms along with the nominal values. Note that the accuracy in absolute composition values is estimated to about  $\pm 5\%$  as can be seen by the obtained  $0^\circ$  values compared to the nominal ones. The ratio values of  $C_{\text{alkyl}}$  to  $C_{\text{hetero}}$  shown in Figure 4 are given in the last column with an accuracy of about  $\pm 8\%$ .

We can now combine the MD simulation trajectories, containing the position of all atoms within the simulation box, with information about the inelastic mean free path  $\lambda$  relevant for the ARXPS experiments shown here (for C 1s and N 1s:  $\lambda \approx 2.8$  nm) and the corresponding signal attenuation  $I(z) = I(0)\exp(-z/(\lambda \cos(\theta)))$  to calculate the  $I(C_{\text{alkyl}})/I(C_{\text{hetero}})$  ratios for layers measured at  $\theta = 0^\circ$  and  $\theta = 80^\circ$ .

The red crosses in Figure 4a (expo MD) show the corresponding ratios considering that each carbon atom in the MD trajectory contributes according to the exponential decay of the ARXPS attenuation. In all cases, the exponential decay started ( $z_0 = 0$ ) at the depth, at which half numerical density is attained (interface midpoint), and all atoms further out were counted undamped. This approach allows for defining the zero for the damping curve and is independent of the exact liftoff of the density profiles (Figure 5). The amount of undamped molecules (that is from  $z_0$  to  $+6k$ ) corresponds to an amount of a  $\sim 0.1$  (C2) to  $0.2$  (C12) nm thick film in the bulk and thus imposes only a minor error on the analysis.

As an alternative approach, the red crosses (step MD) in Figure 4b were calculated using a step function to truncate the contribution from all atoms beyond a depth larger than  $\lambda \cos(\theta)$ . Such step function depths correspond to 2.8 nm for the  $0^\circ$  setup and 0.5 nm for the  $80^\circ$  setup. This means that if one takes into account the liftoff of the density profiles, the ARXPS experiments with the  $80^\circ$  setup effectively probe a layer from  $z = -0.5$  nm to  $z = +6k$ , i.e., 0.92 and 1.31 nm in the  $[C_2C_1\text{Im}][\text{NTf}_2]$  and  $[C_{12}C_1\text{Im}][\text{NTf}_2]$  systems, respectively.

Using either the "exponential" or the "step" approach, only the terminal methyl carbon of the alkyl chain (CT) and the carbon in C2 position (CR) from the MD simulations have been summed up for the analysis. To compare with the ARXPS data, the CT:CR ratios found for the different  $[C_nC_1\text{Im}][\text{NTf}_2]$  systems have been weighted by the factor  $(n-1)/5$  to obtain the  $C_{\text{alkyl}}:C_{\text{hetero}}$  ratio from MD, shown in Figure 4.



**Figure 5.** Intensity attenuation along the direction normal to the surface considering the exponential decays typical of ARXPS experiments with  $0$ ,  $80$ , and  $87.5^\circ$  setups and an inelastic mean free path of 2.8 nm (blue, red, and green lines, respectively). The dotted lines correspond to step functions that yield similar total contributions from nontruncated atoms. The black line is the reduced numerical density profile for one of the interfaces of the  $[C_2C_1\text{Im}][\text{NTf}_2]$  ionic liquid, using the same depth scale.

The agreement in Figure 4a and b between the ARXPS intensity ratios and those obtained from the modeled interface profiles is very good, especially considering the approximations being made, namely using the CR and CT atoms to represent the position of the imidazolium ring and alkyl chain moieties. This agreement validates the trends deduced for the structure of the IL–vacuum interfaces using the present model. The two approaches applied to the analysis of the MD results (exponential vs step function) yield similar results, although the “soft” boundary imposed by the exponential decay is less affected by statistical uncertainties associated with the size of the simulation surfaces or the truncation procedure linked to the step (“hard” boundary) contributions.

Finally, it is now possible to use the ideas stated in the Langmuir principle to estimate the surface tension of the different surfaces. First, we stipulate that the surface tensions of very short and very long alkyl chains define the limiting values. In the picture,  $[C_1C_1\text{Im}][\text{NTf}_2]$  ( $36.3 \text{ mN}\cdot\text{m}^{-1}$ ) represents the contribution of the charged layer (anion and cation ring moieties without side chains) to the surface tension. On the other hand, the systems from  $[C_8C_1\text{Im}][\text{NTf}_2]$  to  $[C_{12}C_1\text{Im}][\text{NTf}_2]$  exhibit almost constant surface tension values around  $29.5 \text{ mN}\cdot\text{m}^{-1}$ . We thus assume that this value is the contribution to the surface tension of the alkyl side chain moieties.

Second, we used exponential and step decays to calculate the occurrence/contribution of NBT, CR, and CT atoms in layers within depth regions from  $z = +k$  to  $-2.8$ ,  $-0.5$ , and  $-0.12$  nm, corresponding to XPS measurements at  $\theta = 0^\circ$ ,  $80^\circ$ ,  $87.5^\circ$  (note that no measurements for the last value exist).

Third, we calculated the volume occupied by the different moieties of the IL (anion, cation ring, alkyl side chain) present in the considered depth region. In order to do so, we weighted the occurrence probabilities of the NBT, CR and CT atoms with the molar volume occupied by the corresponding moieties ( $159$ ,  $82$ , and  $17 \text{ cm}^3\cdot\text{mol}^{-1}$ , for  $[\text{NTf}_2]^-$ ,  $[C_1C_1\text{Im}]^+$  and methylene groups, respectively). For  $[C_4C_1\text{Im}][\text{NTf}_2]$  as an



**Table 3.** Atom,  $x_i$ , and Volume,  $x_{V,i}$ , Fractions in the Bulk, ARXPS Surfaces (0 and 80° setups) and in the Outer Surface (pseudo 87.5° Setup)<sup>a</sup>

$n$	2	4	6	8	10	12	2	4	6	8	10	12
bulk (nominal stoichiometric composition)												
$x_{CR}$	0.333	0.333	0.333	0.333	0.333	0.333						
$x_{CT}$	0.333	0.333	0.333	0.333	0.333	0.333						
$x_{NBT}$	0.333	0.333	0.333	0.333	0.333	0.333						
$x_{V,CR}$	0.318	0.281	0.252	0.228	0.208	0.192						
$x_{V,CT}$	0.066	0.175	0.261	0.331	0.389	0.437						
$x_{V,NBT}$	0.616	0.544	0.487	0.441	0.403	0.371						
$\sigma/\text{mN m}^{-1}$	<b>36.0</b>	<b>35.3</b>	<b>34.7</b>	<b>34.2</b>	<b>33.8</b>	<b>33.4</b>						
step function												
MD using ARXPS surface (0° setup): 3.2–3.6 nm thick surface, from $-6k$ to 2.8 nm in the density profiles												
$x_{CR}$	0.333	0.337	0.332	0.340	0.326	0.319	0.332	0.330	0.329	0.325	0.321	0.315
$x_{CT}$	0.335	0.327	0.334	0.326	0.339	0.354	0.336	0.339	0.342	0.349	0.358	0.369
$x_{NBT}$	0.332	0.336	0.334	0.335	0.335	0.327	0.332	0.330	0.329	0.326	0.321	0.316
$x_{V,CR}$	0.319	0.283	0.251	0.233	0.203	0.181	0.318	0.280	0.249	0.223	0.199	0.178
$x_{V,CT}$	0.066	0.171	0.261	0.324	0.393	0.459	0.067	0.179	0.269	0.346	0.415	0.476
$x_{V,NBT}$	0.614	0.546	0.488	0.443	0.404	0.360	0.615	0.542	0.482	0.431	0.386	0.346
$\sigma/\text{mN m}^{-1}$	<b>36.0</b>	<b>35.3</b>	<b>34.7</b>	<b>34.2</b>	<b>33.7</b>	<b>33.3</b>	<b>36.0</b>	<b>35.2</b>	<b>34.6</b>	<b>34.1</b>	<b>33.6</b>	<b>33.2</b>
MD using ARXPS surface (80° setup): 0.9–1.3 nm thick surface, from $-6k$ to 0.5 nm in the density profiles												
$x_{CR}$	0.341	0.306	0.265	0.198	0.187	0.163	0.296	0.264	0.224	0.187	0.165	0.161
$x_{CT}$	0.330	0.379	0.454	0.576	0.599	0.643	0.396	0.461	0.542	0.616	0.663	0.668
$x_{NBT}$	0.329	0.315	0.282	0.226	0.214	0.193	0.309	0.275	0.233	0.197	0.172	0.171
$x_{V,CR}$	0.326	0.266	0.207	0.134	0.109	0.081	0.303	0.244	0.181	0.128	0.095	0.080
$x_{V,CT}$	0.065	0.205	0.367	0.568	0.650	0.732	0.084	0.265	0.454	0.611	0.713	0.756
$x_{V,NBT}$	0.609	0.529	0.426	0.297	0.241	0.187	0.613	0.491	0.364	0.261	0.192	0.164
$\sigma/\text{mN m}^{-1}$	<b>36.0</b>	<b>35.1</b>	<b>33.9</b>	<b>32.5</b>	<b>32.0</b>	<b>31.4</b>	<b>35.9</b>	<b>34.6</b>	<b>33.3</b>	<b>32.2</b>	<b>31.5</b>	<b>31.2</b>
MD using outer surface (pseudo 87.5° setup): 0.5–0.9 nm thick surface, from $-6k$ to 0.12 nm in the density profiles												
$x_{CR}$	0.070	0.055	0.014	0.001	0.043	0.002	0.110	0.044	0.010	0.004	0.003	0.003
$x_{CT}$	0.756	0.863	0.934	0.985	0.880	0.991	0.724	0.900	0.974	0.988	0.991	0.992
$x_{NBT}$	0.174	0.082	0.052	0.014	0.077	0.007	0.167	0.056	0.016	0.007	0.006	0.005
$x_{V,CR}$	0.124	0.073	0.013	0.001	0.023	0.001	0.189	0.061	0.010	0.003	0.002	0.001
$x_{V,CT}$	0.278	0.715	0.894	0.980	0.896	0.993	0.258	0.786	0.961	0.987	0.992	0.994
$x_{V,NBT}$	0.597	0.212	0.093	0.019	0.081	0.006	0.554	0.153	0.030	0.010	0.006	0.004
$\sigma/\text{mN m}^{-1}$	<b>34.6</b>	<b>31.5</b>	<b>30.2</b>	<b>29.6</b>	<b>30.2</b>	<b>29.5</b>	<b>34.7</b>	<b>31.0</b>	<b>29.8</b>	<b>29.6</b>	<b>29.6</b>	<b>29.5</b>

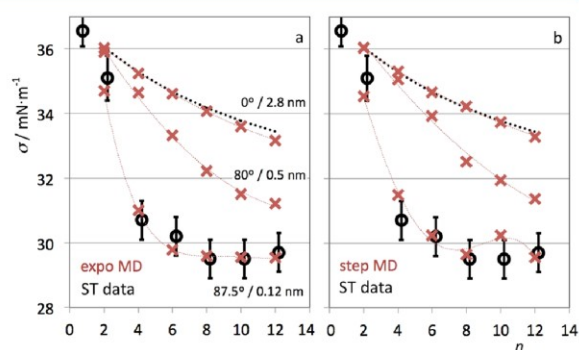
<sup>a</sup>Estimated (see text) surface tension values,  $\sigma$ .

example shown in Figure 3, the weighting factors for NBT, CR, and CT are 159, 82, and  $(4-1) \times 17 = 51$ , respectively).<sup>30</sup>

Fourth, the obtained volume fractions of each type of moiety (step 3) can be multiplied by the corresponding surface tension contribution (step 1) to yield the surface tension of the system.

The values are compiled in Table 3 and plotted in Figure 6 (red crosses). The same procedure applied to the bulk stoichiometry of the CR, CT, and NBT atoms yields the dotted black line, which would represent the surface tension without alkyl enrichment.

It is obvious that the alkyl enrichment at the surface decreases the surface tension values relative to the situation of a bulk-truncated. However, the chain enrichment obtained by MD within the effective probing depth of 0.91 up to 1.31 nm, corresponding to the probing depth of ARXPS in 80° for  $[\text{C}_2\text{C}_1\text{Im}][\text{NTf}_2]$  and  $[\text{C}_{12}\text{C}_1\text{Im}][\text{NTf}_2]$ , respectively, does not lead to the experimentally observed steep initial decrease in surface tension when increasing the alkyl chain; also, the saturation in surface tension above  $[\text{C}_6\text{C}_1\text{Im}][\text{NTf}_2]$  cannot be reproduced. The reason becomes obvious when inspecting the profiles in Figure 3: the 0.91–1.31 nm thick surface between the left-most and right-most dotted lines includes the whole alkyl layer but also a large part of the charged layer, which is not



**Figure 6.** Surface tension values,  $\sigma$ , versus the size of the alkyl chain,  $n$ , in the  $[\text{C}_n\text{C}_1\text{Im}][\text{NTf}_2]$  series. The black circles refer to experimental data.<sup>15</sup> The red crosses refer to MD-calculated values based on the Langmuir principle with six different surface layers: 2.8, 0.5, and 0.12 nm thickness with (a) exponential decays or (b) step decays. The thin red lines are just guides to the eye. The dotted black line corresponds to the application of the Langmuir principle to bulk compositions.

at the outermost surface. This means that the volume fraction of the charged layer as well as its contribution to the surface

tension values will decrease too slowly from  $[C_2C_1Im][NTf_2]$  to  $[C_{12}C_1Im][NTf_2]$ , and does not reach a constant value from  $[C_8C_1Im][NTf_2]$  onward. A constant surface tension would only be achieved at much larger alkyl chain lengths (not studied here).

The important point to be made here is that the surface-sensitive ARXPS studies at  $80^\circ$  that indeed probe the depths mentioned in the previous paragraph are not in disagreement with the surface tension data, if one simply recognizes that the “outer surface” assumed by the Langmuir principle can be thinner than the 0.91–1.31 nm probing depth of the  $80^\circ$  ARXPS measurements.

ARXPS setups with angles larger than  $80^\circ$  could probe such “outer surface” as envisioned by the Langmuir principle. This is, however, experimentally extremely challenging due to the required ultrahigh precision of sample positioning and emission angle, minor deviations from the flat-film geometry or surface roughness introducing shadowing effects, and additionally faces the problem of superimposed elastic scattering contributions. Nevertheless, the density profiles obtained by MD simulation can avoid the need of such much more difficult (to impossible) experiments and can be used to probe directly such “outer surface”.

Since there is no experimental evidence to anchor the position of the “outer” surface, we have decided to fit a single parameter and apply it to all surfaces. Basically, we used different depths and checked what would be the trend observed for the surface tension along the series calculated using the Langmuir principle. A pseudo  $87.5^\circ$  setup, which corresponds to probing the surface to a depth in the 0.54–0.93 range (starting at the liftoff) or a depth of just 0.12 nm after the interface midpoint, yielded the correct surface tension trend (cf. Figure 6).

Although this is an empirical fitting to experimental surface tension data, it is important to stress that the concept behind the Langmuir principle has a critical influence on the surface tension trends along the IL series: the decrease of the surface tension values between  $[C_2C_1Im][NTf_2]$  and  $[C_8C_1Im][NTf_2]$  can be ascribed to the receding presence of the charged layer at the so-called outer layer; the constancy of the values from  $[C_8C_1Im][NTf_2]$  onward denotes its absence for the ILs with longer alkyl side chains.

Finally, the match between surface-sensitive experimental results and MD-generated density profiles enables on one hand the validation of the MD models and simulations that allow for obtaining density profiles, and on the other hand the scrutiny at a molecular level of the species contributing to the surface properties in such structurally complex fluids such as ILs.

## CONCLUSION

The ideas exposed in the formulation of the Langmuir principle almost 90 years ago can be used to assist in the interpretation of surface tension data of ionic liquids and other highly structured fluids. Such use is possible nowadays due to the availability of experimental and simulation techniques that can probe the structure of the free surface of ionic liquids: the combination of angle-resolved X-ray photoelectron spectroscopy experiments and molecular dynamics simulations has allowed for the consistent determination of surface composition. Applying the Langmuir principle of group contributions at the outermost surface in a quantitative way, correct estimation of the complex surface tension trend along the  $[C_nC_1Im][NTf_2]$  series could be derived from the molecular dynamic results. We expect that

future developments in this line of research will include the renewed application of the Langmuir principle to other ionic liquid systems and their mixtures with molecular solvents.

## AUTHOR INFORMATION

### Corresponding Authors

\*E-mail: Florian.Maier@fau.de.

\*E-mail: jnlopes@tecnico.ulisboa.pt.

### ORCID

Karina Shimizu: 0000-0003-2454-1795

Bettina S. J. Heller: 0000-0001-9877-1310

Florian Maier: 0000-0001-9725-8961

Hans-Peter Steinrück: 0000-0003-1347-8962

### Notes

The authors declare no competing financial interest.

## ACKNOWLEDGMENTS

J.N.C.L. and K.S. acknowledge the Fundação para a Ciência e a Tecnologia, Portugal, for financial support (Project UID/QUI/00100/2013, Grant SFRH/BPD/94291/2013). H.-P.S. thanks the European Research Council (ERC) under the European Union's Horizon 2020 research and innovation programme for financial support, in the context of an Advanced Investigator Grant granted to him (Grant Agreement No. 693398-ILID).

## REFERENCES

- (1) Hayes, R.; Warr, G. G.; Atkin, R. Structure and Nanostructure in Ionic Liquids. *Chem. Rev.* **2015**, *115*, 6357–6426.
- (2) Castner, E. W. J.; Wishart, J. F. Spotlight on ionic liquids. *J. Chem. Phys.* **2010**, *132*, 120901–1–120901–9.
- (3) Wilkes, J. S. A short history of ionic liquids—from molten salts to neoteric solvents. *Green Chem.* **2002**, *4*, 73–80.
- (4) Zein El Abedin, S.; Endres, F. Ionic Liquids: The Link to High-Temperature Molten Salts? *Acc. Chem. Res.* **2007**, *40*, 1106–1113.
- (5) MacFarlane, D. R.; Seddon, K. R. Ionic Liquids—Progress on the Fundamental Issues. *Aust. J. Chem.* **2007**, *60*, 3–5.
- (6) Lei, Z.; Chen, B.; Koo, Y.-M.; MacFarlane, D. R. Introduction: Ionic Liquids. *Chem. Rev.* **2017**, *117*, 6633–6635.
- (7) Plechkova, N. V.; Seddon, K. R. Applications of Ionic Liquids in the Chemical Industry. *Chem. Soc. Rev.* **2008**, *37*, 123–150.
- (8) Santos, C. S.; Baldelli, S. Alkyl Chain Interaction at the Surface of Room Temperature Ionic Liquids: Systematic Variation of Alkyl Chain Length (R = C1–C4, C8) in both Cation and Anion of [RMIM][R-OSO<sub>3</sub>] by Sum Frequency Generation and Surface Tension. *J. Phys. Chem. B* **2009**, *113*, 923–933.
- (9) Jasper, J. J. The Surface Tension of Pure Liquid Compounds. *J. Phys. Chem. Ref. Data* **1972**, *1*, 841–1009.
- (10) Deetlefs, M.; Seddon, K. R.; Shara, M. Predicting physical properties of ionic liquids. *Phys. Chem. Chem. Phys.* **2006**, *8*, 642–649.
- (11) Krossing, I.; Slattery, J. M. Semi-Empirical Methods to Predict the Physical Properties of Ionic Liquids: An Overview of Recent Developments. *Z. Phys. Chem.* **2006**, *220*, 1343–1359.
- (12) Guan, W.; Ma, X.-X.; Li, L.; Tong, J.; Fang, D.-W.; Yang, J.-Z. Ionic Parachor and Its Application in Acetic Acid Ionic Liquid Homologue 1-Alkyl-3-methylimidazolium Acetate {[C<sub>n</sub>mim][OAc]} (n = 2,3,4,5,6). *J. Phys. Chem. B* **2011**, *115*, 12915–12920.
- (13) Wu, K.-J.; Zhao, C.-X.; He, C.-H. A simple corresponding-states group-contribution method for estimating surface tension of ionic liquids. *Fluid Phase Equilib.* **2012**, *328*, 42–48.
- (14) Ghasemian Lemraski, E.; Zobeidi, R. Applying parachor method to the prediction of ionic liquids surface tension based on modified group contribution. *J. Mol. Liq.* **2014**, *193*, 204–209.
- (15) Kolbeck, C.; Lehmann, J.; Lovelock, K. R.; Cremer, T.; Paape, N.; Wasserscheid, P.; Fröba, A. P.; Maier, F.; Steinrück, H.-P. Density

and Surface Tension of Ionic Liquids. *J. Phys. Chem. B* **2010**, *114*, 17025–17036.

(16) Langmuir, I. Forces Near the Surfaces of Molecules. *Chem. Rev.* **1930**, *6*, 451–479.

(17) Russina, O.; Triolo, A.; Gontrani, L.; Caminiti, R.; Xiao, D.; Hines, L. G., Jr.; Bartsch, R. A.; Quitevis, E. L.; Pleckhova, N.; Seddon, K. R. Morphology and intermolecular dynamics of 1-alkyl-3-methylimidazolium bis((trifluoromethane)sulfonyl)amide ionic liquids: structural and dynamic evidence of nanoscale segregation. *J. Phys.: Condens. Matter* **2009**, *21*, 424121.

(18) Shimizu, K.; Bernardes, C. E. S.; Canongia Lopes, J. N. Structure and Aggregation in the 1-Alkyl-3-Methylimidazolium Bis-(trifluoromethylsulfonyl)imide Ionic Liquid Homologous Series. *J. Phys. Chem. B* **2014**, *118*, 567–576.

(19) Jiang, W.; Wang, Y.; Yan, T.; Voth, G. A. A Multiscale Coarse-Graining Study of the Liquid/Vacuum Interface of Room-Temperature Ionic Liquids with Alkyl Substituents of Different Lengths. *J. Phys. Chem. C* **2008**, *112*, 1132–1139.

(20) Sanmartin Pensado, A.; Malfreyt, P.; Pádua, A. A. H. Molecular Dynamics Simulations of the Liquid Surface of the Ionic Liquid 1-Hexyl-3-methylimidazolium Bis(trifluoromethanesulfonyl)amide: Structure and Surface Tension. *J. Phys. Chem. B* **2009**, *113*, 14708–14718.

(21) Tariq, M.; Freire, M. G.; Saramago, B.; Coutinho, J. A. P.; Canongia Lopes, J. N.; Rebelo, L. P. N. Surface tension of ionic liquids and ionic liquid solutions. *Chem. Soc. Rev.* **2012**, *41*, 829–868.

(22) Canongia Lopes, J. N.; Pádua, A. A. H. CL&P: A generic and systematic force field for ionic liquids modeling. *Theor. Chem. Acc.* **2012**, *131*, 1129–1140.

(23) Jorgensen, W. L.; Maxwell, D. S.; Tirado-Rives, J. Development and Testing of the OPLS All-Atom Force Field on Conformational Energetics and Properties of Organic Liquids. *J. Am. Chem. Soc.* **1996**, *118*, 11225–11236.

(24) Smith, W.; Forester, T. R. *The DL POLY Package of Molecular Simulation Routines (v.2.2)*; The Council for The Central Laboratory of Research Councils, Daresbury Laboratory, Warrington, 2006.

(25) Lovelock, K. R. J.; Kolbeck, C.; Cremer, T.; Paape, N.; Schulz, P. S.; Wasserscheid, P.; Maier, F.; Steinrück, H.-P. Influence of Different Substituents on the Surface Composition of Ionic Liquids Studied Using ARXPS. *J. Phys. Chem. B* **2009**, *113*, 2854–2864.

(26) Gottfried, J. M.; Maier, F.; Rossa, J.; Gerhard, D.; Schulz, P. S.; Wasserscheid, P.; Steinrück, H.-P. Surface Studies on the Ionic Liquid 1-Ethyl-3-Methylimidazolium Ethylsulfate Using X-Ray Photoelectron Spectroscopy (XPS). *Z. Phys. Chem.* **2006**, *220*, 1439–1453.

(27) Niedermaier, I.; Kolbeck, C.; Steinrück, H.-P.; Maier, F. Dual analyzer system for surface analysis dedicated for angle-resolved photoelectron spectroscopy at liquid surfaces and interfaces. *Rev. Sci. Instrum.* **2016**, *87*, 045105.

(28) Roberts, R. F.; Allara, D. L.; Pryde, C. A.; Buchanan, D. N. E.; Hobbins, N. D. Mean free path for inelastic scattering of 1.2 keV electrons in thin poly(methylmethacrylate) films. *Surf. Interface Anal.* **1980**, *2*, 5–10.

(29) Kolbeck, C.; Cremer, T.; Lovelock, K. R. J.; Paape, N.; Schulz, P. S.; Wasserscheid, P.; Maier, F.; Steinrück, H.-P. Influence of Different Anions on the Surface Composition of Ionic Liquids Studied Using ARXPS. *J. Phys. Chem. B* **2009**, *113*, 8682–8688.

(30) Rebelo, L. P. N.; Canongia Lopes, J. N.; Esperança, J. M. S. S.; Guedes, H. J. R.; Lachwa, J.; Najdanovic-Visak, V.; Visak, Z. P. Accounting for the Unique, Doubly Dual Nature of Ionic Liquids from a Molecular Thermodynamic and Modeling Standpoint. *Acc. Chem. Res.* **2007**, *40*, 1114–1121.

# Surface Enrichment in Equimolar Mixtures of Non-Functionalized and Functionalized Imidazolium-Based Ionic Liquids

Bettina S. J. Heller,<sup>[a]</sup> Claudia Kolbeck,<sup>[a]</sup> Inga Niedermaier,<sup>[a]</sup> Sabine Dommer,<sup>[b]</sup> Jürgen Schatz,<sup>[b]</sup> Patricia Hunt,<sup>[c]</sup> Florian Maier,<sup>[a]</sup> and Hans-Peter Steinrück<sup>[a]</sup>

For equimolar mixtures of ionic liquids with imidazolium-based cations of very different electronic structure, we observe very pronounced surface enrichment effects by angle-resolved X-ray photoelectron spectroscopy (XPS). For a mixture with the same anion, that is, 1-methyl-3-octylimidazolium hexafluorophosphate + 1,3-di(methoxy)imidazolium hexafluorophosphate  $[(C_8C_1Im)[PF_6] + [(MeO)_2Im][PF_6]]$ , we find a strong enrichment of the octyl chain-containing  $[C_8C_1Im]^+$  cation and a corresponding depletion of the  $[(MeO)_2Im]^+$  cation in the topmost layer. For a mixture with different cations and anions, that is,  $[C_8C_1Im][Tf_2N] + [(MeO)_2Im][PF_6]$ , we find both surface enrichment of the

$[C_8C_1Im]^+$  cation and the  $[Tf_2N]^-$  (bis[(trifluoromethyl)sulfonyl]imide) anion, while  $[(MeO)_2Im]^+$  and  $[PF_6]^-$  are depleted from the surface. We propose that the observed behavior in these mixtures is due to a lowering of the surface tension by the enriched components. Interestingly, we observe pronounced differences in the chemical shifts of the imidazolium ring signals of the  $[(MeO)_2Im]^+$  cations as compared to the non-functionalized cations. Calculations of the electronic structure and the intramolecular partial charge distribution of the cations contribute to interpreting these shifts for the two different cations.

## 1. Introduction

Neat ionic liquids (ILs) have been studied extensively since they are promising candidates for different applications,<sup>[1]</sup> e.g. in the fields of catalysis,<sup>[2–4]</sup> fuel cells,<sup>[5,6]</sup> lithium ion batteries,<sup>[7–9]</sup> solvents,<sup>[10,11]</sup> lubricants,<sup>[12,13]</sup> sensors,<sup>[14,15]</sup> and gas separation technologies,<sup>[15–17]</sup> to name only a few. In many of these applications, the surface of the IL plays a decisive role, because it is its interface to the environment. Therefore, tailoring surface properties e.g. by choosing specific anion-cation combinations being preferentially present at the surface is of high relevance. Recently, research started to focus also on IL mixtures, which enable an even higher number of potential anion and cation combinations.<sup>[1,18]</sup> By gaining knowledge about the interface

properties of various anion and cation combinations, we hope to get more insight into the understanding of the outermost surface layer of IL mixtures.

While a number of investigations exists for a variety of IL mixtures concerning bulk physical properties such as viscosity, density, structure, and conductivity,<sup>[19,20]</sup> surface science studies on IL mixtures are less common. The surface composition of binary IL mixtures with non-functionalized imidazolium-based ILs was investigated using various surface science techniques such as time-of-flight secondary ion mass spectrometry (TOF-SIMS),<sup>[21,22]</sup> low-energy ion scattering (LEIS),<sup>[23,24]</sup> Rutherford backscattering (RBS),<sup>[22,25–27]</sup> angle-resolved X-ray photoelectron spectroscopy (ARXPS),<sup>[28–30]</sup> reactive atom scattering-laser-induced fluorescence (RAS-LIF),<sup>[20,31]</sup> and by simulations.<sup>[20,26,32,33]</sup>

Concerning equimolar IL mixtures with different anions, that is,  $[C_nC_1Im][Tf_2N]_{1-x}[PF_6]_x$  TOF-SIMS investigations by Souda indicate a strong surface enrichment of  $[Tf_2N]^-$ .<sup>[21]</sup> By RBS, Nakajima *et al.*<sup>[25]</sup> proposed  $[Tf_2N]^-$  surface enrichment also for  $[C_nC_1Im][Tf_2N]_{0.5}[PF_6]_{0.5}$  ( $n=4, 6$ ), but to a lesser degree. On the other hand, they did not observe a pronounced preferential surface enrichment of any of the anions for  $[C_6C_1Im][Tf_2N]_{0.5}Cl_{0.5}$  and  $[C_6C_1Im][PF_6]_{0.5}Cl_{0.5}$  mixtures.<sup>[25]</sup> In a more recent study, the same group again investigated related IL mixtures with RBS and indeed found some surface enrichment;<sup>[27]</sup> they estimated the mole fraction of the surface composition and explained the observed effects with a simple thermodynamic calculation. The authors concluded that larger ions are surface-enriched compared to smaller ions. Furthermore, in a LEIS study on similar ILs, namely stoichiometric mixtures of  $[C_4C_1Im]^+$  with different anions,  $Cl^-$  or  $I^-$  with  $[Tf_2N]^-$ , and  $[HOSO_3]^-$  with  $[BF_4]^-$ , Lovelock and co-workers<sup>[24]</sup> found strong enrichment of  $[Tf_2N]^-$  and  $[BF_4]^-$ . They suggest that in a mixture with one common

[a] B. S. J. Heller, Dr. C. Kolbeck, Dr. I. Niedermaier, Dr. F. Maier, Prof. Dr. H.-P. Steinrück

Lehrstuhl für Physikalische Chemie II  
Friedrich-Alexander-Universität Erlangen-Nürnberg  
Egerlandstraße 3, 91058 Erlangen (Germany)  
E-mail: Hans-Peter.Steinrueck@fau.de

[b] Dr. S. Dommer, Prof. Dr. J. Schatz  
Lehrstuhl für Organische Chemie I  
Friedrich-Alexander-Universität Erlangen-Nürnberg  
Nikolaus-Fiebiger-Straße 10, 91058 Erlangen (Germany)

[c] Dr. P. Hunt  
Chemistry Department  
Imperial College London  
SW72AZ, London (United Kingdom)

Supporting information for this article is available on the WWW under <https://doi.org/10.1002/cphc.201800216>

© 2018 The Authors. Published by Wiley-VCH Verlag GmbH & Co. KGaA. This is an open access article under the terms of the Creative Commons Attribution Non-Commercial License, which permits use, distribution and reproduction in any medium, provided the original work is properly cited and is not used for commercial purposes.

cation but different anions, the anion with the weaker cation-anion intermolecular interaction is enriched in the outermost surface layer at the expense of the other anion.

Another series of studies addressed mixtures of ILs with the same anion, but imidazolium-based cations with one shorter and one longer alkyl chain. A TOF-SIMS study for  $[C_2C_1Im]_{0.5}[C_8C_1Im]_{0.5}[PF_6]$  and  $[C_2C_1Im]_{1-x}[C_8C_1Im]_x[BF_4]$  reports the long alkyl chains to be located at the outer surface.<sup>[21]</sup> In a comparative RBS and TOF-SIMS study on  $[C_2C_1Im]_{1-x}[C_{10}C_1Im]_x[Tf_2N]$  mixtures ( $x=0.1, 0.5$ ), Nakajima *et al.*<sup>[22]</sup> also proposed surface segregation of the longer chain, but found a higher mole fraction of  $[C_{10}C_1Im]^+$  at the surface in TOF-SIMS. In line with the observations for mixtures with different anions in the above mentioned studies, they attribute the lower degree of surface enrichment found in RBS to a lower surface sensitivity as compared to TOF-SIMS and LEIS. In MD simulations for binary  $[C_2C_1Im]_{1-x}[C_8C_1Im]_x[TfO]$  mixtures, the octyl chain of the  $[C_8C_1Im]^+$  cation was found to be preferentially located at the surface, with a decreasing ratio of the number density along with a higher mole fraction of this cation, in line with trends in the above mentioned experiments.<sup>[33]</sup>

In addition, there are some XPS studies available for IL mixtures with a common cation (anion) but with different anions (cations) of different coordination strength,<sup>[28,29]</sup> which can be understood in terms of interionic partial charge transfer between cations and anions.<sup>[34]</sup> Core level binding energy shifts with respect to the neat ILs indicate that the electronic structure on the ions in the bulk is modified when changing the mixture composition, as has been demonstrated for imidazolium-<sup>[29]</sup> as well as for pyrrolidinium-<sup>[35]</sup> based IL mixtures. It was also shown that specific IL mixtures change the turnover frequency of a catalytic reaction by modifying the anion-catalyst interaction.<sup>[29]</sup> Recently, also a ternary mixture of  $[C_8C_1Im][Tf_2N]_{1-x-y}[SnCl_3]_xCl_y$  was studied by XPS, indicating a partial charge transfer from the  $Cl^-$  anion to the  $[C_8C_1Im]^+$  cation.<sup>[36]</sup> Concerning surface composition, a binary mixture of  $[C_2C_1Im]_{0.5}[C_{12}C_1Im]_{0.5}[Tf_2N]$  was investigated by ARXPS in our group finding no pronounced enrichment of the cation with the longer  $C_{12}$  alkyl chain for this combination.<sup>[30]</sup>

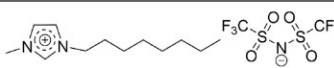
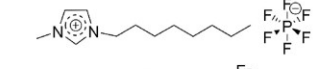
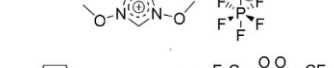
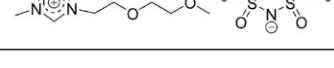
The same  $[C_2C_1Im]_{1-x}[C_{12}C_1Im]_x[Tf_2N]$  mixture as well as a mixture with a fluorinated side chain were recently investigated by RAS-LIF combined with MD simulations.<sup>[31]</sup> It was shown that

the component with the lower surface tension is preferentially located at the surface of the mixture.

Herein, we present for the first time a surface science study of an IL with methoxy (MeO) functionalization at the imidazolium ring, that is, 1,3-di(methoxy)imidazolium hexafluorophosphate  $[(MeO)_2Im][PF_6]$ <sup>[37,38]</sup> (see Table 1), and its equimolar mixtures with ILs containing a non-functionalized  $[C_8C_1Im]^+$  cation and the same or a different anion; the two anions are the medium-sized hexafluorophosphate ( $[PF_6]^-$ ) and the large, less coordinating bis[(trifluoromethyl)sulfonyl]imide ( $[Tf_2N]^-$ ). The tethering of methoxy groups at the imidazolium ring in  $[(MeO)_2Im][PF_6]$  is expected to have a strong influence on the electronic structure of the imidazolium ring compared to 1,3-dialkylimidazolium systems,<sup>[38]</sup> which can be accessed by XPS as has been previously shown for a thiouronium-functionalized IL.<sup>[39]</sup> Dialkoxyimidazolium compounds are interesting due to their ability to dissolve a reasonable amount of the greenhouse gases  $CO_2$ <sup>[40]</sup> and  $N_2O$ .<sup>[41]</sup> They are also suitable in synthesis due to the fact that N-heterocyclic carbenes (NHCs) are easily made from imidazolium-based ILs which then can serve as catalyst or solvent in reactions. It was shown that similar compounds as the  $[(MeO)_2Im][PF_6]$ , e.g. with a bromo-substituent attached to the  $C_2$ -position or with more bulky substituents, form several metal-NHC-complexes.<sup>[37,42]</sup> Furthermore,  $[(MeO)_2Im][PF_6]$  was demonstrated to be catalytically active in a Suzuki coupling reaction, but to a lesser extent than a standard 1,3-bis(2,4,6-trimethylphenyl)imidazolium (IMes) salt due to less bulky substituents at the imidazolium ring.<sup>[38]</sup> Furthermore, di(methoxy)imidazolium-based salts are used for enhancing reactions in water.<sup>[43]</sup>

As experimental method, we use ARXPS for probing the surface layer of the IL samples. Our Dual Analyzer System for Surface Analysis (DASSA)<sup>[44]</sup> setup allows for simultaneously recording spectra in a surface sensitive and a bulk sensitive mode, which directly permits to identify surface enrichment or depletion effects of all atoms (apart from hydrogen) being present in the ions. Compared to LEIS and TOF-SIMS (and to a lower extent also RBS), XPS has the disadvantage that it is sensitive not only to the topmost layer, but depending on the emission angle, the signals stem from the first 7–9 nm (10–15 IL layers; at  $0^\circ$  emission) or from the first 1–1.5 nm (1–2 IL layers; at  $80^\circ$  emission). On the other hand, it is quantitative and

**Table 1.** Summary of ILs investigated in this study.

Chemical formula	Structure	Name
IL1: $[C_8C_1Im][Tf_2N]$		1-methyl-3-octylimidazolium bis[(trifluoromethyl)sulfonyl]imide
IL2: $[C_8C_1Im][PF_6]$		1-methyl-3-octylimidazolium hexafluorophosphate
IL3: $[(MeO)_2Im][PF_6]$		1,3-di(methoxy)imidazolium hexafluorophosphate
IL4: $[Me(EG)_2C_1Im][Tf_2N]$		1-[2-(2-methoxy-ethoxy)ethyl]-3-methylimidazolium bis[(trifluoromethyl)sulfonyl]imide

allows us to differentiate elements in different chemical environments (i.e. the four inequivalent carbon atoms in  $[\text{C}_8\text{C}_1\text{Im}][\text{Tf}_2\text{N}]$  and different O 1s species) by their chemical shift.

## 2. Results and Discussion

We investigated equimolar mixtures of ILs with different cations and anions, namely IL1:  $[\text{C}_8\text{C}_1\text{Im}][\text{Tf}_2\text{N}]$ , IL2:  $[\text{C}_8\text{C}_1\text{Im}][\text{PF}_6]$ , and IL3:  $[(\text{MeO})_2\text{Im}][\text{PF}_6]$ ; for an overview and the full names of these three ILs, see Table 1. In particular, we studied the mixture of IL2 and IL3, who share the same anion, and the mixture of IL1 and IL3 with different anions and cations. For all ILs and IL mixtures, we measured the core levels of all elements by angle-resolved XPS at normal emission ( $0^\circ$ , "bulk sensitive") and at grazing emission ( $80^\circ$ , "surface sensitive"), to elucidate possible surface enrichment effects. Due to the fact that the XPS peaks of the different elements show pronounced chemical shifts for the different cations and anions, we can base all conclusions on the consistent behavior of several signals.

The neat IL1 and IL2 have already been studied in detail in the past, and a pronounced protruding of the alkyl chains towards the vacuum has consistently been reported.<sup>[44–46]</sup> On the other hand, we are not aware of any previous XPS studies of IL3, which contains the very specific  $[(\text{MeO})_2\text{Im}]^+$  cation. Therefore, we studied this neat IL in some detail and compare its spectra to those of IL2, and with another oxygen-containing IL, that is, IL4:  $[\text{Me}(\text{EG})_2\text{C}_1\text{Im}][\text{Tf}_2\text{N}]$  (1-[2-(2-methoxy-ethoxy)ethyl]-3-methylimidazolium bis[(trifluoromethyl)sulfonyl]imide; see Table 1) as reference. This analysis, along with the charge on atoms calculations, will allow for a comparison of the electronic structure of these methoxy and polyethylene-glycol (PEG) ILs. Notably, for none of the ILs Si 2p signals, indicative of surface-active polysiloxane contaminations,<sup>[47,48]</sup> are observed in the presented data, confirming the high purity of our ILs.

IL1, IL2, and IL4 are liquid at room temperature and IL3 has a melting point in the regime of  $83\text{--}84^\circ\text{C}$ . The presented XPS spectra of IL1–IL3 and the respective discussions are based on measurements at  $90^\circ\text{C}$  to enable the comparison of the ILs in their liquid state; IL4 was measured at room temperature. The F 1s peaks of the respective anions are used as an internal reference: Spectra of ILs containing the  $[\text{PF}_6]^-$  anion are referenced to the  $F_{\text{PF}_6}$  peak at 686.8 eV, whereas the  $F_{\text{Tf}_2\text{N}}$  peak of ILs comprising the  $[\text{Tf}_2\text{N}]^-$  anion is set to 688.8 eV. Notably, XPS of IL3 in the solid state at room temperature show the presence of additional O 1s, N 1s, and C 1s signals. These additional signals increase with increasing irradiation time, indicating a decomposition of the  $[(\text{MeO})_2\text{Im}]^+$  cation under X-radiation. By heating the sample to  $90^\circ\text{C}$ , these signals almost disappear from the XPS detection volume, probably due to the evaporation of volatile decomposition products and/or dissolution of non-volatile components into the bulk.

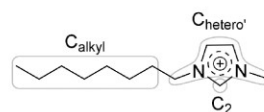
### 2.1. Normal Emission Spectra of the Neat ILs and Both IL Mixtures

In Figure 1, the  $0^\circ$  emission XP spectra of the four ILs and the investigated equimolar mixtures are depicted in the a) F 1s, b) O 1s, c) N 1s, d) C 1s, e) S 2p, and f) P 2p regions. The F 1s region (Figure 1a) shows the characteristic  $F_{\text{PF}_6}$  peak of the  $[\text{PF}_6]^-$  anion at 686.8 eV for IL2, IL3, and the IL2 + IL3 mixture, and the  $F_{\text{Tf}_2\text{N}}$  peak of the  $[\text{Tf}_2\text{N}]^-$  anion at 688.8 eV for IL1 and IL4; for the mixture IL1 + IL3 both F 1s peaks are observed.

In the O 1s region (Figure 1b), we observe no signal for IL2, the  $O_{\text{Tf}_2\text{N}}$  signal at 532.6 eV for IL1, the  $O_{\text{MeO}}$  signal at 535.3 eV for IL3, and the combined  $O_{\text{Tf}_2\text{N}} + O_{\text{EG}}$  signals at 532.7 eV for IL4. The mixture IL2 + IL3 contains the  $O_{\text{MeO}}$  signal and the mixture IL1 + IL3 also the  $O_{\text{Tf}_2\text{N}}$  signal.

In the N 1s region (Figure 1c) of IL1, IL2, IL4, and the mixtures IL1 + IL3 and IL2 + IL3, we find the imidazolium signal,  $N_{\text{im}}$ , at 402.1 eV and for IL1, IL4, and the IL1 + IL3 mixture additionally the  $N_{\text{Tf}_2\text{N}}$  signal at 399.4 eV; for the  $[(\text{MeO})_2\text{Im}]^+$  cation in IL3 and in the mixtures IL1 + IL3 and IL2 + IL3, the imidazolium nitrogen signal,  $N_{\text{MeO}}$ , is found at the significantly higher binding energy of 403.6 eV.

In the C 1s region (Figure 1d), the signal of the carbon atoms,  $C_{\text{hetero}}$ , next to N or O heteroatoms (see Scheme 1) of all

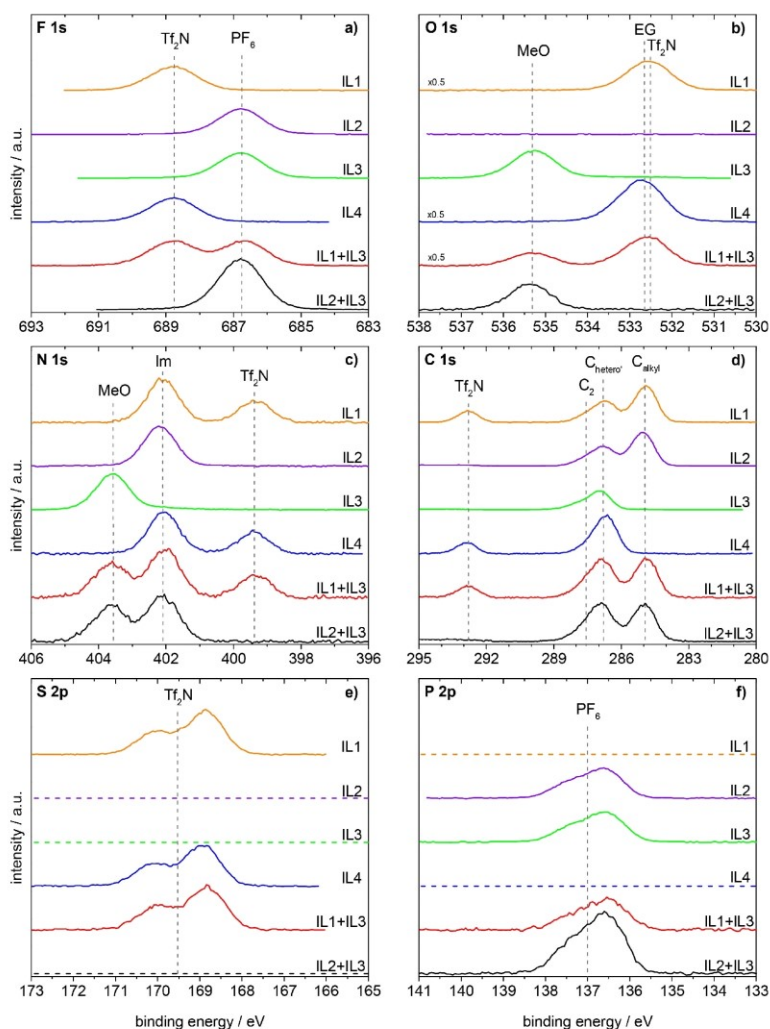


Scheme 1. Definition of the carbon species:  $C_{\text{alkyl}}$ ,  $C_{\text{hetero}}$ , and  $C_2$ .

neat ILs and IL mixtures are found around 287.3 eV (for a more detailed discussion see below); the carbon atoms,  $C_{\text{alkyl}}$ , of the alkyl chain in IL1, IL2, and the mixtures IL1 + IL3 and IL2 + IL3 have binding energies around 285.0 eV, and the carbon atoms,  $C_{\text{Tf}_2\text{N}}$ , of the  $[\text{Tf}_2\text{N}]^-$  anion of IL1, IL4, and the mixture IL1 + IL3 are at 292.8 eV.

In the S 2p and P 2p regions (Figure 1e, f), we observe the spin-orbit peaks of the  $[\text{Tf}_2\text{N}]^-$  and the  $[\text{PF}_6]^-$  anions centered at 169.5 and 137.0 eV, respectively. Note that the binding energies of the anion and cation signals in the neat ILs and also in the equimolar mixtures, all agree to within 0.1 eV. One particular aspect to be mentioned is the fact that in all energy regions the signals of the different anions and cations are significantly separated from each other (see Figure 1), which allows for a detailed quantitative analysis, which is particularly relevant for the equimolar IL mixtures. Taking the atomic sensitivity factors (ASFs) into account, the quantitative analysis of the  $0^\circ$  spectra of all neat ILs is in accordance with the nominally expected atom ratios (see Table S1–S4).

In the following, we will compare the spectra of the four neat ILs in detail. While the spectra of IL1 have already been discussed in the past,<sup>[44–46]</sup> the spectra of IL3,  $[(\text{MeO})_2\text{Im}][\text{PF}_6]$ , and to some extent also IL2 and IL4,  $[\text{Me}(\text{EG})_2\text{C}_1\text{Im}][\text{Tf}_2\text{N}]$ , are presented in Figure 1 for the first time; in case of IL4, the very



**Figure 1.** F 1s, O 1s, N 1s, C 1s, S 2p, and P 2p spectra of the investigated ILs and IL mixtures in  $0^\circ$  emission, measured with Al  $K_{\alpha}$  radiation. Orange: IL1,  $[\text{C}_8\text{C}_1\text{Im}][\text{Tf}_2\text{N}]$ ; violet: IL2,  $[\text{C}_8\text{C}_1\text{Im}][\text{PF}_6]$ ; green: IL3,  $[(\text{MeO})_2\text{Im}][\text{PF}_6]$ ; blue: IL4,  $[\text{Me}(\text{EG})_2\text{C}_1\text{Im}][\text{Tf}_2\text{N}]$ ; red: equimolar mixture of IL1 + IL3,  $[\text{C}_8\text{C}_1\text{Im}][\text{Tf}_2\text{N}] + [(\text{MeO})_2\text{Im}][\text{PF}_6]$ ; black: equimolar mixture of IL2 + IL3,  $[\text{C}_8\text{C}_1\text{Im}][\text{PF}_6] + [(\text{MeO})_2\text{Im}][\text{PF}_6]$ . All spectra are normalized to the fitted peak intensity of the F 1s spectrum of  $[(\text{MeO})_2\text{Im}][\text{PF}_6]$ . Abbreviations: MeO for  $[(\text{MeO})_2\text{Im}]^+$ , Im for N 1s of  $[\text{C}_8\text{C}_1\text{Im}]^+$  and  $[\text{Me}(\text{EG})_2\text{C}_1\text{Im}]^+$ , EG for O 1s of  $[\text{Me}(\text{EG})_2\text{C}_1\text{Im}]^+$ ,  $\text{PF}_6$  for  $[\text{PF}_6]^-$ ,  $\text{Tf}_2\text{N}$  for  $[\text{Tf}_2\text{N}]^-$ .

similar IL 1-[2-(2-Ethoxyethoxy)ethyl]-3-methylimidazolium bis-[(trifluoromethyl)sulfonyl]imide ( $[\text{Et}(\text{EG})_2\text{C}_1\text{Im}][\text{Tf}_2\text{N}]$ ), that is, an IL with an ethyl instead of a methyl group as end group of the long side chain, has already been discussed in detail in ref [47].

### 2.1.1. Comparison of $[\text{C}_8\text{C}_1\text{Im}]^+$ and $[(\text{MeO})_2\text{Im}]^+$

As IL2 and IL3 have the same anion but different cations, we start by comparing the corresponding spectra. The most pronounced difference is observed for the imidazolium N 1s peak, which is shifted from 402.2 eV ( $N_{\text{Im}}$ ) for the  $[\text{C}_8\text{C}_1\text{Im}]^+$  cation in IL2 to 403.6 eV ( $N_{\text{MeO}}$ ) for the  $[(\text{MeO})_2\text{Im}]^+$  cation in IL3,

that is, by 1.4 eV to higher binding energies. Smaller, but significant shifts towards higher binding energy are also found in the C 1s region: For IL2,  $[\text{C}_8\text{C}_1\text{Im}][\text{PF}_6]$ , two signals at 285.1 and 286.8 eV can be distinguished; they are assigned to carbon atoms bound only to hydrogen or carbon ( $\text{C}_{\text{alkyl}}$ ) and to carbon atoms bound to one hetero atom like nitrogen or oxygen ( $\text{C}_{\text{hetero}}$ ), respectively. The small shoulder at 287.7 eV is assigned to the  $\text{C}_2$  carbon atom between the two nitrogen atoms. It carries a major part of the positive charge of the imidazolium ring,<sup>[49,50]</sup> and thus, exhibits a higher binding energy than the other  $\text{C}_{\text{hetero}}$  atoms. For  $[(\text{MeO})_2\text{Im}][\text{PF}_6]$ , the  $\text{C}_{\text{hetero}}$  and  $\text{C}_2$  signals are shifted to 287.0 and 288.1 eV, that is, by 0.2–0.4 eV to higher binding energy, respectively. Due to the presence of methyl

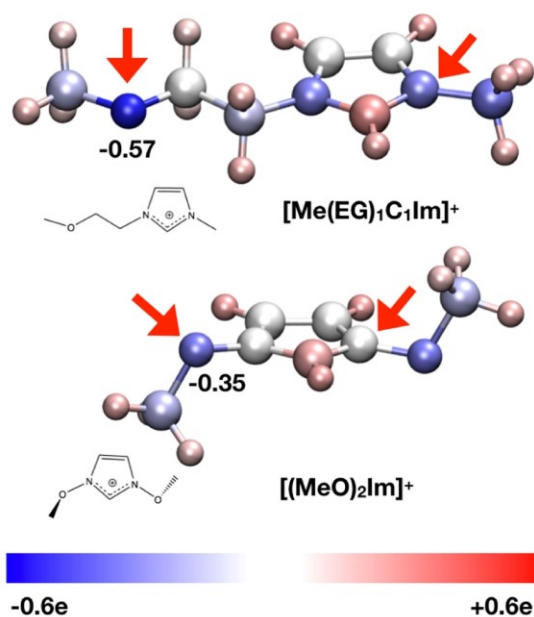
only, and thus, the absence of an alkyl chain, no corresponding signal is observed at 285.0 eV. The shift of the N 1s and C 1s signals of the  $[(\text{MeO})_2\text{Im}]^+$  cation towards higher binding energy by 1.4 and 0.2–0.4 eV, respectively, compared to the  $[\text{C}_8\text{C}_1\text{Im}]^+$  cation, is an indication that the imidazolium ring of  $[(\text{MeO})_2\text{Im}]^+$  has a lower electron density compared to  $[\text{C}_8\text{C}_1\text{Im}]^+$ .

The O 1s spectrum of IL3 shows a very characteristic  $\text{O}_{\text{MeO}}$  peak at 535.3 eV. Since IL2 does not contain an oxygen atom, we compare the spectrum to that of IL4, which also contains an oxygen atom in its functionalized PEG chain of the cation and also in the  $[\text{Tf}_2\text{N}]^-$  anion. The  $\text{O}_{\text{EG}}$  and  $\text{O}_{\text{Tf}_2\text{N}}$  levels have a very similar binding energy within our energy resolution and thus, only a single peak is seen for IL4, which is observed at a slightly higher binding energy of 532.7 eV, as compared to 532.6 eV found for the  $[\text{Tf}_2\text{N}]^-$  anion in IL1. Relative to this peak, the  $\text{O}_{\text{MeO}}$  peak of IL3 is shifted towards higher binding energy by 2.6 eV resulting in a binding energy of 535.3 eV. This value is extraordinarily large and to the best of our knowledge oxygen with such a high binding energy is only described in polymers, e.g. 535.5 eV for peroxy-oxygens in dibenzoyl peroxide.<sup>[51]</sup>

### 2.1.2. Calculations of Atomic Charges in $[\text{C}_2\text{C}_2\text{Im}]^+$ , $[(\text{MeO})_2\text{Im}]^+$ , and $[\text{Me}(\text{EG})_1\text{C}_1\text{Im}]^+$

To elucidate the observed large chemical shifts of IL3 in the O 1s and N 1s regions, atomic charges have been calculated for isolated cations in the gas phase: In an initial-state picture, shifts to higher binding energies as observed for the uncommon  $[(\text{MeO})_2\text{Im}]^+$  cation of IL3 should be due to a decrease in electron density close to the probed atoms. For  $[(\text{MeO})_2\text{Im}]^+$ , two low-energy conformers (based on out-of-plane ether group orientations, see SI for detail) were identified. Atomic and group charges have been determined using both the NBO (natural bond orbital) and ChelpG (charges from electrostatic potential using a grid based method) methodologies. Net NBO charges of  $-0.35$  and  $-0.02$  electrons (e) were found at the  $\text{O}_{\text{MeO}}$  and  $\text{N}_{\text{MeO}}$  atoms, respectively (see Figure 2). The shorter 3-(2-methoxyethyl)-1-methylimidazolium ( $[\text{Me}(\text{EG})_1\text{C}_1\text{Im}]^+$ ) is used as model for  $[\text{Me}(\text{EG})_2\text{C}_1\text{Im}]^+$ . Four stable conformers were obtained for  $[\text{Me}(\text{EG})_1\text{C}_1\text{Im}]^+$  and charge analysis carried out for the highest and lowest energy structures, which also exhibit significant structural differences (see SI for details), yielding NBO charges of  $-0.60$  to  $-0.57$  e at the  $\text{O}_{\text{EG}}$  atoms and  $-0.34$  to  $-0.33$  e at the  $\text{N}_{\text{im}}$  atoms. For comparison  $[\text{C}_2\text{C}_2\text{Im}]^+$ , which is representative of the common  $[\text{C}_8\text{C}_1\text{Im}]^+$  cation of IL1 and IL2, has similar NBO values of  $-0.35$  to  $-0.34$  e for the  $\text{N}_{\text{im}}$  atoms. Apart from differences in absolute values between NBO and ChelpG analysis (due to the very different character of both methods), the relative changes in charge are similar to those identified for the NBO charges (see Table S9 for ChelpG charges).

The atomic charges found for  $\text{N}_{\text{MeO}}$  in  $[(\text{MeO})_2\text{Im}]^+$  are considerably more positive (less negative) than those found for  $[\text{Me}(\text{EG})_1\text{C}_1\text{Im}]^+$  and  $[\text{C}_2\text{C}_2\text{Im}]^+$ . The more positive environment for  $\text{N}_{\text{MeO}}$  is consistent with the higher XPS binding energies



**Figure 2.** Pictorial representation of NBO charge distribution in  $[\text{Me}(\text{EG})_1\text{C}_1\text{Im}]^+$  and  $[(\text{MeO})_2\text{Im}]^+$ ; blue is more negative, white neutral, and red more positive: For both cations, arrows mark the atoms of interest, nitrogen and oxygen.

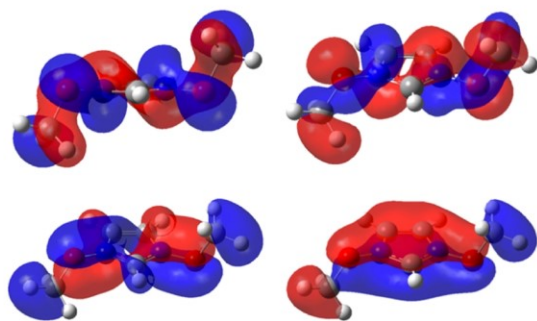
obtained for  $[(\text{MeO})_2\text{Im}]^+$ . The NBO group charge for the imidazolium ring has also been determined;  $+0.93$ ,  $+0.34$ , and  $+0.31$  for  $[(\text{MeO})_2\text{Im}]^+$ ,  $[\text{Me}(\text{EG})_1\text{C}_1\text{Im}]^+$ , and  $[\text{C}_2\text{C}_2\text{Im}]^+$ , respectively, clearly identifying a lower electron density on the imidazolium ring of  $[(\text{MeO})_2\text{Im}]^+$  compared to the latter, which is fully consistent with the XPS binding energies measured.

For oxygen, the NBO atomic charges for  $\text{O}_{\text{MeO}}$  in  $[(\text{MeO})_2\text{Im}]^+$  are also considerably more positive than those found for  $[\text{Me}(\text{EG})_1\text{C}_1\text{Im}]^+$ . These values clearly indicate that electron density at the  $\text{O}_{\text{MeO}}$  atoms is much lower for  $[(\text{MeO})_2\text{Im}]^+$ , which explains the observed strong core level shift of more than  $+2.5$  eV towards higher XPS binding energies. Notably, the examination of the molecular orbitals shows  $p_x$ -orbitals on the  $\text{O}_{\text{MeO}}$  atom interacting with the (aromatic) imidazolium ring  $p_x$ -orbitals, linking them in a Möbius type way (see Figure 3). Thus, delocalization of the  $\text{O}_{\text{MeO}}$  atom lone pair orbitals across the ring  $\pi$ -system is occurring, reducing the overall charge on the  $\text{O}_{\text{MeO}}$  atom.

### 2.1.3. Comparison of the Anion Signals of IL1, IL2, and IL3

To complete the comparison of the spectra of IL3 to the other ILs, we address the anion. Notably, the binding energies for IL2 and IL3 are identical. In the P 2p region, we observe one asymmetric peak, centered at 137.0 eV, due to the non-resolved spin-orbit-splitting of the  $2p_{3/2}$  and  $2p_{1/2}$  levels. In the F 1s spectra, one single peak ( $F_{\text{PF}_6}$ ) is found at 686.8 eV. If we compare the anion signals of IL3 with those of IL1, we find the spin-orbit-split S 2p doublet centered at 169.5 eV in the S 2p





**Figure 3.** Molecular orbitals from  $[(\text{MeO})_2\text{Im}]^+$  showing the  $\text{O}_{\text{MeO}}$  atom participating in aromatic delocalization of the imidazolium ring.

region instead of the P 2p signals. Furthermore, the  $F_{\text{Tf}_2\text{N}}$  peak at 688.8 eV is clearly separated from the  $F_{\text{PF}_6}$  peak, which enables accurate quantification in the mixtures (see below); the anion-related  $N_{\text{Tf}_2\text{N}}$  and  $C_{\text{Tf}_2\text{N}}$  peaks have already been described above.

The analysis of IL1–IL4 shows that the differences of the F 1s, O 1s, N 1s, C 1s, S 2p, and P 2p levels are a clear signature of the respective cations and anions and will serve as extremely helpful, multiple fingerprint in analyzing the IL mixtures below.

#### 2.1.4. Equimolar Mixture of IL2 and IL3

Next we address the equimolar mixture of IL2 and IL3 in Figure 1, that is, a mixture of ILs with the same anion  $[\text{PF}_6]^-$ . Overall, all signals are found at identical binding energies as for the neat ILs. For the F 1s, P 2p, and O 1s regions, in each case only one signal is found, which is due to the anion (F 1s and P 2p) and the  $[(\text{MeO})_2\text{Im}]^+$  cation (O 1s). In the N 1s and C 1s region, the signals of the two cations are superimposed. The  $N_{\text{Im}}$  peak is found at 402.1 eV and the  $N_{\text{MeO}}$  peak at 403.6 eV. The  $C_{\text{hetero}^+ + \text{C}_2}$  signals of  $[\text{C}_8\text{C}_1\text{Im}]^+$  and  $[(\text{MeO})_2\text{Im}]^+$  in the neat ILs are only slightly shifted (0.2–0.4 eV) relative to each other, which leads to a combined peak at 286.9 eV with a high energy shoulder at 287.9 eV, and the well separated  $C_{\text{alkyl}}$  peak at 285.0 eV. Within the margin of error, the binding energies of the F 1s, O 1s, N 1s, C 1s, and P 2p peaks are coinciding with the binding energies of the previously presented IL2 and IL3.

The comparison of the intensity of the two N 1s peaks and the two dominating C 1s peaks yields to an at first sight stunning result: From the IL2:IL3 =  $[\text{C}_8\text{C}_1\text{Im}]^+ : [(\text{MeO})_2\text{Im}]^+ = 1:1$  stoichiometry (50%:50%) of the equimolar IL mixture, one would expect an intensity ratio of 1:1 for the  $N_{\text{Im}}:N_{\text{MeO}}$  signals. Inspection of Figure 1c (and Table S6), however, shows a ratio of 1:0.85 (54%:46%), that is, a reduced amount of  $[(\text{MeO})_2\text{Im}]^+$  in the near-surface region probed by XPS. Since weighting errors can be ruled out due to our accuracy being below 1%, we propose that the observed deviation is due to a pronounced surface enrichment of the  $[\text{C}_8\text{C}_1\text{Im}]^+$  cations in the top most layer, which goes along with a depletion of the  $[(\text{MeO})_2\text{Im}]^+$  cation. Considering an inelastic mean free path of

the C 1s and N 1s electrons of 3 nm (at kinetic energies of  $1150 \pm 60$  eV), the contribution of the topmost layer to the total signal at normal emission is 20–25%. Assuming a simplified model with the topmost layer containing only  $[\text{C}_8\text{C}_1\text{Im}]^+$  cations and all layers underneath being mixed stoichiometrically (1:1), a signal ratio of 1.2:0.8 (60%:40%) is expected in XPS, which would yield an even stronger increase of the nitrogen signals of  $[\text{C}_8\text{C}_1\text{Im}]^+$ , on expense of the  $[(\text{MeO})_2\text{Im}]^+$  signals, than observed by us.

#### 2.1.5. Equimolar Mixture of IL1 and IL3

Finally, we discuss the spectra of the equimolar mixture of IL1 and IL3 in Figure 1, that is, the mixture of ILs with different anions and different cations to search for possible selective enrichment of anions or cations. For this IL mixture, we find contributions from different cations and anions in nearly all regions; only the S 2p and P 2p spectra show solely contributions from one of the anions each. In the F 1s region, we find the  $F_{\text{Tf}_2\text{N}}$  and the  $F_{\text{PF}_6}$  peaks of the two anions at 688.8 and 686.7 eV, respectively. The O 1s region displays the  $O_{\text{Tf}_2\text{N}}$  and  $O_{\text{MeO}}$  peaks at 532.6 and 535.3 eV, respectively. In the N 1s region, we find three peaks, the  $N_{\text{Tf}_2\text{N}}$  peak at 399.4 eV, the  $N_{\text{MeO}}$  peak at 403.6 eV, and the  $N_{\text{Im}}$  peak at 402.0 eV. The carbon region shows the  $C_{\text{Tf}_2\text{N}}$  peak at 292.8 eV, the  $C_{\text{alkyl}}$  peak at 284.9 eV, and the superposition of the  $C_{\text{hetero}^+ + \text{C}_2}$  peaks of the  $[\text{C}_8\text{C}_1\text{Im}]^+$  and  $[(\text{MeO})_2\text{Im}]^+$  cations at 286.8 and 287.8 eV, respectively. Within the margin of error, the binding energies of the F 1s, O 1s, N 1s, C 1s, S 2p, and P 2p peaks are coinciding with the binding energies of the previously presented neat IL1 and IL3.

When comparing the intensities of the different anion and cation signals, we again find apparent deviation from the nominal stoichiometry. From the 50%:50% stoichiometry of the equimolar IL mixture,  $[\text{C}_8\text{C}_1\text{Im}][\text{Tf}_2\text{N}] + [(\text{MeO})_2\text{Im}][\text{PF}_6]$  (IL1 + IL3), one would expect an intensity ratio of 2:2:1 for the  $N_{\text{Im}}:N_{\text{MeO}}:N_{\text{Tf}_2\text{N}}$  signals and of 7:10:2 for the  $C_{\text{alkyl}}:C_{\text{hetero}^+ + \text{C}_2}:C_{\text{Tf}_2\text{N}}$  signals. As for the IL2 + IL3 mixture, the  $[(\text{MeO})_2\text{Im}]^+$  signals are lower than expected from the stoichiometry, which indicates again that this cation is depleted from the surface and that  $[\text{C}_8\text{C}_1\text{Im}]^+$  is enriched at the surface. Information on possible enrichment effects of the anions can be derived also from the F 1s spectra; the ~14% larger peak area of the  $F_{\text{Tf}_2\text{N}}$  as compared to the  $F_{\text{PF}_6}$  peak (Table S5) indicates a depletion of the  $[\text{PF}_6]^-$  anions in the topmost layer.

## 2.2. Angle-Resolved XPS Results

To obtain more detailed information of surface enrichment and depletion effects, we will present and analyze angle-resolved XP spectra of the neat IL2 and IL3, and in particular the IL mixtures in the following. IL1 has already been discussed in literature.<sup>[44–46]</sup> For this IL, a significant increase of the  $C_{\text{alkyl}}$  is observed at  $80^\circ$ , that is, the signal at  $80^\circ$  increases by about 22% (see SI, Figure S1). This behavior is a clear indication of the

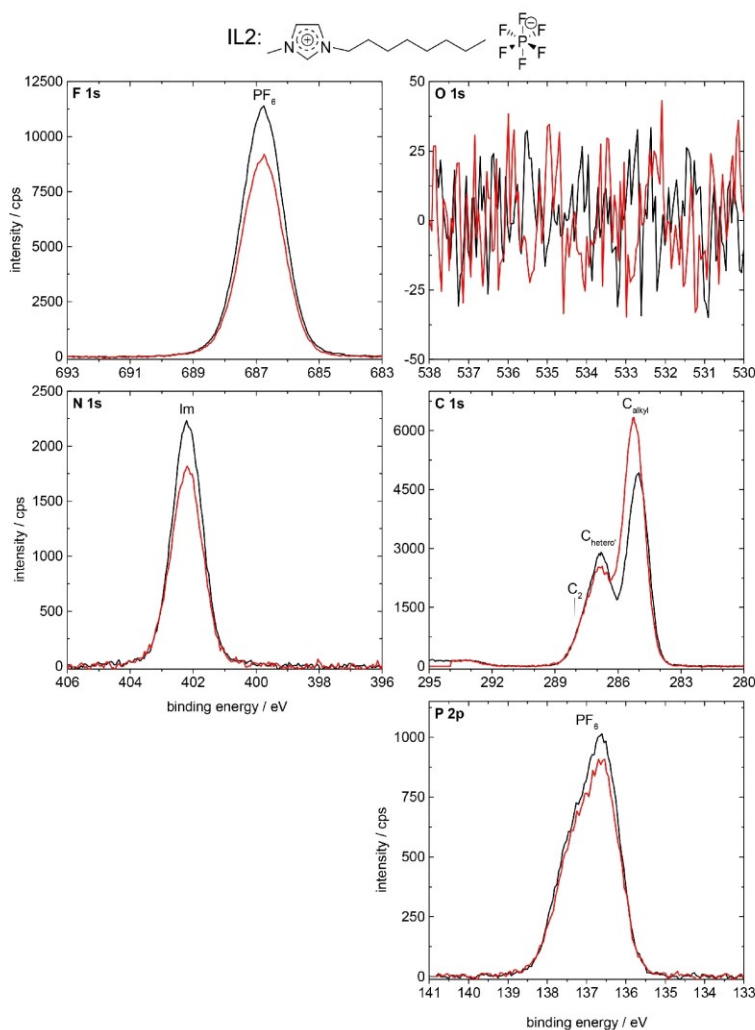
surface enrichment of the alkyl chains by preferential orientation of the cations. Concomitantly, most of the other signals decrease by a factor up to 13%. For IL4, only minor changes with emission angle are seen (Figure S2), indicating the absence of major enrichment/orientation effects at the outer surface. This is in line with our earlier<sup>[47]</sup> observations for other PEG ILs. For the signals of the  $[\text{Tf}_2\text{N}]^-$  anion, we find a minor surface enrichment of the  $\text{CF}_3$  groups and a depletion of the corresponding  $\text{SO}_2$  groups.<sup>[21,22,47,52]</sup>

### 2.2.1. Neat IL2 and IL3

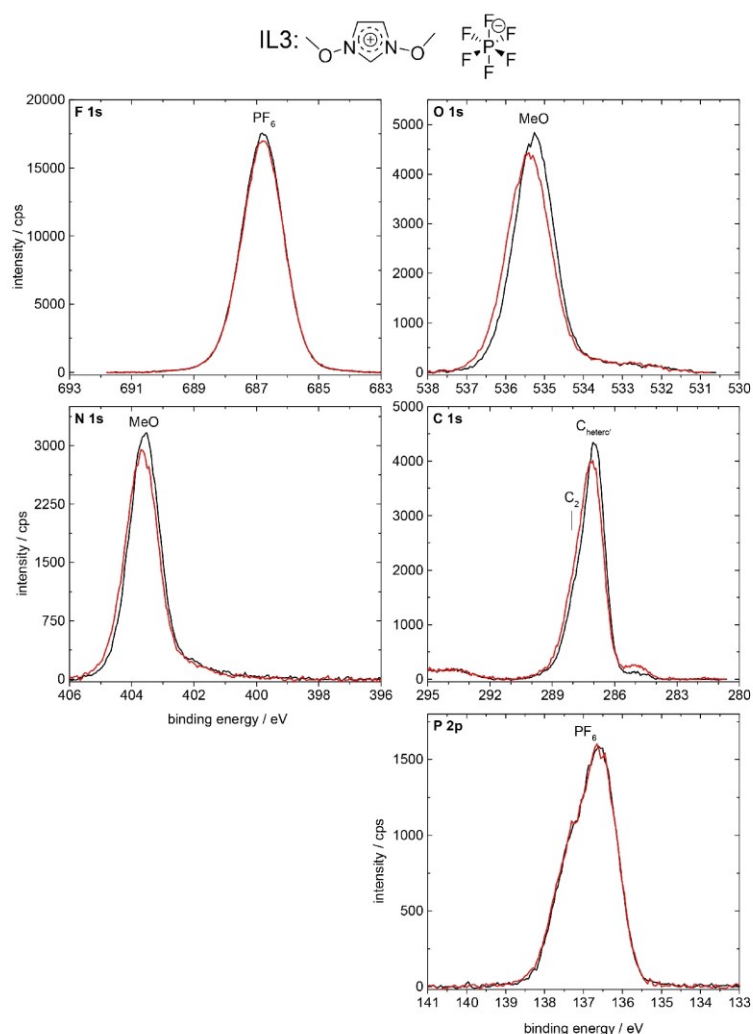
We start with the analysis of the spectra of the neat IL2,  $[\text{C}_8\text{C}_1\text{Im}][\text{PF}_6]$ . In Figure 4, the F 1s, O 1s, N 1s, C 1s, and P 2p spectra are depicted for  $0^\circ$  (black) and  $80^\circ$  (red) emission. We

observe a strong enhancement of the  $\text{C}_{\text{alkyl}}$  signal (increase in peak intensity of 31%) at  $80^\circ$  as compared to  $0^\circ$ , which indicates that the alkyl chain of the  $[\text{C}_8\text{C}_1\text{Im}]^+$  cation is enriched at the surface, pointing away from the surface towards vacuum. For the  $\text{F}_{\text{PF}_6}$ ,  $\text{N}_{\text{Im}}$ ,  $\text{C}_{\text{hetero}+\text{C}_2}$ , and  $\text{P}_{\text{PF}_6}$  signals, we find a damping at  $80^\circ$  due to the surface-enriched alkyl groups on top. This damping is most pronounced for the F 1s level and least pronounced for the P 2p level, which is attributed to the increasingly lower kinetic energy of the emitted photoelectron,  $\sim 800$  eV for F 1s vs.  $\sim 1350$  eV for P 2p.

The F 1s, O 1s, N 1s, C 1s, and P 2p spectra of the neat IL3,  $[(\text{MeO})_2\text{Im}][\text{PF}_6]$ , are depicted in Figure 5 for  $0^\circ$  (black) and  $80^\circ$  (red) emission. We observe no pronounced intensity changes (peak area changes) with emission angle; the apparent lower peak height at  $80^\circ$  for most core levels (0–2%) goes along with a slight peak shift and broadening of the peaks; the latter is



**Figure 4.** F 1s, O 1s, N 1s, C 1s, and P 2p spectra of IL2,  $[\text{C}_8\text{C}_1\text{Im}][\text{PF}_6]$ , in  $0^\circ$  (black) and  $80^\circ$  (red) emission, measured with Al  $K_{\alpha}$  radiation.

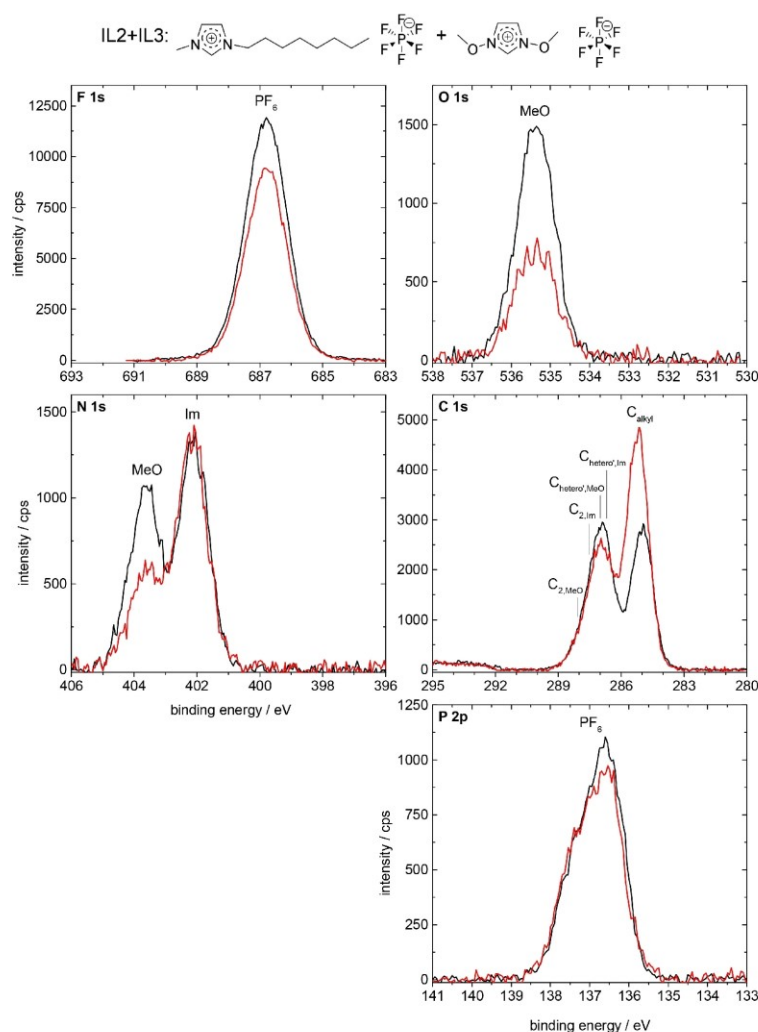


**Figure 5.** F 1s, O 1s, N 1s, C 1s, and P 2p spectra of IL3, [(MeO)<sub>2</sub>Im][PF<sub>6</sub>], in 0° (black) and 80° (red) emission, measured with Al K<sub>α</sub> radiation.

probably due to the inhomogeneous final state screening in the topmost layer, which contributes to 80% of the signals at 80°, but only to 25% of the signal at 0°. The absence of significant signal intensity differences for the various core levels in 80° and 0° emission indicates a homogeneous distribution of anions and cations at the surface and in the bulk of the IL. This is in line with previous experience that surface enrichment effects are typically found for systems with functionalized and non-functionalized alkyl chains with a chain length of at least 4 carbon units.<sup>[52,53]</sup> Notably, the small peak at 285.0 eV, is due to a minor contamination of the IL (see Experimental Section).

### 2.2.2. Equimolar Mixture of IL2 and IL3

Next, we analyze the angle-resolved XP spectra of the equimolar mixture of IL2 and IL3 in Figure 6, that is, the IL mixture of ILs with the identical [PF<sub>6</sub>]<sup>-</sup> anion. The C<sub>alkyl</sub> signal shows a very strong enhancement (increase in peak height of ~69%) at 80° (red) as compared to 0° (black) emission, which indicates that the [C<sub>8</sub>C<sub>1</sub>Im]<sup>+</sup> cation is enriched at the surface with the alkyl chain pointing away from the surface towards vacuum. At the same time, the N<sub>MeO</sub> and O<sub>MeO</sub> signals of the [(MeO)<sub>2</sub>Im]<sup>+</sup> cation show only ~45% intensity at 80° as compared to 0° emission, indicating the depletion of this cation from the topmost layer. For the F<sub>PF6</sub> and P<sub>PF6</sub> signals, a moderate decrease of the 80° signals as compared to 0° signals is observed, very similar to that of the neat IL2, which is again due to the damping of the anions by the surface-enriched octyl



**Figure 6.** F 1s, O 1s, N 1s, C 1s, and P 2p spectra of the equimolar IL2 + IL3 mixture,  $[\text{C}_8\text{C}_1\text{Im}][\text{PF}_6] + [(\text{MeO})_2\text{Im}][\text{PF}_6]$ , in  $0^\circ$  (black) and  $80^\circ$  (red) emission, measured with Al  $K_\alpha$  radiation.

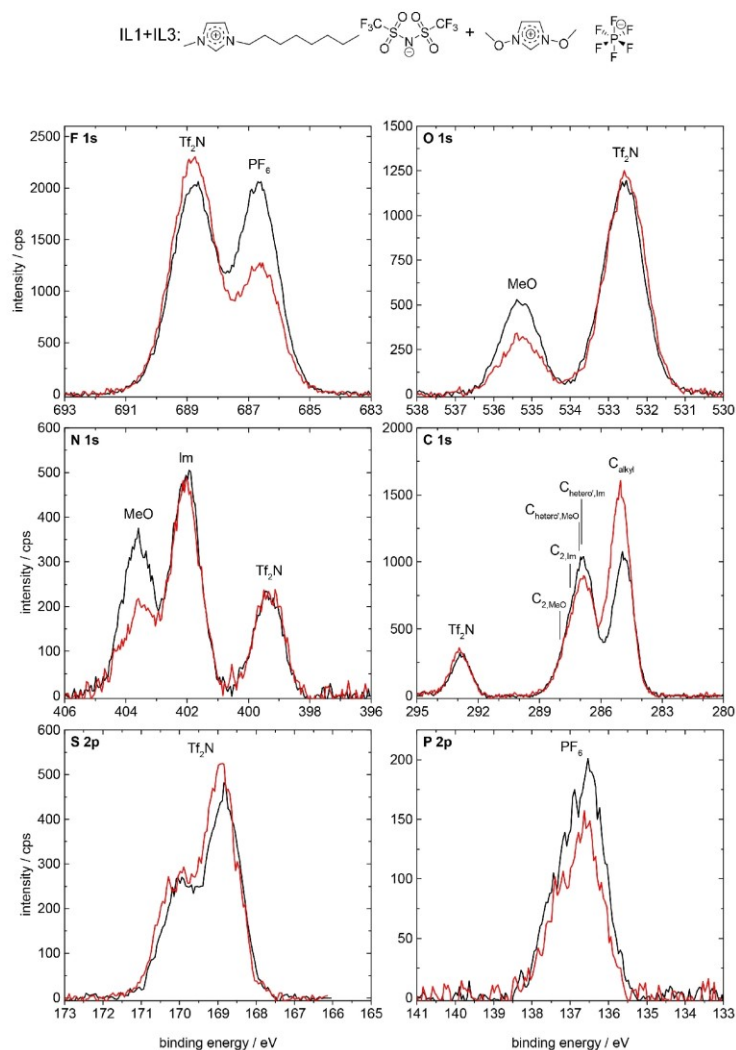
chain of the  $[\text{C}_8\text{C}_1\text{Im}]^+$  cation. Interestingly, the damping of the  $\text{N}_{\text{Im}}$  signal at 402.1 eV is weaker than for the neat IL2. This behavior is attributed to the increased surface sensitivity in  $80^\circ$ , where the contribution from the  $[\text{C}_8\text{C}_1\text{Im}]^+$ -enriched topmost layer dominates ( $\sim 80\%$  of total signal intensity originates from this layer), whereas at  $0^\circ$  this enriched layer has a much smaller contribution (25%), while the majority of the signal (75%) stems from the bulk underneath with a 1:1 composition. The same argument also explains the comparably weak damping of the combined  $\text{C}_{\text{Im}} + \text{C}_{\text{MeO}}$  signal at  $\sim 287$  eV. Taking all these results together, we find a pronounced surface enrichment of the  $[\text{C}_8\text{C}_1\text{Im}]^+$  cation, which goes along with a surface depletion of the  $[(\text{MeO})_2\text{Im}]^+$  cation. From the  $80^\circ$  emission data a concentration of  $\sim 69$  mol% of  $[\text{C}_8\text{C}_1\text{Im}]^+$  is deduced for the first 1–1.5 nm. This conclusion is perfectly in line with the conclusions already drawn above from the comparison of the

$0^\circ$  intensities of the C 1s and N 1s core levels of the different cations discussed in the context of Figure 1. The observed enrichment of  $[\text{C}_8\text{C}_1\text{Im}]^+$  on expense of  $[(\text{MeO})_2\text{Im}]^+$  in the topmost layer is attributed to the thermodynamic driving force to obtain the lowest possible surface tension, that is, surface free energy. Despite the fact that no experimental surface tension values are available for the neat IL3 or for the IL2 + IL3 mixture, it appears plausible that the weakly coordinating  $[\text{C}_8\text{C}_1\text{Im}]^+$  with its long alkyl chain exhibits a considerable lower surface tension than the more polar  $[(\text{MeO})_2\text{Im}]^+$ , and is thus enriched at the surface.<sup>[54]</sup>

### 2.2.3. Equimolar Mixture of IL1 and IL3

Finally, we address the surface composition of the equimolar mixture of IL1 and IL3 (see Figure 7), that is, the mixture of ILs with different cations and anions. The  $C_{\text{alkyl}}$  signal is considerably enhanced (by ~47%) at 80° (red) as compared to 0° (black), which again indicates that the  $[C_8C_1\text{Im}]^+$  cation is enriched at the surface with the alkyl chain preferentially pointing towards the vacuum. Again, also the N 1s and O 1s signals of the  $[(\text{MeO})_2\text{Im}]^+$  cation show a much lower intensity (only ~62%) at 80° emission, due to the depletion of this cation from the topmost layer. These signal changes result in a concentration of ~69 mol% of  $[C_8C_1\text{Im}]^+$  probed in 80° emission for the first 1–1.5 nm. Concerning the anions, we find a pronounced decrease of the  $F_{\text{PF}_6}$  (by 39%) and  $P_{\text{PF}_6}$  signals (by

27%), indicating the depletion of  $[\text{PF}_6]^-$  from the topmost layer. On the other hand, we find a moderate increase (up to 14%) of the  $F_{\text{Tf}_2\text{N}}$ ,  $O_{\text{Tf}_2\text{N}}$ ,  $N_{\text{Tf}_2\text{N}}$ ,  $C_{\text{Tf}_2\text{N}}$  and  $S_{\text{Tf}_2\text{N}}$  signals at 80° as compared to 0°. This increase is in contrast to the neat IL1, where all anion signals decreased by 2–13% in intensities at 80°, and indicates the enrichment of  $[\text{Tf}_2\text{N}]^-$  in the topmost layer of the IL1+IL3 mixture indicating a concentration of ~68 mol% of  $[\text{Tf}_2\text{N}]^-$  in the first 1–1.5 nm. In sum, our ARXPS results clearly show that pronounced surface enrichment of  $[C_8C_1\text{Im}]^+$  and  $[\text{Tf}_2\text{N}]^-$  and depletion of  $[(\text{MeO})_2\text{Im}]^+$  and  $[\text{PF}_6]^-$  also occurs in equimolar IL mixtures with different anions and cations. Concerning the cations, again the  $[C_8C_1\text{Im}]^+$  cation is enriched at the surface, due to its presumed lower contribution to the surface tension. For the anion, we find  $[\text{Tf}_2\text{N}]^-$  enriched at the surface while  $[\text{PF}_6]^-$  is depleted. We attribute this to the lower contribution to



**Figure 7.** F 1s, O 1s, N 1s, C 1s, S 2p, and P 2p spectra of the equimolar IL1 + IL3 mixture,  $[C_8C_1\text{Im}][\text{Tf}_2\text{N}] + [(\text{MeO})_2\text{Im}][\text{PF}_6]$ , in 0° (black) and 80° (red) emission, measured with Al  $K_{\alpha}$  radiation.

the surface tension of the former; indeed, surface tension measurements for  $[\text{C}_8\text{C}_1\text{Im}][\text{Tf}_2\text{N}]$  and  $[\text{C}_8\text{C}_1\text{Im}][\text{PF}_6]$  yield values of 29.5 mN/m for the former and 32.5 mN/m for the latter.<sup>[55]</sup>

### 3. Conclusions

We have studied ILs with a methoxy functionalized imidazolium-based cation, that is,  $[(\text{MeO})_2\text{Im}][\text{PF}_6]$ , and equimolar mixtures of this IL by angle-resolved X-ray photoelectron spectroscopy. In the  $[(\text{MeO})_2\text{Im}][\text{PF}_6] + [\text{C}_8\text{C}_1\text{Im}][\text{PF}_6]$  mixture, the second IL has the same anion, but the non-functionalized  $[\text{C}_8\text{C}_1\text{Im}]^+$  as cation. In the  $[(\text{MeO})_2\text{Im}][\text{PF}_6] + [\text{C}_8\text{C}_1\text{Im}][\text{Tf}_2\text{N}]$  mixture, the second IL consists of different anions and cations. For the neat  $[(\text{MeO})_2\text{Im}][\text{PF}_6]$ , we observe that the tethering of methoxy groups at the imidazolium ring leads to pronounced changes in the electronic structure of the imidazolium rings as compared to the situation for the non-functionalized ring; these changes are reflected by pronounced differential shifts towards higher binding energies of the imidazolium nitrogen and carbon atoms as well as for the oxygen atoms linked to the ring. DFT calculations for the  $[(\text{MeO})_2\text{Im}]^+$  cation combined with an atomic charge analysis are fully in line with the observed XPS shifts in an initial state picture: In contrast to the situation for PEG- or alkyl-chains, the electron density is considerably reduced in the imidazolium ring and also at the oxygen of the methoxy group, when oxygen is directly linked to the nitrogen atoms. For the two equimolar mixtures, we found no additional changes in the electronic structure, that is, the binding energies are unchanged as compared to the neat ILs within the margin of error. For both equimolar mixtures of ILs with different cations ( $[(\text{MeO})_2\text{Im}]^+$  or  $[\text{C}_8\text{C}_1\text{Im}]^+$ ) and anions ( $[\text{PF}_6]^-$  or  $[\text{Tf}_2\text{N}]^-$ ), we always observed pronounced surface enrichment effects by angle-resolved XPS. For the mixture with the same  $[\text{PF}_6]^-$  anion, we find a pronounced enrichment of the octyl chain-containing  $[\text{C}_8\text{C}_1\text{Im}]^+$  cation and a corresponding depletion of the  $[(\text{MeO})_2\text{Im}]^+$  cation in the topmost layer. For a mixture of these cations with different anions, we find surface enrichment of the  $[\text{C}_8\text{C}_1\text{Im}]^+$  cation and the  $[\text{Tf}_2\text{N}]^-$  anion, while  $[(\text{MeO})_2\text{Im}]^+$  and  $[\text{PF}_6]^-$  are depleted from the surface. The observed behavior is proposed to be due to a lowering of surface tension by the enriched components.

## Experimental Section

### Materials

$[\text{C}_8\text{C}_1\text{Im}][\text{PF}_6]$  was purchased from Sigma-Aldrich (purity > 95%).  $[(\text{MeO})_2\text{Im}][\text{PF}_6]$  was synthesized with a purity of > 99%.<sup>[37,38]</sup>  $[\text{Me}(\text{EG})_2\text{C}_1\text{Im}][\text{Tf}_2\text{N}]$  and  $[\text{C}_8\text{C}_1\text{Im}][\text{Tf}_2\text{N}]$  were synthesized as was published earlier,<sup>[45,47]</sup> the PEG-functionalized IL  $[\text{Me}(\text{EG})_2\text{C}_1\text{Im}][\text{Tf}_2\text{N}]$  was used for comparison of binding energy positions.  $[(\text{MeO})_2\text{Im}][\text{PF}_6]$  shows a minor contamination in its solid state at room temperature, which almost disappears by heating the sample to 90 °C. All neat ILs were used without further purification. For ARXPS, a thin layer (thickness about 0.1 mm) of the neat ILs or the equimolar mixtures was placed onto a molybdenum sample holder and transferred to the vacuum chamber via a load-lock, where they remained at least twelve hours for degassing. The equimolar

mixtures of  $[(\text{MeO})_2\text{Im}][\text{PF}_6]$  with  $[\text{C}_8\text{C}_1\text{Im}][\text{Tf}_2\text{N}]$  or  $[\text{C}_8\text{C}_1\text{Im}][\text{PF}_6]$  were prepared with acetonitrile (Sigma-Aldrich, purity 99.8%) as a co-solvent to ensure proper mixing of the respective ILs. They were dripped on the molybdenum sample holder with a disposable glass pipette outside and put into the load-lock after slow evaporation of the co-solvent acetonitrile.

### Angle-Resolved X-Ray Photoelectron Spectroscopy (ARXPS)

All angle-resolved XP spectra were measured with our DASSA<sup>[44]</sup> apparatus, which is a modified Multiprobe<sup>®</sup> XP system (OMICRON NanoTechnology GmbH). To our knowledge, this ARXPS system is the first setup to be equipped with two hemispherical energy analyzers (ARGUS-type). The analyzers are mounted at emission angles  $\vartheta$  of 0° and 80° with respect to the surface normal of a horizontally aligned sample. This enables the simultaneous measurement of 0° and 80° emission spectra of liquids, which would drip off the sample holder upon sample rotation away from the horizontal position. Measuring simultaneously at both angles has the additional advantage that the measuring time for the two spectra is reduced by a factor of two and possible time- (or radiation-) induced changes can be ruled out (or minimized). As X-ray source, we use monochromated Al  $K_{\alpha}$  radiation, impinging onto the sample under the magic angle of 54.7°, with respect to both analyzers. The surface sensitivity of XPS increases with increasing emission angle, proportional to  $1/\cos(\vartheta)$ . Considering the inelastic mean free path of electrons in organic matter of 2.6 (F 1s)–3.3 nm (P 2p)<sup>[56]</sup> at the given kinetic energies of the photoelectrons (–800 (F 1s)–1300 eV (P 2p)), the information depth at 0° amounts to 7–9 nm, while at 80° only the topmost 1–1.5 nm are probed. All 80° spectra are scaled up by a so-called geometry factor obtained for each data set according to ref [44]. Consequently, a larger (smaller) signal at 80° as compared to 0° unambiguously indicates that the corresponding element has a higher (lower) concentration at the surface than in the bulk. Therefore, conclusions about surface enrichment and surface orientation effects are possible.

The X-ray source (XM 1000) was operated at a power of 238 W, with a spot size of the monochromated Al  $K_{\alpha}$  radiation ( $h\nu = 1486.6$  eV) of 1.0 mm × 2.0 mm on the sample. For both analyzers, we used a curved slit of 1.0 mm × 10.0 mm and the high magnification mode. These settings led to an acceptance angle of  $\pm 3.1^\circ$  and a full-width-at-half-maximum (FWHM) of the analysis area of 0.31 mm × 3.2 mm in 0° emission. The pass energy was set to 35 eV resulting in an overall instrumental energy resolution of 0.4 eV.

All spectra were referenced to the F 1s signals of the  $[\text{PF}_6]^-$  and  $[\text{Tf}_2\text{N}]^-$  anions at 686.8 and 688.8 eV, respectively, to compensate for charging effects and different sample work functions. With this binding energy referencing, the  $\text{C}_{\text{alkyl}}$  of  $[\text{C}_8\text{C}_1\text{Im}]^+$  (see Scheme 1 for peak assignment) is located at  $285.0 \pm 0.1$  eV.

The peaks in the different regions were analyzed for quantification. Quantitative analysis was possible by using the intensity of the fitted peaks and taking into account the ASF of each signal.<sup>[44]</sup> For ILs containing the  $[\text{Tf}_2\text{N}]^-$  anion, a three-point linear background was subtracted in C 1s spectra; for all other spectra, a two-point linear background subtraction was used. The signals were fitted with a Gauss-Lorentz function with 30% Lorentz contribution. The XP signals of P 2p and S 2p are composed of two components, namely the spin-orbit-split  $2p_{1/2}$  and  $2p_{3/2}$  levels. The two components always have the same FWHM and binding energy separation (0.90 eV for P 2p and 1.21 eV for S 2p), and an area ratio of 1:2. When fitting the C 1s spectra constraints were employed (for peak assignment see Scheme 1): The area ratios of the  $\text{C}_{\text{hetero}}$ ,  $\text{C}_{\text{alkyl}}$  and  $\text{C}_{\text{alkyl}}$  peaks measured at 0° were set to their nominal

ratios; at 80°, no area constraints were applied for  $C_{\text{alkyl}}$ . For IL1 and IL2 (see Table 1), the separation of  $C_2$  and  $C_{\text{hetero}}$  is set to 0.90 eV, with the FWHM of  $C_{\text{hetero}}$  1.10 times wider than that of  $C_2$  and  $C_{\text{alkyl}}$ . For IL4, the FWHM of  $C_{\text{hetero}}$  is 1.19 times that of  $C_2$ . For IL3, the  $C_{\text{hetero}}$  and  $C_2$  are separated by 1.10 eV, with the FWHM of  $C_{\text{hetero}}$  1.02 times wider than that of  $C_2$ . All fit parameters are extracted by fitting several C 1s spectra as mentioned in ref [44]. Note that in earlier publications  $C_2$  and  $C_{\text{hetero}}$  were combined in one  $C_{\text{hetero}}$  peak due to a lower resolution than for the DASSA setup used here.

### Calculation of Atomic Charges

In order to correlate XPS core level binding energies with the electron density, density functional theory (DFT) calculations were carried out and the atomic partial charges on individual atoms were compared via two charge analysis methods: NBO and ChelpG.<sup>[57,58]</sup> The calculations are performed for  $[(\text{MeO})_2\text{Im}]^+$ ,  $[\text{C}_2\text{C}_2\text{Im}]^+$ , and  $[\text{Me}(\text{EG})\text{C}_1\text{Im}]^+$ . Thereby, the  $[\text{C}_2\text{C}_2\text{Im}]^+$  cation is taken as a model cation for the larger  $[\text{C}_8\text{C}_1\text{Im}]^+$  cation studied by ARXPS as well as for direct comparison with  $[(\text{MeO})_2\text{Im}]^+$  without oxygen being implemented in the cation.

DFT calculations were performed at the B3LYP–D3(BJ)/6-311G(d,p) level using Becke's three-parameter exchange functional in combination with the Lee, Yang, and Parr correlation functional (B3LYP).<sup>[59,60]</sup> Grimme's D3 dispersion correction with Becke-Johnson (BJ) damping was used to account for dispersion.<sup>[61–64]</sup> The 6-311G(d,p) basis set was employed for all calculations. All calculations were carried out employing the Gaussian 09 (revision D.01) suite of programs.<sup>[65]</sup> Structures were fully optimized under no symmetry constraints and maxima and minima have been confirmed by vibrational analysis (one or no imaginary frequencies). NBO analysis employed version 6.0 (not the default version within G09).<sup>[66,67]</sup> All molecular orbitals have been generated using the Gaussview software at the 0.02 au isosurface.<sup>[68]</sup>

The NBO charge analysis is based on atomic orbitals, and as such provides a "localized" view. The electron density is decomposed into a basis of natural atomic orbitals, which can be described as the effective "natural orbitals of an atom" in a particular molecular environment. The negative charge on the atoms is calculated by assigning electron density to atoms on which the basis atomic orbitals are centered; the balance with the positive nucleus charge then provides the NBO charge on this atom.<sup>[57]</sup> The ChelpG charge analysis is based on the electrostatic potential (ESP) created by the DFT-derived electron density. Atomic partial charges are fitted in order to reproduce the ESP (beyond the van-der-Waals radii of all the atoms in the molecule); in this sense the charges produce an "external" view of the ion or molecule. It has been shown that both NBO and ChelpG charge analysis can be well correlated with experimental XPS binding energies and near edge X-ray absorption fine structure (NEXAFS) spectroscopy.<sup>[69,70]</sup> While fitted trends may show a good correlation with both NBO and ChelpG there is a more robust physical basis for the correlation of NBO charges with the experimental data presented here, which leads us to focus on the NBO charges. The ChelpG charges and a discussion of the associated limitations are presented in the SI.

### Acknowledgement

We thank N. Taccardi for providing us with the IL  $[\text{C}_8\text{C}_1\text{Im}][\text{Tf}_2\text{N}]$ . B.S.J.H. and H.-P.S. thank the European Research Council (ERC) under the European Union's Horizon 2020 research and innovation programme for financial support, in the context of the

Advanced Investigator Grant "ILID" to H.-P.S. (Grant Agreement No. 693398-ILID).

### Conflict of Interest

The authors declare no conflict of interest.

**Keywords:** angle-resolved X-ray photoelectron spectroscopy (ARXPS) · density functional theory · electronic structure · ionic liquid mixture · surface science

- [1] N. V. Plechkova, K. R. Seddon, *Chem. Soc. Rev.* **2008**, *37*, 123–150.
- [2] H.-P. Steinrück, *Phys. Chem. Chem. Phys.* **2012**, *14*, 5010–5029.
- [3] U. Kernchen, B. Eitzold, W. Korth, A. Jess, *Chem. Eng. Technol.* **2007**, *30*, 985–994.
- [4] H.-P. Steinrück, J. Libuda, P. Wasserscheid, T. Cremer, C. Kolbeck, M. Laurin, F. Maier, M. Sobota, P. S. Schulz, M. Stark, *Adv. Mater.* **2011**, *23*, 2571–2587.
- [5] T. Yasuda, M. Watanabe, *MRS Bull.* **2013**, *38*, 560–566.
- [6] M. Diaz, A. Ortiz, I. Ortiz, *J. Membr. Sci.* **2014**, *469*, 379–396.
- [7] J. C. Fergie, S. El Khakani, D. D. MacNeil, D. Rochefort, *Phys. Chem. Chem. Phys.* **2013**, *15*, 7713–7721.
- [8] P. M. Bayley, A. S. Best, D. R. MacFarlane, M. Forsyth, *Phys. Chem. Chem. Phys.* **2011**, *13*, 4632–4640.
- [9] S. Ferrari, E. Quartarone, C. Tomasi, D. Ravelli, S. Protti, M. Fagnoni, P. Mustarelli, *J. Power Sources* **2013**, *235*, 142–147.
- [10] C. Capello, U. Fischer, K. Hungerbühler, *Green Chem.* **2007**, *9*, 927–934.
- [11] R. I. Canales, J. F. Brennecke, *J. Chem. Eng. Data* **2016**, *61*, 1685–1699.
- [12] H.-P. Steinrück, P. Wasserscheid, *Catal. Lett.* **2015**, *145*, 380–397.
- [13] H. Xiao, *Tribol. Trans.* **2017**, *60*, 20–30.
- [14] D. S. Silvester, *Analyst* **2011**, *136*, 4871–4882.
- [15] P. Sun, D. W. Armstrong, *Anal. Chim. Acta* **2010**, *661*, 1–16.
- [16] Q. Q. Baltazar, S. K. Leininger, J. L. Anderson, *J. Chromatogr. A* **2008**, *1182*, 119–127.
- [17] C. F. Poole, S. K. Poole, *J. Sep. Sci.* **2011**, *34*, 888–900.
- [18] J. N. Canongia Lopes, T. C. Cordeiro, J. M. S. S. Esperança, H. J. R. Guedes, S. Huq, L. P. N. Rebelo, K. R. Seddon, *J. Phys. Chem. B* **2005**, *109*, 3519–3525.
- [19] M. T. Clough, C. R. Crick, J. Grasvik, P. A. Hunt, H. Niedermeyer, T. Welton, O. P. Whitaker, *Chem. Sci.* **2015**, *6*, 1101–1114.
- [20] D. W. Bruce, C. P. Cabry, J. N. C. Lopes, M. L. Costen, L. D'Andrea, I. Grillo, B. C. Marshall, K. G. McKendrick, T. K. Minton, S. M. Purcell, S. Rogers, J. M. Slattey, K. Shimizu, E. Smoll, M. A. Tesa-Serrate, *J. Phys. Chem. B* **2017**, *121*, 6002–6020.
- [21] R. Souda, *Surf. Sci.* **2010**, *604*, 1694–1697.
- [22] K. Nakajima, M. Miyashita, M. Suzuki, K. Kimura, *J. Chem. Phys.* **2013**, *139*, 224701.
- [23] I. J. Villar Garcia, S. Fearn, G. F. De Gregorio, N. L. Ismail, F. J. V. Gschwend, A. J. S. McIntosh, K. R. J. Lovelock, *Chem. Sci.* **2014**, *5*, 4404–4418.
- [24] I. J. Villar-Garcia, S. Fearn, N. L. Ismail, A. J. S. McIntosh, K. R. J. Lovelock, *Chem. Commun.* **2015**, *51*, 5367–5370.
- [25] K. Nakajima, S. Oshima, M. Suzuki, K. Kimura, *Surf. Sci.* **2012**, *606*, 1693–1699.
- [26] K. Nakajima, S. Nakanishi, Z. Chval, M. Lísal, K. Kimura, *J. Chem. Phys.* **2016**, *145*, 184704.
- [27] K. Nakajima, S. Nakanishi, M. Lísal, K. Kimura, *J. Mol. Liq.* **2017**, *230*, 542–549.
- [28] S. Men, P. Licence, *Chem. Phys. Lett.* **2017**, *681*, 40–43.
- [29] I. J. Villar-Garcia, K. R. J. Lovelock, S. Men, P. Licence, *Chem. Sci.* **2014**, *5*, 2573–2579.
- [30] F. Maier, T. Cremer, C. Kolbeck, K. R. J. Lovelock, N. Paape, P. S. Schulz, P. Wasserscheid, H.-P. Steinrück, *Phys. Chem. Chem. Phys.* **2010**, *12*, 1905–1915.
- [31] E. J. Smoll Jr., M. A. Tesa-Serrate, S. M. Purcell, L. D'Andrea, D. W. Bruce, J. M. Slattey, M. L. Costen, T. K. Minton, K. G. McKendrick, *Faraday Discuss.* **2018**, *206*, 497–522.
- [32] S. Palchowdhury, B. L. Bhargava, *Phys. Chem. Chem. Phys.* **2015**, *17*, 19919–19928.

- [33] S. Palchowdhury, B. L. Bhargava, *J. Phys. Chem. B* **2016**, *120*, 5430–5441.
- [34] T. Cremer, C. Kolbeck, K. R. J. Lovelock, N. Paape, R. Wölfel, P. S. Schulz, P. Wasserscheid, H. Weber, J. Thar, B. Kirchner, F. Maier, H.-P. Steinrück, *Chem. Eur. J.* **2010**, *16*, 9018–9033.
- [35] S. Men, K. R. J. Lovelock, P. Licence, *Phys. Chem. Chem. Phys.* **2011**, *13*, 15244–15255.
- [36] S. Men, P. Licence, *Chem. Phys. Lett.* **2017**, *686*, 74–77.
- [37] G. Laus, A. Schwärzler, P. Schuster, G. Bentivoglio, M. Hummel, K. Wurst, V. Kahlenberg, T. Lörting, J. Schütz, P. Peringer, G. Bonn, G. Nauer, H. Schottenberger, *Z. Naturforsch.* **2007**, *62b*, 295–308.
- [38] S. Bartz, B. Blumenröder, A. Kern, J. Fleckenstein, S. Frohnapfel, J. Schatz, A. Wagner, *Z. Naturforsch.* **2009**, *64b*, 629–638.
- [39] N. Taccardi, I. Niedermaier, F. Maier, H.-P. Steinrück, P. Wasserscheid, *Chem. Eur. J.* **2012**, *18*, 8288–8291.
- [40] A.-L. Revelli, F. Mutelet, J.-N. Jaubert, *J. Phys. Chem. B* **2010**, *114*, 12908–12913.
- [41] A.-L. Revelli, F. Mutelet, J.-N. Jaubert, *J. Phys. Chem. B* **2010**, *114*, 8199–8206.
- [42] G. Laus, K. Wurst, V. Kahlenberg, H. Kopacka, C. Kreutz, H. Schottenberger, *Z. Naturforsch.* **2010**, *65b*, 776–782.
- [43] T. Brendgen, T. Fahlbusch, M. Frank, D. T. Schühle, M. Seßler, J. Schatz, *Adv. Synth. Catal.* **2009**, *351*, 303–307.
- [44] I. Niedermaier, C. Kolbeck, H.-P. Steinrück, F. Maier, *Rev. Sci. Instrum.* **2016**, *87*, 045105.
- [45] C. Kolbeck, T. Cremer, K. R. J. Lovelock, N. Paape, P. S. Schulz, P. Wasserscheid, F. Maier, H.-P. Steinrück, *J. Phys. Chem. B* **2009**, *113*, 8682–8688.
- [46] T. Hammer, M. Reichelt, H. Morgner, *Phys. Chem. Chem. Phys.* **2010**, *12*, 11070–11080.
- [47] C. Kolbeck, M. Killian, F. Maier, N. Paape, P. Wasserscheid, H.-P. Steinrück, *Langmuir* **2008**, *24*, 9500–9507.
- [48] J. M. Gottfried, F. Maier, J. Rossa, D. Gerhard, P. S. Schulz, P. Wasserscheid, H.-P. Steinrück, *Z. Phys. Chem.* **2006**, *220*, 1439–1453.
- [49] C. Iuga, C. Solís, J. R. Alvarez-Idaboy, M. Á. Martínez, M. A. Mondragón, A. Vivier-Bunge, *J. Mol. Model.* **2014**, *20*, 2186–2194.
- [50] T. Yamada, Y. Tominari, S. Tanaka, M. Mizuno, K. Fukunaga, *Materials* **2014**, *7*, 7409–7422.
- [51] A. Dilks, *J. Polym. Sci. Polym. Chem. Ed.* **1981**, *19*, 1319–1327.
- [52] C. Kolbeck, I. Niedermaier, A. Deyko, K. R. J. Lovelock, N. Taccardi, W. Wei, P. Wasserscheid, F. Maier, H.-P. Steinrück, *Chem. Eur. J.* **2014**, *20*, 3954–3965.
- [53] K. R. J. Lovelock, C. Kolbeck, T. Cremer, N. Paape, P. S. Schulz, P. Wasserscheid, F. Maier, H.-P. Steinrück, *J. Phys. Chem. B* **2009**, *113*, 2854–2864.
- [54] M. B. Oliveira, M. Domínguez-Pérez, O. Cabeza, J. A. Lopes-da-Silva, M. G. Freire, J. A. P. Coutinho, *J. Chem. Thermodyn.* **2013**, *64*, 22–27.
- [55] C. Kolbeck, J. Lehmann, K. R. J. Lovelock, T. Cremer, N. Paape, P. Wasserscheid, A. P. Fröba, F. Maier, H.-P. Steinrück, *J. Phys. Chem. B* **2010**, *114*, 17025–17036.
- [56] R. F. Roberts, D. L. Allara, C. A. Pryde, D. N. E. Buchanan, N. D. Hobbins, *Surf. Interface Anal.* **1980**, *2*, 5–10.
- [57] A. E. Reed, L. A. Curtiss, F. Weinhold, *Chem. Rev.* **1988**, *88*, 899–926.
- [58] C. M. Breneman, K. B. Wiberg, *J. Comput. Chem.* **1990**, *11*, 361–373.
- [59] A. D. Becke, *Phys. Rev. A* **1988**, *38*, 3098–3100.
- [60] C. Lee, W. Yang, R. G. Parr, *Phys. Rev. B* **1988**, *37*, 785–789.
- [61] S. Grimme, J. Antony, S. Ehrlich, H. Krieg, *J. Chem. Phys.* **2010**, *132*, 154104.
- [62] S. Grimme, S. Ehrlich, L. Goerigk, *J. Comput. Chem.* **2011**, *32*, 1456–1465.
- [63] A. D. Becke, E. R. Johnson, *J. Chem. Phys.* **2005**, *123*, 154101.
- [64] A. D. Becke, E. R. Johnson, *J. Chem. Phys.* **2006**, *124*, 221101.
- [65] G. W. T. M. J. Frisch, H. B. Schlegel, G. E. Scuseria, M. A. Robb, J. R. Cheeseman, G. Scalmani, V. Barone, B. Mennucci, G. A. Petersson, H. Nakatsuji, M. Caricato, X. Li, H. P. Hratchian, A. F. Izmaylov, J. Bloino, G. Zheng, J. L. Sonnenberg, M. Hada, M. Ehara, K. Toyota, R. Fukuda, J. Hasegawa, M. Ishida, T. Nakajima, Y. Honda, O. Kitao, H. Nakai, T. Vreven, J. Montgomery, J. A., J. E. Peralta, F. Ogliaro, M. Bearpark, J. J. Heyd, E. Brothers, K. N. Kudin, V. N. Staroverov, R. Kobayashi, J. Normand, K. Raghavachari, A. Rendell, J. C. Burant, S. S. Iyengar, J. Tomasi, M. Cossi, N. Rega, J. M. Millam, M. Klene, J. E. Knox, J. B. Cross, V. Bakken, C. Adamo, J. Jaramillo, R. Gomperts, R. E. Stratmann, O. Yazyev, A. J. Austin, R. Cammi, C. Pomelli, J. W. Ochterski, R. L. Martin, K. Morokuma, V. G. Zakrzewski, G. A. Voth, P. Salvador, J. J. Dannenberg, S. Dapprich, A. D. Daniels, Ö. Farkas, J. B. Foresman, J. V. Ortiz, J. Cioslowski, D. J. Fox, *Gaussian 09* **2009**.
- [66] E. D. Glendening, J. K. Badenhop, A. E. Reed, J. E. Carpenter, J. A. Bohmann, C. M. Morales, C. R. Landis, F. Weinhold, Theoretical Chemistry Institute, University of Wisconsin, Madison, WI, 2013; <http://nbo6.chem.wisc.edu/>.
- [67] E. D. Glendening, C. R. Landis, F. Weinhold, *J. Comput. Chem.* **2013**, *34*, 1429–1437.
- [68] GaussView, Version 6, R. Dennington, T. A. Keith, J. M. Millam, Semichem Inc., Shawnee Mission, KS, 2016.
- [69] R. M. Fogarty, R. P. Matthews, M. T. Clough, C. R. Ashworth, A. Brandt-Talbot, P. J. Corbett, R. G. Palgrave, R. A. Bourne, T. W. Chamberlain, T. Vander Hoogerstraete, P. B. J. Thompson, P. A. Hunt, N. A. Besley, K. R. J. Lovelock, *Phys. Chem. Chem. Phys.* **2017**, *19*, 31156–31167.
- [70] R. M. Fogarty, R. Rowe, R. P. Matthews, M. T. Clough, C. R. Ashworth, A. Brandt, P. J. Corbett, R. G. Palgrave, E. F. Smith, R. A. Bourne, T. W. Chamberlain, P. B. J. Thompson, P. A. Hunt, K. R. J. Lovelock, *Faraday Discuss.* **2018**, *206*, 183–201.

Manuscript received: March 12, 2018  
Accepted Article published: April 12, 2018  
Version of record online: May 11, 2018



## Supporting Information

© Copyright Wiley-VCH Verlag GmbH & Co. KGaA, 69451 Weinheim, 2018

### **Surface Enrichment in Equimolar Mixtures of Non-Functionalized and Functionalized Imidazolium-Based Ionic Liquids**

Bettina S. J. Heller, Claudia Kolbeck, Inga Niedermaier, Sabine Dommer, Jürgen Schatz, Patricia Hunt, Florian Maier, and Hans-Peter Steinrück© 2018 The Authors. Published by Wiley-VCH Verlag GmbH & Co. KGaA. This is an open access article under the terms of the Creative Commons Attribution Non-Commercial License, which permits use, distribution and reproduction in any medium, provided the original work is properly cited and is not used for commercial purposes.

## SUPPORTING INFORMATION

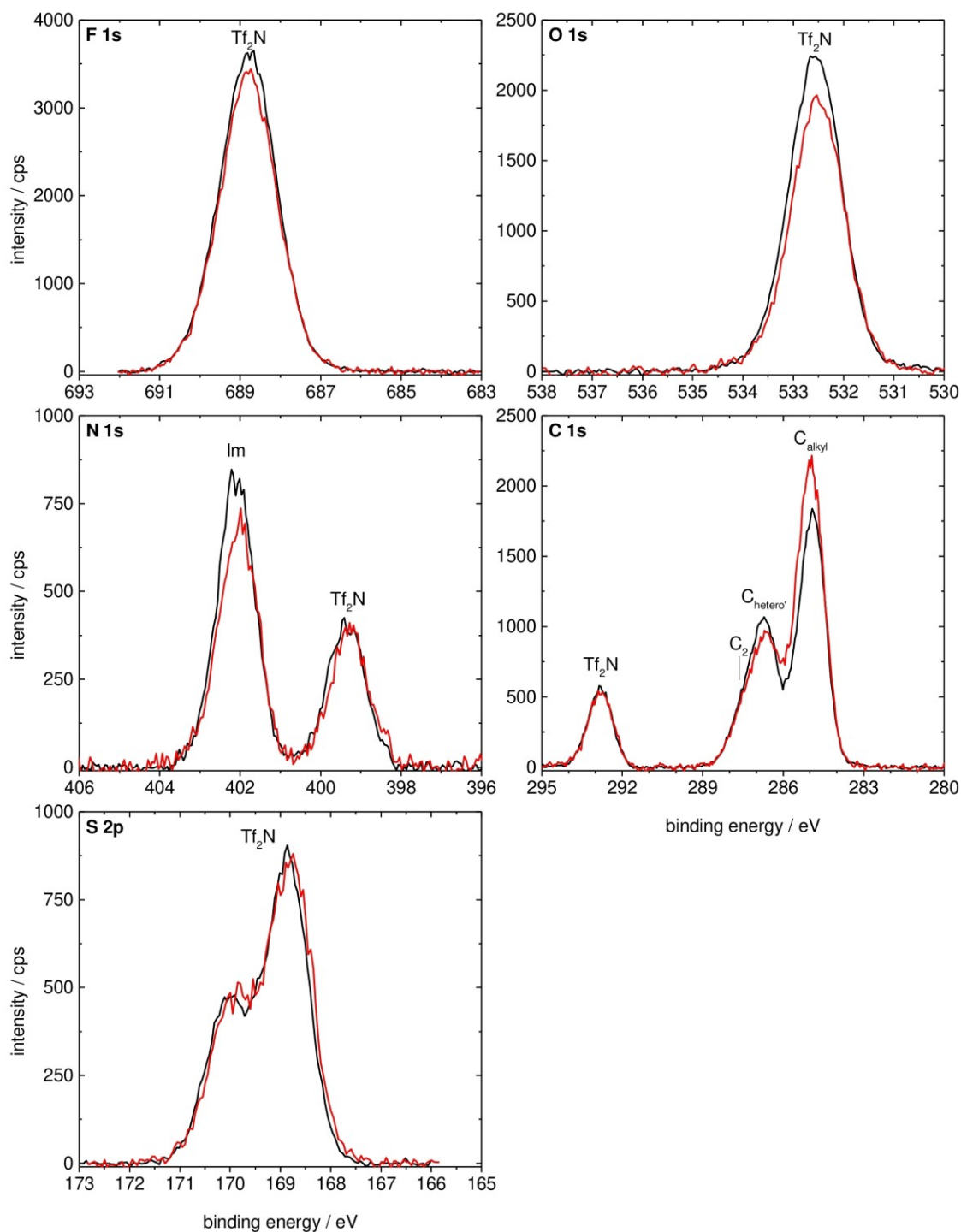
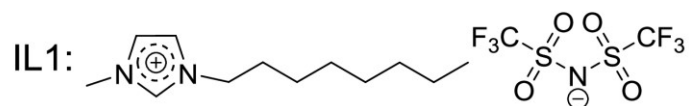


Figure S1: F 1s, O 1s, N 1s, C 1s, and S 2p spectra of IL1,  $[\text{C}_8\text{C}_1\text{Im}][\text{Tf}_2\text{N}]$ , in 0° (black) and 80° (red) emission, measured with  $\text{Al K}_\alpha$  radiation.

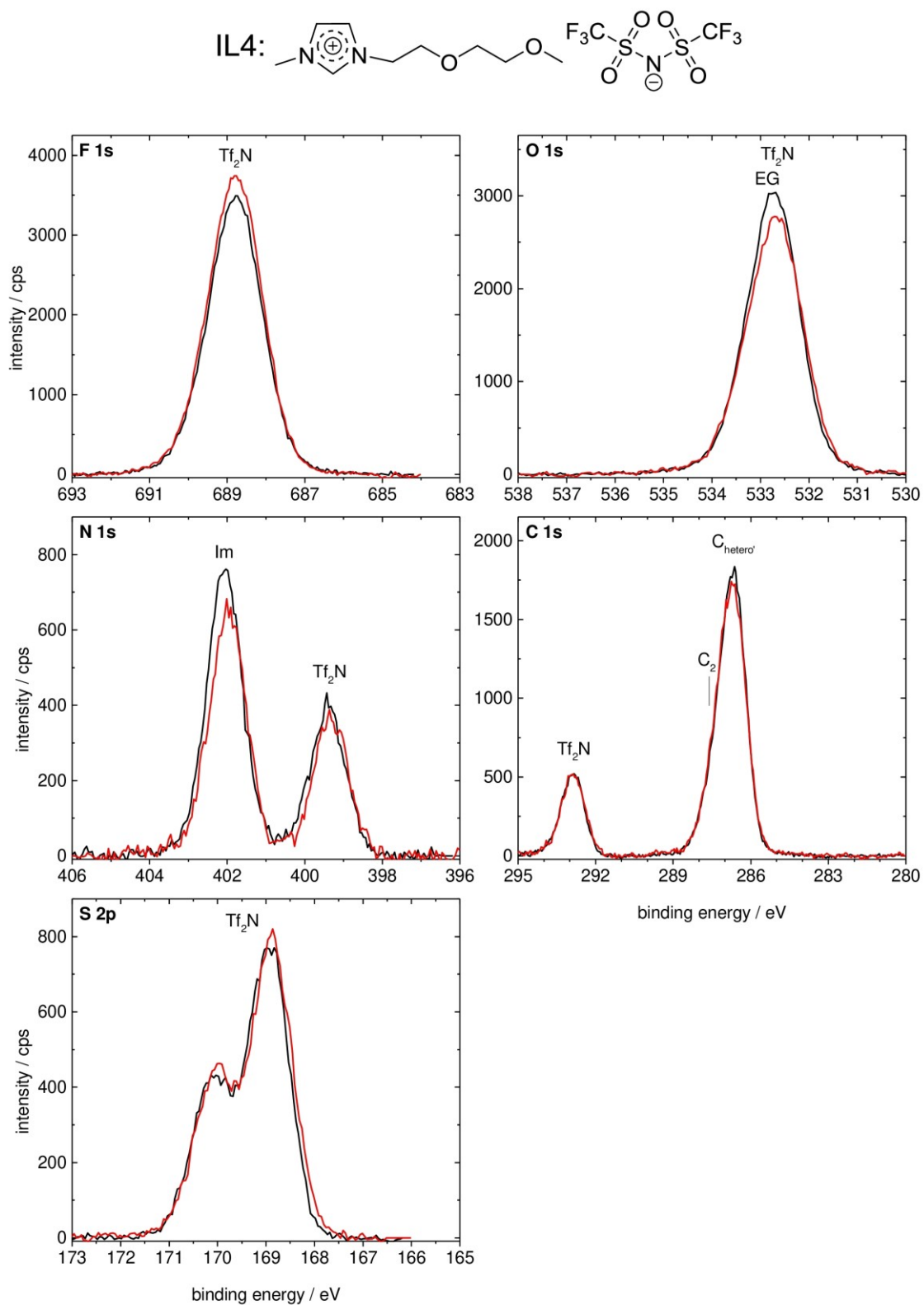


Figure S2: F 1s, O 1s, N 1s, C 1s, and S 2p spectra of IL4,  $[\text{Me}(\text{EG})_2\text{C}_1\text{Im}][\text{Tf}_2\text{N}]$ , in  $0^\circ$  (black) and  $80^\circ$  (red) emission, measured with  $\text{Al K}_\alpha$  radiation.

Table S1: Quantitative analysis of the 0° and 80° emission XP spectra of IL1, [C<sub>8</sub>C<sub>1</sub>Im][Tf<sub>2</sub>N]. The nominal and experimentally determined composition is given for all elements contained in the IL. The ASFs are taken from ref [44].

	<b>F 1s</b> F <sub>Tf2N</sub>	<b>O 1s</b> O <sub>Tf2N</sub>	<b>N 1s</b> N <sub>Im</sub>	<b>N 1s</b> N <sub>Tf2N</sub>	<b>C 1s</b> C <sub>Tf2N</sub>	<b>C 1s</b> C <sub>2</sub>	<b>C 1s</b> C <sub>hetero'</sub>	<b>C 1s</b> C <sub>alkyl</sub>	<b>S 2p</b> S <sub>Tf2N</sub>
<b>ASF</b>	1.00	0.67	0.46	0.46	0.30	0.30	0.30	0.30	0.64
<b>nominal</b>	6	4	2	1	2	1	4	7	2
<b>binding energy / eV</b>	688.8	532.6	402.1	399.4	292.8	287.6	286.7	284.9	169.5
<b>corrected intensity 0°</b>	6468	4462	2146	1077	2158	1113	4452	7483	2196
<b>atom ratio 0°</b>	5.9	4.1	2.0	1.0	2.0	1.0	4.1	6.9	2.0
<b>corrected intensity 80°</b>	6067	3902	1892	1036	2122	1030	4120	9150	2254
<b>atom ratio 80°</b>	5.6	3.6	1.8	1.0	2.0	1.0	3.8	8.4	2.1

Table S2: Quantitative analysis of the 0° and 80° emission XP spectra of IL2, [C<sub>8</sub>C<sub>1</sub>Im][PF<sub>6</sub>]. The nominal and experimentally determined composition is given for all elements contained in the IL. The ASFs are taken from ref [44].

	<b>F 1s</b> F <sub>PF6</sub>	<b>N 1s</b> N <sub>Im</sub>	<b>C 1s</b> C <sub>2</sub>	<b>C 1s</b> C <sub>hetero'</sub>	<b>C 1s</b> C <sub>alkyl</sub>	<b>P 2p</b> P <sub>PF6</sub>
<b>ASF</b>	1.00	0.46	0.30	0.30	0.30	0.46
<b>nominal</b>	6	2	1	4	7	1
<b>binding energy / eV</b>	686.8	402.2	287.7	286.8	285.1	137.1
<b>corrected intensity 0°</b>	18773	5890	3023	12092	20328	3329
<b>atom ratio 0°</b>	6.2	2.0	1.0	4.0	6.7	1.1
<b>corrected intensity 80°</b>	15245	4980	2683	10732	26599	3041
<b>atom ratio 80°</b>	5.0	1.7	0.9	3.6	8.8	1.0

Table S3: Quantitative analysis of the 0° and 80° emission XP spectra of IL3, [(MeO)<sub>2</sub>Im][PF<sub>6</sub>]. The nominal and experimentally determined composition is given for all elements contained in the IL. The ASFs are taken from ref [44].

	<b>F 1s</b> F <sub>PF6</sub>	<b>O 1s</b> O <sub>MeO</sub>	<b>N 1s</b> N <sub>MeO</sub>	<b>C 1s</b> C <sub>2</sub>	<b>C 1s</b> C <sub>hetero'</sub>	<b>P 2p</b> P <sub>PF6</sub>
<b>ASF</b>	1.00	0.67	0.46	0.30	0.30	0.46
<b>nominal</b>	6	2	2	1	4	1
<b>binding energy / eV</b>	686.8	535.3	403.6	288.1	287.0	137.0
<b>corrected intensity 0°</b>	29478	9241	8535	4429	17715	5236
<b>atom ratio 0°</b>	6.3	2.0	1.8	1.0	3.8	1.1
<b>corrected intensity 80°</b>	28912	9290	8563	4519	18077	5265
<b>atom ratio 80°</b>	6.2	2.0	1.8	1.0	3.9	1.1

Table S4: Quantitative analysis of the 0° and 80° emission spectra of IL4, [Me(EG)<sub>2</sub>C<sub>1</sub>Im][Tf<sub>2</sub>N]. The nominal and experimentally determined composition is given for all elements contained in the IL. The ASFs are taken from ref [44].

	<b>F 1s</b> F <sub>Tf2N</sub>	<b>O 1s</b> O <sub>EG</sub>	<b>N 1s</b> N <sub>Im</sub>	<b>N 1s</b> N <sub>Tf2N</sub>	<b>C 1s</b> C <sub>Tf2N</sub>	<b>C 1s</b> C <sub>2</sub>	<b>C 1s</b> C <sub>hetero'</sub>	<b>S 2p</b> S <sub>Tf2N</sub>
<b>ASF</b>	1.00	0.67	0.46	0.46	0.30	0.30	0.30	0.64
<b>nominal</b>	6	6	2	1	2	1	8	2
<b>binding energy / eV</b>	688.8	532.7	402.1	399.4	292.9	287.7	286.7	169.6
<b>corrected intensity</b>	6160	6216	1950	1007	1985	941	7527	1948
<b>atom ratio 0°</b>	6.2	6.3	2.0	1.0	2.0	1.0	7.6	2.0
<b>corrected intensity 80°</b>	6660	6047	1722	926	2026	1030	7382	2005
<b>atom ratio 80°</b>	6.7	6.1	1.7	0.9	2.0	1.0	7.5	2.0

Table S5: Quantitative analysis of the 0° and 80° emission XP spectra of the equimolar IL1+IL3 mixture, [C<sub>8</sub>C<sub>1</sub>Im][Tf<sub>2</sub>N]<sup>+</sup> [(MeO)<sub>2</sub>Im][PF<sub>6</sub>]<sup>-</sup> mixture. The nominal and experimentally determined composition is given for all elements contained in the IL mixture. The ASFs are taken from ref [44].

	<b>F 1s</b> F <sub>Tf2N</sub>	<b>F 1s</b> F <sub>PF6</sub>	<b>O 1s</b> O <sub>MeO</sub>	<b>O 1s</b> O <sub>Tf2N</sub>	<b>N 1s</b> N <sub>MeO</sub>	<b>N 1s</b> N <sub>Im</sub>	<b>N 1s</b> N <sub>Tf2N</sub>	<b>C 1s</b> C <sub>2,Im</sub>	<b>C 1s</b> C <sub>hetero',Im</sub>	<b>C 1s</b> C <sub>alkyl</sub>	<b>C 1s</b> C <sub>2,MeO</sub>	<b>C 1s</b> C <sub>hetero',MeO</sub>	<b>S 2p</b> S <sub>Tf2N</sub>	<b>P 2p</b> P <sub>PF6</sub>
<b>ASF</b>	1.00	1.00	0.67	0.67	0.46	0.46	0.30	0.30	0.30	0.30	0.30	0.30	0.64	0.46
<b>nominal</b>	6	6	2	4	2	2	1	1	4	7	1	4	2	1
<b>binding energy / eV</b>	688.8	686.7	535.3	532.6	403.6	402.0	287.5	286.6	284.9	284.9	288.1	287.0	169.4	137.0
<b>corrected intensity 0°</b>	3696	3254	987	2343	960	1271	628	2513	4398	4398	486	1945	1184	621
<b>atom ratio 0°</b>	6.4	5.6	1.7	4.0	1.7	2.2	1.1	4.3	7.6	7.6	0.8	3.4	2.1	1.1
<b>corrected intensity 80°</b>	4201	1969	645	2432	568	1252	778	3113	6458	6458	198	791	1313	453
<b>atom ratio 80°</b>	7.2	3.4	1.1	4.2	1.0	2.2	1.3	5.4	11.1	11.1	0.3	1.4	2.3	0.8

Table S6: Quantitative analysis of the 0° and 80° emission spectra of the equimolar IL2+IL3 mixture, [C<sub>8</sub>G<sub>1</sub>Im][PF<sub>6</sub>]+[(MeO)<sub>2</sub>Im][PF<sub>6</sub>] mixture. The nominal and experimentally determined composition is given for all elements contained in the IL mixture. The ASFs are taken from ref [44].

	<b>F 1s</b> F <sub>PF6</sub>	<b>O 1s</b> O <sub>MeO</sub>	<b>N 1s</b> N <sub>MeO</sub>	<b>N 1s</b> N <sub>Im</sub>	<b>C 1s</b> C <sub>2,Im</sub>	<b>C 1s</b> C <sub>hetero,Im</sub>	<b>C 1s</b> C <sub>alkyl</sub>	<b>C 1s</b> C <sub>2,MeO</sub>	<b>C 1s</b> C <sub>hetero,MeO</sub>	<b>P 2p</b> P <sub>PF6</sub>
<b>ASF</b>	1.00	0.67	0.46	0.46	0.30	0.30	0.30	0.30	0.30	0.46
<b>nominal</b>	12	2	2	2	1	4	7	1	4	2
<b>binding energy / eV</b>	686.8	535.4	403.6	402.1	287.6	286.7	285.0	288.2	287.1	137.0
<b>corrected intensity 0°</b>	19837	2742	2843	3364	1706	6824	11943	1469	5875	3514
<b>atom ratio 0°</b>	12.2	1.7	1.8	2.1	1.1	4.2	7.4	0.9	3.6	2.2
<b>corrected intensity 80°</b>	15674	1447	1596	3631	1660	6640	20230	1151	4602	3319
<b>atom ratio 80°</b>	9.6	0.9	1.0	2.2	1.0	4.1	12.5	0.7	2.8	2.1

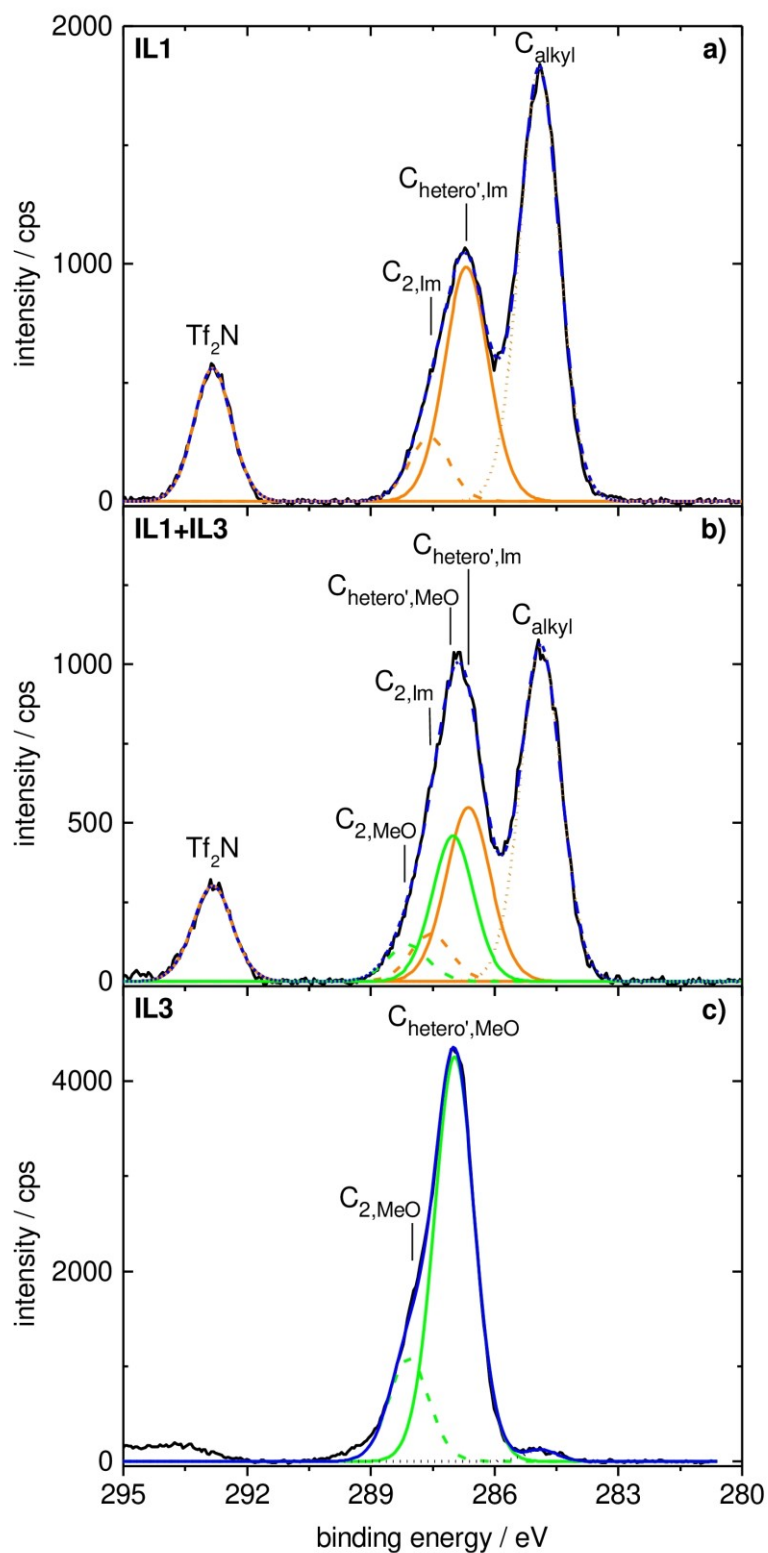


Figure S3: Fits of the C 1s spectra of a) IL1, b) equimolar IL1+IL3 mixture, and c) IL3 indicating all peaks fitted with the constraints mentioned in the Experimental Section.



### DFT calculations and charge analysis:

$[(\text{MeO})_2\text{Im}]^+$ ,  $[\text{C}_2\text{C}_2\text{Im}]^+$ , and  $[\text{Me}(\text{EG})_1\text{C}_1\text{Im}]^+$  can take on a range of structural conformers (see Figure S4). In  $[(\text{MeO})_2\text{Im}]^+$  and  $[\text{C}_2\text{C}_2\text{Im}]^+$ , the alkyl and methoxy arms can be positioned forward, backward, or perpendicular to the imidazolium ring. In  $[\text{Me}(\text{EG})_1\text{C}_1\text{Im}]^+$  the ether chain can be orientated all trans or it can wrap around such that the  $\text{O}_{\text{EG}}$  atom interacts with the H atoms of the imidazolium ring.

To ensure that all relevant conformers of  $[\text{C}_2\text{C}_2\text{Im}]^+$  and  $[(\text{MeO})_2\text{Im}]^+$  have been located, a relaxed potential energy surface (PES) has been generated by systematically varying the torsion angles  $\tau$  of the arms  $\tau(\text{C}_2\text{-N-C-C})$  in  $[\text{C}_2\text{C}_2\text{Im}]^+$  or  $\tau(\text{C}_2\text{-N-O-C})$  in  $[(\text{MeO})_2\text{Im}]^+$  allowing for the relaxation of all other internal coordinates (see Figure S5). The angles  $\tau$  have been rotated, in steps of  $10^\circ$ , through  $360^\circ$ .  $[\text{C}_2\text{C}_2\text{Im}]^+$  exhibits four minima,  $[(\text{MeO})_2\text{Im}]^+$  exhibits only two minima due to instability of the in-plane orientations of the methoxy groups. For both cations, the “up-down” conformer has the lowest energy (ground state). For  $[\text{C}_2\text{C}_2\text{Im}]^+$ , the barrier for interconversion between the minima is very low and the alkyl arms will rotate freely in solution at room temperature. For  $[(\text{MeO})_2\text{Im}]^+$ , the barriers for rotation are higher and more limited rotation is expected.

For the charge analysis we have selected the “up-down” (ground state) for both  $[\text{C}_2\text{C}_2\text{Im}]^+$  and  $[(\text{MeO})_2\text{Im}]^+$ . As the rotational profile for  $[\text{C}_2\text{C}_2\text{Im}]^+$  is shallow, we have selected the transition state “front-back (TS)” as the second conformer for charge analysis. The minimum “up-front” (+1.2 kJ/mol) has been selected as the second conformer for analysis of  $[(\text{MeO})_2\text{Im}]^+$ . Key conformer energies are reported in Table S7.

$[\text{Me}(\text{EG})_1\text{C}_1\text{Im}]^+$  with its shorter side chain is used as model for the cation of  $[\text{Me}(\text{EG})_2\text{C}_1\text{Im}][\text{Tf}_2\text{N}]$  (IL4). The ether chain of  $[\text{Me}(\text{EG})_1\text{C}_1\text{Im}]^+$  can take a range of orientations, the two key torsion angles are  $\tau_1=\tau(\text{C}_2\text{-N-C-C})$  and  $\tau_2=\tau(\text{N-C-C-O})$ ; relaxed PESs for these angles are shown in Figure S6. Note the significantly different vertical energy scales between the PESs of Figure S5 and S6. The gauche geometries, with the ether chain rotated to interact with the imidazolium ring, are substantially more stable than the planar linear trans conformers. However, in solution it is anticipated that the ether chains can associate with adjacent cation molecules, and thus, planar linear conformations will be stabilized. Hence, both the gauche “folded” and trans “linear” conformers have been selected for charge analysis. Key conformer energies are reported in Table S8.

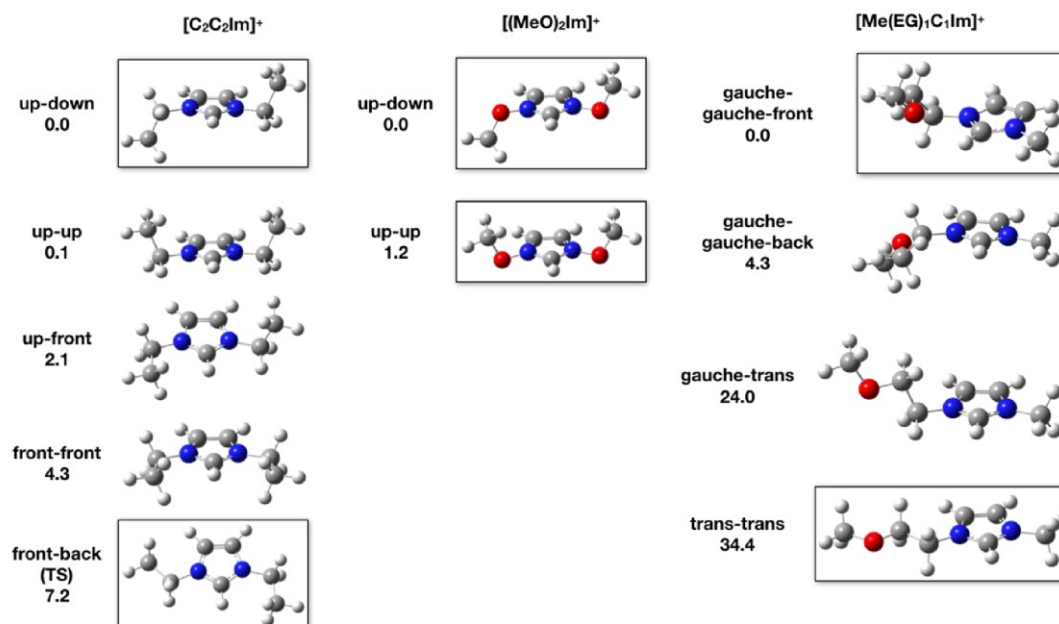


Figure S4: Optimized conformers of  $[\text{C}_2\text{C}_2\text{Im}]^+$ ,  $[(\text{MeO})_2\text{Im}]^+$ , and  $[\text{Me}(\text{EG})_1\text{C}_1\text{Im}]^+$  (energies in kJ/mol relative to the lowest-energy ground state); “boxed” conformers are those selected for charge analysis.

Table S7: Critical point energies in kJ/mol for  $[(\text{MeO})_2\text{Im}]^+$  and  $[\text{C}_2\text{C}_2\text{Im}]^+$ , \* indicates a transition state structure, - indicates no critical point was located. Bold values indicate states of the discussed NBO and ChelpG analysis.

	$[(\text{MeO})_2\text{Im}]^+$	$[\text{C}_2\text{C}_2\text{Im}]^+$
up-down	<b>0.0</b>	<b>0.0</b>
up-front	10.2*	2.1
up-up	<b>1.2</b>	0.1
front-front	-	4.3
up-back	9.2*	5.0*
front-back	-	<b>7.1*</b>

Table S8: Critical point energies in kJ/mol for  $[\text{Me}(\text{EG})_1\text{C}_1\text{Im}]^+$  for the different conformers analyzed (torsion angles are also shown). Bold values indicate states of the discussed NBO and ChelpG analysis.

	$\tau_1, \tau_2$ ( $^\circ$ )	$[\text{Me}(\text{EG})_1\text{C}_1\text{Im}]^+$
gauche-gauche-front	61, -66	<b>0.0</b>
gauche-gauche-back	-117, -64	4.3
gauche-trans	99, 180	24.0
trans-trans	180, 180	<b>34.4</b>

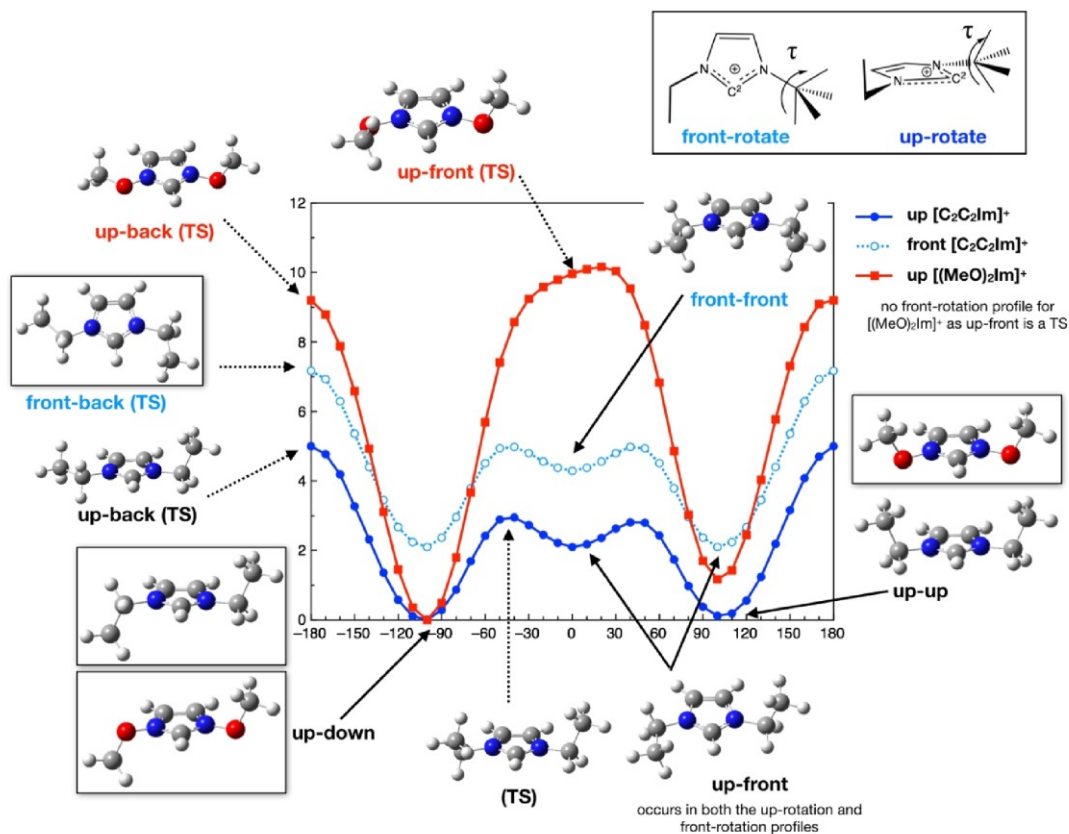


Figure S5: Relaxed scan of the alkyl/methoxy chain rotational potential energy surfaces, energy in kJ/mol.

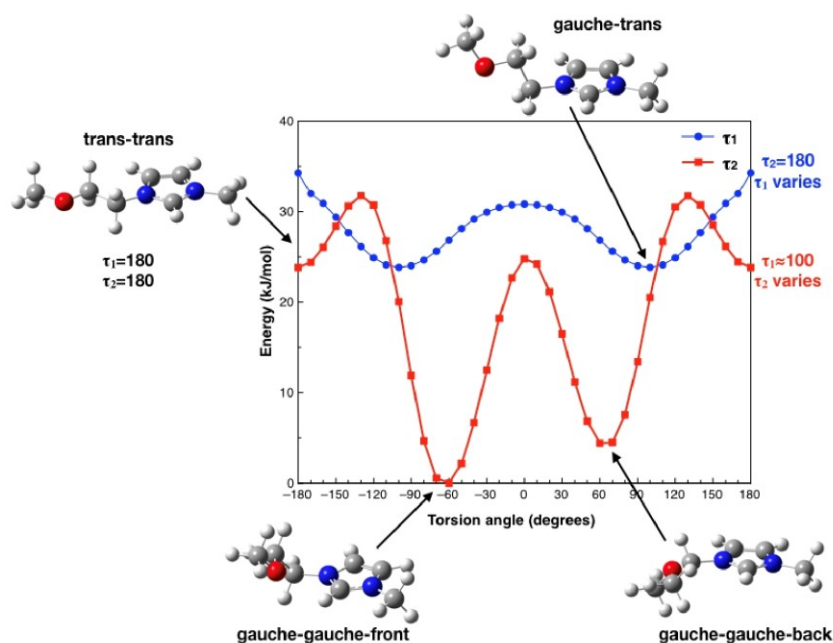
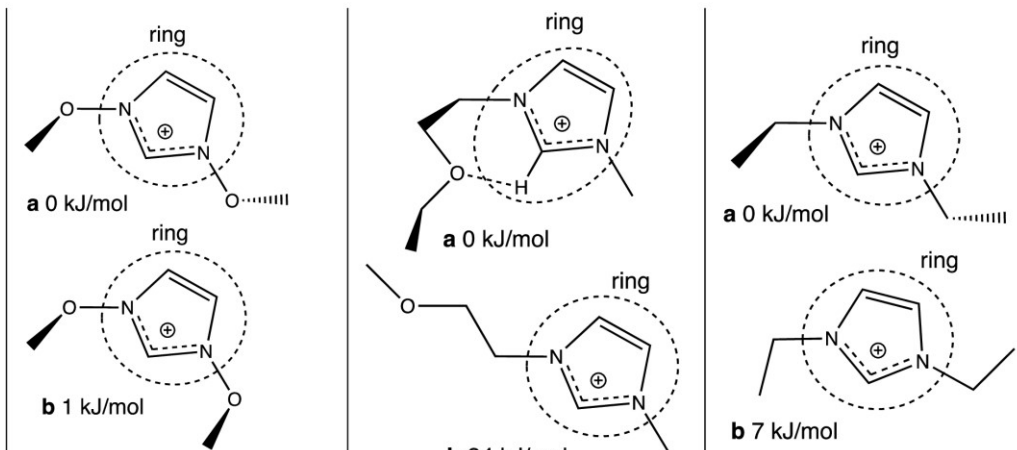


Figure S6: Relaxed scan for  $[\text{Me}(\text{EG})_1\text{C}_1\text{Im}]^+$   $\tau_1 = \tau(\text{C}_2\text{-N-C-C})$  and  $\tau_2 = \tau(\text{N-C-C-O})$  angles, energy in kJ/mol.

Initial results from the NBO and ChelpG charge analysis are summarized in Table S9. The significantly different structures yield qualitatively similar results. Note that the maximum difference in the oxygen atom charges from  $[(\text{MeO})_2\text{Im}]^+$  to  $[\text{Me}(\text{EG})_1\text{C}_1\text{Im}]^+$  is more pronounced in the NBO analysis compared to the ChelpG analysis (NBO: +0.25 e vs. ChelpG: +0.13 e). NBO is known to produce larger charge polarization than ChelpG. The ChelpG charges are based on the external potential while the NBO charges are based on the electron density close to the atomic center. Thus, conceptually, the NBO method represents changes close to the nucleus, and thus, is expected to better reflect the core level orbitals probed by XPS. Nevertheless, charge analysis models should be considered as qualitative rather than quantitative; notably, in our analysis here, the two methods are qualitatively consistent. A visual representation NBO charges are depicted in Figure S7, where atoms are color coded on a scale from bright blue for negative through white (for neutral) to bright red for positive charge.

Table S9: NBO and ChelpG (in brackets) partial charge values in units of the elementary charge  $e$  for key atoms and groups, carried out for the conformers marked in Figure S4.



	$[(\text{MeO})_2\text{Im}]^+$		$[\text{Me}(\text{EG})_1\text{C}_1\text{Im}]^+$		$[\text{C}_2\text{C}_2\text{Im}]^+$	
	<b>a</b> up-down	<b>b</b> up-up	<b>a</b>	<b>b</b>	<b>a</b> up-down	<b>b</b> front-back (TS)
<b>N</b>	-0.02 (+0.29)	-0.02 (+0.28)	-0.34 (+0.15)	-0.33 (+0.14)	-0.35 (+0.06)	-0.34 (+0.06)
<b>O</b>	-0.35 (-0.28)	-0.35 (-0.25)	-0.60 (-0.32)	-0.57 (-0.38)	-	-
<b>ring</b>	+0.93 (+0.92)	+0.93 (+0.92)	+0.34 (+0.57)	+0.34 (+0.56)	+0.31 (+0.46)	+0.32 (+0.43)

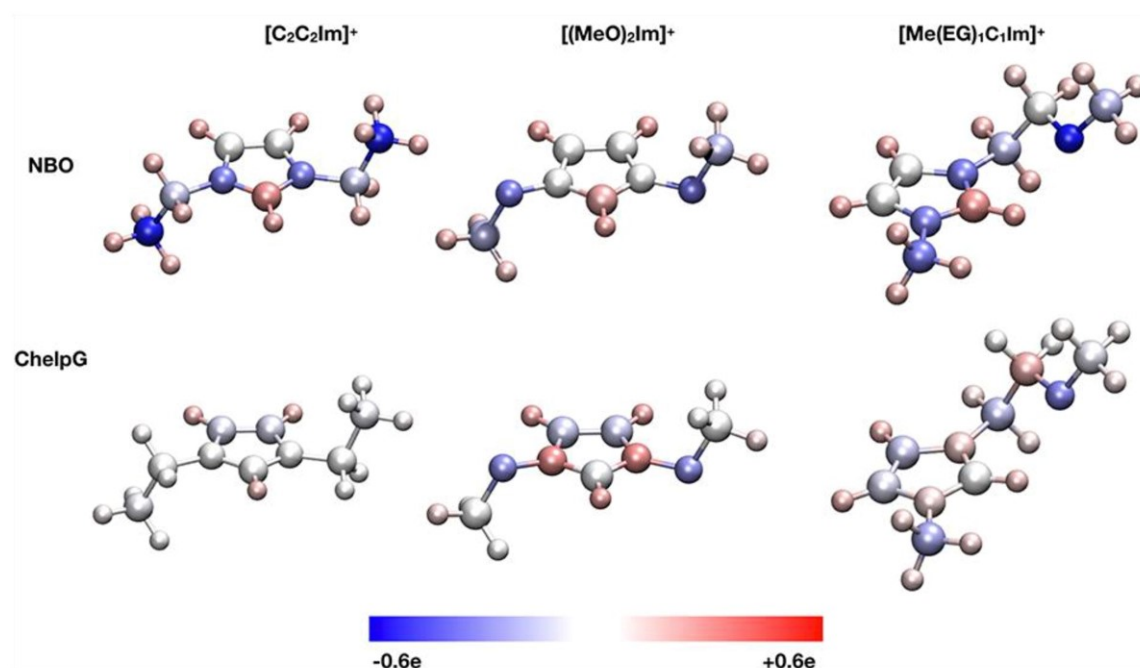


Figure S7: Pictorial representation of charge distribution in the lowest energy conformers of  $[\text{C}_2\text{C}_2\text{Im}]^+$ ,  $[(\text{MeO})_2\text{Im}]^+$ , and  $[\text{Me}(\text{EG})_1\text{C}_1\text{Im}]^+$  with color ranging from bright blue ( $-0.6\text{ e}$ ) through white (neutral) to bright red ( $+0.6\text{ e}$ ).

#### *Discussion of the NBO vs. the ChelpG charge analysis methods.*

While the results of the NBO and ChelpG analysis are both termed "charges" they report on different aspects of the electronic structure. The NBO method identifies the localized electron density at atomic sites. The ChelpG method, in contrast, is based on the electrostatic potential (ESP) far from the atoms (evaluated beyond the van der Waals radius). While fitted trends may show a good correlation with both NBO and ChelpG there are concerns with the ChelpG charges which lead us to focus primarily on the NBO charges. There are three reasons why the ChelpG charges have not been the focus of attention: concerns with the physical underpinning of the ChelpG analysis, concerns that charges are unreliable for buried atoms using the ChelpG analysis and concerns regarding the conformer dependence of ChelpG charges. Each of these is discussed further below.

#### *Concerns with the physical underpinning of the ChelpG analysis*

The charge obtained from fitting an ESP close to atomic centers is unreliable, this is why the ESP data points are taken from beyond the van der Waals radii of the atoms. However, the XPS technique employed here is probing the core orbitals of an atom. Thus, the influence of these states on the ESP is strongly shielded. The NBO method is a localized method, which explicitly includes core electron density. Thus, while fitted trends may show a good

correlation with both NBO and ChelpG there is a more robust physical basis for the correlation of the NBO charges with the experimental data.

*Concerns with the "buried atom" conformation of the ChelpG analysis*

Based on previous studies comparing XPS spectra to ChelpG charges, significant conformer dependence was determined for conformers with the charge-bearing atom buried or exposed within an IL ion-pair. In the documented case, a S atom showed a conformer-based charge variation of 0.5e.<sup>[1]</sup> The NBO charges were established as more reliable in this respect. Thus, while the ChelpG charges for the trans  $[\text{Me}(\text{EG})_1\text{C}_1\text{Im}]^+$  conformer can be considered reasonably reliable, those for the internal H-bonding gauche  $[\text{Me}(\text{EG})_1\text{C}_1\text{Im}]^+$  conformer (with the buried O atom) cannot be considered as reliable, weakening the possibility that the lower charge is physically reasonable.

*A choice made on which conformers to focus upon in the analysis*

The NBO and ChelpG charges for the lowest energy conformers of N-O-Me oxygen (-0.35 e, -0.28 e) vs. those for N-CH<sub>2</sub>-CH<sub>2</sub>-O-Me oxygen (-0.60 e, -0.32 e) exhibit a difference of (-0.25 e, -0.04 e). However, we do not believe this is the best comparison to make. Conformer **b** for  $[(\text{MeO})_2\text{Im}]^+$  is essentially iso-energetic with conformer **a** at the level of theory applied. Both conformers can be expected to be present at the same concentration, thus, taking the average charge between these two conformers is reasonable. Thus, for N-O-Me, the average charges on oxygen in  $[(\text{MeO})_2\text{Im}]^+$  to be considered are -0.35 (NBO) and -0.27 e (ChelpG).

Internal H-bonding is expected to be maximized for the isolated  $[\text{Me}(\text{EG})_1\text{C}_1\text{Im}]^+$  cations, however, this is not expected in a liquid environment: The O atom can H-bond with other cations and the imidazolium C<sub>2</sub>-H can associate with the anion. Moreover, alkyl chain aggregation can be expected as nano-scale domains are well known to form in ILs; computed rotational profiles for the ethylene-glycol arm indicated movement was accessible at room temperature. Hence, we did not expect the internal H-bonding gauche  $[\text{Me}(\text{EG})_1\text{C}_1\text{Im}]^+$  cation to predominate in the IL, rather the trans-conformer **b** will be of increased importance. Thus, for  $[\text{Me}(\text{EG})_1\text{C}_1\text{Im}]^+$ , the charges to be considered are -0.59 (NBO) and -0.35 e (ChelpG) where 0.35 e is the average of the gauche and trans conformer charges of -0.32 and -0.38 e, respectively.

Given the assumptions made above, the NBO and ChelpG average charges for N-O-Me oxygen (-0.35 e, -0.27 e) in  $[(\text{MeO})_2\text{Im}]^+$  vs. those for N-CH<sub>2</sub>-CH<sub>2</sub>-O-Me in  $[\text{Me}(\text{EG})_1\text{C}_1\text{Im}]^+$  (-0.57 e, -0.35 e) exhibit a difference of -0.22 and -0.08 e. NBO charges are known to be more "polarized" than ChelpG charges which is reflected in the results obtained here. Nevertheless, the *qualitative trend* is that the charge on the oxygen atoms of  $[(\text{MeO})_2\text{Im}]^+$  is

less negative than for  $[\text{Me}(\text{EG})_1\text{C}_1\text{Im}]^+$ . This qualitative interpretation is strengthened by the strong difference observed in XPS binding energies.

To further investigate environmental effects, "buried charge" and conformer dependence, additional supporting calculations have been carried out.

To extend the ion gas phase calculations, a continuum solvation model for ILs introduced by Bernales and co-workers, that is, the so-called "generic ionic liquid solvation model based on density" (GIL-SMD),<sup>[1]</sup> has been employed. Each of the gas-phase optimized cations discussed above has been placed into the continuum medium and evaluated. Where available, values specific to the  $[\text{PF}_6]^-$  anion have been used (i.e. beta value, number of halogen atoms); the specific GIL-SMD parameters employed are:  $\text{eps} = 11.50$ ,  $\text{epsinf} = 2.0449$ ,  $\text{SurfaceTensionAtInterface} = 61.24$ ,  $\text{HBondAcidity} = 0.229$ ,  $\text{HBondBasicity} = 0.265$ ,  $\text{CarbonAromaticity} = 0.188$ ,  $\text{ElectronegativeHalogenicity} = 0.375$ . For details on the GIL-SMD, and parameter definitions see ref [1].

Moreover, gas-phase calculations were carried out on isolated cation- $[\text{PF}_6]^-$  ion pairs for all three imidazolium cations. The lowest energy cation conformers with  $[\text{PF}_6]^-$  placed in the front and top positions (known lowest energy conformers for imidazolium based ILs) have been sampled. Typically, the larger and more diffuse the anion, the more pronounced the preference for the anion-pi "top" conformer over the H-bonding "front in-plane" interaction. For each cation investigated here,  $[\text{PF}_6]^-$  was found to be unstable in the front position, and the ion-pair structures optimized to  $[\text{PF}_6]^-$  in a top position. Final low-energy structures are depicted in Figure S8.

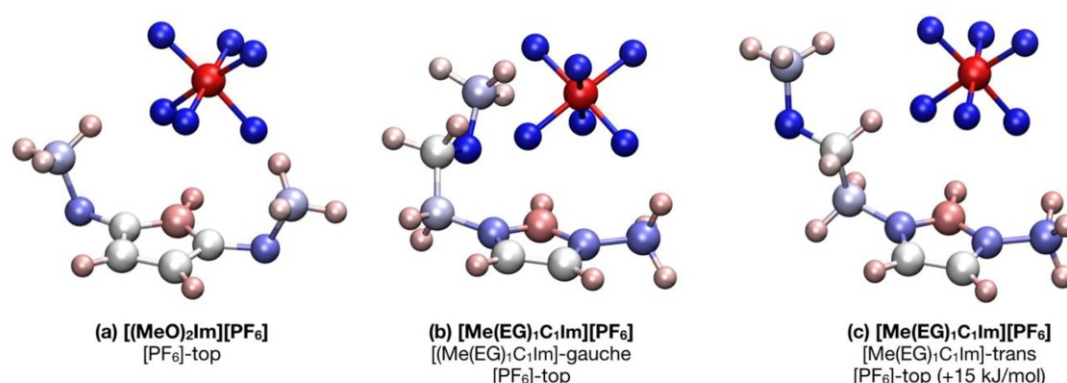


Figure S8: A color mapped representation of the NBO charges for (a)  $[(\text{MeO})_2\text{Im}][\text{PF}_6]$  (b) gauche- $[\text{Me}(\text{EG})_1\text{C}_1\text{Im}][\text{PF}_6]$  and (c) trans- $[\text{Me}(\text{EG})_1\text{C}_1\text{Im}][\text{PF}_6]$ . Color scale is bright red (+0.6 e) through white to bright blue (-0.6 e).

The NBO (ChelpG) charges on the oxygen atoms for the gas-phase, GIL-SMD, and explicit ion-pair calculations are given in Table S10. The NBO charge varies very little between the different conformers, if a continuum solvation environment is included or not, or if explicit ion-pairs are considered or not. The ChelpG charges show a tendency to move towards more negative values on going from the gas phase, through continuum solvation, to explicit ion-pairing. Thus, the more sophisticated calculations (employing an SMD or ion-pair model) add additional support to the gas-phase based conclusion that the charge of the oxygen atoms is more negative in  $[\text{Me}(\text{EG})_1\text{C}_1\text{Im}]^+$  compared to  $[(\text{MeO})_2\text{Im}]^+$ .

Table S10: Oxygen atom partial charges in units of  $e$  derived from NBO (in brackets: ChelpG charges) of the isolated cations in the gas-phase, of the cations in the continuum solvation environment (GIL-SMD), and of the ion pairs in the gas phase; values are given for the most-relevant configurations.

O charge NBO (ChelpG)	gas-phase	GIL-SMD	ion-pair $[\text{PF}_6]^-$
$[(\text{MeO})_2\text{Im}]^+$	-0.35 (-0.28)	-0.37 (-0.32)	-0.36 (-0.32)
$[\text{Me}(\text{EG})_1\text{C}_1\text{Im}]^+$ trans	-0.57 (-0.38)	-0.59 (-0.43)	-0.58 (-0.48)
$[\text{Me}(\text{EG})_1\text{C}_1\text{Im}]^+$ gauche	-0.60 (-0.32)	-0.61 (-0.34)	-0.60 (-0.47)

- [1] V. S. Bernales, A. V. Marenich, R. Contreras, C. J. Cramer and D. G. Truhlar, *J. Phys. Chem. B*, 2012, **116**, 9122–9129.



## Ionic Liquids

# Temperature-Dependent Surface Enrichment Effects in Binary Mixtures of Fluorinated and Non-Fluorinated Ionic Liquids

Bettina S. J. Heller,<sup>[a]</sup> Matthias Lexow,<sup>[a]</sup> Francesco Greco,<sup>[a]</sup> Sunghwan Shin,<sup>[a]</sup> Gabriel Partl,<sup>[b]</sup> Florian Maier,<sup>[a]</sup> and Hans-Peter Steinrück\*<sup>[a]</sup>

**Abstract:** Using angle-resolved X-ray photoelectron spectroscopy (ARXPS), we investigate the topmost nanometers of various binary ionic liquid (IL) mixtures at different temperatures in the liquid state. The mixtures consist of ILs with the same  $[\text{PF}_6]^-$  anion but two different cations, namely 3-methyl-1-(3,3,4,4,4-pentafluorobutyl)imidazolium hexafluorophosphate,  $[\text{PFBMIm}][\text{PF}_6]$ , and 1-butyl-3-methylimidazolium hexafluorophosphate,  $[\text{C}_4\text{C}_1\text{Im}][\text{PF}_6]$ , with 10, 25, 50 and 75 mol% content of  $[\text{PFBMIm}][\text{PF}_6]$ . We observe a preferential enrichment of the fluorinated chain in the topmost layer,

relative to the bulk composition, which is most pronounced for the lowest content of  $[\text{PFBMIm}][\text{PF}_6]$ . Upon cooling the mixtures stepwise from 95 °C until surface charging effects in XPS indicate solidification, we observe a pronounced increase in surface enrichment of the fluorinated chain with decreasing temperature in the liquid state. In contrast to the mixtures with lower  $[\text{PFBMIm}][\text{PF}_6]$  contents, cooling the 75 mol% mixture additionally shows an abrupt decrease of the fluorinated chain signal before complete solidification occurs, which is assigned to partial precipitation effects.

## Introduction

Ionic liquids (ILs) carrying fluorinated alkyl chains, in the following called fluorinated ILs, represent an interesting class of ILs because they often exhibit unique properties such as high thermal and chemical stability, and high gas solubility. Moreover, they commonly show low surface tension and/or are chemically and biologically inert.<sup>[1]</sup> Therefore, they are potential candidates to substitute fluorinated organic compounds in different applications, for example, as surfactants, gas absorbents, lubricants and refrigerants.<sup>[1a,2]</sup> It has also been shown that fluorinated ILs can be used as gas carriers,<sup>[1a,d]</sup> electrolytes in fuel and solar cells, and in lithium batteries,<sup>[1b,2,3]</sup> in catalysis<sup>[2,4]</sup> and in many more applications.

While non-fluorinated ILs are known to form bulk nanostructures consisting of polar and nonpolar domains, fluorinated ILs

typically exhibit additional nonpolar fluorinated domains, in which the fluorinated chains preferentially agglomerate.<sup>[1a-c,5]</sup> Alkylated and fluorinated chains can be present either in one single IL (e.g. alkyl chains in the cation and fluorinated chains in the anion or vice versa<sup>[1b]</sup>), or in IL mixtures with one IL containing alkyl chains and the other one containing fluorinated chains. Changing the relative chain length in one IL or the molar ratio of the two ILs in the mixture influences the related properties and the domain structure.<sup>[5,6]</sup> It should be emphasized that using IL mixtures allows for fine-tuning the properties in a very subtle way. Applying IL mixtures instead of using one neat IL becomes even more beneficial in the context of the European chemical registration process REACH: If one could achieve specific properties by employing adequate mixtures of pre-registered ILs instead of synthesizing a new task-specific IL, a lengthy and costly registration process could be avoided. The enormous effort to register a new chemical is demonstrated by the fact that among the many ILs synthesized today, as of June 2019 only eight ILs based on the standard 1-ethyl-3-methylimidazolium cation (see Table S1 in the Supporting Information) have been approved by REACH and only about six further imidazolium salts with melting points below 100 °C have been registered.<sup>[7]</sup>

Many investigations have been carried out in the last decades on IL mixtures and their composition-dependent physico-chemical bulk properties such as viscosity, thermal behavior, density and molar volume, conductivity, solvation abilities, influence on chemical reactivity as well as bulk microscopic structure (e.g., see reviews in Ref. [8] and references therein, and Ref. [9]). In contrast, much less studies are available on the surface properties of IL mixtures, despite the fact that the composition of the topmost layers can differ considerably from the

[a] B. S. J. Heller, M. Lexow, F. Greco, Dr. S. Shin, Dr. F. Maier, Prof. Dr. H.-P. Steinrück  
Lehrstuhl für Physikalische Chemie II  
Friedrich-Alexander-Universität Erlangen-Nürnberg, Egerlandstraße 3, 91058 Erlangen (Germany)  
E-mail: hans-peter.steinrueck@fau.de

[b] Dr. G. Partl  
Institut für Allgemeine, Anorganische und Theoretische Chemie  
Leopold-Franzens-Universität Innsbruck  
Innrain 80–82, 6020 Innsbruck (Austria)

Supporting information and the ORCID identification number(s) for the author(s) of this article can be found under:  
<https://doi.org/10.1002/chem.201904438>.

© 2019 The Authors. Published by Wiley-VCH Verlag GmbH & Co. KGaA. This is an open access article under the terms of the Creative Commons Attribution License, which permits use, distribution and reproduction in any medium, provided the original work is properly cited.

bulk composition.<sup>[6,8b,10]</sup> In many of the aforementioned applications, particularly those involving systems where a thin IL film coats a high surface area support, the surface, that is, the IL/vacuum(gas) interface plays an important role for the overall performance. Therefore, investigations of the topmost layers of IL mixtures are getting more into the focus of research. A variety of studies has been performed, using reactive-atom scattering with laser-induced fluorescence detection (RAS-LIF),<sup>[6a,c]</sup> neutron scattering,<sup>[6c]</sup> small-angle X-ray scattering<sup>[6c]</sup> and X-ray reflectivity,<sup>[11]</sup> time of flight secondary ion mass spectrometry (TOF-SIMS),<sup>[12]</sup> Rutherford backscattering spectroscopy (RBS),<sup>[12a,13]</sup> low-energy ion scattering (LEIS),<sup>[14]</sup> X-ray photoelectron spectroscopy (XPS)<sup>[6b,10a,15]</sup> and molecular dynamics (MD) simulations.<sup>[1b,5-6,13b,16]</sup>

Surface studies of ILs with both alkylated and fluorinated chains are quite rare. In case of neat ILs, Luis et al.<sup>[1b]</sup> recently measured the surface tension of  $[C_nC_1\text{Im}][C_4F_9SO_3]$  ( $[C_4F_9SO_3]$  = perfluorobutanesulfonate) with alkyl chain lengths  $n=2, 4, 6, 8, 10$  and  $12$ , and correlated the derived values with MD simulations. The latter revealed that for cations with less than four carbon atoms in the alkyl chain, the outer surface is dominated by the presence of the fluorinated butyl chains of the anion, with the polar head groups preferentially forming a confined sub-surface layer. Longer alkyl chains ( $n > 4$ ) start to penetrate the fluorinated surface layer pushing the polar head groups of the anion and cation even further away from the outer surface. These findings are in line with the decrease in measured surface tension of the ILs up to  $n=8$ , where a maximum number of both fluorinated and alkylated chains (and a minimum number of polar head groups) are present at the outer surface. For even longer alkyl chains ( $n > 8$ ), the surface tension increases again due to the fact that the longer alkyl chains dominate the outer surface, as evidenced by MD simulations.

In the case of  $[C_6C_n\text{Im}]_{1-x}[C_6C_n\text{ImF}_3]_x[\text{TF}_2\text{N}]$  mixtures, RAS-LIF measurements performed by Smoll et al.<sup>[6a]</sup> showed that the fluorinated chain is again preferentially enriched at the surface. By investigating different stoichiometries, they found a large surface excess of the fluorinated chains compared to the nominal bulk composition, particularly at the lowest mole fraction of the fluorinated IL.

In this study, we present a detailed angle-resolved XPS (ARXPS) study under clean ultra-high vacuum (UHV) conditions on neat  $[\text{PFBMIm}][\text{PF}_6]$  and  $[\text{C}_4\text{C}_1\text{Im}][\text{PF}_6]$  (see Figure 1), and mixtures thereof in four molar ratios (10, 25, 50 and 75 mol %). Both ILs are comprised of the same hexafluorophosphate ( $[\text{PF}_6]^-$ ) anion and similar imidazolium-based cations. In

$[\text{C}_4\text{C}_1\text{Im}]^+$ , the butyl chain is fully hydrogenated, and in  $[\text{PFBMIm}]^+$  its terminal ethyl moiety is fluorinated. We analyzed the temperature dependence of the surface composition upon cooling from  $95^\circ\text{C}$ , where all mixtures are in their liquid state, until their solidification. We observe a very pronounced surface enrichment of the fluorinated  $[\text{PFBMIm}]^+$  chains relative to the bulk composition, which increases with decreasing temperature and decreasing mole fraction of  $[\text{PFBMIm}][\text{PF}_6]$ .

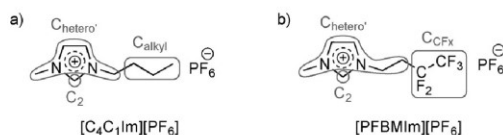
## Experimental Section

Materials:  $[\text{C}_4\text{C}_1\text{Im}][\text{PF}_6]$  was purchased from Iolitec (purity 99.5%). The synthesis of  $[\text{PFBMIm}][\text{PF}_6]$  has been reported before.<sup>[17]</sup> All neat ILs investigated in this study were used as supplied. To prepare the IL mixtures, acetonitrile (Sigma-Aldrich, purity 99.8%) was used as a co-solvent to ensure proper mixing of the ILs. For the ARXPS measurements of the neat ILs and the mixtures, a layer of up to 0.5 mm thickness was prepared on a molybdenum sample holder reservoir. Subsequently, the sample holder was placed into the load-lock of our vacuum chamber and degassed for at least twelve hours.

Angle-resolved X-ray photoelectron spectroscopy (ARXPS): The ARXPS experiments were performed in our DASSA (Dual Analyzer System for Surface Analysis) setup, for details see Ref. [18]. Simultaneous acquisition of ARXP spectra at two fixed emission angles of  $\vartheta=0^\circ$  (normal emission) and  $80^\circ$  (grazing emission) with respect to the surface normal of a horizontally mounted sample was achieved by two hemispherical energy analyzers (ARGUS-type). This reduces the total measurement time and thus the exposure of the sample to X-rays by a factor of two, which in turn minimizes radiation damage. Furthermore, the spectra at  $0^\circ$  and  $80^\circ$  correspond to the sample under exactly identical conditions. A monochromated X-ray source with Al  $K_{\alpha}$  radiation (XM 1000,  $h\nu=1486.6$  eV, 238 W) was used as X-ray source. Survey scans were recorded with a pass energy of 150 eV and region scans with 35 eV; for the latter, the overall energy resolution is 0.4 eV. The binding energy scale was referenced to the Fermi level of Au.

In organic matter, the information depth of photoelectrons after excitation with Al  $K_{\alpha}$  radiation at  $0^\circ$  is 7 to 9 nm (depending on the kinetic energy). At  $80^\circ$ , it decreases to 1.0 to 1.5 nm, making the measurement very surface sensitive:  $\approx 80\%$  of the signal originates from the topmost molecular layer. Each set of  $80^\circ$  spectra was scaled up by an individual geometry factor to compensate for lower intensity compared to  $0^\circ$  spectra.<sup>[18]</sup> After this normalization, intensity differences between  $80^\circ$  and  $0^\circ$  emission angle directly reflect a higher/lower concentration of the respective species at the surface than in the bulk. This allows us to reveal surface enrichment and molecular orientation effects.

For the quantitative analysis of the spectra, we used atomic sensitivity factors (ASFs).<sup>[18]</sup> As the C 1s signal from the  $\text{CF}_3$  group of the  $[\text{PFBMIm}]^+$  cation overlaps with the shake-up of the aromatic system of the cation, the intensity of this peak is set equal to that of the  $\text{CF}_2$  peak. CasaXPS (version 2.3.16) was used for subtracting the background and for peak fitting (pseudo-Voigt function with 30% Lorentzian contribution). In the F 1s, N 1s and P 2p spectra, a two-point linear background was subtracted, whereas a three-point linear background was used for the C 1s spectra. The P 2p signal is composed of the spin-orbit-split  $2p_{1/2}$  and  $2p_{3/2}$  components, which have the same full width at half maximum (FWHM), are separated by 0.9 eV, and have an area ratio of 1:2. The FWHM of the F 1s peaks of the  $\text{CF}_x$  groups ( $x=2$  and  $3$ ) and the  $[\text{PF}_6]^-$



**Figure 1.** Molecular structures of a) 1-butyl-3-methylimidazolium hexafluorophosphate,  $[\text{C}_4\text{C}_1\text{Im}][\text{PF}_6]$ , and b) 3-methyl-1-(3,3,4,4,4-pentafluorobutyl)imidazolium hexafluorophosphate,  $[\text{PFBMIm}][\text{PF}_6]$ , including the denotation of the carbon atoms,  $\text{C}_2$ ,  $\text{C}_{\text{hetero}}$ ,  $\text{C}_{\text{alkyl}}$  and  $\text{C}_{\text{CF}_x}$  in gray.

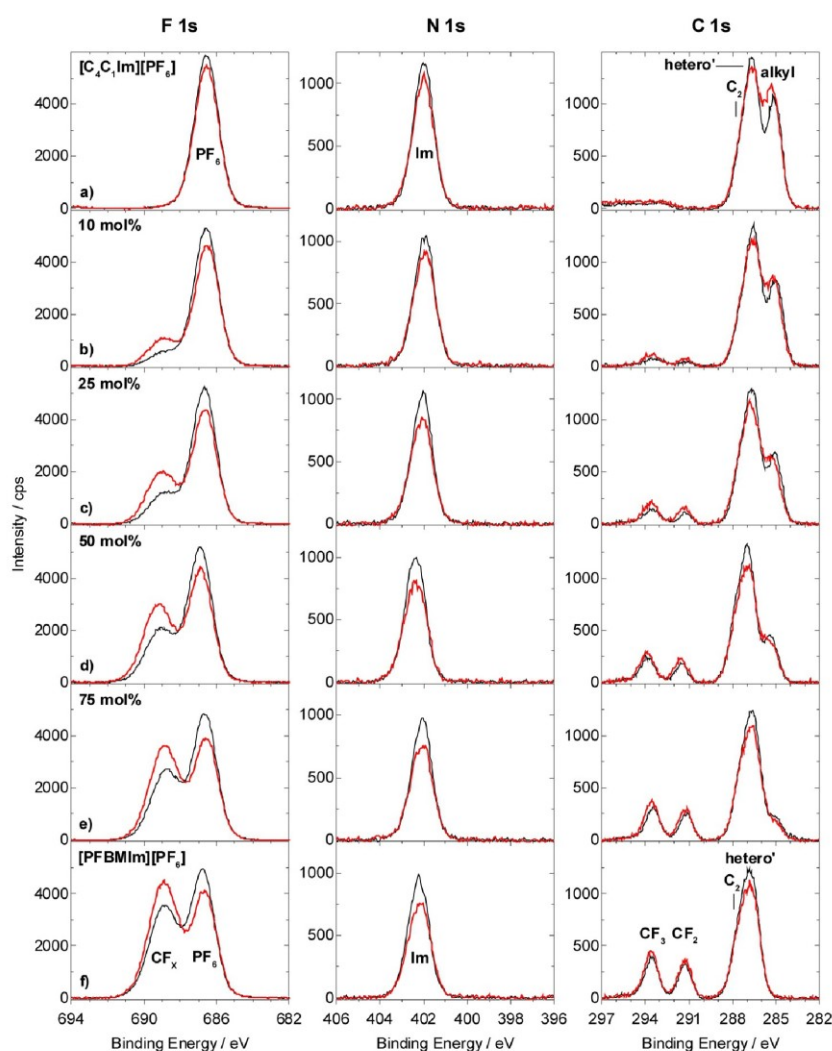
anions are  $1.94 \pm 0.1$  and  $1.47 \pm 0.1$  eV, respectively. For the C 1s peaks (see Figure 1 for nomenclature), the following constraints were applied: For neat [PFBMIm][PF<sub>6</sub>] and for the mixtures, C<sub>hetero'</sub> is 1.33 times wider than C<sub>2</sub> and these two peaks are separated by 1.02 eV; for neat [C<sub>4</sub>C<sub>1</sub>Im][PF<sub>6</sub>], C<sub>2</sub> and C<sub>hetero'</sub> are separated by 0.9 eV, and the FWHM of the C<sub>hetero'</sub> and C<sub>alkyl</sub> peaks is set to 1.1 and 1.11 times that of C<sub>2</sub>, respectively.

The sample temperature was measured with a type K thermocouple attached to the molybdenum sample reservoir with an accuracy of  $\pm 5$  °C, and a stability of  $\pm 1$  °C.<sup>[19]</sup>

## Results and Discussion

We investigated various mixtures of 3-methyl-1-(3,3,4,4,4-pentafluorobutyl)imidazolium hexafluorophosphate,

[PFBMIm][PF<sub>6</sub>], and 1-butyl-3-methylimidazolium hexafluorophosphate, [C<sub>4</sub>C<sub>1</sub>Im][PF<sub>6</sub>], (see Figure 1 for structures) by temperature-dependent ARXPS. The two ILs have different cations but the same anion, [PF<sub>6</sub>]<sup>-</sup>. Apart from the neat ILs, the mixtures with molar ratios of 10, 25, 50 and 75 mol% of [PFBMIm][PF<sub>6</sub>] were studied. In the following, we first present the data for the two neat ILs and the mixtures at 95 °C. At this temperature, all ILs and mixtures are liquid (the glass transition temperature of [C<sub>4</sub>C<sub>1</sub>Im][PF<sub>6</sub>] is  $-77$  °C<sup>[20]</sup> and the melting point of [PFBMIm][PF<sub>6</sub>] is  $66$  °C<sup>[17]</sup>). We restricted our investigations to 95 °C and below because of a rise in background pressure to above  $5 \times 10^{-9}$  mbar at higher temperatures. Thereafter, we discuss their temperature-dependent behavior. In all figures, the spectra in black correspond to an emission angle of 0°, and the red spectra to 80°.



**Figure 2.** F 1s (left), N 1s (center) and C 1s (right) spectra, at 0° (black) and 80° (red) emission: a) Neat [C<sub>4</sub>C<sub>1</sub>Im][PF<sub>6</sub>], b)–e) mixtures of [PFBMIm][PF<sub>6</sub>] with [C<sub>4</sub>C<sub>1</sub>Im][PF<sub>6</sub>] at molar ratios of b) 10 mol% [PFBMIm][PF<sub>6</sub>], c) 25 mol% [PFBMIm][PF<sub>6</sub>], d) 50 mol% [PFBMIm][PF<sub>6</sub>] and e) 75 mol% [PFBMIm][PF<sub>6</sub>], and f) neat [PFBMIm][PF<sub>6</sub>]. All spectra were acquired at a sample temperature of 95 °C.

### Neat $[C_4C_1Im][PF_6]$

In Figure 2a, the  $0^\circ$  emission XP spectra of  $[C_4C_1Im][PF_6]$  are depicted, for a temperature of  $95^\circ C$ . The F 1s spectrum (left panel) shows the  $F_{PF_6}$  peak of the  $[PF_6]^-$  anion at 686.6 eV. The single peak in the N 1s region (center panel) at 402.0 eV is assigned to the imidazolium nitrogen atoms,  $N_{Im}$ . In the C 1s spectrum (right panel), the  $C_{alkyl}$  peak at lowest binding energy of  $\approx 285$  eV stems from the three alkyl carbon atoms only bound to hydrogen and carbon atoms, and the peak at higher binding energy consists of two contributions: The smaller  $C_2$  peak at 287.5 eV is due to the carbon atom bound to two nitrogen atoms, and the  $C_{hetero}$  peak at 286.6 eV due to carbon atoms bound to one nitrogen atom. In the P 2p region (see Figure S1a in the Supporting Information), the unresolved spin-orbit peaks of the phosphorus atom of the  $[PF_6]^-$  anion are centered at 136.9 eV. Notably, no signals of possible surface-active contaminations<sup>[21]</sup> from the synthesis are observed in the O 1s and Si 2p region (see Figure S1a in the Supporting Information), confirming the purity of  $[C_4C_1Im][PF_6]$ . Within the margin of error ( $\pm 10\%$ ), the quantitative analysis at  $0^\circ$  agrees very well with the nominal composition of  $[C_4C_1Im][PF_6]$  (see Table 1 a).

When comparing the  $80^\circ$  (red) and  $0^\circ$  (black) emission spectra of  $[C_4C_1Im][PF_6]$  in Figure 2a, we find a slight increase of the  $C_{alkyl}$  signal at  $80^\circ$ , indicating a slight enrichment of the butyl chain at the IL/vacuum interface. Such an enrichment is generally known in literature for non-functionalized  $[C_nC_1Im]^+$  cations with alkyl chains with  $n \geq 4$ .<sup>[22]</sup> In line with this enrichment, we find a decrease of the  $F_{PF_6}$  and  $N_{Im}$  signals at  $80^\circ$ , indicating a slight depletion of the  $[PF_6]^-$  anion and the imidazolium ring of the cation from the IL/vacuum interface.

### Neat $[PFBMIm][PF_6]$

The XP spectra of  $[PFBMIm][PF_6]$  are depicted in Figure 2 f. We recently investigated ultrathin layers of this IL on a Ag(111) surface in the monolayer range, using a non-monochromated  $AlK_\alpha$  X-ray source in another XP setup.<sup>[17]</sup> In the following, we now present the high-resolution spectra of a thick film.

At  $0^\circ$  emission (black spectrum), the F 1s spectrum (left panel) displays two peaks, which arise from the fluorine atoms in two different chemical environments: The peak at 688.9 eV stems from the five  $F_{CF_x}$  atoms ( $CF_x = CF_2$  and  $CF_3$  groups) of the fluorinated chain in the  $[PFBMIm]^+$  cation, and the peak at 686.8 eV from the six  $F_{PF_6}$  atoms of the  $[PF_6]^-$  anion. In the N 1s region (center panel), a single peak is observed at 402.2 eV, due to the  $N_{Im}$  atoms of the imidazolium ring. In the C 1s region (right panel), the peaks at 293.6 and 291.3 eV stem from the  $C_{CF_3}$  and  $C_{CF_2}$  groups of the fluorinated butyl chain of the  $[PFBMIm]^+$  cation. The peak at lower binding energy consists of two peaks due to the  $C_2$  atom at 287.8 eV and the  $C_{hetero}$  atoms at 286.8 eV. The P 2p spectrum (Figure S1f in the Supporting Information) displays the spin-orbit-split  $P_{PF_6}$  peak of the anion centered at 137.0 eV. Again, the absence of O 1s and Si 2p signals (see Figure S1f in the Supporting Information) indicates that  $[PFBMIm][PF_6]$  is clean.<sup>[21]</sup> This is further

**Table 1.** Quantitative analysis of the  $0^\circ$  and  $80^\circ$  XP spectra at  $95^\circ C$ . Nominal and experimentally determined contents (mole fraction) are given for all elements using ASFs from Ref. [18]. a) Neat  $[C_4C_1Im][PF_6]$ , b)–e) mixtures of  $[PFBMIm][PF_6]$  with  $[C_4C_1Im][PF_6]$  at molar ratios of b) 10 mol%  $[PFBMIm][PF_6]$ , c) 25 mol%  $[PFBMIm][PF_6]$ , d) 50 mol%  $[PFBMIm][PF_6]$  and e) 75 mol%  $[PFBMIm][PF_6]$ , and f) neat  $[PFBMIm][PF_6]$ .

Core levels	F 1s	F 1s	N 1s	C 1s	C 1s	C 1s	C 1s	P 2p
a) $[C_4C_1Im][PF_6]$	$F_{CF_x}$	$F_{PF_6}$	$N_{Im}$	$C_{CF_x}$	$C_2$	$C_{hetero}$	$C_{alkyl}$	$P_{PF_6}$
BE/eV	–/–	686.6	402.0	–/–	287.5	286.6	285.1	136.9
ASF	1.00	1.00	0.46	0.30	0.30	0.30	0.30	0.46
nominal	–/–	6.0	2.0	–/–	1.0	4.0	3.0	1.0
$0^\circ$ emission	–/–	6.4	2.0	–/–	0.9	3.8	2.9	1.1
$80^\circ$ emission	–/–	6.0	1.9	–/–	0.9	3.7	3.4	1.1
b) 10 mol% $[PFBMIm][PF_6]$	$F_{CF_x}$	$F_{PF_6}$	$N_{Im}$	$C_{CF_x}$	$C_2$	$C_{hetero}$	$C_{alkyl}$	$P_{PF_6}$
nominal	0.5	6.0	2.0	0.2	1.0	4.1	2.7	1.0
$0^\circ$ emission	0.9	6.2	2.0	0.2	0.7	4.3	2.3	1.1
$80^\circ$ emission	1.6	5.4	1.8	0.4	0.6	4.3	2.3	1.1
c) 25 mol% $[PFBMIm][PF_6]$	$F_{CF_x}$	$F_{PF_6}$	$N_{Im}$	$C_{CF_x}$	$C_2$	$C_{hetero}$	$C_{alkyl}$	$P_{PF_6}$
nominal	1.3	6.0	2.0	0.5	1.0	4.3	2.3	1.0
$0^\circ$ emission	1.8	6.1	1.9	0.5	0.8	4.4	1.8	1.1
$80^\circ$ emission	3.0	5.2	1.7	0.8	0.7	4.2	1.7	1.0
d) 50 mol% $[PFBMIm][PF_6]$	$F_{CF_x}$	$F_{PF_6}$	$N_{Im}$	$C_{CF_x}$	$C_2$	$C_{hetero}$	$C_{alkyl}$	$P_{PF_6}$
nominal	2.5	6.0	2.0	1.0	1.0	4.5	1.5	1.0
$0^\circ$ emission	3.1	6.1	1.9	0.9	0.9	4.4	1.2	1.1
$80^\circ$ emission	4.5	5.1	1.7	1.2	0.8	4.1	1.0	1.0
e) 75 mol% $[PFBMIm][PF_6]$	$F_{CF_x}$	$F_{PF_6}$	$N_{Im}$	$C_{CF_x}$	$C_2$	$C_{hetero}$	$C_{alkyl}$	$P_{PF_6}$
nominal	3.8	6.0	2.0	1.5	1.0	4.8	0.8	1.0
$0^\circ$ emission	4.2	6.0	1.9	1.4	1.0	4.6	0.5	1.1
$80^\circ$ emission	5.8	4.9	1.7	1.8	1.0	4.2	0.4	1.0
f) $[PFBMIm][PF_6]$	$F_{CF_x}$	$F_{PF_6}$	$N_{Im}$	$C_{CF_x}$	$C_2$	$C_{hetero}$	$C_{alkyl}$	$P_{PF_6}$
BE/eV	688.9	686.8	402.2	291.3/ 293.6	287.8	286.8	–/–	137.0
nominal	5.0	6.0	2.0	2.0	1.0	5.0	–/–	1.0
$0^\circ$ emission	5.6	6.0	1.9	1.8	1.0	4.6	–/–	1.1
$80^\circ$ emission	7.0	5.0	1.7	2.1	1.0	4.1	–/–	1.0

confirmed by the fact that the quantitative analysis at  $0^\circ$  agrees very well with the nominally expected composition of  $[PFBMIm][PF_6]$  (see Table 1 f).

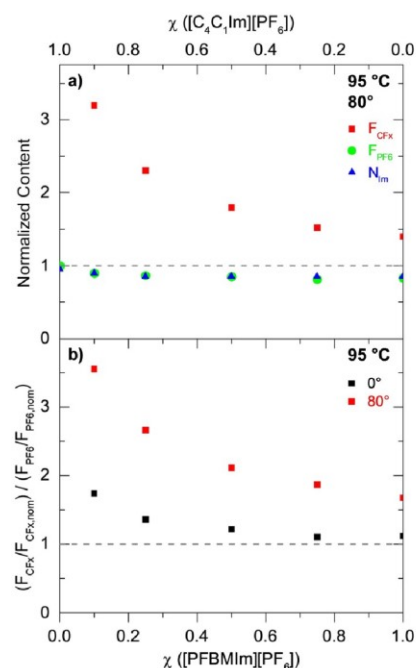
Next, we compare the spectra at  $80^\circ$  in Figure 2 f to those at  $0^\circ$  emission. In the F 1s spectrum, clearly a strong increase of the  $F_{CF_x}$  peak of the fluorinated chain at  $80^\circ$  is observed that goes along with a pronounced decrease of the  $F_{PF_6}$  signal. This behavior indicates that the fluorinated chain of the cation is enriched at the IL/vacuum interface, while the  $[PF_6]^-$  anion is surface-depleted. The enrichment of the fluorinated chain is also reflected by the increase of the  $C_{CF_3}$  and  $C_{CF_2}$  peaks in the C 1s region at  $80^\circ$ . This increase goes along with a decrease of the  $C_2$  and  $C_{hetero}$  peaks and also of the  $N_{Im}$  signal in the N 1s region; both observations indicate a surface depletion of the imidazolium ring of the  $[PFBMIm]^+$  cation. In the P 2p spectrum, changing the emission angle from  $0^\circ$  to  $80^\circ$  emission leads to a small decrease.

**Mixtures of [PFBMIm][PF<sub>6</sub>] and [C<sub>4</sub>C<sub>1</sub>Im][PF<sub>6</sub>]**

To search for preferential enrichment effects of different cations in mixtures of [PFBMIm][PF<sub>6</sub>] and [C<sub>4</sub>C<sub>1</sub>Im][PF<sub>6</sub>] as a function of the composition, we studied four mixtures with molar ratios of 10, 25, 50 and 75 mol% of [PFBMIm][PF<sub>6</sub>]. The corresponding XP spectra are depicted in Figure 2b–2e, respectively, for emission angles of 0° (black) and 80° (red).

We start with the discussion of the F 1s spectra (left panel) at 0°. In addition to the F<sub>PF<sub>6</sub></sub> peak of the anion at 686.7 eV, all spectra display the F<sub>CF<sub>x</sub></sub> peak of the cation at 688.9 eV. The intensity of the latter peak increases with increasing molar ratio, as is expected. In all cases, the N 1s spectra (center panel) show a single peak, N<sub>Im</sub>, at 402.1 eV originating from the nitrogen atoms in the imidazolium rings of both the [PFBMIm]<sup>+</sup> and the [C<sub>4</sub>C<sub>1</sub>Im]<sup>+</sup> cations. In the C 1s region (right panel), we find five peaks for all mixtures. The peaks at 293.6 and 291.3 eV are due to the C<sub>CF<sub>3</sub></sub> and C<sub>CF<sub>2</sub></sub> atoms of the [PFBMIm]<sup>+</sup> cation, respectively. The C<sub>alkyl</sub> peak of the [C<sub>4</sub>C<sub>1</sub>Im]<sup>+</sup> cation is observed at 285.1 eV, and the C<sub>hetero</sub> peak with the C<sub>2</sub> shoulder is found at 286.7 and 287.7 eV, respectively. The spin-orbit-split P 2p peaks of the [PF<sub>6</sub>]<sup>-</sup> anion are centered at 137.0 eV (see Figure S1b–S1e in the Supporting Information). Within the margin of error (±0.2 eV) the peaks in all regions have the same binding energy like in the neat ILs. Again, no signals are detected in the Si 2p and O 1s spectra (Figure S1b–S1e in the Supporting Information), verifying that no contaminations are transferred to the mixture by using acetonitrile as a co-solvent when preparing the mixtures. Within the margin of error, the quantitative analyses are in line with the nominal compositions of the mixtures of [PFBMIm][PF<sub>6</sub>] and [C<sub>4</sub>C<sub>1</sub>Im][PF<sub>6</sub>], except for a general too high content of F<sub>CF<sub>x</sub></sub> atoms and a too low content of C<sub>alkyl</sub> atoms, derived from the bulk-sensitive measurements at 0° (Table 1b–1f). This observation indicates that strong enrichment and depletion effects are not only visible in 80° measurements but also in 0° emission (see also below). Recently, the deviation from the nominal bulk values at 0° emission, and therefore the pronounced enrichment/depletion of one of the species of mixtures, was reported by our group and others.<sup>[6b,10a]</sup>

Next, we analyze the XP spectra at 80°. For all mixtures, a significant increase of the F<sub>CF<sub>x</sub></sub> peak at 688.9 eV indicates a clear surface enrichment of the fluorinated chain, similar to the observation for neat [PFBMIm][PF<sub>6</sub>]. Interestingly, the increase of the F<sub>CF<sub>x</sub></sub> signal at 80° relative to that at 0° is most pronounced for the mixture with the lowest molar ratio of 10 mol% [PFBMIm][PF<sub>6</sub>]. With increasing molar ratio, this enhancement continuously decreases. To visualize this behavior, we plotted the normalized F<sub>CF<sub>x</sub></sub> content, that is, the experimentally determined content (mole fraction) divided by the nominal content (see Table 1) as a function of the molar ratio in Figure 3a (red squares). A value of 1.0 would represent the situation, where the surface composition is identical to that in the bulk, that is, no surface enrichment. Figure 3a shows a strong increase of the normalized F<sub>CF<sub>x</sub></sub> content with decreasing molar ratio of [PFBMIm][PF<sub>6</sub>]. This behavior clearly indicates that the surface enrichment of the fluorinated chain in the outermost



**Figure 3.** a) Normalized content of F<sub>CF<sub>x</sub></sub> (red squares), F<sub>PF<sub>6</sub></sub> (green circles) and N<sub>Im</sub> (blue triangles) for 80° emission (data from Figure 2 and Table 1a–1f). In each case, the experimentally determined content is divided by the nominal content. b) Ratio of the normalized F<sub>CF<sub>x</sub></sub> and F<sub>PF<sub>6</sub></sub> contents, at 0° (black) and 80° (red) emission angle. In all cases, the sample temperature was 95 °C. The dashed horizontal lines indicate the nominal compositions.

layer (relative to the bulk) strongly increases for low molar ratios, that is, the surface of the mixture is preferentially terminated with the fluorinated chain.

This enrichment of the fluorinated chain is also detected in the C 1s region (Figure 2b–2e, right panel) at 80°, where we observe an intensity increase of the C<sub>CF<sub>3</sub></sub> and C<sub>CF<sub>2</sub></sub> peaks. Generally, the effect is less pronounced than in the F 1s region, which is due to the higher kinetic energy of the C 1s photoelectrons of around 1200 eV as compared to around 800 eV for F 1s, which leads to a larger information depth of the former. In contrast to the increase of the F<sub>CF<sub>x</sub></sub> signal of the fluorinated chains of [PFBMIm]<sup>+</sup>, the C<sub>alkyl</sub> signal of the alkyl chains of [C<sub>4</sub>C<sub>1</sub>Im]<sup>+</sup> has decreased at 80° for all IL mixtures. This behavior is in contrast to the situation for neat [C<sub>4</sub>C<sub>1</sub>Im][PF<sub>6</sub>] in Figure 2a and for neat ILs with longer alkyl chains,<sup>[22]</sup> and indicates that the alkyl chains in the mixtures studied here are depleted from the liquid/vacuum interface. The driving force is a competing effect between the fluorinated chain of the [PFBMIm]<sup>+</sup> cation and the non-fluorinated side chain of the [C<sub>4</sub>C<sub>1</sub>Im]<sup>+</sup> cation: The selective enrichment of the [PFBMIm]<sup>+</sup> cations is attributed to a (typically) larger surface tension of ILs with an alkyl chain compared to a fluorinated chain.<sup>[1b,6a,23]</sup>

The analysis of the F<sub>PF<sub>6</sub></sub> and P<sub>PF<sub>6</sub></sub> signals of the [PF<sub>6</sub>]<sup>-</sup> anion, as well as the C<sub>hetero</sub> and N<sub>Im</sub> signals of the imidazolium ring of the cation at 80° show for all mixtures (Figure 2b–2e and Figure S1b–S1e in the Supporting Information) more or less the

same behavior as for the two neat ILs (Figure 2a and 2f). The 80° signals are up to 20% smaller than the 0° signals, which results from the damping of the corresponding signals by the surface-enriched alkyl and fluorinated chains. In Figure 3a, we plotted the normalized  $F_{\text{PF}_6}$  and  $N_{\text{Im}}$  contents (green circles and blue triangles, respectively) as a function of the molar ratio. For both, we find values smaller than 1.0, which reflect the described damping. The data corresponding to the anion and the imidazolium ring are identical, indicating that both are at the same distance from the surface.

To visualize the relative enrichment of the fluorinated chain of the cation relative to the anion (and thus also to the cation head group), we plot the ratio of the normalized  $F_{\text{CF}_x}$  and  $F_{\text{PF}_6}$  contents (data from Figure 3a), that is,  $(F_{\text{CF}_x}/F_{\text{CF}_x,\text{nom}})/(F_{\text{PF}_6}/F_{\text{PF}_6,\text{nom}})$ , as a function of the molar ratio in Figure 3b. We will use this type of presentation later for the temperature-dependent studies. The strong increase of the 80° signal with decreasing molar ratio again reflects the pronounced surface enrichment of the fluorinated chain of the  $[\text{PFBMIm}]^+$  cation. Interestingly, we also find a clear increase of the ratio of the normalized  $F_{\text{CF}_x}$  and  $F_{\text{PF}_6}$  contents for 0°. This behavior again indicates that strong selective enrichment effects are not only observed at 80° but also at 0° (see above).

#### Temperature dependence of surface enrichment

As a next step, we address the temperature dependence of the XP spectra for the two neat ILs and the IL mixtures, by cooling the ILs from 95°C down to the temperature, where solidification starts, which is typically indicated by the onset of charging. The F 1s and C 1s spectra of the neat ILs and the IL mixtures are shown in Figures 4a–4f and 5a–5f, respectively. Due to the higher surface sensitivity, we focus on the spectra at 80°, since enrichment/depletion effects are better visible at this angle than at 0° emission. The quantitative analysis of the ratios of the normalized  $F_{\text{CF}_x}$  and  $F_{\text{PF}_6}$  contents at 80° and also at 0° are shown in Figure 6b–6f.

For neat  $[\text{C}_4\text{C}_1\text{Im}][\text{PF}_6]$ , we find a slight continuous decrease of the  $F_{\text{PF}_6}$  signal in Figure 4a by around 15% upon cooling from 95°C to –55°C. The  $C_{\text{hetero}}$  signal in Figure 5a shows a comparable decrease of 8%; in contrast to this behavior, the  $C_{\text{alkyl}}$  continuously increases. At 95°C, the  $C_{\text{alkyl}}$  peak is smaller than the  $C_{\text{hetero}}$  peak, but at –55°C the intensities are reversed. This behavior indicates an increasing surface enrichment of the butyl chain with decreasing temperature. Similar effects have been observed in literature<sup>[24]</sup> for  $[\text{C}_6\text{C}_1\text{Im}]\text{X}$  with  $\text{X}^- = \text{Br}$ ,  $[\text{TfO}]$ ,  $[\text{Tf}_2\text{N}]$  and  $[\text{C}_n\text{C}_1\text{Im}][\text{TfO}]$  ( $n=4, 8, 18$ ). We assign these effects to the increase in magnitude of the entropic term  $-T\Delta S^0$  with temperature, which favors a more random distribution of the constituents with increasing temperature. This term counteracts the enthalpic driving force favoring surface enrichment of the fluorinated chain at low temperature, due to lowering of the surface tension (see above).

Upon further temperature decrease, the  $C_{\text{alkyl}}$  intensity continues to increase, until at –70°C charging and peak broadening starts (not shown). This temperature is in accordance with the glass transition temperature of  $[\text{C}_4\text{C}_1\text{Im}][\text{PF}_6]$  at around

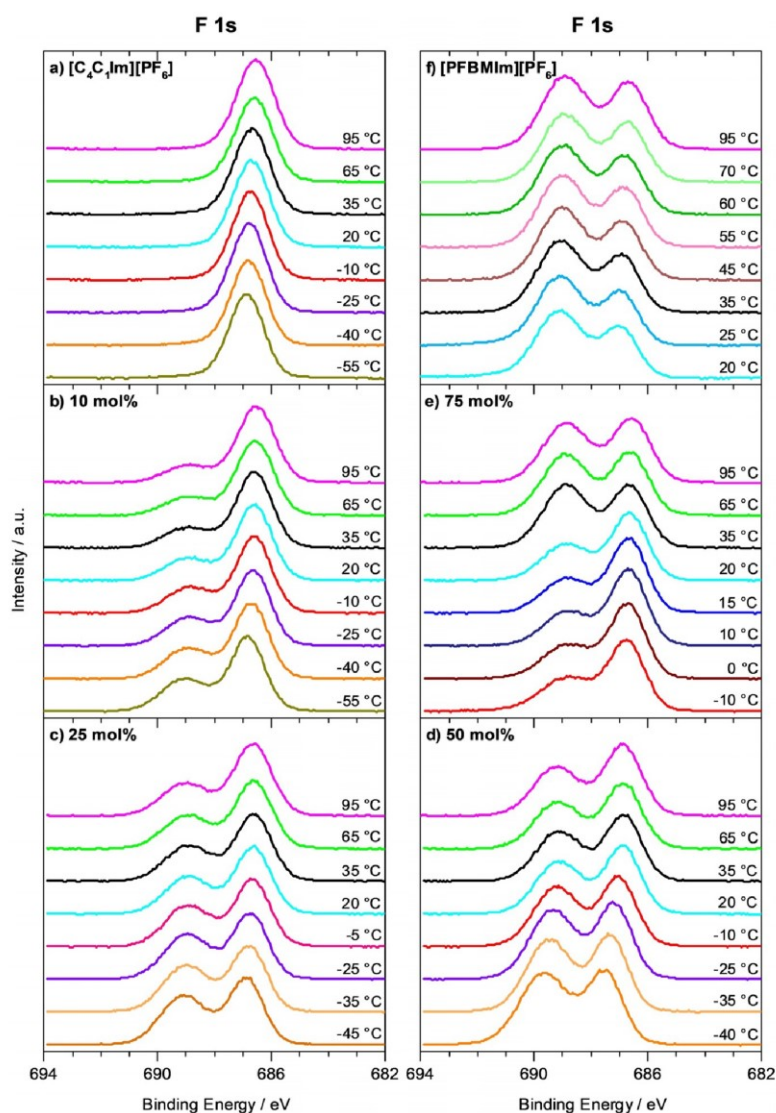
–77°C.<sup>[20]</sup> Subsequent heating the sample up to 95°C yields the same spectra (within the margin of error) as observed before starting the cooling experiment.

For neat  $[\text{PFBMIm}][\text{PF}_6]$ , we again observe a slow decrease of the  $F_{\text{PF}_6}$  peak at 80° during cooling from 95 to 25°C in Figure 4f; at the same time, the  $F_{\text{CF}_x}$  intensity remains more or less unchanged. The resulting increase of the ratio of the normalized  $F_{\text{CF}_x}$  and  $F_{\text{PF}_6}$  contents in Figure 6f indicates a slight increase of the surface enrichment of the fluorinated chain with decreasing temperature. No significant changes are initially observed in the C 1s region (Figure 5f, spectra at 95°C and 55°C). Starting at 20°C, peak broadening and an intensity decrease of all IL peaks indicate the onset of solidification of  $[\text{PFBMIm}][\text{PF}_6]$ . Since bulk  $[\text{PFBMIm}][\text{PF}_6]$  melts at 66°C,<sup>[17]</sup> the onset of solidification at a temperature as low as at 20°C indicates that this IL undergoes supercooling. Upon heating the IL back to 95°C, we observe an intensity loss of about 18% of the  $F_{\text{PF}_6}$  signal (not shown), whereas the  $F_{\text{CF}_x}$  signal completely recovers (to within 3%). A closer look to the other spectra in 80° emission shows that the N 1s XP spectrum shows a shoulder towards lower binding energy, indicating radiation damage<sup>[25]</sup> over a prolonged exposure to X-rays (notably, the conclusions derived here are not affected by beam damage).

Next, we discuss the behavior for the different IL mixtures upon cooling. The F 1s and C 1s spectra for selected temperatures are shown in Figures 4b–4e and 5b–5e, respectively. The lowest possible temperature for XPS upon cooling depends on the molar ratio, because the solidification temperature increases with increasing  $[\text{PFBMIm}][\text{PF}_6]$  content. Overall, the ILs with molar ratios of 10, 25 and 50 mol%  $[\text{PFBMIm}][\text{PF}_6]$  display the same behavior. Upon cooling from 95°C to lower temperatures, the  $F_{\text{CF}_x}$  peaks gain intensity and the ratios of the normalized  $F_{\text{CF}_x}$  and  $F_{\text{PF}_6}$  contents for 80° in Figure 6b–6d increase. Notably, for 0° this increase is much less pronounced (black symbols in Figure 6). The increase of the  $F_{\text{CF}_x}$  intensity (see Figure 4b–4d) detected in 80° indicates an increasing surface enrichment of the fluorinated chain of the  $[\text{PFBMIm}]^+$  cation in the IL mixtures upon cooling. The driving force for the increase of surface enrichment of the fluorinated chains at lower temperatures, or—in other words—the higher degree of disorder at higher temperatures in the mixtures is again attributed to the entropic contributions.

Below a certain temperature for each mixture (about –55°C for 10 mol%, –45°C for 25 mol% and –35°C for 50 mol%), all signals shift towards higher binding energy and peak broadening indicates solidification and therefore charging (note that for a given mixture these temperatures were found to vary by  $\pm 5^\circ\text{C}$  due to the supercooling effects). The corresponding data is not included in Figures 4–6. The intensities of the  $C_{\text{CF}_3}$  and  $C_{\text{CF}_2}$  peaks in Figure 5b–5d increase slightly upon cooling, as expected. If the mixtures are subsequently heated to 95°C, nearly the original F 1s and C 1s spectra are obtained, confirming reversibility of the temperature-dependent experiment without notable changes due to prolonged X-ray exposure.

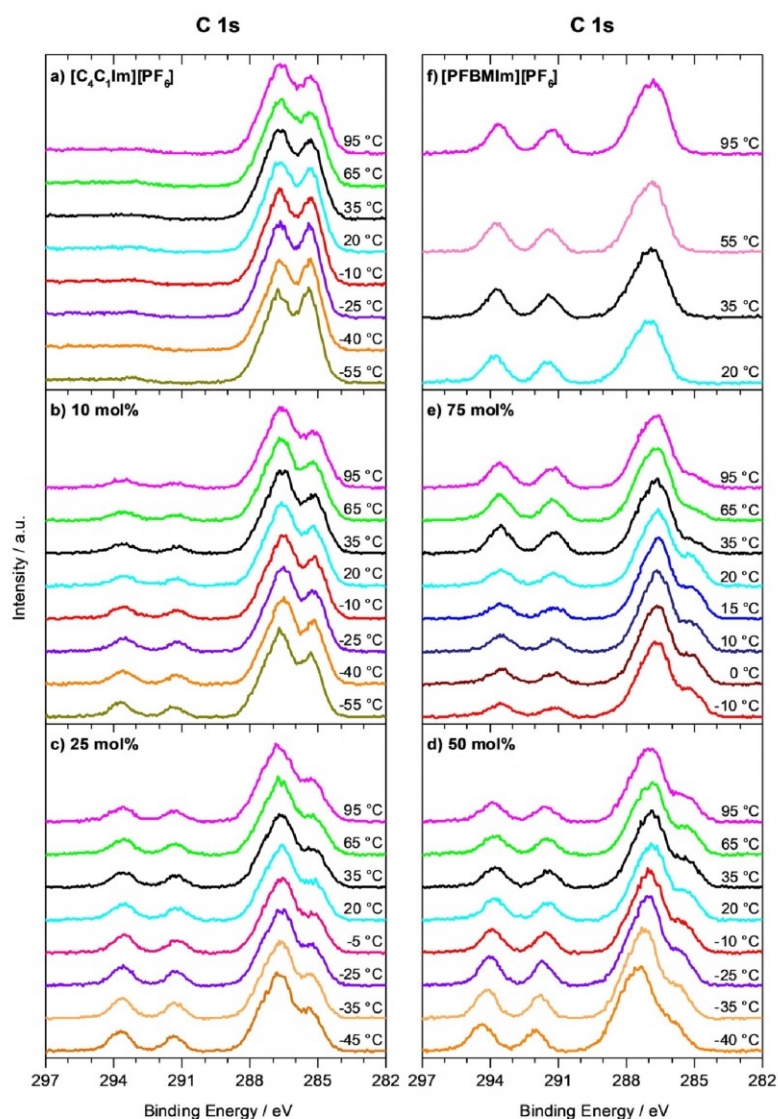
For the molar ratio of 75 mol%  $[\text{PFBMIm}][\text{PF}_6]$ , we observe a quite different behavior. Initially, the F 1s and C 1s spectra in Figures 4e and 5e, respectively, and the ratio of the normal-



**Figure 4.** F 1s spectra measured at 80° emission, collected during cooling from 95 °C to lower temperatures: a) Neat  $[C_4C_1Im][PF_6]$ , b)–e) mixtures of  $[PFBMIm][PF_6]$  with  $[C_4C_1Im][PF_6]$  at molar ratios of b) 10 mol%  $[PFBMIm][PF_6]$ , c) 25 mol%  $[PFBMIm][PF_6]$ , d) 50 mol%  $[PFBMIm][PF_6]$  and e) 75 mol%  $[PFBMIm][PF_6]$ , and f) neat  $[PFBMIm][PF_6]$ .

ized  $F_{CFx}$  and  $F_{PF_6}$  contents at 80° and also at 0° in Figure 6e show the same continuous increase than found for the lower molar ratios. This behavior again indicates an increasing surface enrichment of the fluorinated chain of the  $[PFBMIm]^+$  cation in the mixture with decreasing temperature. Between 35 and 20 °C, however, the  $F_{CFx}$  intensity decreases by about 40% while the  $F_{PF_6}$  intensity stays constant. This leads to a pronounced decrease of their ratio in Figure 6e. Upon further cooling, the ratio slightly increases again, with a similar slope than above 35 °C. Peak broadening due to charging starts at -10 °C indicating the onset of solidification of the  $[PFBMIm][PF_6]$ -depleted mixture. The corresponding C 1s spectra of the 75 mol% mixture (see Figure 5e) display an intensity

increase of the  $C_{alkyl}$  peak between 35 and 20 °C, whereas the  $C_{CF_2}$  and  $C_{CF_3}$  peaks lose intensity. No further changes are observed until the start of peak broadening at -10 °C. We assign the sharp decrease of the peaks of the fluorinated chain ( $F_{CFx}$ ,  $C_{CF_3}$  and  $C_{CF_2}$ ) to a partial solidification of a  $[PFBMIm][PF_6]$ -rich or pure  $[PFBMIm][PF_6]$  phase, which is depleted from the outer surface beyond the XPS information depth, or even forms a solid precipitate at the buried solid/liquid interface with the support. The remaining liquid mixture is therefore  $[PFBMIm][PF_6]$ -depleted and  $[C_4C_1Im][PF_6]$ -rich, which leads to the decrease of the  $F_{CFx}$  signal and an increase of the  $C_{alkyl}$  signal. The peak broadening at -10 °C then indicates the solidification of this residual mixture. After subsequent heating of the mixture

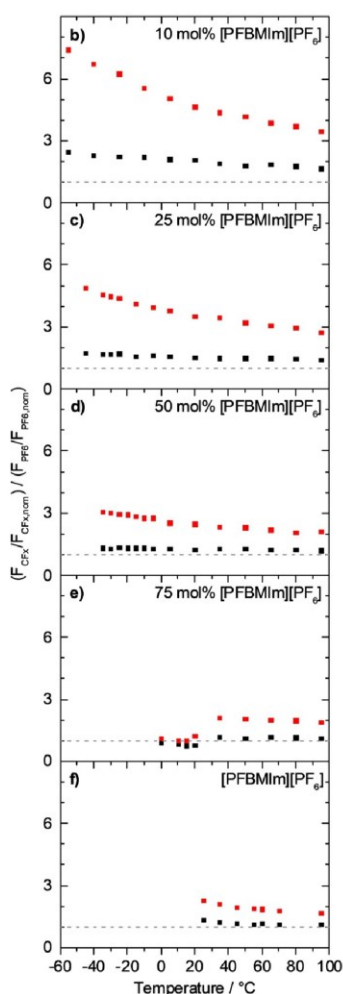


**Figure 5.** C 1s spectra measured at 80° emission, collected during cooling from 95 °C to lower temperatures: a) Neat  $[C_4C_1Im][PF_6]$ , b)–e) mixtures of  $[PF_6Im][PF_6]$  with  $[C_4C_1Im][PF_6]$  at molar ratios of b) 10 mol%  $[PF_6Im][PF_6]$ , c) 25 mol%  $[PF_6Im][PF_6]$ , d) 50 mol%  $[PF_6Im][PF_6]$  and e) 75 mol%  $[PF_6Im][PF_6]$ , and f) neat  $[PF_6Im][PF_6]$ .

to 95 °C, we find the same peak intensities (within the margin of error) as before the cooling experiment; this behavior signals the re-dissolution and mixing of  $[PF_6Im][PF_6]$  and  $[C_4C_1Im][PF_6]$  during heating the mixture. Notably, the precipitation of one of the ILs from the mixture was only observed for high  $[PF_6Im][PF_6]$  content such as 75 mol% (a very similar behavior was also detected for a 85 mol% mixture, see Figure S2 in the Supporting Information), and not in any of the other mixtures (10, 25 and 50 mol% mixtures). It should be noted that the magnitude of the abrupt decrease of the ratio in Figure 6e between 35 and 20 °C varied from experiment to experiment. Such a behavior is typical for liquids that show su-

percooling, as slight contaminations or other disturbances might induce or prevent spontaneous solidification. Recently, a similar phenomenon was reported for mixtures of  $Cs[Tf_2N]$  and  $[PPh_4][Tf_2N]$ , where the temperature-dependent depletion of tetraphenylphosphonium,  $[PPh_4]^+$ , from the near-surface region (information depth) was observed by XPS.<sup>[19]</sup> In order to correlate surface phenomena as described in this last section with liquid-solid phase transitions in the bulk of IL mixtures in more detail, a combination of surface-sensitive ARXPS with other methods such as differential scanning calorimetry, scattering or microscopy techniques would be very helpful, but are out of the scope of this article.





**Figure 6.** Ratio of the normalized  $F_{\text{CFX}}$  and  $F_{\text{PFO}}$  contents, at  $0^\circ$  (black) and  $80^\circ$  (red) emission angle, obtained during cooling from  $95^\circ\text{C}$  to lower temperatures. a) Neat  $[\text{C}_4\text{C}_1\text{Im}][\text{PF}_6]$ : Not shown, since this IL contains no  $F_{\text{CFX}}$  signal from a fluorinated chain, b)–e) mixtures of  $[\text{PFBMIm}][\text{PF}_6]$  with  $[\text{C}_4\text{C}_1\text{Im}][\text{PF}_6]$  at molar ratios of b) 10 mol%  $[\text{PFBMIm}][\text{PF}_6]$ , c) 25 mol%  $[\text{PFBMIm}][\text{PF}_6]$ , d) 50 mol%  $[\text{PFBMIm}][\text{PF}_6]$  and e) 75 mol%  $[\text{PFBMIm}][\text{PF}_6]$ , and f) neat  $[\text{PFBMIm}][\text{PF}_6]$ . The dashed horizontal lines indicate the nominal compositions.

## Conclusions

We used angle-resolved X-ray photoelectron spectroscopy to study mixtures of fluorinated and non-fluorinated ILs, namely  $[\text{PFBMIm}][\text{PF}_6]$  and  $[\text{C}_4\text{C}_1\text{Im}][\text{PF}_6]$ , with molar ratios of 10, 25, 50 and 75 mol%  $[\text{PFBMIm}][\text{PF}_6]$ , along with the two neat ILs, at  $95^\circ\text{C}$  and while cooling to lower temperatures. The two ILs contain the same anion,  $[\text{PF}_6]^-$ , but different cations. By performing very surface-sensitive measurements at an emission angle of  $80^\circ$ , we observe surface enrichment of the fluorinated chain for neat  $[\text{PFBMIm}][\text{PF}_6]$  relative to the bulk composition. This effect is in line with the general observation that fluorinated groups in the outermost layer lead to a lower surface ten-

sion than alkyl groups.<sup>[1b,6a,23]</sup> The lower the molar ratio of  $[\text{PFBMIm}][\text{PF}_6]$  in the mixture, the more pronounced is the surface enrichment of the fluorinated chain relative to the bulk composition. Upon cooling the mixtures from their liquid phase at  $95^\circ\text{C}$  to their solidification, we observe a similar behavior for the 10, 25 and 50 mol% mixtures, and also for neat  $[\text{PFBMIm}][\text{PF}_6]$ : Decreasing the temperature leads to an increase in surface enrichment of the fluorinated chain of  $[\text{PFBMIm}][\text{PF}_6]$  (relative to the bulk composition), which is detected in the F 1s and C 1s spectra. We attribute the observed behavior to entropic reasons, namely a less pronounced enrichment of the fluorinated chains, that is, a lower degree of order, at high temperatures. The 75 mol% mixture shows the same increase in enrichment of the fluorinated chain as the other mixtures when cooling down to  $35^\circ\text{C}$ . Upon further cooling to  $20^\circ\text{C}$ , however, the surface enrichment of the fluorinated chain decreases drastically. This observation is attributed to a (partial) precipitation of the pure  $[\text{PFBMIm}][\text{PF}_6]$ , which in turn results in a  $[\text{C}_4\text{C}_1\text{Im}][\text{PF}_6]$ -rich phase at the topmost layer of the mixture. This change in composition is also reflected by an increase of the  $C_{\text{alkyl}}$  peak in the C 1s spectrum when comparing the  $35^\circ\text{C}$  and  $20^\circ\text{C}$  spectra.

## Acknowledgements

B.S.J.H., M.L., F.G. and H.-P.S. thank the European Research Council (ERC) under the European Union's Horizon 2020 research and innovation programme for financial support, in the context of the Advanced Investigator Grant "ILID" to H.-P.S. (Grant Agreement No. 693398-ILID). S.S. thanks the Alexander von Humboldt Foundation for a research fellowship. F.M. gratefully acknowledges Dr. R. Kalb and Dr. J. Zelenka (proionic GmbH) for help on ionic liquids currently registered by REACH.

## Conflict of interest

The authors declare no conflict of interest.

**Keywords:** ionic liquids • mixtures • photoelectron spectroscopy • surface enrichment

- [1] a) A. B. Pereiro, M. J. Pastoriza-Gallego, K. Shimizu, I. M. Marrucho, J. N. Canongia Lopes, M. M. Piñeiro, L. P. N. Rebelo, *J. Phys. Chem. B* **2013**, *117*, 10826–10833; b) A. Luís, K. Shimizu, J. M. M. Araújo, P. J. Carvalho, J. A. Lopes-da-Silva, J. N. Canongia Lopes, L. P. N. Rebelo, J. A. P. Coutinho, M. G. Freire, A. B. Pereiro, *Langmuir* **2016**, *32*, 6130–6139; c) T. L. Greaves, D. F. Kennedy, Y. Shen, A. Hawley, G. Song, C. J. Drummond, *Phys. Chem. Chem. Phys.* **2013**, *15*, 7592–7598; d) L. Zhou, J. Fan, X. Shang, *Materials* **2014**, *7*, 3867–3880.
- [2] M. L. Ferreira, M. J. Pastoriza-Gallego, J. M. M. Araújo, J. N. Canongia Lopes, L. P. N. Rebelo, M. M. Piñeiro, K. Shimizu, A. B. Pereiro, *J. Phys. Chem. C* **2017**, *121*, 5415–5427.
- [3] S. Tsuzuki, T. Umecky, H. Matsumoto, W. Shinoda, M. Mikami, *J. Phys. Chem. B* **2010**, *114*, 11390–11396.
- [4] J. van den Broeke, F. Winter, B.-J. Deelman, G. van Koten, *Org. Lett.* **2002**, *4*, 3851–3854.
- [5] O. Hollóczki, M. Macchiagodena, H. Weber, M. Thomas, M. Brehm, A. Stark, O. Russina, A. Triolo, B. Kirchner, *ChemPhysChem* **2015**, *16*, 3325–3333.

- [6] a) E. J. Smoll, Jr., M. A. Tesa-Serrate, S. M. Purcell, L. D'Andrea, D. W. Bruce, J. M. Slattery, M. L. Costen, T. K. Minton, K. G. McKendrick, *Faraday Discuss.* **2018**, *206*, 497–522; b) Y. Zhang, Y. Khalifa, E. J. Maginn, J. T. Newberg, *J. Phys. Chem. C* **2018**, *122*, 27392–27401; c) D. W. Bruce, C. P. Cabry, J. N. C. Lopes, M. L. Costen, L. D'Andrea, I. Grillo, B. C. Marshall, K. G. McKendrick, T. K. Minton, S. M. Purcell, S. Rogers, J. M. Slattery, K. Shimizu, E. Smoll, M. A. Tesa-Serrate, *J. Phys. Chem. B* **2017**, *121*, 6002–6020.
- [7] ECHA—European Chemicals Agency, echa.europa.eu, accessed June 2019; personal communication with proionic GmbH.
- [8] a) M. T. Clough, C. R. Crick, J. Gråsvik, P. A. Hunt, H. Niedermeyer, T. Welton, O. P. Whitaker, *Chem. Sci.* **2015**, *6*, 1101–1114; b) H. Niedermeyer, J. P. Hallett, I. J. Villar-Garcia, P. A. Hunt, T. Welton, *Chem. Soc. Rev.* **2012**, *41*, 7780–7802.
- [9] a) M. Chakraborty, T. Ahmed, R. S. Dhale, D. Majhi, M. Sarkar, *J. Phys. Chem. B* **2018**, *122*, 12114–12130; b) R. S. Dhale, P. K. Sahu, M. Sarkar, *J. Phys. Chem. B* **2017**, *121*, 7934–7945; c) D. C. Khara, J. P. Kumar, N. Mondal, A. Samanta, *J. Phys. Chem. B* **2013**, *117*, 5156–5164; d) S. N. Baker, G. A. Baker, F. V. Bright, *Green Chem.* **2002**, *4*, 165–169; e) S. K. Das, P. K. Sahu, M. Sarkar, *J. Fluoresc.* **2013**, *23*, 1217–1227.
- [10] a) B. S. J. Heller, C. Kolbeck, I. Niedermaier, S. Dommer, J. Schatz, P. Hunt, F. Maier, H.-P. Steinrück, *ChemPhysChem* **2018**, *19*, 1733–1745; b) M. B. Oliveira, M. Domínguez-Pérez, O. Cabeza, J. A. Lopes-da-Silva, M. G. Freire, J. A. P. Coutinho, *J. Chem. Thermodyn.* **2013**, *64*, 22–27; c) C. Ridings, G. G. Warr, G. G. Andersson, *J. Phys. Chem. Lett.* **2017**, *8*, 4264–4267.
- [11] F. Wu, W. V. Karunaratne, C. J. Margulis, *J. Phys. Chem. C* **2019**, *123*, 4914–4925.
- [12] a) K. Nakajima, M. Miyashita, M. Suzuki, K. Kimura, *J. Chem. Phys.* **2013**, *139*, 224701; b) R. Souda, *Surf. Sci.* **2010**, *604*, 1694–1697.
- [13] a) K. Nakajima, S. Oshima, M. Suzuki, K. Kimura, *Surf. Sci.* **2012**, *606*, 1693–1699; b) K. Nakajima, S. Nakanishi, Z. Chval, M. Lísal, K. Kimura, *J. Chem. Phys.* **2016**, *145*, 184704; c) K. Nakajima, S. Nakanishi, M. Lísal, K. Kimura, *J. Mol. Liq.* **2017**, *230*, 542–549.
- [14] I. J. Villar-Garcia, S. Fearn, N. L. Ismail, A. J. S. McIntosh, K. R. J. Lovelock, *Chem. Commun.* **2015**, *51*, 5367–5370.
- [15] a) I. J. Villar-Garcia, K. R. J. Lovelock, S. Men, P. Licence, *Chem. Sci.* **2014**, *5*, 2573–2579; b) S. Men, P. Licence, *Chem. Phys. Lett.* **2017**, *681*, 40–43; c) F. Maier, T. Cremer, C. Kolbeck, K. R. J. Lovelock, N. Paape, P. S. Schulz, P. Wasserscheid, H.-P. Steinrück, *Phys. Chem. Chem. Phys.* **2010**, *12*, 1905–1915; d) S. Men, P. Licence, *Chem. Phys. Lett.* **2017**, *686*, 74–77; e) S. Men, K. R. J. Lovelock, P. Licence, *Phys. Chem. Chem. Phys.* **2011**, *13*, 15244–15255.
- [16] a) S. Palchowdhury, B. L. Bhargava, *Phys. Chem. Chem. Phys.* **2015**, *17*, 19919–19928; b) S. Palchowdhury, B. L. Bhargava, *J. Phys. Chem. B* **2016**, *120*, 5430–5441.
- [17] M. Lexow, B. S. J. Heller, G. Partl, R. G. Bhui, F. Maier, H.-P. Steinrück, *Langmuir* **2019**, *35*, 398–405.
- [18] I. Niedermaier, C. Kolbeck, H.-P. Steinrück, F. Maier, *Rev. Sci. Instrum.* **2016**, *87*, 045105.
- [19] R. G. Bhui, P. Schreiber, B. S. J. Heller, M. Scheuermeyer, P. Wasserscheid, H.-P. Steinrück, F. Maier, *J. Mol. Liq.* **2019**, *275*, 290–296.
- [20] P. B. P. Serra, F. M. S. Ribeiro, M. A. A. Rocha, M. Fulem, K. Růžička, J. A. P. Coutinho, L. M. N. B. F. Santos, *J. Mol. Liq.* **2017**, *248*, 678–687.
- [21] a) C. Kolbeck, M. Killian, F. Maier, N. Paape, P. Wasserscheid, H.-P. Steinrück, *Langmuir* **2008**, *24*, 9500–9507; b) J. M. Gottfried, F. Maier, J. Rossa, D. Gerhard, P. S. Schulz, P. Wasserscheid, H.-P. Steinrück, *Z. Phys. Chem.* **2006**, *220*, 1439–1453.
- [22] a) C. Kolbeck, I. Niedermaier, A. Deyko, K. R. J. Lovelock, N. Taccardi, W. Wei, P. Wasserscheid, F. Maier, H.-P. Steinrück, *Chem. Eur. J.* **2014**, *20*, 3954–3965; b) K. R. J. Lovelock, C. Kolbeck, T. Cremer, N. Paape, P. S. Schulz, P. Wasserscheid, F. Maier, H.-P. Steinrück, *J. Phys. Chem. B* **2009**, *113*, 2854–2864.
- [23] T. L. Merrigan, E. D. Bates, S. C. Dorman, J. H. Davis Jr, *Chem. Commun.* **2000**, 2051–2052.
- [24] C. Kolbeck, A. Deyko, T. Matsuda, F. T. U. Kohler, P. Wasserscheid, F. Maier, H.-P. Steinrück, *ChemPhysChem* **2013**, *14*, 3726–3730.
- [25] a) T. Cremer, M. Stark, A. Deyko, H.-P. Steinrück, F. Maier, *Langmuir* **2011**, *27*, 3662–3671; b) C. Kolbeck, T. Cremer, K. R. J. Lovelock, N. Paape, P. S. Schulz, P. Wasserscheid, F. Maier, H.-P. Steinrück, *J. Phys. Chem. B* **2009**, *113*, 8682–8688.

Manuscript received: September 26, 2019

Accepted manuscript online: October 21, 2019

Version of record online: January 7, 2020

# CHEMISTRY

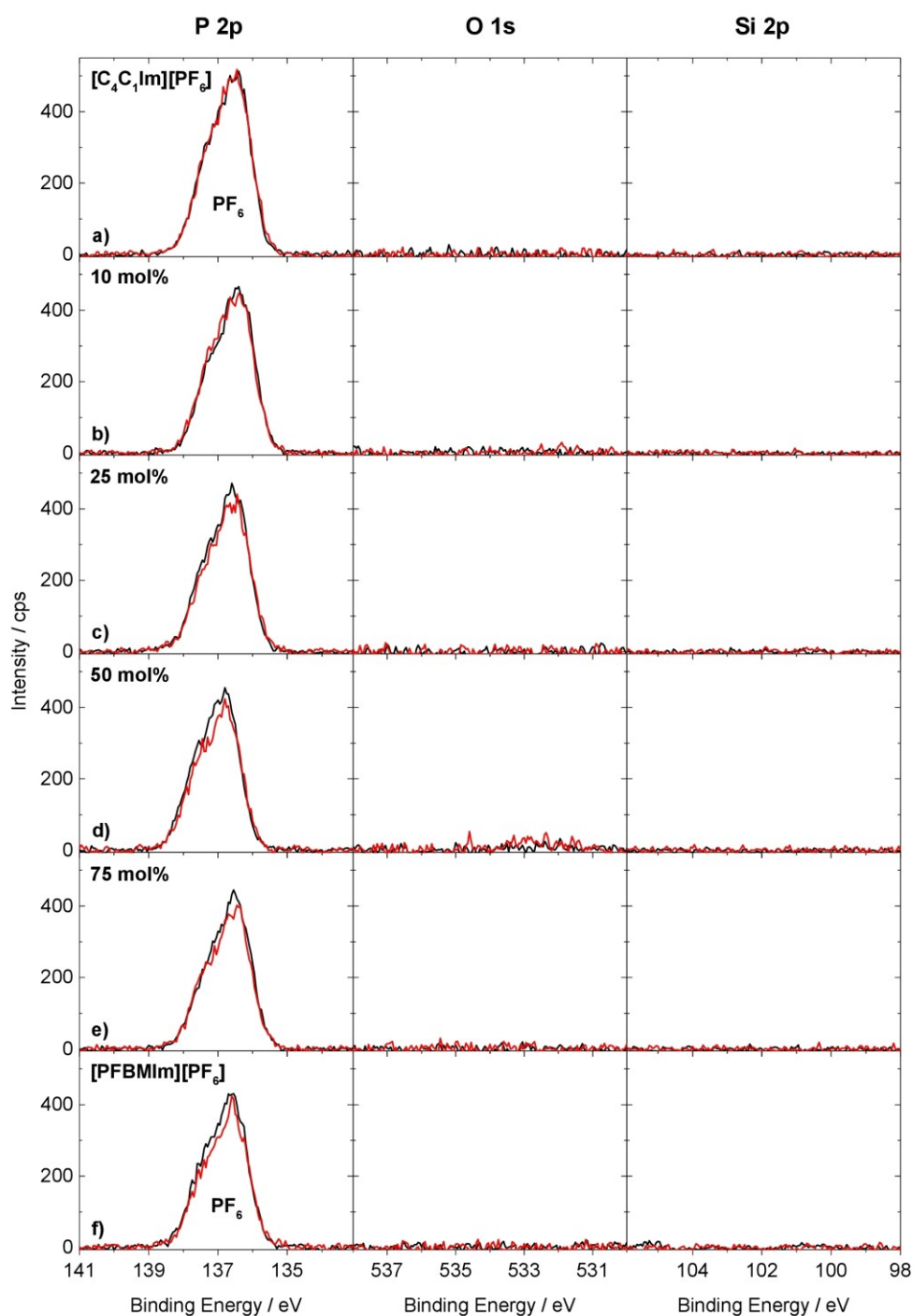
## A **European** Journal

### Supporting Information

#### **Temperature-Dependent Surface Enrichment Effects in Binary Mixtures of Fluorinated and Non-Fluorinated Ionic Liquids**

Bettina S. J. Heller,<sup>[a]</sup> Matthias Lexow,<sup>[a]</sup> Francesco Greco,<sup>[a]</sup> Sunghwan Shin,<sup>[a]</sup> Gabriel Partl,<sup>[b]</sup> Florian Maier,<sup>[a]</sup> and Hans-Peter Steinrück\*<sup>[a]</sup>

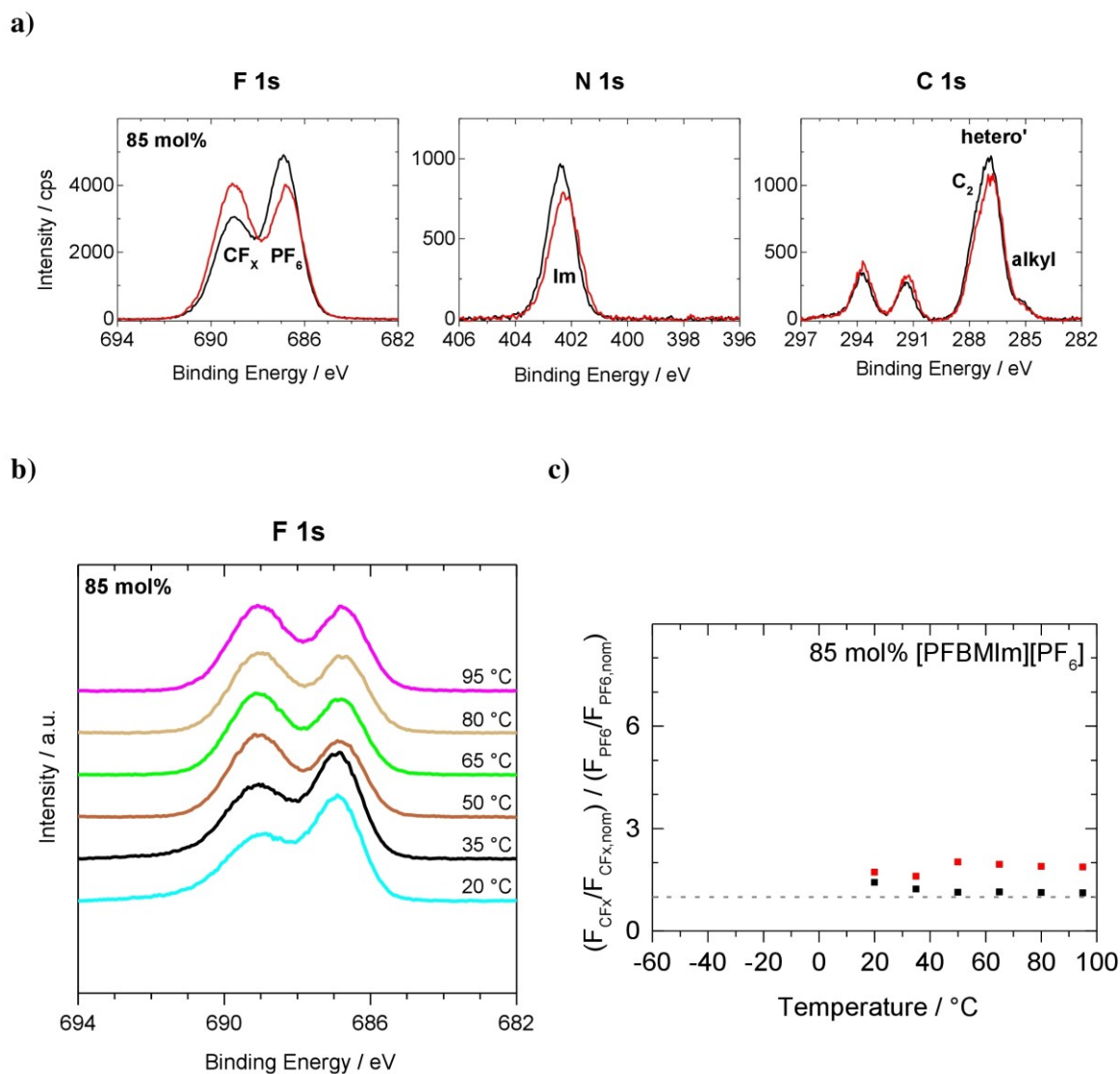
chem\_201904438\_sm\_miscellaneous\_information.pdf



**Figure S1:** P 2p (left), O 1s (center) and Si 2p (right) spectra, at 0° (black) and 80° (red) emission: a) Neat [C<sub>4</sub>C<sub>1</sub>Im][PF<sub>6</sub>], b) – e) mixtures of [C<sub>4</sub>C<sub>1</sub>Im][PF<sub>6</sub>] with [PFBMIm][PF<sub>6</sub>] at molar ratios of b) 10 mol% [PFBMIm][PF<sub>6</sub>], c) 25 mol% [PFBMIm][PF<sub>6</sub>], d) 50 mol% [PFBMIm][PF<sub>6</sub>] and e) 75 mol% [PFBMIm][PF<sub>6</sub>], and f) neat [PFBMIm][PF<sub>6</sub>]. In all cases, the sample temperature was 95 °C.

**Table S1:** List of the eight 1-ethyl-3-methylimidazolium [C<sub>2</sub>C<sub>1</sub>Im][X] ILs, registered by REACH in June 2019.

- [X] = [benzoate]<sup>-</sup>, registered by BASF SE
- = [MeSO<sub>3</sub>]<sup>-</sup>, methanesulfonate, registered by BASF SE
- = [EtSO<sub>4</sub>]<sup>-</sup>, ethylsulphate, registered by BASF SE
- = [Otf]<sup>-</sup>, trifluoromethanesulfonate, registered by BASF SE
- = Cl<sup>-</sup>, chloride registered by BASF SE
- = [DCA]<sup>-</sup>, N-cyanocyanamide, registered by BASF SE
- = [BF<sub>4</sub>]<sup>-</sup>, tetrafluoroborate, registered by proionic GmbH
- = [OAc]<sup>-</sup>, acetate, registered by proionic GmbH



**Figure S2:** Mixture of [PFBMIm][PF<sub>6</sub>] and [C<sub>4</sub>C<sub>1</sub>Im][PF<sub>6</sub>] at a molar ratio of 85 mol% [PFBMIm][PF<sub>6</sub>]. a) F 1s (left), N 1s (center) and C 1s (right) spectra, at 0° (black) and 80° (red) emission, acquired at a sample temperature of 95 °C. b) F 1s spectra measured at 80° emission, collected during cooling from 95 °C to lower temperatures. c) Ratio of the normalized F<sub>CF<sub>x</sub></sub> and F<sub>PF<sub>6</sub></sub> contents, obtained from spectra at 0° (black) and 80° (red) emission angle during cooling from 95 °C to lower temperatures.



## Pronounced surface enrichment of fluorinated ionic liquids in binary mixtures with methoxy-functionalized ionic liquids

Bettina S.J. Heller, Ulrike Paap, Florian Maier, Hans-Peter Steinrück\*

*Lehrstuhl für Physikalische Chemie II, Friedrich-Alexander-Universität Erlangen-Nürnberg, Egerlandstraße 3, 91058 Erlangen, Germany*

### ARTICLE INFO

#### Article history:

Received 17 December 2019

Received in revised form 20 February 2020

Accepted 25 February 2020

Available online 27 February 2020

#### Keywords:

Ionic liquid

Mixture

X-ray photoelectron spectroscopy

Surface enrichment

### ABSTRACT

Different binary mixtures of two functionalized ionic liquids (ILs), namely 1,3-di(methoxy)imidazolium hexafluorophosphate, [(MeO)<sub>2</sub>Im][PF<sub>6</sub>], and 3-methyl-1-(3,3,4,4,4-pentafluorobutyl)imidazolium hexafluorophosphate, [PFBMIm][PF<sub>6</sub>], are investigated in the liquid state by angle-resolved X-ray photoelectron spectroscopy (ARXPS). Both ILs consist of the same [PF<sub>6</sub>]<sup>−</sup> anion but differ in the functionalization of the cation: [(MeO)<sub>2</sub>Im][PF<sub>6</sub>] has an oxygen atom directly bound to each nitrogen atom of the imidazolium ring whereas in [PFBMIm][PF<sub>6</sub>] the two terminal carbon atoms of the butyl chain are fully fluorinated. Due to different electronic structures of the cations of both ILs, the ARXP signals of the two cations and of the anion can be well distinguished, which allows to identify preferential chain orientation as well as enrichment and depletion effects at the surface. In the mixtures with 50, 90 and 95 mol% [(MeO)<sub>2</sub>Im][PF<sub>6</sub>], a very pronounced enrichment of the [PFBMIm]<sup>+</sup> cation at the IL/vacuum interface is observed. The fluorinated chain points towards the vacuum side and thereby attenuates the signal of the [PF<sub>6</sub>]<sup>−</sup> anion. Decreasing the temperature from 95 °C to close to the solidification temperatures of the mixtures leads to a more pronounced surface enrichment of the [PFBMIm]<sup>+</sup> cation and of the fluorinated chain.

© 2020 The Authors. Published by Elsevier B.V. This is an open access article under the CC BY license (<http://creativecommons.org/licenses/by/4.0/>).

### 1. Introduction

Ionic liquids (ILs), salts with melting points typically below 100 °C, are nowadays used in many applications like lubrication [1–3], gas separation [4,5], extraction [6–9], energy storage [2,10] and catalysis [3,11,12], due to their unique physico-chemical properties such as their very low vapor pressure. By introducing functional groups into the IL ions or by combining various anions and cations in IL mixtures, the specific properties of the IL system can be well adapted to the respective technical requirements [6,11,13,14]. In many of the aforementioned applications, the interface of the IL and the gas phase plays a significant role, in particular for new catalysis concepts using thin films of ILs on high surface-area supports, such as Supported Ionic Liquid Phase (SILP) [15–17] materials and Solid Catalyst with Ionic Liquid Layer (SCILL) [16,18] systems. The composition of the outermost IL surface layer can be very different to the bulk composition. The thermodynamic driving force to minimize surface free energy can lead to preferential enrichment and depletion effects [19]. Moreover, some functional groups exhibit pronounced orientation effects in the outermost layer [20]. Investigating the IL/gas-vacuum interface is thus of high relevance from a fundamental point of view, in order to obtain an atomistic understanding of molecular liquid surfaces. This knowledge

will then allow for optimizing the performance of IL systems in specific applications.

For this reason, several investigations of IL mixtures [21], have been carried out using surface-sensitive techniques – often under ultra-high vacuum (UHV) conditions – such as reactive-atom scattering-laser-induced fluorescence (RAS-LIF) [22,23], time-of-flight secondary mass spectrometry (TOF-SIMS) [24,25], low-energy ion scattering (LEIS) [26], X-ray photoelectron spectroscopy (XPS) [27–34], Rutherford backscattering spectroscopy (RBS) [25,35–37], metastable induced electron spectroscopy (MIES) [38] and simulations [14,22,23,33,36,39–42]. Most of these studies addressed mixtures of non-functionalized ILs, with only a few including also functionalized ILs. We therefore set out to perform a detailed, temperature-dependent study of IL mixtures containing two functionalized ILs.

Among the many known functional moieties in ILs, alkoxy groups are of high interest. It is generally known that functionalization with oxygen atoms, that is, ester, ether or hydroxyl, often decreases the toxicity of the IL and also improves biodegradability [43,44]. Due to their ether group, additional hydrogen bond acceptor sites are present in alkoxy-functionalized ILs, which leads to interesting properties [6,45]. Alkoxy-functionalization at the imidazolium ring allows for, e.g. the transformation into N-heterocyclic carbenes (NHCs) and eventually into organometallic moieties for IL-based organometallic catalysis [45–47]. By adding unsaturated substituents to the oxygen atom, a selective extraction of metals has been proposed [45]. Alkoxy-functionalized ILs are also

\* Corresponding author.

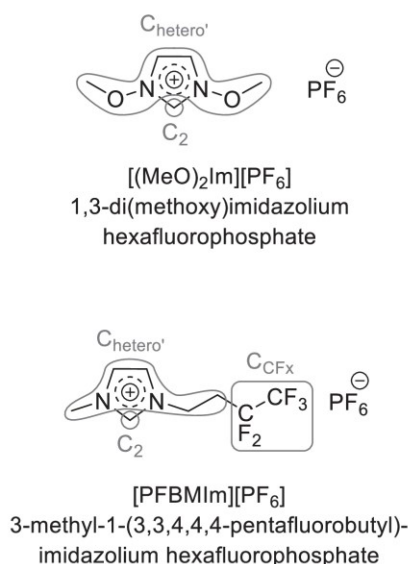
E-mail address: [hans-peter.steinrueck@fau.de](mailto:hans-peter.steinrueck@fau.de) (H.-P. Steinrück).

able to dissolve greenhouse gases like CO<sub>2</sub> [48] and N<sub>2</sub>O [49] as well as being used in liquid-phase microextraction of analgesics (e.g. ibuprofen) and estrogens from aqueous samples [6].

As one of the first surface science studies of functionalized/non-functionalized IL mixtures, we investigated the IL/vacuum interface of the alkoxy IL 1,3-di(methoxy)imidazolium hexafluorophosphate ( $[(\text{MeO})_2\text{Im}][\text{PF}_6]$ ; see Fig. 1) and its equimolar mixtures with non-functionalized ILs such as 1-methyl-3-octylimidazolium bis[(trifluoromethyl)sulfonyl]imide,  $[\text{C}_8\text{C}_1\text{Im}][\text{Tf}_2\text{N}]$ , and 1-methyl-3-octylimidazolium hexafluorophosphate,  $[\text{C}_8\text{C}_1\text{Im}][\text{PF}_6]$ , using angle-resolved XPS (ARXPS) and density functional theory (DFT) [27]. DFT showed that the electronic structure of the  $[(\text{MeO})_2\text{Im}]^+$  cation differs considerably from that of the non-functionalized  $[\text{C}_8\text{C}_1\text{Im}]^+$  cation: Due to the electron withdrawing oxygen atoms next to the imidazolium nitrogen atoms, the ring of  $[(\text{MeO})_2\text{Im}]^+$  is more positively charged, which was confirmed by the fact that the N 1s core level are strongly shifted to higher binding energy by more than 1 eV. This pronounced shift enables a clear distinction of the methoxy-functionalized and the non-functionalized cations. In the mixtures, a surface depletion of the  $[(\text{MeO})_2\text{Im}]^+$  cation relative to the  $[\text{C}_8\text{C}_1\text{Im}]^+$  cation and a surface enrichment of the  $[\text{Tf}_2\text{N}]^-$  anion relative to the  $[\text{PF}_6]^-$  anion was deduced. These deviations from the bulk compositions were attributed to the differences in surface tension of the neat ILs.

Very recently, our group published the results of ARXPS investigations on the IL/vacuum interface of the fluorine-functionalized IL 3-methyl-1-(3,3,4,4,4-pentafluorobutyl)imidazolium hexafluorophosphate ( $[\text{PFBMIm}][\text{PF}_6]$ ; see Fig. 1) and of its mixtures with the non-functionalized counterpart IL 1-butyl-3-methylimidazolium hexafluorophosphate,  $[\text{C}_4\text{C}_1\text{Im}][\text{PF}_6]$  [28]. A pronounced surface enrichment of the partially fluorinated chain with respect to the fully hydrogenated butyl chain was found at 95 °C. With decreasing temperature and with decreasing content of  $[\text{PFBMIm}][\text{PF}_6]$ , the enrichment effects were observed to be more pronounced. One drawback of this study was related to the difficulty to distinguish the imidazolium head groups by XPS because of the virtually identical imidazolium ring signals.

The data presented herein show for the first time the influence of two different functional groups on the surface composition of IL



**Fig. 1.** Structure of 1,3-di(methoxy)imidazolium hexafluorophosphate,  $[(\text{MeO})_2\text{Im}][\text{PF}_6]$ , (top) and 3-methyl-1-(3,3,4,4,4-pentafluorobutyl)imidazolium hexafluorophosphate,  $[\text{PFBMIm}][\text{PF}_6]$ , (bottom). The peak assignment in the C 1s spectra of the C<sub>2</sub>, C<sub>hetero'</sub> and C<sub>CFx</sub> is indicated in gray.

mixtures, as a function of bulk composition and temperature. Furthermore, due to the different electronic structures of  $[(\text{MeO})_2\text{Im}]^+$  and  $[\text{PFBMIm}]^+$ , with well-separated signals in the N 1s spectra, simultaneous information acquisition about the side chains in the cations and the related cationic head groups is possible by ARXPS. In comparison to the previous study [28], we find a much more pronounced enrichment of the cations with the fluorinated chain.

## 2. Experimental section

### 2.1. Materials

$[\text{PFBMIm}][\text{PF}_6]$  and  $[(\text{MeO})_2\text{Im}][\text{PF}_6]$  were synthesized as published earlier [47,50,51]. No further purification of the ILs was carried out prior to the investigations. For the preparation of the mixtures with 50, 90 and 95 mol%  $[(\text{MeO})_2\text{Im}][\text{PF}_6]$ , acetonitrile from Sigma-Aldrich (purity 99.8%) was used as a co-solvent to ensure proper mixing of  $[(\text{MeO})_2\text{Im}][\text{PF}_6]$  and  $[\text{PFBMIm}][\text{PF}_6]$ . The mixtures as well as the neat ILs were placed on a molybdenum sample holder with a thickness up to 0.5 mm. Degassing of the samples was carried out in the load-lock of our vacuum chamber for at least 12 h. Samples were measured under UHV conditions in the liquid state at 95 °C and lower temperatures till solidification occurred.

### 2.2. Angle-resolved X-ray photoelectron spectroscopy

The ARXPS measurements were performed with a monochromated Al K<sub>α</sub> X-ray source ( $h\nu = 1486.6$  eV) at a power of 238 W. The data was acquired with two identical hemispherical ARGUS-type analyzers which are mounted at  $\theta = 0^\circ$  (normal emission) and  $80^\circ$  (grazing emission) with respect to the surface normal of a horizontally mounted sample. For more details see Ref. [52]. High-resolution spectra were recorded with a pass energy of 35 eV resulting in an energy resolution of 0.4 eV. The Fermi level of a polycrystalline Au sample was used to reference the binding energy of all spectra. Small deviations from sample to sample ( $\pm 0.2$  eV) did not affect the results discussed here, and thus no corrections were applied. At lower temperatures, shifts to higher binding energies were used to detect sample solidification by XPS as has been done before [28]. For the temperature-dependent measurements, the temperature was measured directly at the molybdenum reservoir filled with IL with an accuracy of  $\pm 5$  °C [53].

Depending on the kinetic energy, the information depth of XPS in organic matter is 7 to 9 nm in  $0^\circ$  emission. At an emission angle of  $80^\circ$ , it decreases by about a factor of six, resulting in a more surface-sensitive measurement of the first 1 to 1.5 nm. To allow for visualizing enrichment/depletion effects through direct comparison, all  $80^\circ$  measurements were scaled up by an individual geometry factor to account for the overall lower transmission in this geometry (for details see Ref. [52]). Atomic sensitivity factors (ASFs) were applied to enable a quantitative analysis of the individual core levels [52]. The data were analyzed using CasaXPS (version 2.3.16Dev6), and for peak fitting a pseudo-Voigt function with 30% Lorentzian contribution was used. In general, a two-point linear background was subtracted from all spectra except for the C 1s spectra where a three-point linear background was applied. For the mixtures, the full width at half maximum (FWHM) in the N 1s spectra was set equal for the N<sub>MeO</sub> and N<sub>PF6</sub> peaks (for peak assignments, see Fig. 1 and text below), and in the F 1s spectra the FWHM of the F<sub>PF6</sub> peak was 0.79 times that of the F<sub>CFx</sub> peak. Only for the 95 mol%  $[(\text{MeO})_2\text{Im}][\text{PF}_6]$  mixture with its very small N<sub>PF6</sub> intensity, additional constraints were applied for the nitrogen peak separation ( $1.40 \pm 0.04$  eV, as deduced from the measurements of the other two mixtures) to obtain unambiguous fitting results. Since the C<sub>CF3</sub> peak of the  $[\text{PFBMIm}]^+$  cation in the C 1s spectra overlaps with the shake-up of the C<sub>hetero'</sub> peak of the imidazolium ring, the CF<sub>3</sub> signal was set equal to the CF<sub>2</sub> signal to quantify the intensity of the first one. The intensity ratio of the C<sub>hetero'</sub> and C<sub>2</sub> intensities was constraint to the nominal



ratios in the mixtures, e.g. 4:1 for neat  $[(\text{MeO})_2\text{Im}][\text{PF}_6]$  and 4.5:1 for the 50 mol%  $[(\text{MeO})_2\text{Im}][\text{PF}_6]$  mixture. For neat  $[\text{PFBMIm}][\text{PF}_6]$ , the  $\text{C}_2$  and  $\text{C}_{\text{hetero}'}$  peak separation was fixed to 1.02 eV, with the FWHM of the latter 1.33 times larger than that of the former. The spin-orbit-split P  $2p_{1/2}$  and P  $2p_{3/2}$  levels with an intensity ratio of 1:2 have equal FWHM and are separated by 0.9 eV. All XP spectra are normalized to the overall intensity of the  $[(\text{MeO})_2\text{Im}][\text{PF}_6]$  measurement to account for small differences in the photon flux of the X-rays during the course of the measurements.

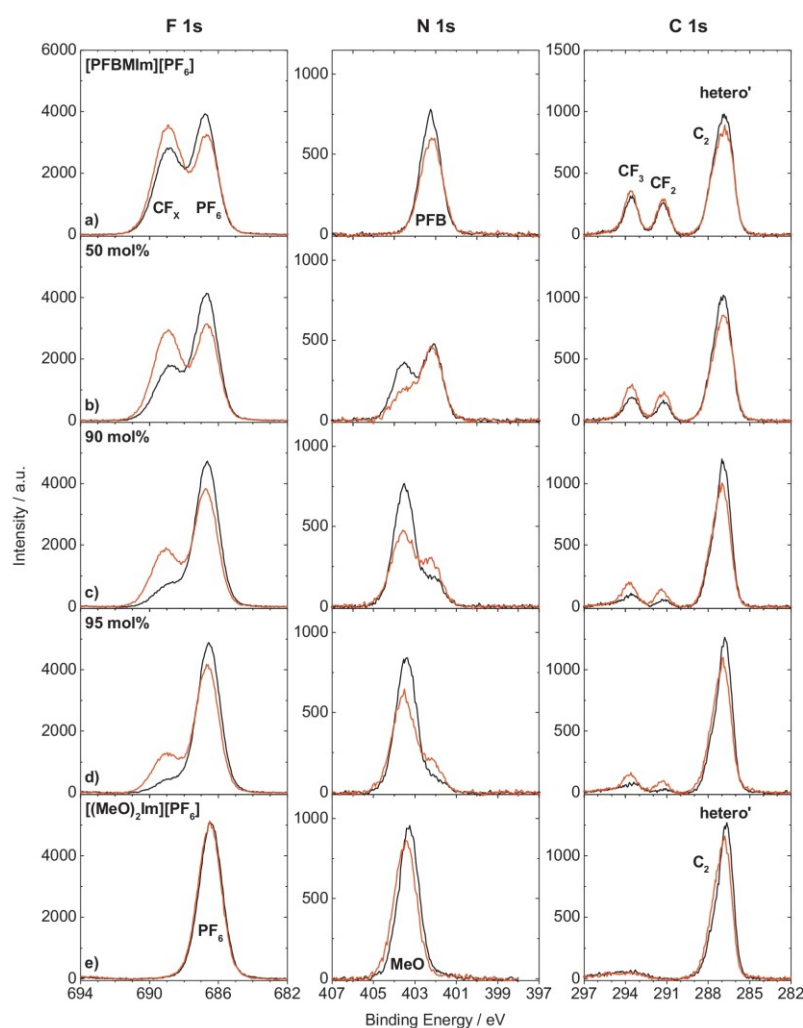
### 3. Results and discussion

We performed temperature-dependent ARXPS measurements of several mixtures of two ILs, that is, 3-methyl-1-(3,3,4,4,4-pentafluorobutyl)imidazolium hexafluorophosphate,  $[\text{PFBMIm}][\text{PF}_6]$ , and 1,3-di(methoxy)imidazolium hexafluorophosphate,  $[(\text{MeO})_2\text{Im}][\text{PF}_6]$ ; see Fig. 1. We will present data for three mixtures with 50, 90 and 95 mol%  $[(\text{MeO})_2\text{Im}][\text{PF}_6]$ . As reference data, we will also briefly address the spectra of the neat ILs which have been published recently [27,28]. The two ILs consist of the same  $[\text{PF}_6]^-$  anion, but differ in the

functionalization of their cation. To ensure measurements in the liquid state, the starting temperature was 95 °C (90 °C for  $[(\text{MeO})_2\text{Im}][\text{PF}_6]$  in Ref. [27]), because the melting point of neat  $[\text{PFBMIm}][\text{PF}_6]$  and  $[(\text{MeO})_2\text{Im}][\text{PF}_6]$  are 66 [50] and 83–84 °C, respectively [27]. In the following, we first present the spectra at 95 °C in detail, followed by the discussion of the temperature-dependent behavior (down to the different solidification temperatures as lowest limit). We will particularly focus on enrichment and depletion effects.

#### 3.1. ARXPS measurements at 95 °C

We first address the spectra of the neat ILs. The F 1s spectrum of  $[\text{PFBMIm}][\text{PF}_6]$  in Fig. 2a (left panel) shows two distinct peaks. The  $F_{\text{CF}_x}$  peak at 688.9 eV results from the fluorine atoms in the  $\text{CF}_2$  and  $\text{CF}_3$  groups in the fluorinated chain of the  $[\text{PFBMIm}]^+$  cation, and the  $F_{\text{PF}_6}$  peak at 686.8 eV from the  $[\text{PF}_6]^-$  anion. The comparison of the spectra in the two experimental geometries reveals an increase of the  $F_{\text{CF}_x}$  intensity and a decrease of the  $F_{\text{PF}_6}$  intensity at 80° compared to 0°. This behavior indicates an enrichment of the fluorinated chain due to a preferential orientation towards the vacuum side, and simultaneously



**Fig. 2.** F 1s (left), N 1s (center) and C 1s (right) spectra, at 0° (black) and 80° (red) emission: a) Neat  $[\text{PFBMIm}][\text{PF}_6]$ , b) – d) mixtures of  $[(\text{MeO})_2\text{Im}][\text{PF}_6]$  and  $[\text{PFBMIm}][\text{PF}_6]$  at molar ratios of b) 50 mol%  $[(\text{MeO})_2\text{Im}][\text{PF}_6]$ , c) 90 mol%  $[(\text{MeO})_2\text{Im}][\text{PF}_6]$  and d) 95 mol%  $[(\text{MeO})_2\text{Im}][\text{PF}_6]$ , and e) neat  $[(\text{MeO})_2\text{Im}][\text{PF}_6]$ . All spectra were acquired at a sample temperature of 95 °C and are normalized to the overall intensity of  $[(\text{MeO})_2\text{Im}][\text{PF}_6]$  to compensate for differences in X-ray flux.

a depletion of the  $[\text{PF}_6]^-$  anion, at the outermost surface. This surface enrichment of the fluorinated chain is also evident in the C 1s region (right panel) through the higher  $80^\circ$  intensity of the  $\text{C}_{\text{CF}_2}$  and  $\text{C}_{\text{CF}_3}$  peaks at 291.3 and 293.6 eV, respectively. Notably, this effect is less pronounced than for the  $\text{F}_{\text{CF}_x}$  signal due to the higher kinetic energy (1200 vs. 800 eV for F 1s) and consequently higher inelastic mean free path of the emitted C 1s electrons. In contrast, the C 1s and N 1s signals from the imidazolium head group, that is,  $\text{C}_{\text{hetero}'}$  at 286.8 eV and  $\text{C}_2$  at 287.8 eV (for assignment see Fig. 1) and  $\text{N}_{\text{PF}_6}$  at 402.2 eV, show a lower signal at  $80^\circ$  than at  $0^\circ$ . The same is true for the  $\text{P}_{\text{PF}_6}$  peak of the  $[\text{PF}_6]^-$  anion, which is centered at 137.0 eV (Figs. S1a and S2). The decrease of these peaks at  $80^\circ$  is explained by the enrichment of the fluorinated chain of the  $[\text{PFBMIm}]^+$  cation at the IL/vacuum interface, which leads to an attenuation of the signals from species underneath. Notably, both the quantitative analysis provided in Table 1a, and the absence of any detectable signals of common surface active impurities in the O 1s and Si 2p regions (Figs. S1a and S2) confirm a high purity of  $[\text{PFBMIm}][\text{PF}_6]$  within the detection limits of XPS [20].

Next, we discuss the ARXP spectra of neat  $[(\text{MeO})_2\text{Im}][\text{PF}_6]$  in Fig. 2e, measured at  $95^\circ\text{C}$ , which are virtually identical to those reported at  $90^\circ\text{C}$  [27]. In the F 1s region (left panel), the  $\text{F}_{\text{PF}_6}$  peak of the  $[\text{PF}_6]^-$  anion is located at 686.5 eV; the corresponding  $\text{P}_{\text{PF}_6}$  peak in the P 2p region is located at 136.7 eV (see Figs. S1e and S3). The peaks of the  $[(\text{MeO})_2\text{Im}]^+$  cation are detected at the following energies:  $\text{O}_{\text{MeO}}$  at 535.0 eV,  $\text{N}_{\text{MeO}}$  at 403.3 eV,  $\text{C}_2$  at 287.8 eV and  $\text{C}_{\text{hetero}'}$  at 286.7 eV. Notably, the  $\text{N}_{\text{MeO}}$  signal of  $[(\text{MeO})_2\text{Im}][\text{PF}_6]$  is located at +1.1 eV higher binding energy than the  $\text{N}_{\text{PF}_6}$  signal of  $[\text{PFBMIm}][\text{PF}_6]$ , which is due to a difference in the electronic structure of the cations as shown by DFT calculations combined with atomic charge analysis by our group [27]. This difference in N 1s binding energy allows for unambiguous identification and analysis of surface enrichment/depletion effects of the cationic head groups in the mixtures by ARXPS. The comparison of the neat  $[(\text{MeO})_2\text{Im}][\text{PF}_6]$  spectra recorded in  $0^\circ$  and  $80^\circ$  emission shows no difference in the F 1s region and only minor differences in the N 1s and C 1s peak areas (Table 1e), indicating the absence of significant

surface enrichment or depletion for any part of  $[(\text{MeO})_2\text{Im}][\text{PF}_6]$ . Again, the good agreement of the quantitative analysis in Table 1e and the absence of any detectable signals in the Si 2p region (Figs. S1e and S3) confirms a high purity of this IL within the detection limits of XPS [20].

After discussing the two neat ILs, we turn to mixtures of  $[(\text{MeO})_2\text{Im}][\text{PF}_6]$  and  $[\text{PFBMIm}][\text{PF}_6]$  in three different compositions, with 50, 90 and 95 mol%  $[(\text{MeO})_2\text{Im}][\text{PF}_6]$ . In the analysis of the spectra, we are particularly interested in obtaining information about selective enrichment/depletion of the cations in those mixtures. The F 1s, N 1s and C 1s spectra measured at a temperature of  $95^\circ\text{C}$  are shown in Fig. 2b – 2d, and in Figs. S4, S5 and S6; spectra in black are measured at  $0^\circ$ , spectra in red at  $80^\circ$  emission angle. The corresponding O 1s and P 2p regions are shown in Fig. S1b – S1d, and in Figs. S4, S5 and S6. The binding energy positions of the peaks in the mixtures are in accordance with the peak positions detected in the neat ILs to within  $\pm 0.2$  eV. In the F 1s region (Fig. 2b – 2d-left panel), two peaks are detected. The  $\text{F}_{\text{CF}_x}$  peak at  $\sim 688.8$  eV solely stems from the fluorinated chain of the  $[\text{PFBMIm}]^+$  cation of one IL, and the  $\text{F}_{\text{PF}_6}$  peak at  $\sim 686.6$  eV is due to the common  $[\text{PF}_6]^-$  anion of both ILs in the mixture. The decreasing intensity of the  $\text{F}_{\text{CF}_x}$  peak at  $0^\circ$  upon increasing the  $[(\text{MeO})_2\text{Im}]^+$  content from 0 mol% (a), to 50 mol% (b), to 90 mol% (c) and finally to 95 mol% (d) reflects the decreasing  $[\text{PFBMIm}]^+$  content of the mixtures. Interestingly, the decrease of the  $\text{F}_{\text{CF}_x}$  peak is much less pronounced at  $80^\circ$ : Relative to the intensities measured in  $0^\circ$ , the  $80^\circ$  spectra of the 50, 90 and 95 mol% mixtures show an increase of the  $\text{F}_{\text{CF}_x}$  intensity by a factor of 1.68, 2.55 and 2.87, respectively, which indicates a selective surface enrichment of the cation with the fluorinated chain. At the same time, the relative intensity of the  $\text{F}_{\text{PF}_6}$  peak decreases by a factor of 0.75, 0.81 and 0.86 in  $80^\circ$  for the 50, 90 and 95 mol%  $[(\text{MeO})_2\text{Im}][\text{PF}_6]$  mixtures, respectively. This decrease is attributed to the preferential orientation of the fluorinated chain towards the vacuum side, and the resulting attenuation of the  $[\text{PF}_6]^-$  signal relative to the bulk composition. This effect was already observed for neat  $[\text{PFBMIm}][\text{PF}_6]$  and is maintained in the mixtures.

**Table 1**

Quantitative analysis of the  $0^\circ$  and  $80^\circ$  XP spectra of  $[\text{PFBMIm}][\text{PF}_6]$ ,  $[(\text{MeO})_2\text{Im}][\text{PF}_6]$  and their mixtures with 50, 90 and 95 mol%  $[(\text{MeO})_2\text{Im}][\text{PF}_6]$  at  $95^\circ\text{C}$ . The ASFs are taken into account as published earlier [52].

a) $[\text{PFBMIm}][\text{PF}_6]$	F 1s $\text{F}_{\text{CF}_x}$	F 1s $\text{F}_{\text{PF}_6}$	O 1s $\text{O}_{\text{MeO}}$	N 1s $\text{N}_{\text{MeO}}$	N 1s $\text{N}_{\text{PF}_6}$	C 1s $\text{C}_{\text{CF}_x}$	C 1s $\text{C}_2$	C 1s $\text{C}_{\text{hetero}'}$	P 2p $\text{P}_{\text{PF}_6}$
Binding Energy/eV	688.9	686.8	—/—	—/—	402.2	291.3/293.6	287.8	286.8	137.0
ASF	1.00	1.00	0.67	0.46	0.46	0.30	0.30	0.30	0.46
Nominal	5.00	6.00	—/—	—/—	2.00	2.00	1.00	5.00	1.00
$0^\circ$ emission	5.55	5.99	—/—	—/—	1.93	1.84	0.99	4.61	1.08
$80^\circ$ emission	7.04	5.00	—/—	—/—	1.69	2.12	1.03	4.14	0.99
b) 50 mol% $[(\text{MeO})_2\text{Im}][\text{PF}_6]$	$\text{F}_{\text{CF}_x}$	$\text{F}_{\text{PF}_6}$	$\text{O}_{\text{MeO}}$	$\text{N}_{\text{MeO}}$	$\text{N}_{\text{PF}_6}$	$\text{C}_{\text{CF}_x}$	$\text{C}_2$	$\text{C}_{\text{hetero}'}$	$\text{P}_{\text{PF}_6}$
Nominal	2.89	6.94	1.16	1.16	1.16	1.16	1.16	5.20	1.16
$0^\circ$ emission	3.71	6.84	0.97	0.97	1.26	1.16	1.06	4.78	1.21
$80^\circ$ emission	6.25	5.17	0.50	0.53	1.30	1.82	0.96	4.34	1.09
c) 90 mol% $[(\text{MeO})_2\text{Im}][\text{PF}_6]$	$\text{F}_{\text{CF}_x}$	$\text{F}_{\text{PF}_6}$	$\text{O}_{\text{MeO}}$	$\text{N}_{\text{MeO}}$	$\text{N}_{\text{PF}_6}$	$\text{C}_{\text{CF}_x}$	$\text{C}_2$	$\text{C}_{\text{hetero}'}$	$\text{P}_{\text{PF}_6}$
Nominal	0.66	7.95	2.38	2.38	0.26	0.26	1.32	5.43	1.32
$0^\circ$ emission	1.55	7.91	2.13	2.05	0.45	0.38	1.20	4.9	1.41
$80^\circ$ emission	3.97	6.47	1.43	1.38	0.80	1.04	1.10	4.53	1.27
d) 95 mol% $[(\text{MeO})_2\text{Im}][\text{PF}_6]$	$\text{F}_{\text{CF}_x}$	$\text{F}_{\text{PF}_6}$	$\text{O}_{\text{MeO}}$	$\text{N}_{\text{MeO}}$	$\text{N}_{\text{PF}_6}$	$\text{C}_{\text{CF}_x}$	$\text{C}_2$	$\text{C}_{\text{hetero}'}$	$\text{P}_{\text{PF}_6}$
Nominal	0.34	8.10	2.56	2.56	0.13	0.14	1.35	5.47	1.35
$0^\circ$ emission	0.93	8.14	2.47	2.33	0.20	0.16	1.25	5.06	1.46
$80^\circ$ emission	2.68	7.03	1.90	1.78	0.52	0.62	1.20	4.88	1.39
e) $[(\text{MeO})_2\text{Im}][\text{PF}_6]^a$	$\text{F}_{\text{CF}_x}$	$\text{F}_{\text{PF}_6}$	$\text{O}_{\text{MeO}}$	$\text{N}_{\text{MeO}}$	$\text{N}_{\text{PF}_6}$	$\text{C}_{\text{CF}_x}$	$\text{C}_2$	$\text{C}_{\text{hetero}'}$	$\text{P}_{\text{PF}_6}$
Binding Energy/eV	—/—	686.5	535.0	403.3	—/—	—/—	287.8	286.7	136.7
Nominal	—/—	6.00	2.00	2.00	—/—	—/—	1.00	4.00	1.00
$0^\circ$ emission	—/—	6.29	2.03	1.90	—/—	—/—	0.93	3.73	1.10
$80^\circ$ emission	—/—	6.30	2.04	1.86	—/—	—/—	0.93	3.72	1.15

<sup>a</sup> Note that the binding energies of all core levels are by 0.3 eV smaller than those in Ref. [27].

In the N 1s region of the three mixtures, we observe two peaks, the  $N_{MeO}$  peak due to the  $[(MeO)_2Im]^+$  cation at  $\sim 403.5$  eV, and the  $N_{PF6}$  peak due to the  $[PF6Im]^+$  cation at  $\sim 402.1$  eV. In the mixture with 50 mol%  $[(MeO)_2Im][PF_6]$ , the intensities of the  $N_{PF6}$  peak at  $0^\circ$  and  $80^\circ$  emission are identical within the margin of error, whereas the intensity of the  $N_{MeO}$  peak is by a factor of 0.55 smaller at  $80^\circ$ . These relative intensities contain information about the position of the cationic head groups of the two ILs in the mixture relative to each other. From the observed behavior, we conclude that the  $[PF6Im]^+$  cation is preferentially located closer to the IL/vacuum interface compared to the  $[(MeO)_2Im]^+$  cation, which is in line with the surface enrichment of the fluorinated chains discussed above.

We attribute the observed surface enrichment behavior in the mixtures to the fact that the system tries to minimize its surface free energy. As shown recently by a comparative ARXPS and molecular dynamic simulation study [54], groups generally lowering the surface tension for ILs such as long alkyl chains [55] are preferentially surface-enriched whereas groups leading to an increase in surface tension are surface-depleted. Typically, ILs with a fluorinated chain exhibit a lower surface tension compared to their alkylated IL counterparts [22,42]. This is underlined by the surface enrichment of the fluorinated chains of the  $[PF6Im]^+$  cations with respect to the butyl chains recently deduced by ARXPS for mixtures of  $[PF6Im][PF_6]$  and  $[C_4C_1Im][PF_6]$  [28]. Unfortunately, the exact surface tension values of  $[PF6Im][PF_6]$  and  $[(MeO)_2Im][PF_6]$  are not known yet at any temperatures. It is nevertheless reasonable to assume that the former has a lower surface tension than the latter. At least what is known for imidazolium cations containing oxygen is that the surface tension of a polyethylene glycol IL,  $[Me(EG)_2C_1Im][Tf_2N]$ , with two oxygen atoms in the side chain is larger than the surface tension of  $[C_8C_1Im][Tf_2N]$  [56], which is in line with our argumentation.

For the 90 and 95 mol%  $[(MeO)_2Im][PF_6]$  mixtures, we find the same trend as for the 50 mol% mixture, but the enrichment/depletion effects are more pronounced. With respect to the bulk composition, we see an increase of the  $N_{PF6}$  signal by a factor of 1.78 and 2.65, respectively, when going from  $0^\circ$  to  $80^\circ$ , while the  $N_{MeO}$  signal decreases by a factor of 0.67 and 0.76, respectively. Remarkably, (without applying any constraints) the depletion behavior of the  $O_{MeO}$  peak is identical to that of the  $N_{MeO}$  signal (to within 3%), indicating a reliability of our measurements because these two atoms are directly bound to each other. The surface enrichment of the  $[PF6Im]^+$  cation with its fluorinated chain is also evident from the C 1s spectra: The intensities of the  $C_{CF_3}$  and  $C_{CF_2}$  peaks also strongly increase when changing the detection angle from  $0^\circ$  to  $80^\circ$  emission. The other two signals of the IL mixtures, that is,  $C_2 + C_{hetero}$  and  $P_{PF_6}$ , are damped by up to 10% due to the attenuation by the surface-enriched fluorinated chain. The pronounced enrichment and depletion of the ions in the mixtures can also be deduced from the quantitative analysis of all signals in Table 1b–d.

For further analysis of the enrichment/depletion of the different cations in the mixture, we plotted the normalized content, that is, the ratio of the experimentally determined content and the nominal content (see Table 1) in Fig. 3a for  $80^\circ$  emission. A value of 1.0 represents the situation, where the surface composition is identical to that in the bulk, a value larger than 1.0 indicates surface enrichment of the respective atom. The red squares represent the normalized  $F_{CFx}$  content of the fluorinated chain of the  $[PF6Im]^+$  cation. The higher the mole fraction of  $[(MeO)_2Im][PF_6]$  in the mixture, the higher is the normalized  $F_{CFx}$  content, and thus the surface enrichment of the fluorinated chain. The same trend, but less pronounced holds true for the  $N_{PF6}$  content (blue triangles), which reflects the enrichment of the whole  $[PF6Im]^+$  cation since the  $N_{PF6}$  signal originates from the cationic head group. In contrast, the normalized  $N_{MeO}$  content (orange diamonds) is below the nominal ratio, indicating a depletion of the  $[(MeO)_2Im]^+$  cation from the surface. The graph also contains the normalized  $F_{PF_6}$  content (green circles) representing all anions in the mixtures. The normalized  $F_{PF_6}$  ratio is close to the nominally expected ratio included as gray

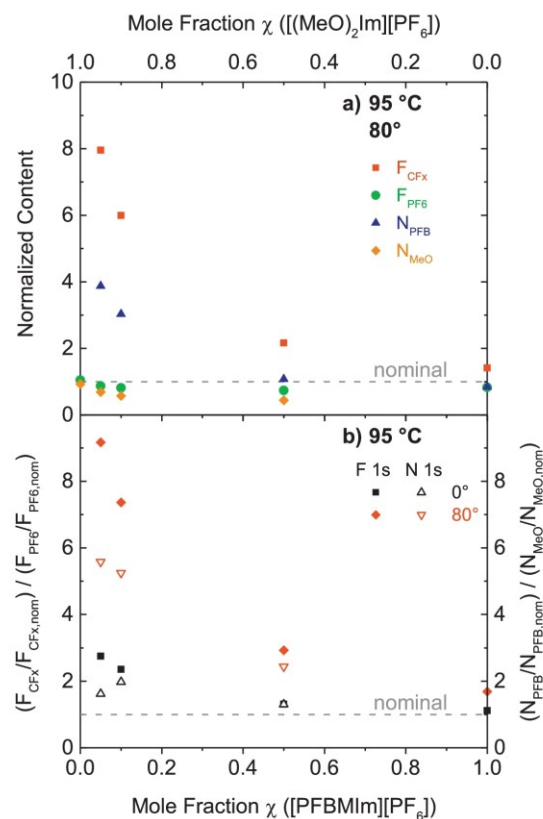


Fig. 3. a) Normalized content of  $F_{CFx}$  (red squares),  $F_{PF_6}$  (green circles),  $N_{PF_6}$  (blue triangles) and  $N_{MeO}$  (orange diamonds). b) Ratio of the normalized  $F_{CFx}$  and  $F_{PF_6}$  contents (full symbols) and ratio of the normalized  $N_{PF_6}$  and  $N_{MeO}$  content (open symbols) at  $0^\circ$  (black) and  $80^\circ$  (red). The sample temperature was  $95^\circ C$ . The dashed gray lines indicate the nominal ratios.

dashed line. This is not unexpected due to charge neutrality reasons: Each imidazolium ring is preferentially located close to the counter anion. The  $F_{PF_6}$  signal thus represents in a first approximation the mean localization of the charged head groups.

In Fig. 3b, we thus plot the ratio of the normalized  $F_{CFx}$  and  $F_{PF_6}$  signals (full symbols; from Fig. 3a) vs. the mole fraction of the ILs (top scale for mole fraction of  $[(MeO)_2Im]^+$ , bottom scale for mole fraction of  $[PF6Im]^+$ ) for the  $0^\circ$  (black squares) and the  $80^\circ$  (red diamonds) data. Notably, for neat  $[PF6Im][PF_6]$ , the value of  $\sim 1.8$  at  $80^\circ$  as compared to  $\sim 1.1$  at  $0^\circ$  reflects the preferential orientation of the  $[PF6Im]^+$  cations with the fluorinated chains pointing towards the vacuum in the outermost surface layer. Larger ratio values than 1.8 in the mixtures indicate an enrichment of the  $[PF6Im]^+$  cations with their fluorinated chains by preferential surface segregation at the cost of the  $[(MeO)_2Im]^+$  cations. At  $80^\circ$  emission, we find values of  $\sim 2.9$ ,  $\sim 7.4$  and  $\sim 9.2$  for the mixtures with 50, 90 and 95 mol%  $[(MeO)_2Im][PF_6]$ , respectively, which indicates an increasingly pronounced surface enrichment of the  $[PF6Im]^+$  cation (relative to its concentration in the bulk). In our previous work [28], we investigated mixtures of  $[PF6Im][PF_6]$  and  $[C_4C_1Im][PF_6]$ , which also showed an enrichment of the fluorinated chain of the  $[PF6Im]^+$  cation compared to the  $[C_4C_1Im]^+$  cation. However, the enrichment effects were much less pronounced, that is, for a mixture with 90 mol%  $[C_4C_1Im][PF_6]$  a ratio of the normalized  $F_{CFx}$  and  $F_{PF_6}$  contents of  $\sim 3.5$  was observed (as compared to  $\sim 7.4$  here) at  $80^\circ$  emission angle and a temperature of  $95^\circ C$  [28]. Notably, the very pronounced surface enrichment of the  $[PF6Im]^+$  cation for the 90 and

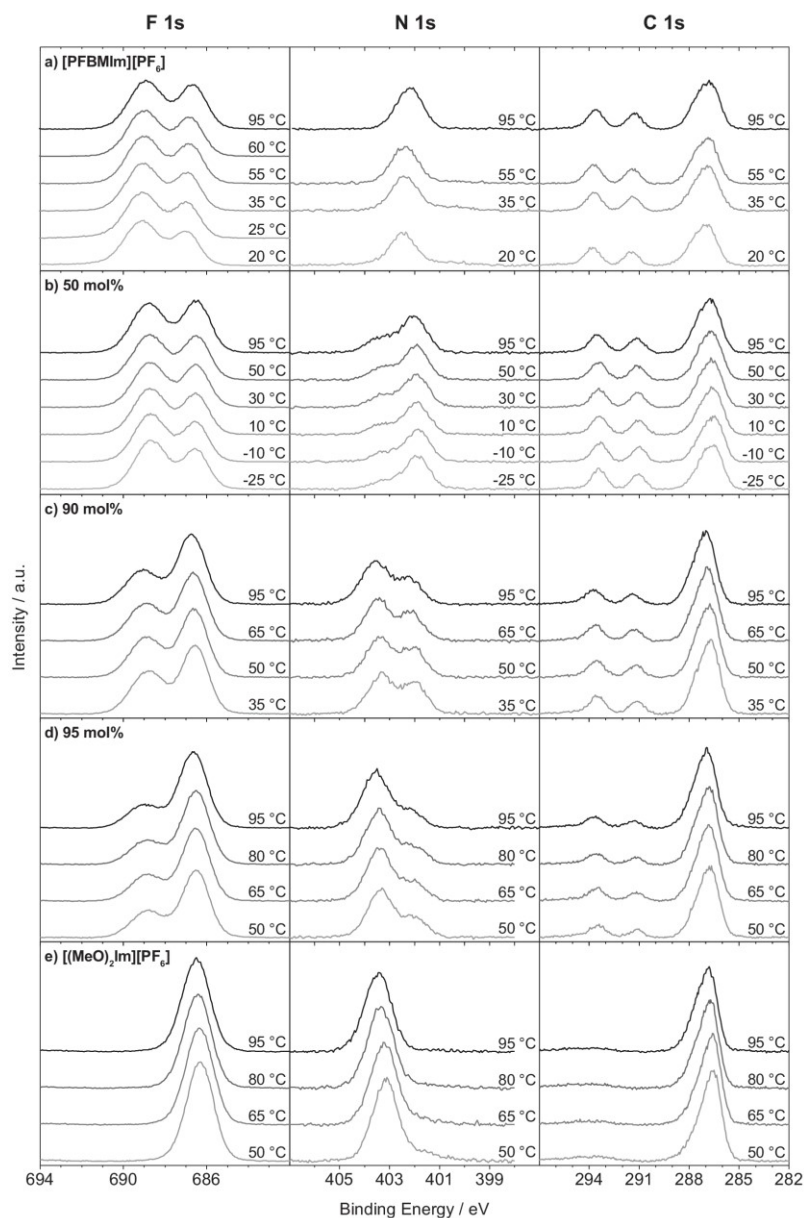
95 mol% [(MeO)<sub>2</sub>Im][PF<sub>6</sub>] mixtures can even be observed in the much more bulk-sensitive 0° geometry, where XPS integrates over the first 7 to 9 nm (see Fig. 3b), as shown for different systems by our group and others [27,28,33].

The ratios of the normalized N<sub>PFB</sub> and N<sub>MeO</sub> contents along with the nominal value (gray dashed line) are shown in Fig. 3b (open symbols). Overall, we observe the same trend as for the F<sub>CFX</sub> and F<sub>PF6</sub> data. This behavior confirms that with higher [(MeO)<sub>2</sub>Im][PF<sub>6</sub>] content a more pronounced enrichment of the [PFBMIm]<sup>+</sup> cation occurs compared to the [(MeO)<sub>2</sub>Im]<sup>+</sup> cation, which means that the [PFBMIm]<sup>+</sup> cation is located closer to the IL/vacuum interface than the other head group. Interestingly, the effect of surface enrichment is less pronounced than for the

F<sub>CFX</sub> and F<sub>PF6</sub> data (i.e. at 90 mol% the ratio is ~5.2 instead of ~7.4 for the latter). This is attributed to the fact that the N<sub>PFB</sub> and N<sub>MeO</sub> show only the effect of the relative enrichment of the cations, whereas the F<sub>CFX</sub> and F<sub>PF6</sub> data include the preferential enrichment of the fluorinated chain (see above).

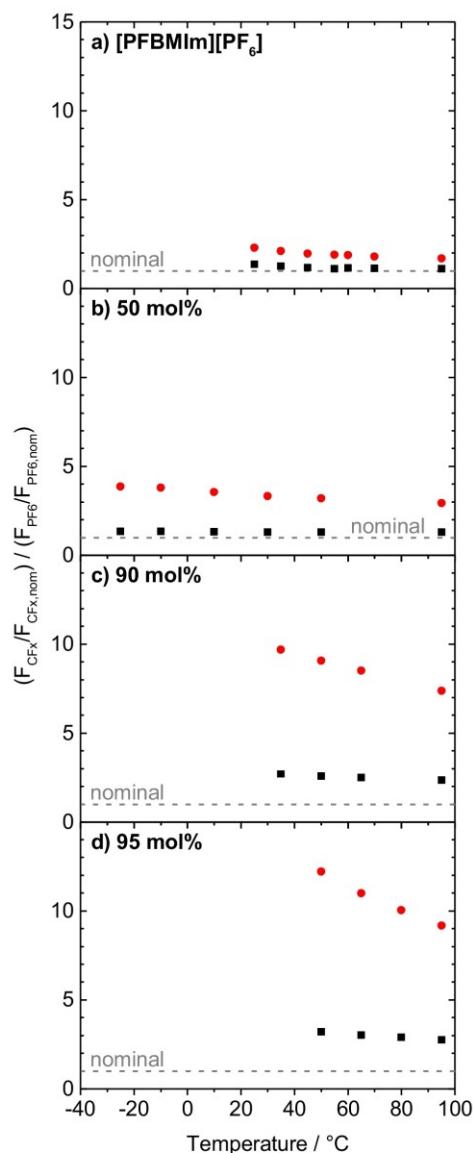
### 3.2. Temperature-dependent ARXPS

After having discussed the results at the highest temperature of 95 °C, we now address the temperature-dependent XP spectra, starting with the two neat ILs during cooling to the onset of solidification. Since changes in enrichment and depletion are more obvious at 80° electron



**Fig. 4.** F 1s, N 1s and C 1s spectra measured at 80° emission during cooling from 95 °C to lower temperatures: a) Neat [PFBMIm][PF<sub>6</sub>], b) – d) mixtures of [(MeO)<sub>2</sub>Im][PF<sub>6</sub>] and [PFBMIm][PF<sub>6</sub>] at molar ratios of b) 50 mol% [(MeO)<sub>2</sub>Im][PF<sub>6</sub>], c) 90 mol% [(MeO)<sub>2</sub>Im][PF<sub>6</sub>] and d) 95 mol% [(MeO)<sub>2</sub>Im][PF<sub>6</sub>], and e) neat [(MeO)<sub>2</sub>Im][PF<sub>6</sub>]. The intensities are normalized to the overall intensity of [(MeO)<sub>2</sub>Im][PF<sub>6</sub>] to compensate for differences in X-ray flux.

emission, we focus from here on only on these surface-sensitive spectra. First, we summarize the cooling experiments of [PFBMIm][PF<sub>6</sub>] from 95 °C to its onset of solidification around 20 °C, which have been described in more detail elsewhere [28]. Note the solidification occurs significantly below the melting point of 66 °C [50], which is indicative of a supercooling. In the left panel of Fig. 4a, decreasing the temperature leaves the F<sub>CFX</sub> signal almost unchanged, whereas the F<sub>PF6</sub> signal decreases significantly. The resulting relative increase of the F<sub>CFX</sub> intensity compared to the F<sub>PF6</sub> intensity upon lowering the temperature (see Fig. 5a) is attributed to a more pronounced orientation of the fluorinated side chains towards the vacuum side, with the polar head groups more confined underneath. This interpretation is confirmed by a



**Fig. 5.** Ratio of the normalized F<sub>CFX</sub> and F<sub>PF6</sub> content, at 0° (black squares) and 80° (red circles) emission, obtained during cooling from 95 °C to lower temperatures. a) Neat [PFBMIm][PF<sub>6</sub>], b) – d) mixtures of [(MeO)<sub>2</sub>Im][PF<sub>6</sub>] and [PFBMIm][PF<sub>6</sub>] at molar ratios of b) 50 mol% [(MeO)<sub>2</sub>Im][PF<sub>6</sub>], c) 90 mol% [(MeO)<sub>2</sub>Im][PF<sub>6</sub>] and d) 95 mol% [(MeO)<sub>2</sub>Im][PF<sub>6</sub>], and e) neat [(MeO)<sub>2</sub>Im][PF<sub>6</sub>]: Not shown due to the lack of F<sub>CFX</sub> signal of a fluorinated side chain. The dashed horizontal lines indicate the nominal composition.

concomitant small decrease in N<sub>PF6</sub> and C<sub>hetero</sub> intensity originating from the cationic head group (see Fig. 4a-middle and right panels). It should be mentioned that a small shoulder at lower binding energies evolves in the C 1s and N 1s region at lower temperatures due to some beam damage [57,58] of the IL by the extended X-ray exposure, which does not affect the conclusions derived here. The overall small shift of all peaks to higher binding energy upon cooling is attributed to the onset of charging in the supercooled phase, which starts already at around 60 °C.

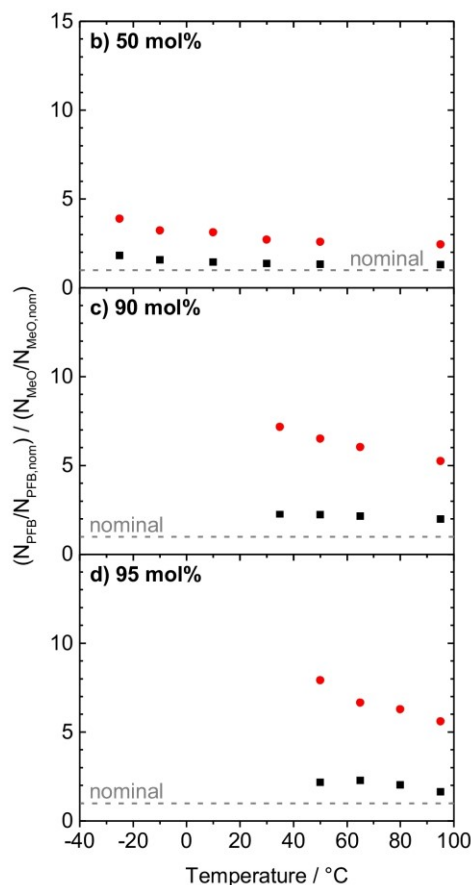
Similar to [PFBMIm][PF<sub>6</sub>], neat [(MeO)<sub>2</sub>Im][PF<sub>6</sub>] can be supercooled well below its melting point without pronounced charging effects due to solidification. In Fig. 4e, selected spectra from 95 °C down to 50 °C are shown; note that beam damage effects become also visible at lower temperatures by a second peak arising in the N 1s spectra (see Fig. S7e-middle panel). Apart from this effect, no significant intensity changes with decreasing temperature are seen in the F 1s, N 1s and C 1s regions. Hence, no significant preferential orientation occurs in the surface layer of [(MeO)<sub>2</sub>Im][PF<sub>6</sub>] even at 50 °C. Note that a moderate shift towards lower binding energies takes place (overall –0.3 eV between the 95 and 50 °C spectra), which is attributed to the beam damage effect mentioned above; when heating the sample back to 95 °C, all peaks shift back to their original binding energy position and the shoulder in the N 1s spectrum is more or less gone.

Finally, we discuss the temperature dependence of the mixtures with 50, 90 and 95 mol% [(MeO)<sub>2</sub>Im][PF<sub>6</sub>]. The corresponding F 1s, N 1s and C 1s spectra for selected temperatures are shown in Fig. 4b–d. Depending on the composition of the mixture, the lower temperature limits for XPS measurements of the (supercooled) liquids differ. In general, the lower the [(MeO)<sub>2</sub>Im][PF<sub>6</sub>] content, the lower the solidification temperature, as indicated by the onset of charging of the samples. During cooling down from 95 °C, for all mixtures the enrichment/depletion effects described in the previous section become much more pronounced. In Fig. 5b–d, the quantitative analysis, that is, the ratios of the normalized F<sub>CFX</sub> and F<sub>PF6</sub> contents are depicted. While this ratio remains almost constant with decreasing temperature in 0° emission for the three mixtures, in 80° emission it increases significantly. The effect is most pronounced for the mixture with 95 mol% [(MeO)<sub>2</sub>Im][PF<sub>6</sub>], reaching a value of ~12.2 at 50 °C compared to 9.2 at 95 °C. This is mainly due to an increase of the F<sub>CFX</sub> intensity and a less pronounced decrease of the F<sub>PF6</sub> intensity. We observe the same trend in the N 1s region (see Fig. 4b–d-middle panel): The N<sub>MeO</sub> intensity decreases with decreasing temperature whereas the N<sub>PF6</sub> signal increases. The ratio of the normalized N<sub>PF6</sub> and N<sub>MeO</sub> contents in Fig. 6b–d increases in 80° emission when decreasing the temperature. This again implies the increase of the surface enrichment of the [PFBMIm]<sup>+</sup> cation along with a surface depletion of the [(MeO)<sub>2</sub>Im]<sup>+</sup> cation upon cooling the mixtures. In the C 1s region (Fig. 4b–d-right panel), a slight enrichment of the C<sub>CF2</sub> and C<sub>CF3</sub> peaks is detected but due to the low mole fraction of [PFBMIm][PF<sub>6</sub>] in the mixtures changes are less obvious than for the F<sub>CFX</sub> signal.

We attribute the observed overall behavior mostly to entropic reasons. At lower temperature, the enthalpic driving force of surface enrichment of the [PFBMIm]<sup>+</sup> cation with its fluorinated chain, which lowers the surface tension of the mixture, dominates. At higher temperatures, the entropic term  $-T \cdot \Delta S^\circ$  (note that  $\Delta S^\circ$  is negative because of the demixing effect by surface enrichment) gains weight and induces a decrease in surface order towards a more random distribution of the [(MeO)<sub>2</sub>Im]<sup>+</sup> and [PFBMIm]<sup>+</sup> cations with their fluorinated chains. Thus, when cooling from 95 °C to lower temperature, we observe an increase of surface enrichment due to a smaller entropic contribution to the free energy.

#### 4. Conclusions

We present temperature-dependent angle-resolved X-ray photoelectron spectroscopy measurements of mixtures of two functionalized



**Fig. 6.** Ratio of the normalized  $N_{PFB}$  and  $N_{MeO}$  content, at 0° (black squares) and 80° (red circles) emission, obtained during cooling from 95 °C to lower temperatures. a) Neat [PFBMIm][PF<sub>6</sub>]; Not shown due to the lack of  $N_{MeO}$  signal, b) – d) mixtures of [(MeO)<sub>2</sub>Im][PF<sub>6</sub>] and [PFBMIm][PF<sub>6</sub>] at molar ratios of b) 50 mol% [(MeO)<sub>2</sub>Im][PF<sub>6</sub>], c) 90 mol% [(MeO)<sub>2</sub>Im][PF<sub>6</sub>] and d) 95 mol% [(MeO)<sub>2</sub>Im][PF<sub>6</sub>], and e) neat [(MeO)<sub>2</sub>Im][PF<sub>6</sub>]; Not shown due to the lack of  $N_{PFB}$  signal. The dashed horizontal lines indicate the nominal composition.

ILs with the same [PF<sub>6</sub>]<sup>−</sup> anion in the liquid state. [PFBMIm][PF<sub>6</sub>] is fully fluorinated at the two terminal carbon atoms of the butyl chain whereas [(MeO)<sub>2</sub>Im][PF<sub>6</sub>] contains an oxygen atom next to each nitrogen atom of the imidazolium ring. Measurements were performed for the two neat ILs and for mixtures with 50, 90 and 95 mol% [(MeO)<sub>2</sub>Im][PF<sub>6</sub>], from 95 °C to lower temperatures. While no surface enrichment is observed for neat [(MeO)<sub>2</sub>Im][PF<sub>6</sub>], a moderate surface enrichment of the fluorinated chain is found for neat [PFBMIm][PF<sub>6</sub>], which is attributed to a preferential orientation of the chains towards the vacuum in order to minimize surface free energy. Decreasing the [PFBMIm][PF<sub>6</sub>] content in the mixtures by adding more and more [(MeO)<sub>2</sub>Im][PF<sub>6</sub>] shows a significantly more pronounced enrichment of the fluorinated chain and of the cationic head group of the [PFBMIm]<sup>+</sup> cation compared to the bulk composition. This strong enrichment is attributed to preferential surface segregation of the [PFBMIm]<sup>+</sup> cations replacing the [(MeO)<sub>2</sub>Im]<sup>+</sup> cations in this interface region. By decreasing the temperature of the mixtures till solidification is reached, these effects become even more pronounced. Our study shows that the introduction of suitable functional groups in IL molecules for controlling surface activity and the suitable choice of composition using IL mixtures allow for modifying the surface of an IL system to a large extent, which is important for many large-surface area applications involving IL films.

### CRediT authorship contribution statement

**Bettina S.J. Heller:** Conceptualization, Methodology, Validation, Formal analysis, Investigation, Writing - original draft, Writing - review & editing, Visualization. **Ulrike Paap:** Validation, Investigation, Writing - review & editing. **Florian Maier:** Conceptualization, Writing - review & editing, Supervision, Project administration. **Hans-Peter Steinrück:** Conceptualization, Writing - review & editing, Supervision, Funding acquisition.

### Declaration of competing interest

The authors declare that they have no known competing financial interests or personal relationships that could have appeared to influence the work reported in this paper.

### Acknowledgments

We thank G. Partl and S. Dommer for providing us with [PFBMIm][PF<sub>6</sub>] and [(MeO)<sub>2</sub>Im][PF<sub>6</sub>], respectively. B.S.J.H., U.P. and H.-P.S. thank the European Research Council (ERC) under the European Union's Horizon 2020 research and innovation programme for financial support, in the context of the Advanced Investigator Grant "ILID" to H.-P.S. (Grant Agreement No. 693398-ILID).

### Appendix A. Supplementary data

Supplementary data to this article can be found online at <https://doi.org/10.1016/j.molliq.2020.112783>.

### References

- [1] H. Xiao, Tribol. Trans. 60 (2017) 20–30.
- [2] T. Torimoto, T. Tsuda, K.-i. Okazaki, S. Kuwabata, Adv. Mater. 22 (2010) 1196–1221.
- [3] H.-P. Steinrück, P. Wasserscheid, Catal. Lett. 145 (2015) 380–397.
- [4] C.F. Poole, S.K. Poole, J. Sep. Sci. 34 (2011) 888–900.
- [5] L. Zhou, J. Fan, X. Shang, Materials 7 (2014) 3867–3880.
- [6] F. Meischl, M. Harder, C.G. Kirchner, J. Krenser, C.W. Huck, G.K. Bonn, M. Rainer, J. Mol. Liq. 289 (2019), 111157.
- [7] P. Sun, D.W. Armstrong, Anal. Chim. Acta 661 (2010) 1–16.
- [8] R.I. Canales, J.F. Brennecke, J. Chem. Eng. Data 61 (2016) 1685–1699.
- [9] M.J. Trujillo-Rodríguez, H. Nan, M. Varona, M.N. Emaus, I.D. Souza, J.L. Anderson, Anal. Chem. 91 (2019) 505–531.
- [10] S. Tsuzuki, T. Umecky, H. Matsumoto, W. Shinoda, M. Mikami, J. Phys. Chem. B 114 (2010) 11390–11396.
- [11] N.V. Plechkova, K.R. Seddon, Chem. Soc. Rev. 37 (2008) 123–150.
- [12] S. Marullo, C. Rizzo, F. D'Anna, Front. Chem. 7 (2019) 134.
- [13] M.L. Ferreira, M.J. Pastoriza-Gallego, J.M.M. Araújo, J.N. Canongia Lopes, L.P.N. Rebelo, M.M. Piñeiro, K. Shimizu, A.B. Pereira, J. Phys. Chem. C 121 (2017) 5415–5427.
- [14] A.S.L. Gouveia, C.E.S. Bernardes, E.I. Lozinskaya, A.S. Shaplov, J.N. Canongia Lopes, I.M. Marrucho, Phys. Chem. Chem. Phys. 21 (2019) 23305–23309.
- [15] J.M. Marinkovic, A. Riisager, R. Franke, P. Wasserscheid, M. Haumann, Ind. Eng. Chem. Res. 58 (2019) 2409–2420.
- [16] H.-P. Steinrück, J. Libuda, P. Wasserscheid, T. Cremer, C. Kolbeck, M. Laurin, F. Maier, M. Sobota, P.S. Schulz, M. Stark, Adv. Mater. 23 (2011) 2571–2587.
- [17] A. Riisager, R. Fehrmann, M. Haumann, B.S.K. Gorle, P. Wasserscheid, Ind. Eng. Chem. Res. 44 (2005) 9853–9859.
- [18] U. Kemchen, B. Etzold, W. Korth, A. Jess, Chem. Eng. Technol. 30 (2007) 985–994.
- [19] H.-P. Steinrück, Phys. Chem. Chem. Phys. 14 (2012) 5010–5029.
- [20] C. Kolbeck, I. Niedermaier, A. Deyko, K.R.J. Lovelock, N. Taccardi, W. Wei, P. Wasserscheid, F. Maier, H.-P. Steinrück, Chem. Eur. J. 20 (2014) 3954–3965.
- [21] H. Niedermeyer, J.P. Hallett, I.J. Villar-Garcia, P.A. Hunt, T. Welton, Chem. Soc. Rev. 41 (2012) 7780–7802.
- [22] E.J. Smoll Jr., M.A. Tesa-Serrate, S.M. Purcell, L. D'Andrea, D.W. Bruce, J.M. Slattery, M.L. Costen, T.K. Minton, K.G. McKendrick, Faraday Discuss. 206 (2018) 497–522.
- [23] D.W. Bruce, C.P. Cabry, J.N. Canongia Lopes, M.L. Costen, L. D'Andrea, I. Grillo, B.C. Marshall, K.G. McKendrick, T.K. Minton, S.M. Purcell, S. Rogers, J.M. Slattery, K. Shimizu, E. Smoll, M.A. Tesa-Serrate, J. Phys. Chem. B 121 (2017) 6002–6020.
- [24] R. Souda, Surf. Sci. 604 (2010) 1694–1697.
- [25] K. Nakajima, M. Miyashita, M. Suzuki, K. Kimura, J. Chem. Phys. 139 (2013) 224701.
- [26] I.J. Villar-Garcia, S. Fearn, N.L. Ismail, A.J.S. McIntosh, K.R.J. Lovelock, Chem. Commun. 51 (2015) 5367–5370.
- [27] B.S.J. Heller, C. Kolbeck, I. Niedermaier, S. Dommer, J. Schatz, P. Hunt, F. Maier, H.-P. Steinrück, ChemPhysChem 19 (2018) 1733–1745.
- [28] B.S.J. Heller, M. Lexow, F. Greco, S. Shin, G. Partl, F. Maier, H.-P. Steinrück, Chem. Eur. J. 26 (2020) 1117–1126.

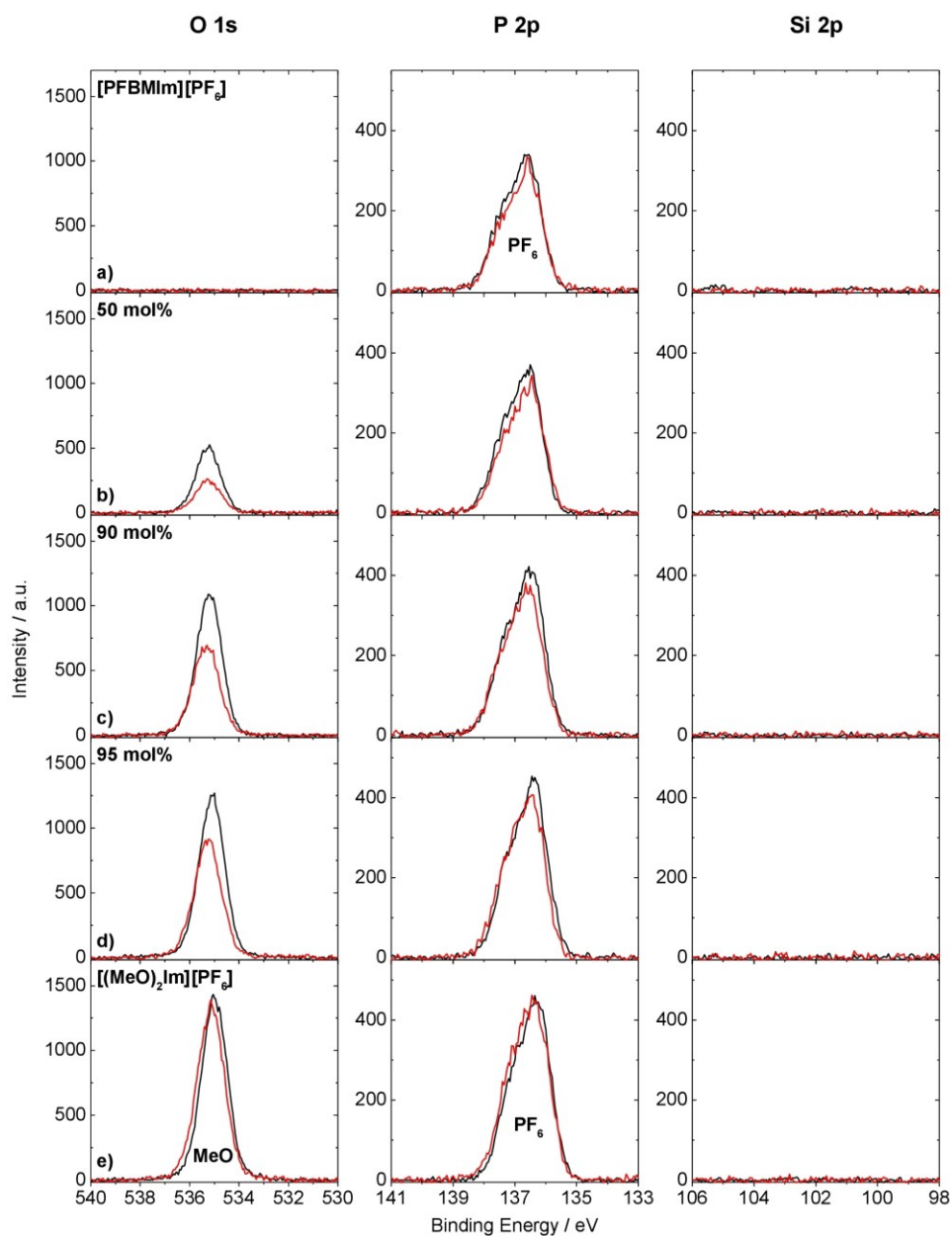
- [29] S. Men, P. Licence, Chem. Phys. Lett. 681 (2017) 40–43.
- [30] S. Men, P. Licence, Chem. Phys. Lett. 686 (2017) 74–77.
- [31] F. Maier, T. Cremer, C. Kolbeck, K.R.J. Lovelock, N. Paape, P.S. Schulz, P. Wasserscheid, H.-P. Steinrück, Phys. Chem. Chem. Phys. 12 (2010) 1905–1915.
- [32] I.J. Villar-García, K.R.J. Lovelock, S. Men, P. Licence, Chem. Sci. 5 (2014) 2573–2579.
- [33] Y. Zhang, Y. Khalifa, E.J. Maginn, J.T. Newberg, J. Phys. Chem. C 122 (2018) 27392–27401.
- [34] S. Men, K.R.J. Lovelock, P. Licence, Phys. Chem. Chem. Phys. 13 (2011) 15244–15255.
- [35] K. Nakajima, S. Oshima, M. Suzuki, K. Kimura, Surf. Sci. 606 (2012) 1693–1699.
- [36] K. Nakajima, S. Nakanishi, Z. Chval, M. Lísal, K. Kimura, J. Chem. Phys. 145 (2016) 184704.
- [37] K. Nakajima, S. Nakanishi, M. Lísal, K. Kimura, J. Mol. Liq. 230 (2017) 542–549.
- [38] C. Ridings, G.G. Warr, G.G. Andersson, J. Phys. Chem. Lett. 8 (2017) 4264–4267.
- [39] O. Hollóczki, M. Macchiagodena, H. Weber, M. Thomas, M. Brehm, A. Stark, O. Russina, A. Triolo, B. Kirchner, ChemPhysChem 16 (2015) 3325–3333.
- [40] S. Palchowdhury, B.L. Bhargava, Phys. Chem. Chem. Phys. 17 (2015) 19919–19928.
- [41] S. Palchowdhury, B.L. Bhargava, J. Phys. Chem. B 120 (2016) 5430–5441.
- [42] A. Luís, K. Shimizu, J.M.M. Araújo, P.J. Carvalho, J.A. Lopes-da-Silva, J.N. Canongia Lopes, L.P.N. Rebelo, J.A.P. Coutinho, M.G. Freire, A.B. Pereira, Langmuir 32 (2016) 6130–6139.
- [43] Y. Deng, P. Besse-Hoggan, M. Sancelme, A.-M. Delort, P. Husson, M.F. Costa Gomes, J. Hazard. Mater. 198 (2011) 165–174.
- [44] C. Froschauer, R. Salchner, G. Laus, H.K. Weber, R. Tessadri, U. Griesser, K. Wurst, V. Kahlenberg, H. Schottenberger, Aust. J. Chem. 66 (2013) 391–395.
- [45] G. Laus, A. Schwärzler, G. Bentivoglio, M. Hummel, V. Kahlenberg, K. Wurst, E. Kristeva, J. Schütz, H. Kopacka, C. Kreutz, G. Bonn, Y. Andriyko, G. Nauer, H. Schottenberger, Z. Naturforsch. 63b (2008) 447–464.
- [46] G. Laus, K. Wurst, V. Kahlenberg, H. Kopacka, C. Kreutz, H. Schottenberger, Z. Naturforsch. 65b (2010) 776–782.
- [47] G. Laus, A. Schwärzler, P. Schuster, G. Bentivoglio, M. Hummel, K. Wurst, V. Kahlenberg, T. Lörting, J. Schütz, P. Peringer, G. Bonn, G. Nauer, H. Schottenberger, Z. Naturforsch. 62b (2007) 295–308.
- [48] A.-L. Revelli, F. Mutelet, J.-N. Jaubert, J. Phys. Chem. B 114 (2010) 12908–12913.
- [49] A.-L. Revelli, F. Mutelet, J.-N. Jaubert, J. Phys. Chem. B 114 (2010) 8199–8206.
- [50] M. Lexow, B.S.J. Heller, G. Partl, R.G. Bhuin, F. Maier, H.-P. Steinrück, Langmuir 35 (2019) 398–405.
- [51] S. Bartz, B. Blumenröder, A. Kern, J. Fleckenstein, S. Frohnepfel, J. Schatz, A. Wagner, Z. Naturforsch. 64b (2009) 629–638.
- [52] I. Niedermaier, C. Kolbeck, H.-P. Steinrück, F. Maier, Rev. Sci. Instrum. 87 (2016), 045105.
- [53] R.G. Bhuin, P. Schreiber, B.S.J. Heller, M. Scheuermeyer, P. Wasserscheid, H.-P. Steinrück, F. Maier, J. Mol. Liq. 275 (2019) 290–296.
- [54] K. Shimizu, B.S.J. Heller, F. Maier, H.-P. Steinrück, J.N. Canongia Lopes, Langmuir 34 (2018) 4408–4416.
- [55] M. Tariq, M.G. Freire, B. Saramago, J.A.P. Coutinho, J.N. Canongia Lopes, L.P.N. Rebelo, Chem. Soc. Rev. 41 (2012) 829–868.
- [56] C. Kolbeck, J. Lehmann, K.R.J. Lovelock, T. Cremer, N. Paape, P. Wasserscheid, A.P. Fröba, F. Maier, H.-P. Steinrück, J. Phys. Chem. B 114 (2010) 17025–17036.
- [57] T. Cremer, M. Stark, A. Deyko, H.-P. Steinrück, F. Maier, Langmuir 27 (2011) 3662–3671.
- [58] C. Kolbeck, T. Cremer, K.R.J. Lovelock, N. Paape, P.S. Schulz, P. Wasserscheid, F. Maier, H.-P. Steinrück, J. Phys. Chem. B 113 (2009) 8682–8688.

## **Supporting Information**

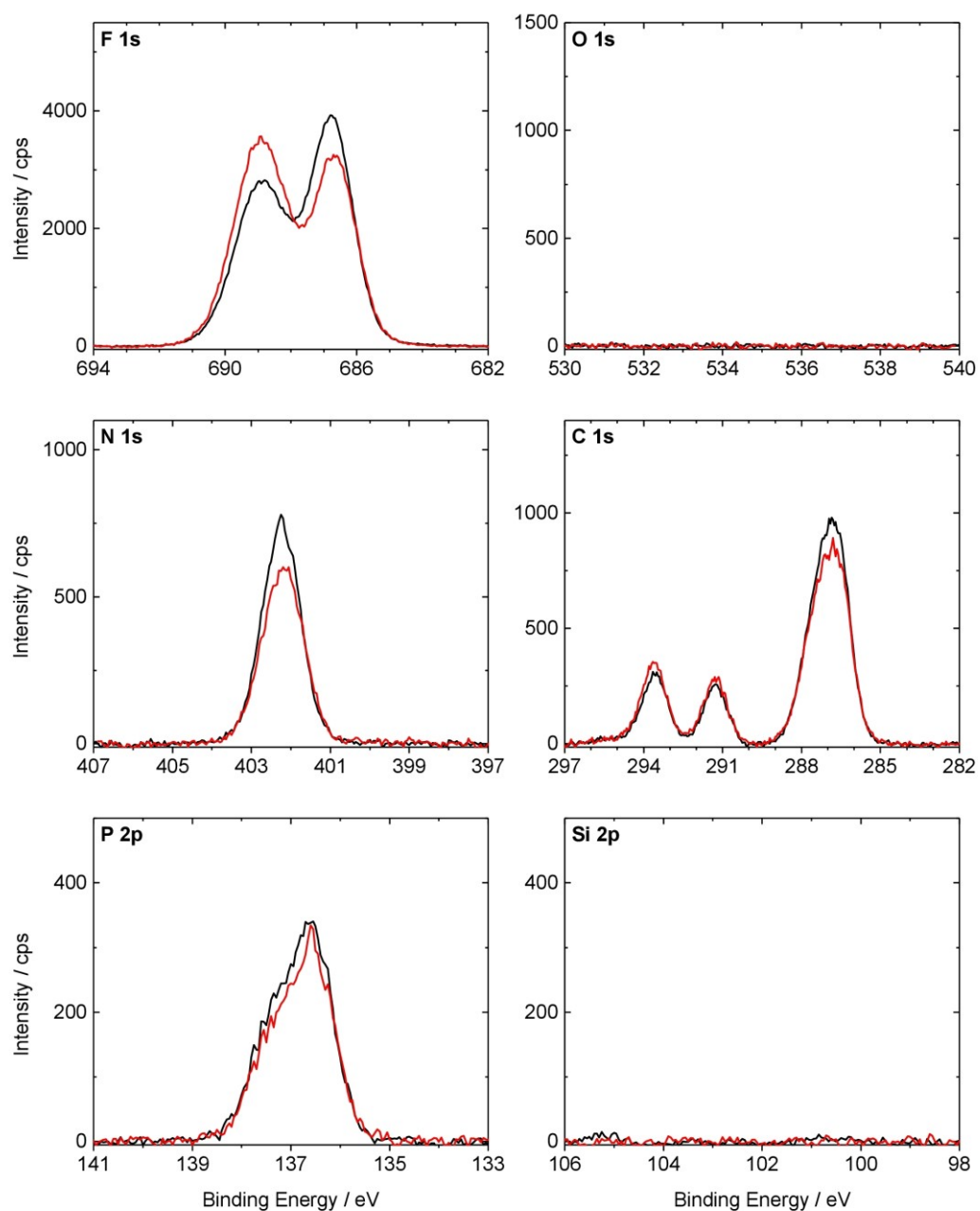
### **Pronounced surface enrichment of fluorinated ionic liquids in binary mixtures with methoxy-functionalized ionic liquids**

Bettina S. J. Heller, Ulrike Paap, Florian Maier, Hans-Peter Steinrück

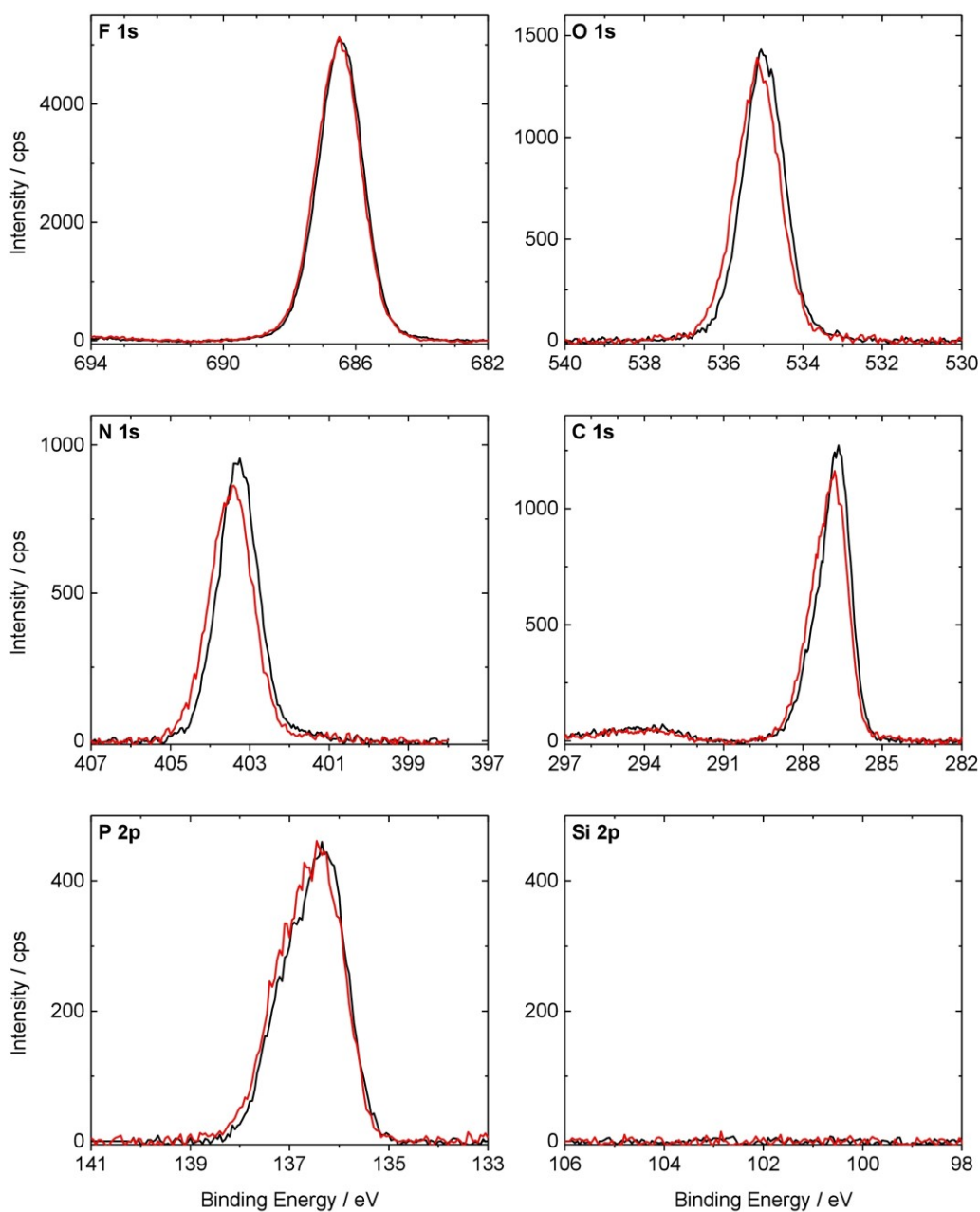




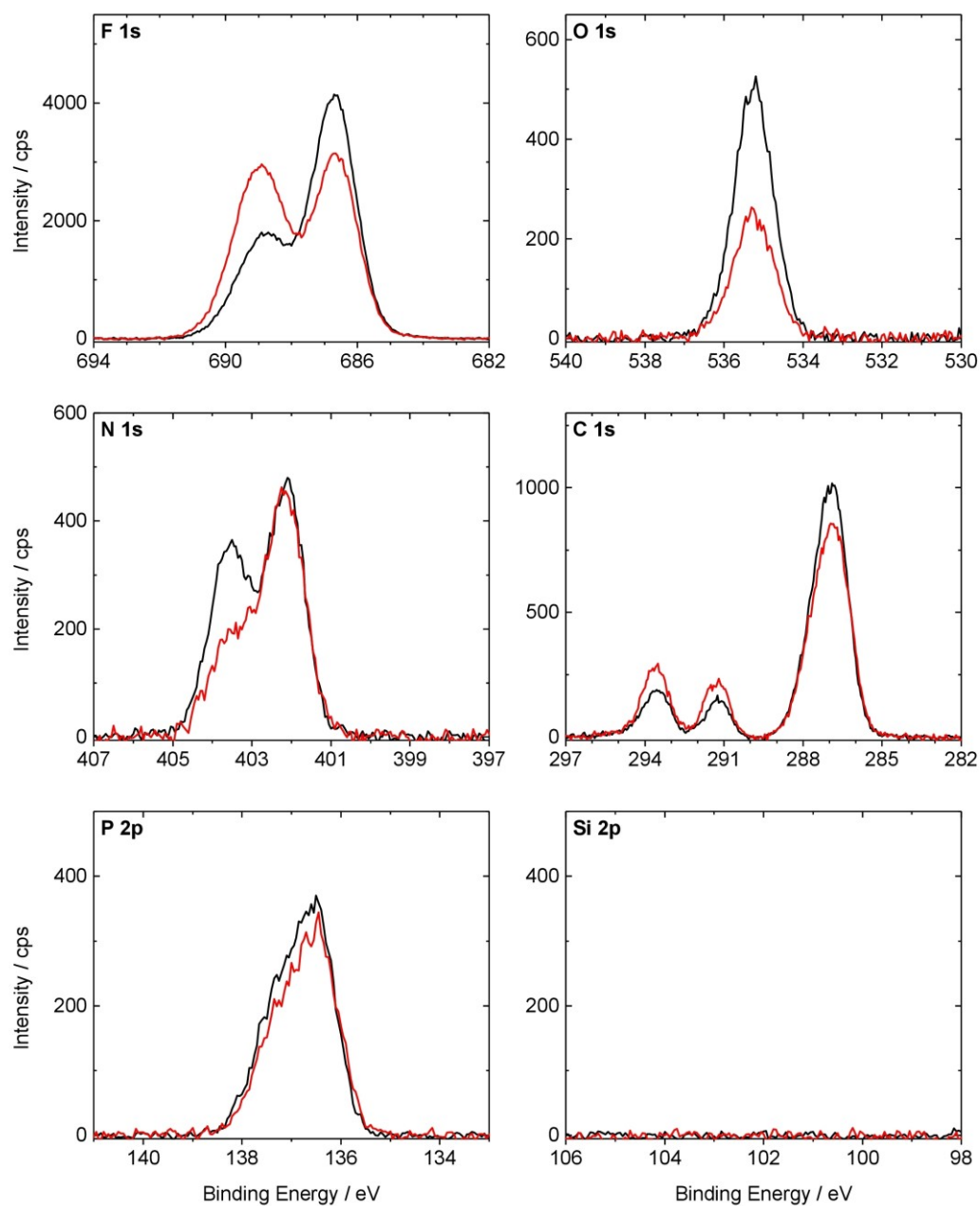
**Figure S1:** O 1s (left), P 2p (center) and Si 2p (right) spectra, at 0° (black) and 80° (red) emission: a) Neat [PFBMIm][PF<sub>6</sub>], b) – d) mixtures of [(MeO)<sub>2</sub>Im][PF<sub>6</sub>] and [PFBMIm][PF<sub>6</sub>] at molar ratios of b) 50 mol% [(MeO)<sub>2</sub>Im][PF<sub>6</sub>], c) 90 mol% [(MeO)<sub>2</sub>Im][PF<sub>6</sub>] and d) 95 mol% [(MeO)<sub>2</sub>Im][PF<sub>6</sub>], and e) neat [(MeO)<sub>2</sub>Im][PF<sub>6</sub>]. All spectra were acquired at a sample temperature of 95 °C and are normalized to the overall intensity of [(MeO)<sub>2</sub>Im][PF<sub>6</sub>] to compensate for differences in X-ray flux.



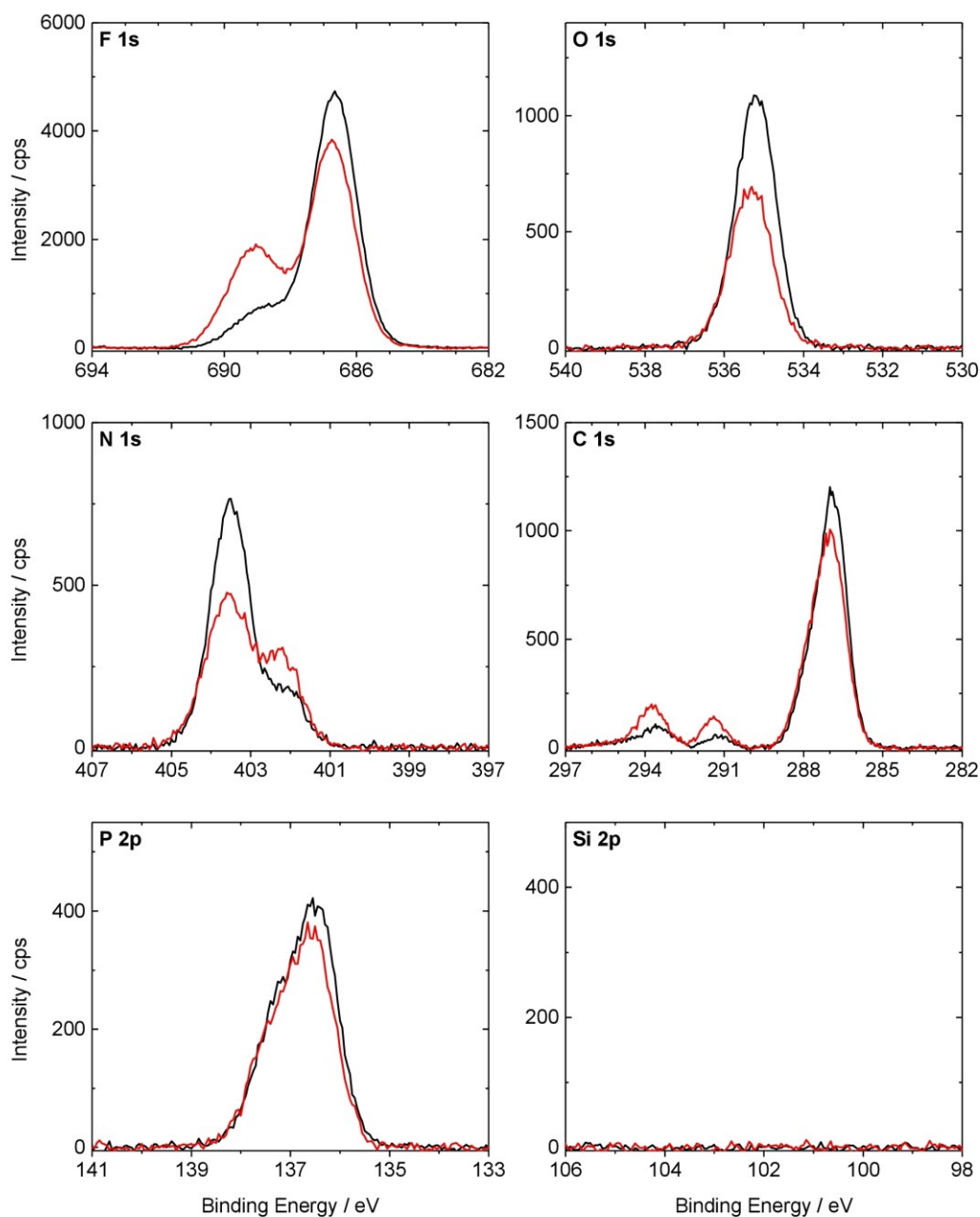
**Figure S2:** F 1s, O 1s, N 1s, C 1s, P 2p and Si 2p spectra of [PFBMIm][PF<sub>6</sub>] in 0° (black) and 80° (red) emission, measured at 95 °C and normalized to the overall intensity of [(MeO)<sub>2</sub>Im][PF<sub>6</sub>] to compensate for differences in X-ray flux.



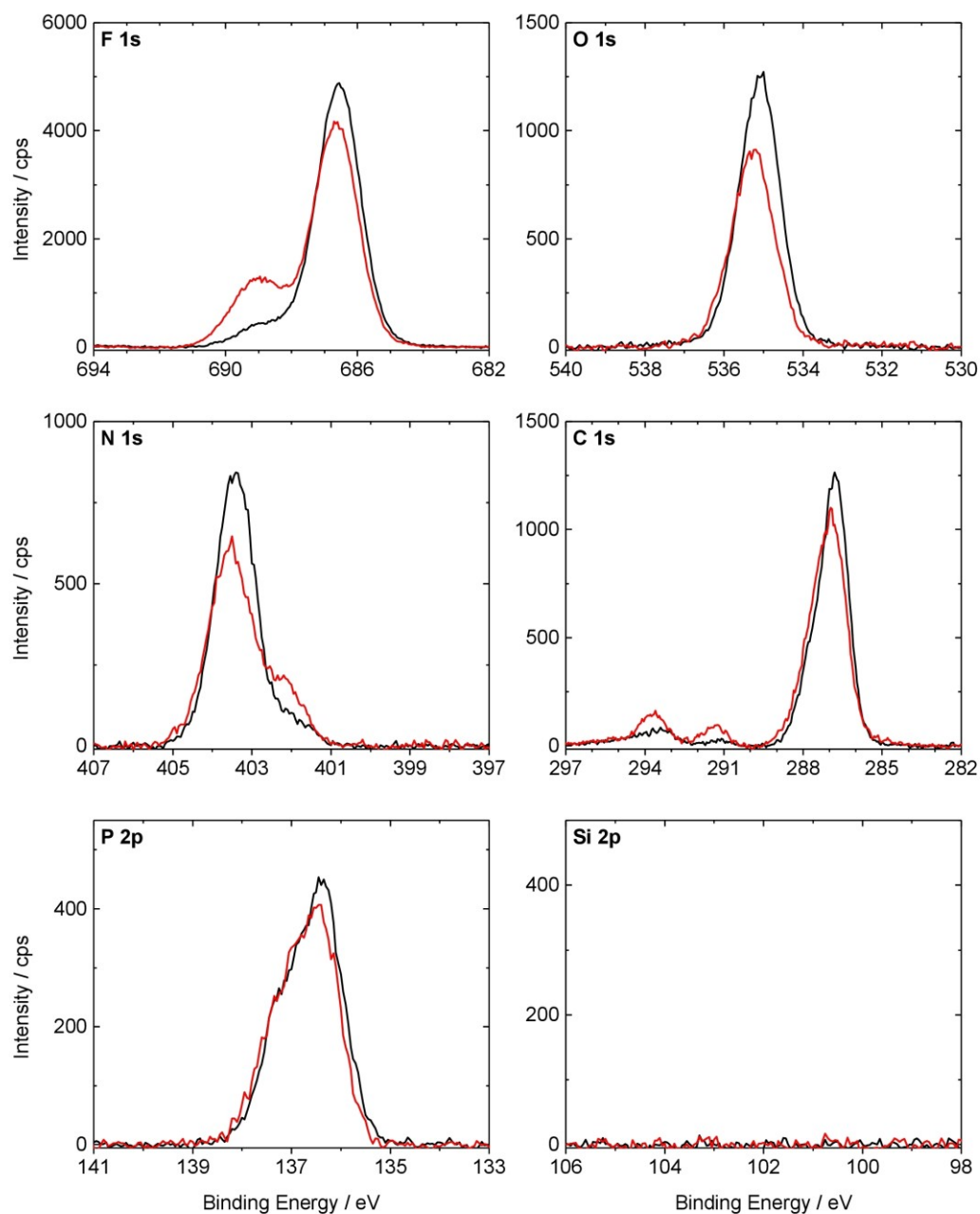
**Figure S3:** F 1s, O 1s, N 1s, C 1s, P 2p and Si 2p spectra of  $[(\text{MeO})_2\text{Im}][\text{PF}_6]$  in  $0^\circ$  (black) and  $80^\circ$  (red) emission, measured at  $95^\circ\text{C}$ .



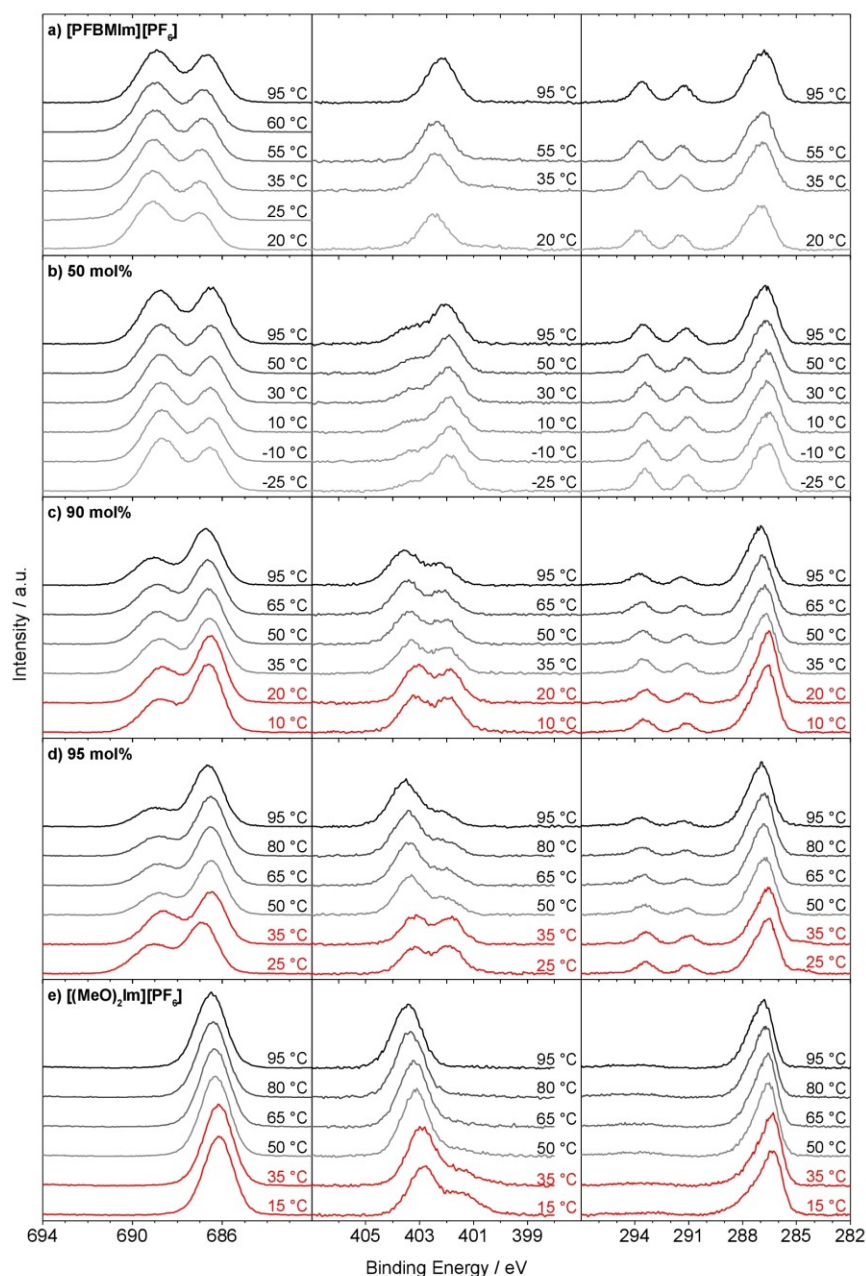
**Figure S4:** F 1s, O 1s, N 1s, C 1s, P 2p and Si 2p spectra of a mixture of  $[(\text{MeO})_2\text{Im}][\text{PF}_6]$  and  $[\text{PFBMIm}][\text{PF}_6]$  with 50 mol%  $[(\text{MeO})_2\text{Im}][\text{PF}_6]$  content in  $0^\circ$  (black) and  $80^\circ$  (red) emission, measured at  $95^\circ\text{C}$  and normalized to the overall intensity of  $[(\text{MeO})_2\text{Im}][\text{PF}_6]$  to compensate for differences in X-ray flux.



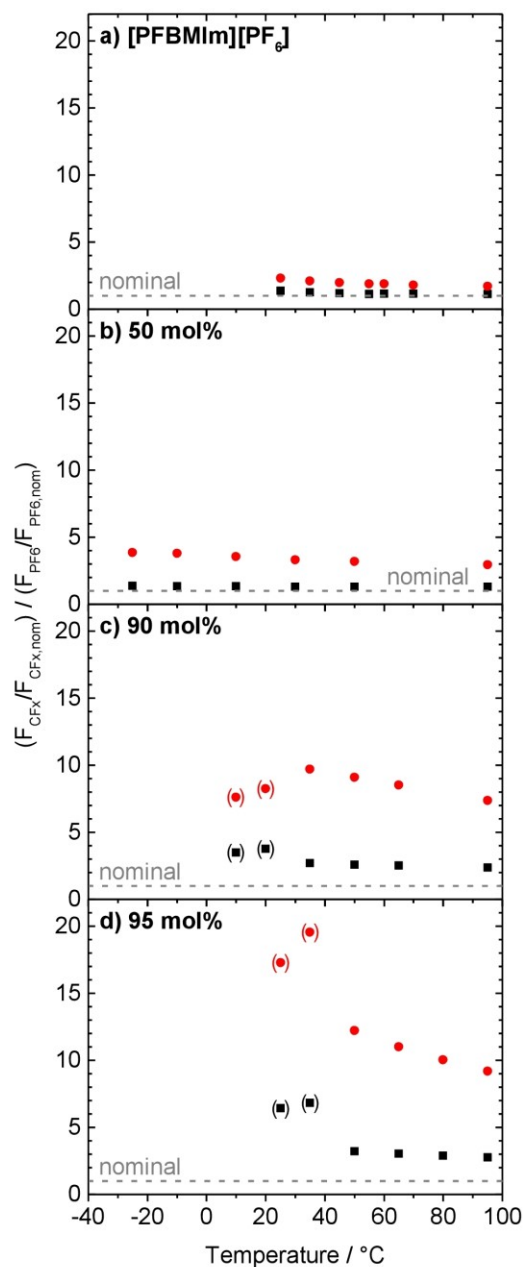
**Figure S5:** F 1s, O 1s, N 1s, C 1s, P 2p and Si 2p spectra of a mixture of  $[(\text{MeO})_2\text{Im}][\text{PF}_6]$  and  $[\text{PFBMIm}][\text{PF}_6]$  with 90 mol%  $[(\text{MeO})_2\text{Im}][\text{PF}_6]$  content in  $0^\circ$  (black) and  $80^\circ$  (red) emission, measured at  $95^\circ\text{C}$  and normalized to the overall intensity of  $[(\text{MeO})_2\text{Im}][\text{PF}_6]$  to compensate for differences in X-ray flux.



**Figure S6:** F 1s, O 1s, N 1s, C 1s, P 2p and Si 2p spectra of a mixture of [(MeO)<sub>2</sub>Im][PF<sub>6</sub>] and [PFBMIm][PF<sub>6</sub>] with 95 mol% [(MeO)<sub>2</sub>Im][PF<sub>6</sub>] content in 0° (black) and 80° (red) emission, measured at 95 °C and normalized to the overall intensity of [(MeO)<sub>2</sub>Im][PF<sub>6</sub>] to compensate for differences in X-ray flux.

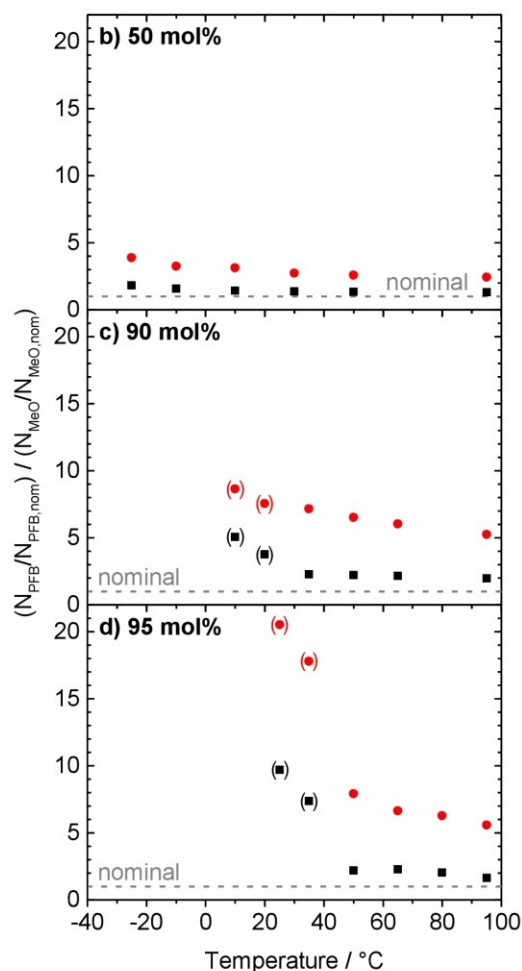


**Figure S7:** F 1s, N 1s and C 1s spectra measured at 80° emission during cooling from 95 °C to lower temperatures including the spectra when solidification was observed (red): a) Neat [PFBMIm][PF<sub>6</sub>], b) – d) mixtures of [(MeO)<sub>2</sub>Im][PF<sub>6</sub>] and [PFBMIm][PF<sub>6</sub>] at molar ratios of b) 50 mol% [(MeO)<sub>2</sub>Im][PF<sub>6</sub>], c) 90 mol% [(MeO)<sub>2</sub>Im][PF<sub>6</sub>] and d) 95 mol% [(MeO)<sub>2</sub>Im][PF<sub>6</sub>], and e) neat [(MeO)<sub>2</sub>Im][PF<sub>6</sub>]. The intensities are normalized to the overall intensity of [(MeO)<sub>2</sub>Im][PF<sub>6</sub>] to compensate for differences in X-ray flux.



**Figure S8:** Ratio of the normalized  $F_{CFX}$  and  $F_{PF6}$  content, at 0° (black squares) and 80° (red circles) emission, obtained during cooling from 95 °C to lower temperatures. a) Neat [PFBMIm][PF<sub>6</sub>], b) – d) mixtures of [(MeO)<sub>2</sub>Im][PF<sub>6</sub>] and [PFBMIm][PF<sub>6</sub>] at molar ratios of b) 50 mol% [(MeO)<sub>2</sub>Im][PF<sub>6</sub>], c) 90 mol% [(MeO)<sub>2</sub>Im][PF<sub>6</sub>] and d) 95 mol% [(MeO)<sub>2</sub>Im][PF<sub>6</sub>], and e) neat [(MeO)<sub>2</sub>Im][PF<sub>6</sub>]: Not shown due to the lack of  $F_{CFX}$  signal of a fluorinated side chain. The dashed horizontal lines indicate the nominal composition. Data points recorded when solidification was observed are shown in parenthesis.





**Figure S9:** Ratio of the normalized  $N_{\text{PFB}}$  and  $N_{\text{MeO}}$  content, at 0° (black squares) and 80° (red circles) emission, obtained during cooling from 95 °C to lower temperatures. a) Neat [PFBMIm][PF<sub>6</sub>]: Not shown due to the lack of  $N_{\text{MeO}}$  signal, b) – d) mixtures of [(MeO)<sub>2</sub>Im][PF<sub>6</sub>] and [PFBMIm][PF<sub>6</sub>] at molar ratios of b) 50 mol% [(MeO)<sub>2</sub>Im][PF<sub>6</sub>], c) 90 mol% [(MeO)<sub>2</sub>Im][PF<sub>6</sub>] and d) 95 mol% [(MeO)<sub>2</sub>Im][PF<sub>6</sub>], and e) neat [(MeO)<sub>2</sub>Im][PF<sub>6</sub>]: Not shown due to the lack of  $N_{\text{PFB}}$  signal. The dashed horizontal lines indicate the nominal composition. Data points recorded when solidification was observed are shown in parenthesis.



## ARTICLE

<https://doi.org/10.1038/s41467-018-08063-3>

OPEN

# Few layer 2D pnictogens catalyze the alkylation of soft nucleophiles with esters

Vicent Lloret<sup>1</sup>, Miguel Ángel Rivero-Crespo<sup>2</sup>, José Alejandro Vidal-Moya<sup>2</sup>, Stefan Wild<sup>1</sup>, Antonio Doménech-Carbó<sup>3</sup>, Bettina S.J. Heller<sup>4</sup>, Sunghwan Shin<sup>4</sup>, Hans-Peter Steinrück<sup>4</sup>, Florian Maier<sup>4</sup>, Frank Hauke<sup>1</sup>, Maria Varela<sup>5</sup>, Andreas Hirsch<sup>1</sup>, Antonio Leyva-Pérez<sup>2</sup> & Gonzalo Abellán<sup>1,6</sup>

Group 15 elements in zero oxidation state (P, As, Sb and Bi), also called pnictogens, are rarely used in catalysis due to the difficulties associated in preparing well-structured and stable materials. Here, we report on the synthesis of highly exfoliated, few layer 2D phosphorene and antimonene in zero oxidation state, suspended in an ionic liquid, with the native atoms ready to interact with external reagents while avoiding aerobic or aqueous decomposition pathways, and on their use as efficient catalysts for the alkylation of nucleophiles with esters. The few layer pnictogen material circumvents the extremely harsh reaction conditions associated to previous superacid-catalyzed alkylations, by enabling an alternative mechanism on surface, protected from the water and air by the ionic liquid. These 2D catalysts allow the alkylation of a variety of acid-sensitive organic molecules and giving synthetic relevancy to the use of simple esters as alkylating agents.

<sup>1</sup>Department of Chemistry and Pharmacy & Joint Institute of Advanced Materials and Processes (ZMP), Friedrich-Alexander-Universität Erlangen-Nürnberg (FAU), Dr.-Mack-Straße 81, 90762 Fürth, Germany. <sup>2</sup>Instituto de Tecnología Química, Universidad Politécnica de Valencia, Consejo Superior de Investigaciones Científicas, Avda. de los Naranjos s/n, 46022 Valencia, Spain. <sup>3</sup>Departamento de Química Analítica, Universidad de Valencia, Dr. Moliner, 50, 46100 Burjassot, Valencia, Spain. <sup>4</sup>Chair of Physical Chemistry II, Friedrich-Alexander-Universität Erlangen-Nürnberg (FAU), Egerlandstr. 3, 91058 Erlangen, Germany. <sup>5</sup>Departamento de Física de Materiales, Universidad Complutense de Madrid, Instituto Pluridisciplinar, Instituto de Magnetismo Aplicado, Madrid 28040, Spain. <sup>6</sup>Instituto de Ciencia Molecular (ICMol), Universidad de Valencia, Catedrático José Beltrán 2, 46980 Paterna, Valencia, Spain. These authors contributed equally: Vicent Lloret, Miguel Ángel Rivero-Crespo. Correspondence and requests for materials should be addressed to A.L.-P. (email: [anleyva@itq.upv.es](mailto:anleyva@itq.upv.es)) or to G.A. (email: [gonzalo.abellan@fau.de](mailto:gonzalo.abellan@fau.de))

Two-dimensional (2D) materials have attracted great attention in the last years due to their outstanding physical properties and their potential applications in optoelectronics, sensors, energy storage, and catalysis<sup>1</sup>. In contrast to the most studied material graphene, the layered allotropes of group 15 elements (P, As, Sb, and Bi, also called pnictogens) have been fairly less developed. 2D pnictogens exhibit a marked puckered structure<sup>2–4</sup> with dative electron lone pairs located on the surface atoms, which results in semiconducting character and good electronic mobility<sup>4,5</sup>, and also in the ability to easily adsorb and stabilize, particularly well, unsaturated organic molecules through van der Waals interactions<sup>6,7</sup>. Thus, 2D pnictogens might, in principle, act as catalysts in synthetic organic transformations involving unsaturated molecules, in a completely different way as graphene does<sup>8,9</sup>. This concept, however, requires a new methodology to synthesize large amounts of exfoliated material, thus exposing most of the catalysts atoms to the outer space for maximizing interaction with substrate molecules.

Alkylation reactions are fundamental in biochemistry and organic synthesis. Nature makes use of alkyl phosphates, sulfonates, and esters as alkylating agents, under metal-free physiological conditions<sup>10,11</sup>. In contrast, synthetic methods generally employ energetically higher alkyl halides and alcohols as alkylating agents under very strong basic or acidic conditions (i.e., Williamson synthesis)<sup>12</sup>, and the synthetic alkylation protocols reported with poly-oxygenated compounds need expensive and toxic metal catalysts, such as the palladium-catalyzed Tsuji–Trost allylation reaction<sup>13</sup>, the Hantzsch ester-assisted hafnium-catalyzed alkylation of quinones<sup>14</sup>, and the gold-catalyzed alkylation with alkynylbenzoic acids<sup>15</sup>, among some others<sup>16,17</sup>. Thus, the discovery of a simple, metal-free, biomimetic alkylation reaction with readily available poly-oxygenated molecules<sup>18</sup> remains a challenge in organic synthesis and catalysis, furthermore attractive if selective and functional-group tolerant<sup>19,20</sup>.

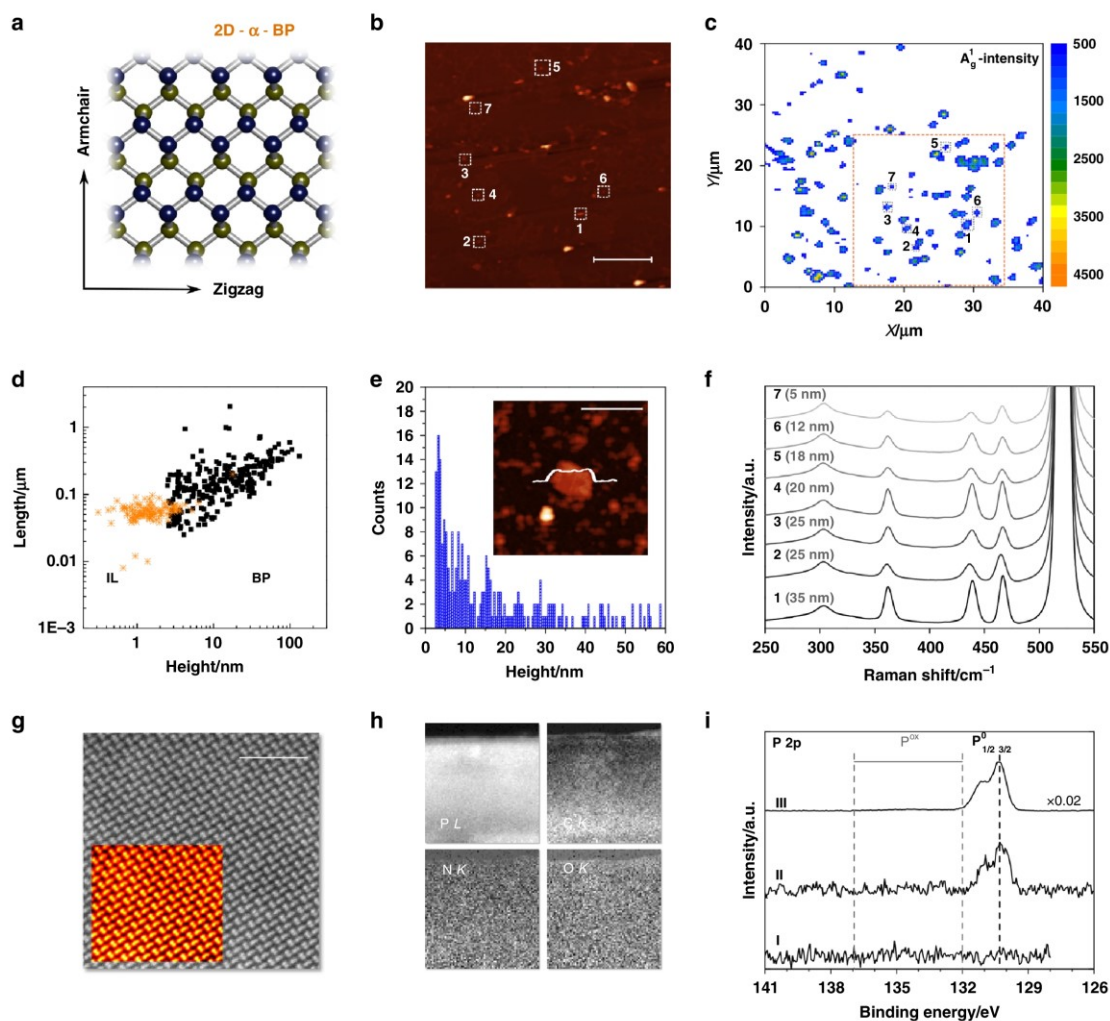
Here, we show the synthesis of two different exfoliated, few layer 2D pnictogens, phosphorene (few-layer black phosphorous (FL-BP)) and antimonene (FL-Sb), and their use as catalysts in the alkylation of alcohols, thiols, and indoles with simple esters, in good yields and with excellent selectivity. To our knowledge, this is the first organic reaction catalyzed by pristine 2D-pnictogens reported so far. Mechanistic studies unveil that the catalytic FL pnictogen selectively adsorbs the nucleophile and ester on surface, with the help of the electronic stabilization generated by the few layers underneath. FL-Sb exhibits a better performance than FL-BP, in accordance with its higher polarizability, enabling acid-sensitive aromatic derivatives to be selectively alkylated with simple esters.

## Results and Discussion

**Synthesis and characterization of FL-BP and FL-Sb in bmim-BF<sub>4</sub>.** Figures 1a and 2a show the structure of FL-BP and FL-Sb nanosheets, respectively, produced by liquid phase exfoliation (LPE)<sup>21,22</sup>. This technique is often carried out in amide solvents such as *N*-cyclohexyl-2-pyrrolidone (CHP) or *N*-methyl-2-pyrrolidone (NMP). Here, the ionic liquid (IL) 1-butyl-3-methylimidazolium tetrafluoroborate (bmim-BF<sub>4</sub>) is used on the basis of its excellent oxidation protection behavior for FL-BP<sup>23</sup>. Sonication of ground BP or Sb crystals dispersed in bmim-BF<sub>4</sub> was performed in an argon-filled glovebox (<0.1 ppm of H<sub>2</sub>O and O<sub>2</sub>) to yield brownish, open-air stable suspensions of unoxidized FL-BP or Sb nanosheets, after removing the unexfoliated particles by a two-step centrifugation process, 14,000g during 1 min, and then at 2000 and 100g for 60 min for FL-BP and FL-Sb, respectively. The samples were stored under ambient conditions over weeks with no signature of degradation. In order to provide statistical information of the thicknesses and lateral dimensions of

the as-prepared nanosheets, topographic atomic force microscopy (AFM) characterization, and spectroscopic micro-Raman mapping of >150 nanosheets, spin-coated onto SiO<sub>2</sub>/Si wafers, was performed. The results showed that the BP particles have median values of *ca.* 150 nm in lateral dimensions and average thicknesses of 13 nm, with thinner particles down to a few nanometers being predominant (see Supplementary Figures 1–7). Particles smaller than 2 nm were excluded from statistics since capillary and adhesion effects of the IL account for average motifs of *ca.* 60 nm in lateral dimensions and *ca.* 1.8 nm in thickness (see Supplementary Figures 8 and 9)<sup>24</sup>. It is worth noting the general difficulties associated to AFM measurements in the presence of ILs, due to the high viscosity, adhesion forces, and formation of IL aggregates. The corresponding scanning Raman microscopy (SRM) spectra (>14,000 single point spectra), with an excitation wavelength of 532 nm, unambiguously showed the characteristic modes of BP, labeled A<sub>g</sub><sup>1</sup>, B<sub>2g</sub>, and A<sub>g</sub><sup>2</sup>, with no signature of oxidation attending to the A<sub>g</sub><sup>1</sup>/A<sub>g</sub><sup>2</sup> > 0.6 intensity ratio statistics, independent of the orientation (see Fig. 1 and Supplementary Figures 1–7 in Supplementary Information for additional Raman and AFM characterization)<sup>23,25</sup>. Aberration corrected scanning transmission electron microscopy (STEM) combined with electron energy-loss spectroscopy (EELS) was used to investigate the local structure and chemistry of the flakes. An atomic-resolution high-angle annular dark field (HAADF) STEM image of the FL-BP sample acquired down the [110] crystallographic direction, with the electron beam perpendicular to the platelet plane, is shown in Fig. 1g (both raw and Fourier filtered data, Supplementary Figure 10 displays a low magnification image of the flake). The samples exhibit a very high degree of crystallinity, showing the characteristic puckered structure over regions of hundreds of nanometers. The lattice shows high uniformity with the presence of very few defects or dislocations. Analysis by EELS shows that the IL locates and nanometrically covers the edges of the 2D material, as assessed by the P L<sub>2,3</sub>-edges, the C K-edge, the N K-edge, and the O K-edge chemical maps in Fig. 1h, with onsets near 132, 284, 401, and 532 eV, respectively. X-ray diffraction (XRD) of a FL-BP sample, measured after washing with tetrahydrofuran under nitrogen atmosphere, ultracentrifugation and evaporation of the solvent, shows a spectrum consistent with BP, with the typical 020, 040, and 060 planes and without any sign of degradation nor oxidation, and when the sample was exposed to the ambient, the peak intensities rapidly decreased (Supplementary Figure 10). These results infer the high surface area of the FL-BP synthesized here.

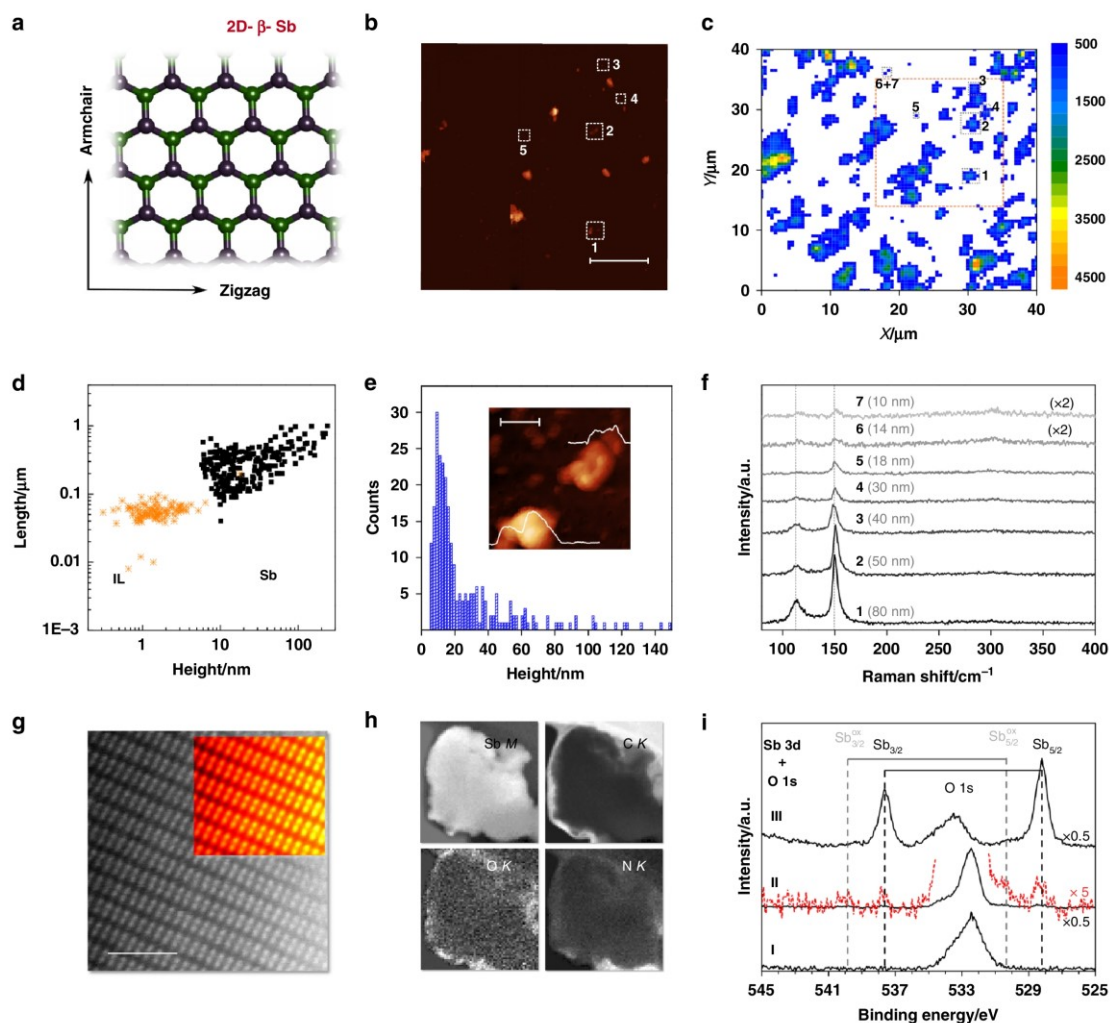
To confirm the zero oxidation state of P and rule out partial reduction of oxidized P species in EELS by the electron beam, X-ray photoelectron spectroscopy (XPS) studies have been carried out under ultra-high vacuum (UHV) conditions on highly concentrated IL FL-BP suspensions (FL-BP<sub>sus</sub>) coating a clean Au foil as support. The overview spectrum of FL-BP<sub>sus</sub> shows the expected IL core levels (Supplementary Figure 11) and, additionally, typical Si/O/C signals of trace bulk contamination after contact with glassware grease, due to surface enrichment effects as it is often the case in XP spectra for IL systems<sup>26</sup>. At around 130 eV binding energy, a small signal of the spin-orbit split P 2p<sub>1/2,3/2</sub> signal is detected that is absent for the neat IL (Fig. 1i, spectra II and III). The binding energy position of the P 2p<sub>3/2</sub> level at 130.2 eV can be unambiguously assigned to BP in oxidation state zero and the absence of signals between 132 and 137 eV rules out significant oxidized P species being present<sup>27</sup>. By heating the FL-BP<sub>sus</sub> sample above 150 °C for 1 h in UHV, most of the IL was gone by thermal desorption (and partial decomposition), which led to an increase of the BP signal intensity as dominating remaining species by a factor around 50 (Fig. 1i, spectrum III); again, no oxidized P species could be



**Fig. 1** Characterization of exfoliated black phosphorus. **a** Top view of the orthorhombic structure ( $C_{mce}$  space group) of BP. Upper plane P atoms marked in blue, lower plane in yellow. **b** Representative AFM topography image (inset, scale bar  $5\ \mu\text{m}$ ) of the exfoliated sample spin-coated onto  $\text{SiO}_2/\text{Si}$  substrates. **c** The corresponding Raman  $A_1^g$  ( $\lambda_{\text{exc}} = 532\ \text{nm}$ ) mapping of the same BP flakes ( $>14,000$  single point spectra over a surface area of  $40\ \mu\text{m}^2$  using a step size of  $0.5\ \mu\text{m}$ ). The numbers denote the areas in which the Raman spectra shown in **(f)** were recorded. **d** Plot of the nanosheet length as a function of the flake height (obtained from AFM) considering a total amount of 252 replicates as well as the data corresponding to the IL blank (sample size = 116) Supporting Information S8 and 9). **e** Histogram of the apparent thickness of the exfoliated FL-BP obtained from AFM (sample size = 252). The inset shows an AFM image of a nanosheet along with its corresponding height profile of ca. 6 nm (inset, scale bar 400 nm). **f** Raman spectra of the nanosheets indicated in **b** and **c** (the numbers labeling the spectra in **f** correspond to the nanosheets marked by numbers in **b** and **c**). **g** Atomic resolution HAADF image acquired down the  $[110]$  axis, from the edge of a free-standing portion of a flake. The inset exhibits the raw image and a Fourier filtered (FFT) version, in false color. The scale bar represents 2 nm. **h** Compositional maps derived from electron energy-loss spectroscopy (EELS) measurements acquired on the free-standing portion of the BP flake. The P  $L_{2,3}$ , C K, N K, and O K maps for this area are shown, the scale bar represents 20 nm. Data acquired at 80 kV. **i** XPS P 2p region of the neat  $\text{bmim-BF}_4$  IL (I), the highly concentrated FL-BP suspension (II) showing only P in oxidation state zero at P  $2p_{3/2} = 130.2\ \text{eV}$  (region for oxidized P species is indicated), and after removal of most of the IL by heating in UHV (III); spectra are offset and rescaled for sake of clarity. Source data are provided as a Source Data file

detected. In order to check if the heated FL-BP<sub>sus</sub> sample with most of the protecting IL removed was now prone to oxidation, this sample was subsequently exposed to air under ambient conditions for about one day and measured again. XPS clearly revealed a broad oxide P component around 134 eV (Supplementary Figure 12, spectrum IV) as has already been observed for in situ oxidation studies of BP<sup>27</sup>.

In the case of FL-Sb, the shorter out-of-plane atom-to-atom distances, which are indicative of stronger interlayer interactions, usually hampers mechanical exfoliation. However, the LPE approach here used was able to give median values of 310 nm in lateral dimensions and ca. 32 nm in thickness (extracted from  $>150$  flakes), as it can be observed in Fig. 2 and Supplementary Figures 13–18, with a minimum observed apparent thickness of 4 nm<sup>22</sup>. The SRM



**Fig. 2** Characterization of exfoliated antimonene. FL-Sb analysis. **a** Top view of the rhombohedral structure (R3m space group) of Sb. Upper plane atoms marked in green, lower plane in purple. **b** Representative AFM topography image (inset, scale bar 5  $\mu\text{m}$ ) of the exfoliated sample spin-coated onto  $\text{SiO}_2/\text{Si}$  substrates. **c** The corresponding Raman  $A_1^g$  ( $\lambda_{\text{exc}} = 532 \text{ nm}$ ) mapping of the same Sb flakes (>14,000 single point spectra over a surface area of  $40 \mu\text{m}^2$  using a step size of  $0.5 \mu\text{m}$ ). The numbers denote the areas in which the Raman spectra shown in **(f)** were recorded. **d** Plot of the nanosheet length as a function of the flake height (obtained from AFM), including the data corresponding to the IL blank (Supplementary Figures 8 and 9) considering a total amount of 271 and 116 replicates, respectively. **e** Histogram of the apparent thickness of the exfoliated FL-Sb obtained from AFM (sample size = 271). The inset shows an AFM image of a nanosheet along with its corresponding height profiles of ca. 4 and 18 nm, respectively (inset, scale bar 100 nm). **f** Raman spectra of the nanosheets indicated in **b** and **c** (the numbers labeling the spectra in **f** correspond to the nanosheets marked by numbers in **b** and **c**). **g** Atomic resolution HAADF image acquired on the edge of a free-standing portion of a flake, near the edge, along with a Fourier filtered (FFT) image in the inset, acquired down the [210] orientation. The scale bar is 2 nm. **h** Compositional maps, derived from EEL spectrum images of the flake (from the area highlighted with a green rectangle in Supplementary Figure 21). Sb  $M_{4,5}$ , C K, O K, and N K maps corresponding to this area are shown. Data acquired at 80 kV. **i** XPS Sb 3d and O 1s region of the neat bmim-BF<sub>4</sub> IL (I) showing oxygen signals from an IL related surface contamination layer, of the highly concentrated FL-Sb suspension (II) showing small signals of nonoxidized ( $\text{Sb } 3d_{5/2}$  at 528.2 eV) and minor contributions from oxidized (530.3 eV) antimony next to the oxygen contamination, and after removal of most of the IL by heating in UHV (III); spectra are offset and rescaled for sake of clarity. Source data are provided as a Source Data file

mappings revealed the characteristic main phonon peaks, the  $A_1^g$  mode at  $149.8 \text{ cm}^{-1}$  and  $E_g$  mode at  $110 \text{ cm}^{-1}$ , even for the thinnest particles with no signature of oxidation (peaks related to the formation of  $\text{Sb}_2\text{O}_3$  or  $\text{Sb}_2\text{O}_5$ ). A phonon softening effect (blueshift) was observed when the sample thickness decreases from the bulk to ca. 10 nm, in good agreement with theoretical predictions and recent

reports (Fig. 2f and Supplementary Figures 19 and 20)<sup>4,22,28,29</sup>. The  $E_g/A_1^g$  intensity ratio (measured using 532 nm excitation wavelength) increases from 0.37 to 0.79 with thickness decreasing from 80 to 10 nm (Supplementary Figure 19)<sup>29</sup>.

FL-Sb electron microscopy images denote irregularly shaped submicrometric flakes, with lateral sizes in the range of hundreds

of nm, as assessed by a low-magnification HAADF image of a flake and the atomic-resolution image of the crystal structure (Fig. 2g and Supplementary 21), both obtained at an acceleration voltage of 80 kV to prevent beam-induced damage. This structure agrees with that of  $\beta$ -antimony along the [2 1 0] direction. Again, the samples are highly crystalline and no major defects were observed. EELS maps exhibit a C-rich coating consisting of an amorphous layer a few nanometers thick, as well as the presence of O, N, and C mostly located around the edges (Fig. 2h). The seemingly preferential location of the IL molecules along the edges is in good agreement with the expected higher polarity of the unsaturated atoms of the 2D material<sup>6,23,30</sup>.

As done for the FL-BP system, highly concentrated IL FL-Sb suspensions (FL-Sb<sub>sus</sub>) were investigated using XPS. Next to the broad O 1s signal at 533 eV from the surface enriched IL contamination (see also overview spectrum shown in Supplementary Figure 22), the Sb 3d region between 525 and 545 eV of the FL-Sb<sub>sus</sub> sample (Fig. 2i, spectrum II) reveals very weak Sb 3d<sub>3/2,5/2</sub> signals from antimony in oxidation state zero at 528.2 eV for the 3d<sub>5/2</sub> level, along with minor contributions from Sb in higher oxidation state at around 530.3 eV (Fig. 2i, magnified red spectrum II)<sup>31,32</sup>. Removing most of the excess IL by heating in UHV clearly showed Sb signals originating mostly from bulk antimony zero (Fig. 2i, spectrum III). Exposing the heated FL-Sb<sub>sus</sub> sample without the protecting IL medium for several hours to air led to a drastic decrease in Sb(0) and concomitant increase of the oxidized Sb species (Supplementary Figure 23, spectrum IV); these findings thus strongly supports the role of bmim-BF<sub>4</sub> stabilizing the P and Sb pnictogens in IL solution against oxidation.

**Catalytic alkylation with esters.** Substitution reactions are fundamental transformations in organic chemistry that, due to their bimolecular nature and in order to be performed selectively, require the use of a catalyst able to activate the substrates orthogonally. Highly polarized Lewis bases are, in principle, suitable species to carry out a bimolecular and orthogonal catalytic activation, and FL-BP and FL-Sb may act in this way due to the intrinsic electron richness of the bulk atoms (base) combined with the expected stabilization of the in situ generated cationic charge.

As a reaction proof, the *tert*-butylation of alcohols, a longstanding challenge in organic synthesis<sup>33</sup>, was studied. Current methodologies at laboratory<sup>34</sup> or industrial scale<sup>35</sup> for this reaction are still based on Friedel–Crafts type chemistry, with isobutylene or *tert*-butyl alcohol as alkylating agents under very strong reaction conditions. These harsh protocols are substrate-limiting and particularly unselective in the presence of aromatic rings<sup>36</sup>, despite synthetically elaborated, energetically richer and expensive *tert*-butylated reagents have been prepared on purpose to mitigate these drawbacks<sup>37</sup>.

Table 1 shows the results for the reaction between benzylic alcohol **1** and *tert*-butyl acetate **2**, in the presence of different catalysts. FL-BP and FL-Sb exclusively gives *tert*-butyl ether **3** after 20 h at 75 °C, in reasonable yields and with >99% selectivity (the rest is unreacted material, entries 2 and 3). In contrast, other bifunctional layered materials (entries 4–7) and semiconductors with high surface area (entries 8–10), and also inorganic and organic bases of different strength (entries 11–18), do not show any significant catalytic activity under these reaction conditions.

Isotopic experiments with <sup>18</sup>O-**1** confirm that the oxygen atom of the alcohol stays intact in product **3**, which suggests that an ester C–O alkyl cleavage (AL mechanism) operates, as reported with superacids (*H*<sub>0</sub> < 0) such as HSO<sub>3</sub>F–SbF<sub>5</sub>–SO<sub>2</sub><sup>33</sup>. Notice that, for any weaker acid, the AL mechanism is rapidly undertook by the more common acyl cleavage (AC) mechanism, to give the

trans-esterification reaction. Indeed, acetic acid (AcOH) is too weak to catalyze the reaction between **1** and **2** (entry 19), sulfuric and triflimidic acid show moderate catalytic activity and give ester **3'** as the major product (entries 20 and 21), and only the superacid triflic acid (HOTf) shows catalytic activity but with still poor selectivity towards **3** (entry 22). The increase in selectivity for **3** with acid strength is in good agreement with the need of forming the carbocation intermediate of the AL mechanism, to trigger the unimolecular A<sub>AL</sub>1 reaction and give ether **3**. Strong Lewis acids were also tried (entries 23–32), and while some of them showed some activity (entries 24–25, 29, and 31–32), their activity corresponds exclusively to the Brønsted acidity of the in situ hydrolyzed anions, as confirmed by the lack of activity when the proton quencher 2,6-*di*-*tert*-butylpyridine is used. Notice that the harsh reaction conditions associated with superacids are incompatible with most functional organic groups, thus any other nucleophile beyond water has not regularly been employed for the superacid-catalyzed alkylation with esters, as far as we know. The initial turnover frequency (TOF<sub>0</sub>) for FL-BP and FL-Sb (20 and 73 h<sup>-1</sup>, respectively) are in the range of the strong acids (between 8 and 155 h<sup>-1</sup>), which reflects the good intrinsic activity per atom of the pnictogen 2D materials. Strong Brønsted solid acids such as sulphated zirconia and silica–alumina gave only a marginal catalytic activity.

Figure 3 shows the scope for the FL-Sb catalyzed reaction, with different nucleophiles and esters. The results show that a variety of *tert*-butyl esters give ether **3** in >70% yield, up to 2-gram scale, including unsaturated esters and carbonates, and that benzylic (products **4** and **10**) and alkyl alcohols (products **5** and **11**), thiols (products **6**–**7**), indoles, either in the carbon (products **8a**–**9a**) or nitrogen atom (products **8b**–**9b**), and phenols (product **11**) can be alkylated with acetates having either *tert*-butyl, cinnamyl, benzyl, and prenyl moieties (in blue). Acid-sensitive functionalities are tolerated under the reaction conditions, such as ether, prenyl, trifluoroacetate and lactone groups (in red). The uniqueness of this synthetic approach is illustrated, for instance, for allylic benzylic alcohols, since product **10** has not been synthesized so far and none of the nine methods reported previously for the generic structure, according to a literature searching, provides a so simple, direct and efficient method as 2D-pnictogens do (Table S1).

Recovery tests (Supplementary Figure 24) show that FL-BP and FL-Sb can be reused at least three times under ambient conditions before deactivation occurs. STEM analysis of the reused samples shows a progressive amorphization of the edges (see Supplementary Figure 25 for further details), which is significantly alleviated by reusing the material under N<sub>2</sub> atmosphere, thus prolonging catalyst lifetime<sup>23,38</sup>. In order to further assess the stability of the material *in operando* conditions, <sup>31</sup>P magic angle spinning nuclear magnetic resonance (MAS NMR) spectra of the FL-BP catalysts were recorded under reaction conditions. The results (Supplementary Figure 26, top) show that the FL-BP catalyst keeps the original signal at 18 ppm during reaction<sup>39</sup>, without any trace of phosphoric acid (0 ppm), phosphonium compounds, or other potential oxidized and hydrolyzed species. The measurement was also performed in statics (Supplementary Figure 26, bottom), and the deconvoluted spectrum fits to two components, one corresponding to P in zero oxidation state and the other corresponding to P–O, which accounts for 8% out of the total. Electrochemistry measurements (Supplementary Figure 27) strongly supports the absence of neat oxidation P or Sb species during reaction<sup>40</sup>, since no significant changes in the 2D pnictogen signals were found, and if any, they correlate with particle aggregation/fractioning processes rather than the formation of phosphonium or further oxidized P and Sb forms. Following this rationale, and in order to increase the

**Table 1 Results for the catalytic alkylation of 1 with 2. Conversion of 1 is the sum of 3 and 3' yields, the rest is unreacted material**

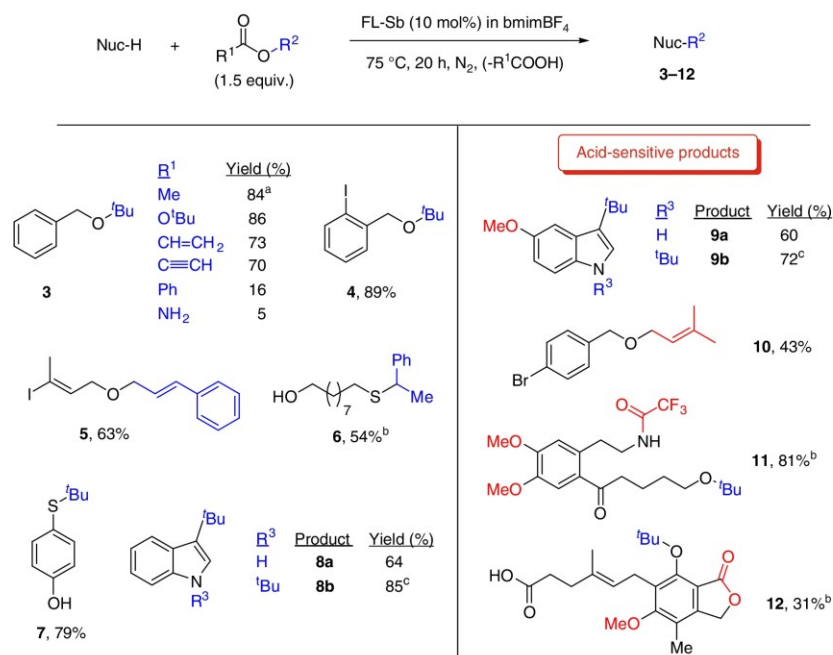
Entry	Catalyst	TOF <sub>0</sub> (h <sup>-1</sup> )	Yield of 3 (%)	Yield of 3' (%)	Selectivity AL/AC (%)
1	None	—	—	—	—
2	<b>Phosphorene (FL-BP)</b>	<b>20.1</b>	<b>46</b>	<1	>99
3	<b>Antimonene (FL-Sb)</b>	<b>73.2</b>	<b>57</b>	<1	>99
4	Graphene	—	4	<1	—
5	Boron nitride	—	3	<1	—
6	Hydrotalcite	—	<1	<1	—
7	Sepiolite	—	6	<1	—
8	Nano-TiO <sub>2</sub>	—	2	<1	—
9	Nano-CeO <sub>2</sub>	—	<1	<1	—
10	Nano-Fe <sub>2</sub> O <sub>3</sub>	—	<1	<1	—
11	K <sub>3</sub> PO <sub>4</sub>	—	<1	<1	—
12	Na <sub>2</sub> CO <sub>3</sub>	—	<1	<1	—
13	Pyridine	—	<1	<1	—
14	Et <sub>3</sub> N	—	<1	<1	—
15	KOAc	—	<1	<1	—
16	KO <sup>t</sup> Bu	—	<1	<1	—
17	DABCO	—	<1	<1	—
18	NanoMgO	—	<1	<1	—
19	HOAc	—	<1	<1	—
20	H <sub>2</sub> SO <sub>4</sub>	23.7	24	46	35
21	HNTf <sub>2</sub>	7.6	8	14	25
22	HOTf	154.2	48	52	48
23	MnOAc <sub>2</sub>	—	0	—	—
24 <sup>a</sup>	FeCl <sub>2</sub>	2.2	33	<1	>99
25 <sup>a</sup>	CoCl <sub>2</sub>	7.4	44	<1	>99
26	CuCl	—	2	—	—
27	AgMeSO <sub>4</sub>	—	2	<1	—
28	Pd(OAc) <sub>2</sub>	—	6	—	—
29 <sup>a</sup>	PtCl <sub>2</sub>	—	25	<1	>99
30	Au(OH) <sub>3</sub>	—	0	—	—
31 <sup>a</sup>	Bi(OTf) <sub>3</sub>	6.0	37	10	79
32 <sup>a</sup>	CeCl <sub>3</sub>	7.0	52	<1	>99
33	Sulphated zirconia	—	11	<1	>99
34	SiO <sub>2</sub> -Al <sub>2</sub> O <sub>3</sub> (13%)	—	0	—	—

<sup>a</sup>No catalytic activity if 2,6-di-tert-butylpyridine (30 mol%) is added during reaction

catalyst lifetime, sonication of the IL mixture was carried out before each reuse, and in this way, only a minor loss of final yield was observed after six reuses, thus doubling the catalytic performance without sonication.

Figure 4a shows the rate equation of the reaction between 1 and 2 derived from kinetic experiments (Supplementary Figure 28), with either FL-BP or FL-Sb catalyst. The results give  $v_0 = K_{app1}[P \text{ or } Sb][1][2]$ , that indicates that the three species, i.e., the alcohol, the ester and the pnictogen catalyst, are involved in the rate-determining step of the reaction. This equation rate differs significantly from a classical A<sub>AL</sub>1 mechanism<sup>33,41,42</sup>, where the nucleophile does not participate in the rate-limiting step since only carbocation formation controls the overall

reaction rate. Accordingly, kinetic experiments with HOTf, under the reaction conditions employed here, show that 1 does not participate during the rate determining step, with an equation rate  $v_0 = K_{app2}[H^+][2]$ . This result confirms that the classical A<sub>AL</sub>1 mechanism operates with HOTf in BMIM-BF<sub>4</sub> (Supplementary Figure 29), and that it is different from that with FL-BP or FL-Sb. Analysis of the reaction gas phase by gas chromatography coupled to mass spectrometry (GC-MS) shows that nearly 0.5 equivalents of 2 are transformed to isobutylene gas during the HOTf-catalyzed reaction, regardless if 1 is present or not, while only traces of isobutylene gas are detected with the FL-BP catalyst. Control experiments with isobutylene or styrene as reagents, instead of the corresponding esters, discard alkenes as



**Fig. 3** Substrate scope for the FL-Sb catalyzed alkylation with esters. R<sup>1</sup> is Me (acetate) unless otherwise indicated. In blue, the introduced alkyl moiety; in red, particularly acid-sensitive functional groups. **a** 2-gram scale. **b** 25 mol% catalyst, 48 h. **c** Three equivalents of ester

alkylating agents under the present reaction conditions. Notice that isobutylene is a typical by-product of long-lived *tert*-butyl cations, and the preferential formation with HOTf and the different equation rates illustrate the striking differences between the FL-pnictogen and the superacid catalyst mechanisms.

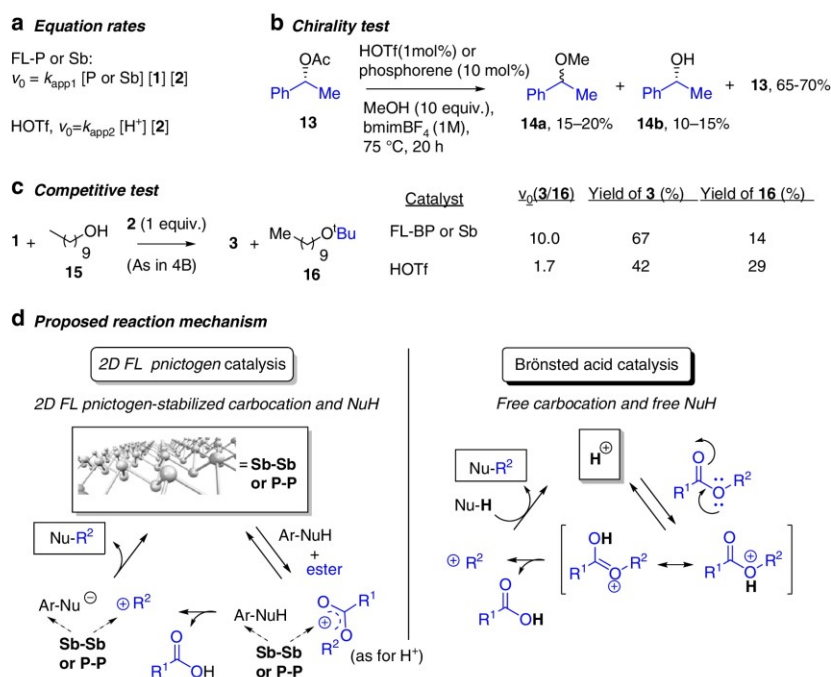
To further check the formation of carbocations or not during 2D pnictogen catalysis, *R*-1-phenylethanol acetate **13** was used as the alkylating agent for methanol. The results in Fig. 4b show that a racemic mixture of the alkylated product 1-phenylethyl methyl ether **14a**, together with isomerically pure 1-phenylethanol **14b** and starting **13**, were found as main products with FL-BP catalyst. This result unambiguously demonstrates that the alkyl moiety is transformed on the 2D pnictogen surface into a carbocation, at some point before transferring, since it is able to racemize prior to nucleophile addition. Of course, this also occurs with HOTf catalyst; however, the different equation rates and isobutylene yield found for the 2D pnictogen and HOTf catalysts suggest different carbocation managing during the alkylation reaction. Released acetic acid or traces of water do not act as nucleophiles towards the carbocation in both cases.

Figure 4c shows competitive tests between benzyl alcohol **1** and decyl alcohol **15** with **2**. The relative initial rates and final yields differ dramatically for FL-BP and HOTf; while FL-BP shows one order of magnitude (10.0) higher formation rate for the aromatic than for the alkyl alcohol, HOTf shows a relative rate of 1.7. These values give 6 times higher selectivity for aromatic substrates with FL-BP. Another clear difference is found in the corresponding Hammett plots: while electron withdrawing groups on the benzyl alcohol increase the reaction rate with the FL-BP catalyst, electron donor groups increase the rate with HOTf catalyst, the latter being the expected behavior for a free nucleophile (Supplementary Figure 30). Kinetic experiments with isotopically labeled D<sub>2</sub>-1 (PhCD<sub>2</sub>OH) give a significant secondary kinetic

isotopic effect of 1.4(5) for the FL-BP catalyst. This last result, together with the Hammett plot, suggests an electron donation of the exfoliated material to the aromatic ring and then, in a lesser extent, to the alcohol by induction effects, in accordance to the known ability of 2D-BP<sup>6</sup> and 2D-Sb<sup>7</sup> to transfer electron charge to planar aromatic molecules.

Calorimetry measurements with **1** and FL-BP (Supplementary Figure 31) show that the aromatic alcohol strongly adsorbs to the BP surface, even at just 30 °C. Taft plots (Supplementary Figure 32) shows a clear positive slope for the 2D materials, which indicates that bulkiness on the aromatic ring diminishes reactivity. Decoupling steric and inductive effects by least-squares Taft regression analysis<sup>43</sup> (Tables S2–S4) confirms the need of co-planarity of the aromatic alcohol with the 2D catalyst, since the  $\delta$  values obtained by the Taft regression analysis are the same than the Hammett plot, within the experimental error ( $-0.3 \pm 0.5$  for HOTf,  $0.89 \pm 0.08$  FL-BP, and  $0.5 \pm 0.3$  for Sb-BP). 2D nanosheets with different thickness were prepared by different ultra-centrifugation steps, with nearly one order of magnitude accessible bulk and edge atoms (Supplementary Figs. 33–38)<sup>21</sup>, and kinetic results for the alkylation of **1** with **2** showed that the TOF<sub>0</sub> increases for the centrifuged samples. Since unsaturated P atoms in vertexes and edges are likely oxidized under reaction conditions and do not participate during catalysis, these results indicate that the catalysis is directly related to the number of atoms on the bulk (Supplementary Figure 39)<sup>21,44</sup>. When nitrobenzene was used as an inhibitor reagent, the alkylation rate of **1** with **2** was progressively quenched up to 20 mol% of nitrobenzene (respect to FL-BP, Supplementary Figure 40), which indicates that the high electron-deficient aromatic ring of nitrobenzene is strongly adsorbing to the bulk atoms of the 2D material. This inhibition value fits well to the number of P atoms present on





**Fig. 4** Mechanistic studies. Experimental evidences and proposed mechanisms for FL-BP, FL-Sb, and HOTf catalyzed-alkylation of nucleophiles with esters in bmim-BF<sub>4</sub>

the whole bulk surface. These results point again to bulk P or Sb atoms as responsible for the catalysis.

P and Sb are very suitable atoms to stabilize carboxoniums, furthermore if the carbocation-oxonium equilibrium on surface is shifted toward the latter and assures a short living of the former. Indeed, low amounts of isobutylene were found during the alkylation reaction with FL-BP and FL-Sb, which supports a short living carbocation. A Hammett plot with different *para*-substituted *tert*-butyl benzoate esters shows that a positive charge is formed in the ester during reaction, thus carboxoniums can be presumed as intermediates (Supplementary Figure 41).

With all these data in hand, a very plausible mechanism for the 2D FL pnictogen-catalyzed alkylation of **1** with **2** is shown in Fig. 4d along the classical AL mechanism with HOTf for comparison, are shown in Fig. 4d. For the 2D FL pnictogen, the electron-rich 2D surface transfers electron density to the adsorbed aromatic nucleophile, which generates a deficiency of charge in the material stabilized by the few layers underneath<sup>6,7</sup> that activates the ester group and stabilizes a carboxonium intermediate, rapidly trapped by the nucleophile on surface and, thus, regenerating the electro-neutrality of the catalytic material. The higher polarizability of Sb vs. P explains the higher catalytic activity of the former. Notice that the activation of the ester occurs only after the bulk atoms act as a Lewis base, the natural behavior of 2D-BP and 2D-Sb, which enables a unique mechanism for the nanometric FL-BP and FL-Sb.

The transition state energetic values for FL-BP, calculated by an Eyring plot with the reaction between **1** and **2**, are  $\Delta H^\ddagger = 49.1$  (4) kJ mol<sup>-1</sup> and  $\Delta S^\ddagger = 0.0(2)$  kJ·(mol K)<sup>-1</sup>, and the unchanged entropy is consistent with both reactants binding to bulk P atoms, to couple rapidly after carbocation formation. In clear contrast, the mechanism for the superacid HOTf shows the formation of a free carbocation in solution, then trapped by the nucleophile. The

mechanisms proposed in Fig. 4d satisfactorily explain the experimental differences observed for the 2D-pnictogen and HOTf catalysts, and in particular, the equation rate, higher reactivity of EW aromatic nucleophiles and carbocation racemization without alkene formation for the 2D-pnictogen catalyst. Other potential mechanisms for the alkylation reaction such as the formation of phosphonium intermediates, or neat redox processes on the pnictogen surface fostered by their narrow homo-lumo gap, seems not to be pointed out by the experimental evidences shown above.

The particular nature of the 2D-pnictogen materials described here, embedded in water- and oxygen-protecting ILs, and with a high basal area, allows organic catalysis, and not necessarily other expected applications for BP. For instance, water splitting under typical experimental conditions did not give any H<sub>2</sub> formation. The suitability of FL-BP and FL-Sb for organic catalysis is further supported by the preliminary positive results found for the catalytic Bailly–Hillman reaction (Supplementary Figure 42), a representative carbon–carbon bond-forming reaction.

2D-pnictogens widens and complements graphene catalysis (carbocatalysis), since when graphene is doped with precisely pinpointed heteroatoms, typically nitrogen, its catalytic activity equals simple metal catalysts (Table S5), which is not more what 2D-pnictogens make naturally here, without any additional modification. This rationale drives to think that 2D-pnictogens are potential advanced versions of doped graphene and extremely promising catalysts in organic reactions.

## Discussion

2D nanosheets of BP and Sb, exfoliated in the IL bmim-BF<sub>4</sub>, catalyze the alkylation of soft nucleophiles with alkyl esters, in good yields and selectivity, particularly for aromatic substrates.

The 2D few layer materials circumvent superacid-mediated alkylations by enabling a surface mechanism with concomitant activation of the aromatic nucleophile and ester on surface, which allows acid-sensitive molecules to be alkylated. As far as we know, this is the first example of catalytic application of pristine FL-BP and FL-Sb in organic synthesis, beyond recent examples on photonic excitation or with supported metal nanoparticles<sup>45–49</sup>, thus expanding the list of potential applications for these promising materials.

## Methods

**Materials and exfoliation process.** Throughout all experiments, BP and Sb with purity higher than 99.999% (Smart Elements) were used.

Afterwards, the FL-BP flakes were transferred onto Si/SiO<sub>2</sub> substrates (300 nm oxide layer). The exfoliation was performed in argon filled LABmasterpro sp glove box (MBraun) equipped with a gas purifier and solvent vapor removal unit (oxygen and water content lower than 0.1 ppm).

Solvent purification: anhydrous, 99.9% purity 1-butyl-3-methylimidazolium tetrafluoroborate (bmim-BF<sub>4</sub>) was purchased from Sigma-Aldrich. The bmim-BF<sub>4</sub> was pump frozen, and the O<sub>2</sub> was removed by vacuum. This procedure was iteratively repeated a minimum of four cycles to remove traces of oxygen.

**Exfoliation of layered pnictogens.** LPE in bmim-BF<sub>4</sub> under inert conditions: BP was exfoliated under inert conditions by sonication in an argon-filled glovebox (O<sub>2</sub> < 0.1 ppm; H<sub>2</sub>O < 0.1 ppm) using a Bandelin Sonoplus 3100, 25% amplitude, 12 h, pulse 2 s on, 2 s off. Sb was exfoliated under the same inert conditions by sonication using 40% amplitude, 16 h, pulse 2 s on, 2 s off. The starting concentrations were 1.25 and 2.5 mg mL<sup>-1</sup> for BP and Sb, respectively. The resultant dispersions were decanted and transferred into vials. All solvent transfer was carried out in the glovebox.

**Centrifugation.** Centrifugation was carried out in a MPW-350R centrifuge using 2 mL Eppendorfs. A two-step process was followed; first supernatant dispersion was centrifuged 14,000g during 1 min, and afterwards the resulting supernatant was submitted to a second step at 2000 and 100g for 60 min for FL-BP and FL-Sb, respectively. The final concentrations were determined by ICP-OES being ca. 0.125 and 0.075 mg mL<sup>-1</sup> for FL-BP and FL-Sb, respectively. Longer centrifugations periods were performed to prepare samples of different thickness.

**Photoluminescence.** PL of the different centrifuged samples was acquired on a Horiba Scientific Fluorolog-3 system equipped with 450 W Xe halogen lamp, double monochromator in excitation (grating 600 lines/mm blazed at 500 nm) and emission (grating 100 lines/mm blazed at 780 nm) and a nitrogen cooled InGaS diode array detector (Symphony iHR 320). Spectra were obtained at 5 °C measured (spectral region of 550–1300 nm) with a 550 nm cutoff filter in emission. Excitation and emission band widths were typically 10 nm and integration times 2 s.

**Surface preparation.** SiO<sub>2</sub> surfaces were sonicated for 15 min. in acetone and 15 min in 2-propanol and then dried under an argon flow.

Immediately after the removal from the inert atmosphere, images of FL-BP flakes were recorded under an optical microscope (Zeiss Axio Imager M1m), using different objectives enabling their relocalization in Raman and AFM measurements.

**Raman spectroscopy.** Raman spectra were acquired on a LabRam HR Evolution confocal Raman microscope (Horiba) equipped with an automated XYZ table using 0.80 NA objectives. All measurements were conducted using an excitation wavelength of 532 nm, with an acquisition time of 2 s and a grating of 1800 grooves/mm. To minimize the photo-induced laser oxidation of the samples, the laser intensity was kept at 5% (0.88 mW). The step sizes in the Raman mappings were in the 0.2–0.5 μm range depending on the experiments. Data processing were performed using Lab Spec 5 as evaluation software. When extracting mean intensities of individual BP Raman modes, it is important to keep each spectral range constant, e.g., from 355 to 370 cm<sup>-1</sup> and from 460 to 475 cm<sup>-1</sup> because otherwise the resulting value of the A<sub>1g</sub>/A<sub>2g</sub>-ratio can be slightly influenced. The same applies to Sb E<sub>g</sub>/A<sub>1g</sub> ratio analyses.

**Atomic force microscopy.** AFM was carried out using a Bruker Dimension Icon microscope in tapping-mode. The samples were prepared by spin coating a solution of a given sample at 5000 rpm. Bruker Scanasyt-Air silicon tips on nitride levers with a spring constant of 0.4 N m<sup>-1</sup> were used to obtain images resolved by 512 × 512 or 1024 × 1024 pixels.

**Scanning transmission electron microscopy.** STEM observations were carried out in a JEOL ARM200CF operated at 80 kV and equipped with a spherical

aberration corrector and a Gatan Quantum EELS, at the ICTS-ELECOMI Centro Nacional de Microscopía Electronica at UCM (Spain). Compositional maps were produced using a multiple linear least squares fit of the data to reference EEL spectra.

**X-ray photoelectron spectroscopy.** XPS measurements were carried out in an ultra-high vacuum (UHV, base pressure < 1 × 10<sup>-10</sup> mbar) system dedicated for angle-resolved XPS at UHV-compatible liquid samples such as ILS<sup>50</sup>. Spectra were collected in normal emission (information depth in ILS: 7–9 nm, depending on electron kinetic energy) using monochromated Al Kα radiation (1486.6 eV) and a pass energy of the hemispherical electron analyzer of 35 eV (overall energy resolution: 0.4 eV). Binding energies are referenced to C 1s for aliphatic carbon of the IL (285.0 ± 0.1 eV) and Au 4f<sub>7/2</sub> (84.0 ± 0.1 eV) of clean gold. XPS-detection limit typically is around 1 at% depending on relative XPS cross-sections and signal-to-background situation for the trace atom<sup>51</sup>. The FL-Sb and FL-BP solutions employed for our catalysis studies with an overall P- and Sb-content around 0.1 mg/mL (that is, below 0.01 at% for P and Sb) were thus below the XPS detection limit as has been tested: only bmim-BF<sub>4</sub> signals could be detected along with a Si/O/C containing trace contamination that commonly shows up in IL-XPS investigations due to surface enrichment effects, and is typically due to contact with glassware grease<sup>26</sup>. Hence, highly concentrated suspensions (2D-inks) of FL-BP and FL-Sb were prepared by filtering the dispersions through a 0.2 μm reinforced cellulose membrane filter (Sartorius) in the glove box to remove most of the IL. The filtration was stopped just before the initial amount passed the filter, which allowed collecting the 2D-ink consisting of highly concentrated FL-BP/Sb material from the filter surface with a Teflon spatula. The 2D-inks were transferred to air and spread onto clean gold foils that were mounted on XPS sample holders. After exposure for several hours to air, the sample holders were introduced into the UHV system. Spectra were taken for the pristine samples and after heating in UHV in order to remove most of bmim-BF<sub>4</sub> by thermal evaporation (and partial decomposition as proven by XPS) to maximize P and Sb signal intensities. The heated samples were then exposed to air for about one day and measured again.

**General reaction procedure.** The corresponding nucleophile (0.1 mmol) and alkylating ester (0.15 mmol) were added under ambient conditions to a solution/dispersion of the corresponding catalyst (0.005 mmol for Brønsted acids and organic and inorganic bases, 0.02 for P, 0.01 mmol for Sb, and 1 mg for solids) in bmim-BF<sub>4</sub> (100 mg), placed in a 2 mL vial equipped with a magnetic stir bar. The vial was sealed and the resulting mixture was magnetically stirred at the required temperature for 4–20 h. Then, the reaction mixture was cooled and extracted with diethyl ether (1.5 mL). The extracts were analyzed by GC and GC-MS after adding dodecane (22.4 μL, 0.2 mmol) as an external standard, and the products were isolated by preparative thin-layer chromatography.

For kinetics, each point was taken from an individual reaction. For preparation purposes, scale is proportionally increased up to grams of starting material. For reuses, 2 mmol of starting materials are used and volatiles are removed from the extracted reaction mixture, under vacuum at room temperature for 15 min, prior to addition of fresh reactants. For longer catalyst lifetime, sonication after each reaction cycle of the IL mixture under inert atmosphere was carried out.

**Calorimetry.** 750 mg of IL-FL-BP (750 mg) was evacuated under vacuum for 30 min in a glass line, and a glass ampule was made in-situ, when still under vacuum. The ampule is submerged in a 1 M solution of benzyl alcohol in diethyl ether, inside the calorimetry apparatus, and then broken. Exchanged energy was measured at 30 °C during 2–4 h.

**Electrochemistry.** Voltammetric experiments were performed using a CH 660c equipment on FL-BP and FL-Sb diluted in the IL, after successive additions of BrOAc and *t*-BuOAc until 1 M concentration. Glassy carbon electrode (geometrical area 0.071 cm<sup>2</sup>) was used as a working electrode, completing the three-electrode arrangement with a Pt mesh counter electrode and a Pt wire pseudo-reference electrode. A second series of experiments were performed in 0.10 M potassium phosphate buffer at pH 7.0 after forming a fine deposit of FL-BP and FL-Sb on glassy carbon electrode via transfer of 20 μL of each one of the above IL solutions, after 30 min of reaction, plus of 20 μL ethanol, evaporation at air and drying with a smooth paper tissue.

**Photocatalysis.** The photocatalytic water splitting is performed with a solar simulator light source (Newport<sup>®</sup>, Oriel Instruments, model 69921) equipped with a Xe lamp (1000 W) coupled with an AM1.5 filter that provides simulated concentrated sunlight in UV-visible range. 50 mg of FL-BP or FL-Sb were dispersed in 20 mL pure H<sub>2</sub>O and then N<sub>2</sub> was purged into the reactor (quartz cell, 50 mL volume). Gas samples were periodically taken and analyzed in a micro-GC, using Ar as a standard.

## Data availability

The authors declare that all other data supporting the findings of this study are available within the paper and its Supplementary information files. The source data

underlying Figs. 1b, 2b–f, Figs. 1, 2h, I, and Supplementary Figs. 1–S9, Supplementary Figs. 11–S17, Supplementary Figs. 19, 20, Supplementary Figs. 22–24, Supplementary Figs. 28–30, Supplementary Figs. 32, Supplementary Figs. 34–40 are provided as a Source Data file. The Source Data file can be found in: Materials Cloud Archive [<https://archive.materialscloud.org/2018.0021/v1>]

Received: 8 September 2018 Accepted: 12 December 2018

Published online: 31 January 2019

## References

- Mannix, A. J., Kiraly, B., Hersam, M. C. & Guisinger, N. P. Synthesis and chemistry of elemental 2D materials. *Nat. Rev. Chem.* **1**, s41570–016 (2017). 0014–0016.
- Ling, X., Wang, H., Huang, S., Xia, F. & Dresselhaus, M. S. The renaissance of black phosphorus. *Proc. Natl Acad. Sci.* **112**, 4523–4530 (2015).
- Pumera, M. & Sofer, Z. 2D monoelemental arsenene, antimonene, and bismuthene: beyond black phosphorus. *Adv. Mater.* **29**, 1605299 (2017).
- Ares, P., Palacios, J. J., Abellán, G., Gómez-Herrero, J. & Zamora, F. Recent progress on antimonene: a new bidimensional material. *Adv. Mater.* **30**, 1703771 (2018).
- Chen, P., Li, N., Chen, X., Ong, W.-J. & Zhao, X. The rising star of 2D black phosphorus beyond graphene: synthesis, properties and electronic applications. *2D Mater.* **5**, 014002 (2018).
- Abellán, G. et al. Noncovalent functionalization of black phosphorus. *Angew. Chem. Int. Ed.* **55**, 14557–14562 (2016).
- Abellán, G. et al. Noncovalent functionalization and charge transfer in antimonene. *Angew. Chem. Int. Ed.* **56**, 14389–14394 (2017).
- Navalon, S., Dhakshinamoorthy, A., Alvaro, M. & García, H. Carbocatalysis by graphene-based materials. *Chem. Rev.* **114**, 6179–6212 (2014).
- Navalon, S., Dhakshinamoorthy, A., Alvaro, M., Antonietti, M. & García, H. Active sites on graphene-based materials as metal-free catalysts. *Chem. Soc. Rev.* **46**, 4501–4529 (2017).
- Kiser, P. D. et al. Catalytic mechanism of a retinoid isomerase essential for vertebrate vision. *Nat. Chem. Biol.* **11**, nchembio.1799 (2015).
- Sanchez, C. et al. Lifetime and reactivity of an ultimate tamoxifen carcinogen: the tamoxifen carbocation. *J. Am. Chem. Soc.* **120**, 13513–13514 (1998).
- Watson, A. J. A. & Williams, J. M. J. The give and take of alcohol activation. *Science* **329**, 635–636 (2010).
- Trost, B. M. & Van Vranken, D. L. Asymmetric transition metal-catalyzed allylic alkylations. *Chem. Rev.* **96**, 395–422 (1996).
- Xu, X.-L. & Li, Z. Catalytic electrophilic alkylation of p-quinones through a redox chain reaction. *Angew. Chem.* **129**, 8308–8312 (2017).
- Asao, N., Aikawa, H., Tago, S. & Umetsu, K. Gold-catalyzed etherification and Friedel–Crafts alkylation using ortho-alkynylbenzoic acid alkyl ester as an efficient alkylating agent. *Org. Lett.* **9**, 4299–4302 (2007).
- Manbeck, K. A., Kundu, S., Walsh, A. P., Brennessel, W. W. & Jones, W. D. Carbon–oxygen bond activation in esters by platinum(0): cleavage of the less reactive bond. *Organometallics* **31**, 5018–5024 (2012).
- Liu, X., Jia, J. & Rueping, M. Nickel-catalyzed C–O bond-cleaving alkylation of esters: direct replacement of the ester moiety by functionalized alkyl chains. *ACS Catal.* **7**, 4491–4496 (2017).
- Oliver-Meseguer, J., Cabrero-Antonino, J. R., Domínguez, I., Leyva-Pérez, A. & Corma, A. Small gold clusters formed in solution give reaction turnover numbers of 107 at room temperature. *Science* **338**, 1452–1455 (2012).
- Leyva-Pérez, A., Doménech-Carbó, A. & Corma, A. Unique distal size selectivity with a digold catalyst during alkyne homocoupling. *Nat. Commun.* **6**, 6703 (2015).
- Fortea-Pérez, F. R. et al. The MOF-driven synthesis of supported palladium clusters with catalytic activity for carbene-mediated chemistry. *Nat. Mater.* **16**, 760–766 (2017).
- Hanlon, D. et al. Liquid exfoliation of solvent-stabilized few-layer black phosphorus for applications beyond electronics. *Nat. Commun.* **6**, 8563 (2015).
- Gibaja, C. et al. Few-layer antimonene by liquid-phase exfoliation. *Angew. Chem. Int. Ed.* **55**, 14345–14349 (2016).
- Abellán, G. et al. Fundamental insights into the degradation and stabilization of thin layer black phosphorus. *J. Am. Chem. Soc.* **139**, 10432–10440 (2017).
- Kashin, A. S., Galkin, K. I., Khokhlova, E. A. & Ananikov, V. P. Direct observation of self-organized water-containing structures in the liquid phase and their influence on 5-(hydroxymethyl)furfural formation in ionic liquids. *Angew. Chem. Int. Ed.* **55**, 2161–2166 (2016).
- Favron, A. et al. Photooxidation and quantum confinement effects in exfoliated black phosphorus. *Nat. Mater.* **14**, 826–832 (2015).
- Gottfried, J. M. et al. Surface studies on the ionic liquid 1-ethyl-3-methylimidazolium ethylsulfate using X-ray photoelectron spectroscopy (XPS). *Z. Für Phys. Chem.* **220**, 1439–1453 (2006).
- Kuntz, K. L. et al. Control of surface and edge oxidation on phosphorene. *ACS Appl. Mater. Interfaces* **9**, 9126–9135 (2017).
- Ares, P. et al. Mechanical Isolation of highly stable antimonene under ambient conditions. *Adv. Mater.* **28**, 6332–6336 (2016).
- Fortin-Deschênes, M. et al. Synthesis of antimonene on germanium. *Nano Lett.* **17**, 4970–4975 (2017).
- Walia, S. et al. Ambient protection of few-layer black phosphorus via sequestration of reactive oxygen species. *Adv. Mater.* **29**, 1700152 (2017).
- Bodenes, L., Darwiche, A., Monconduit, L. & Martinez, H. The solid electrolyte interphase a key parameter of the high performance of Sb in sodium-ion batteries: comparative X-ray photoelectron spectroscopy study of Sb/Na-ion and Sb/Li-ion batteries. *J. Power Sources* **273**, 14–24 (2015).
- Powell, C. J. Recommended Auger parameters for 42 elemental solids. *J. Electron Spectrosc. Relat. Phenom.* **185**, 1–3 (2012).
- Yates, K. Kinetics of ester hydrolysis in concentrated acid. *Acc. Chem. Res.* **4**, 136–144 (1971).
- Chen, X. et al. Synthesis of tert-butyl acetate via eco-friendly additive reaction over mesoporous silica catalysts with balanced Brønsted and Lewis acid sites. *J. Porous Mater.* **23**, 255–262 (2016).
- King, D. L., Cooper, M. D. & Faber, M. A. Acid catalyzed process. *US Patent* **4**, 868–343 (1989).
- Bandini, M., Fagioli, M. & Umani-Ronchi, A. Solid acid-catalysed Michael-type conjugate addition of indoles to electron-poor CC bonds: towards high atom economical semicontinuous processes. *Adv. Synth. Catal.* **346**, 545–548 (2004).
- Bartoli, G. et al. Unusual and unexpected reactivity of t-butyl dicarbonate (Boc<sub>2</sub>O) with alcohols in the presence of magnesium perchlorate. a new and general route to t-butyl ethers. *Org. Lett.* **7**, 427–430 (2005).
- Huang, Y. et al. Interaction of black phosphorus with oxygen and water. *Chem. Mater.* **28**, 8330–8339 (2016).
- Wang, Y. et al. Degradation of black phosphorus: a real-time <sup>31</sup>P NMR study. *2D Mater.* **3**, 035025 (2016).
- Wang, L., Sofer, Z. & Pumera, M. Voltammetry of layered black phosphorus: electrochemistry of multilayer phosphorene. *ChemElectroChem* **2**, 324–327 (2015).
- Olah, G. A. & Kiovsky, T. E. Stable carbonium ions. II. Fluorobenzenonium ions. *J. Am. Chem. Soc.* **89**, 5692–5694 (1967).
- Jerry, M. *Advanced Organic Chemistry: Reactions Mechanisms and Structure*. (McGraw Hill Book Company, New York, 1968).
- Pavelich, W. A. & Taft, R. W. Jr. The evaluation of inductive and steric effects on reactivity, the methoxide ion catalyzed rates of methanolysis of *l*-menthyl esters in methanol. *J. Am. Chem. Soc.* **79**, 4935–4940 (1957).
- Üzengi Aktürk, O., Aktürk, E. & Ciraci, S. Effects of adatoms and physisorbed molecules on the physical properties of antimonene. *Phys. Rev. B* **93**, 035450 (2016).
- Wang, H. et al. Ultrathin black phosphorus nanosheets for efficient singlet oxygen generation. *J. Am. Chem. Soc.* **137**, 11376–11382 (2015).
- Mayorga-Martinez, C. C., Mohamad Latiff, N., Eng, A. Y. S., Sofer, Z. & Pumera, M. Black phosphorus nanoparticle labels for immunoassays via hydrogen evolution reaction mediation. *Anal. Chem.* **88**, 10074–10079 (2016).
- Hu, J. et al. Band gap engineering in a 2D material for solar-to-chemical energy conversion. *Nano Lett.* **16**, 74–79 (2015).
- Lei, W. et al. Bandgap- and local field-dependent photoactivity of Ag/black phosphorus nanohybrids. *ACS Catal.* **6**, 8009–8020 (2016).
- Caporali, M. et al. Decoration of exfoliated black phosphorus with nickel nanoparticles and its application in catalysis. *Chem. Commun.* **53**, 10946–10949 (2017).
- Niedermaier, I., Kolbeck, C., Steinrück, H.-P. & Maier, F. Dual analyzer system for surface analysis dedicated for angle-resolved photoelectron spectroscopy at liquid surfaces and interfaces. *Rev. Sci. Instrum.* **87**, 045105 (2016).
- Shard, A. G. Detection limits in XPS for more than 6000 binary systems using Al and Mg Kα X-rays. *Surf. Interface Anal.* **46**, 175–185 (2014).

## Acknowledgments

We thank the European Research Council (ERC Starting Grant 804110 to G.A., and ERC Advanced Grant 742145 B-PhosphoChem to A.H.) for financial support. The research leading to these results was partially funded by the European Union Seventh Framework Program under grant agreement No. 604391 Graphene Flagship. G.A. has received financial support through the Postdoctoral Junior Leader Fellowship Program from “la Caixa” Banking Foundation (LCF/BQ/PI18/11630018). G.A. thanks support by the Deutsche Forschungsgemeinschaft (DFG; FLAG-ERA AB694/2-1), the Generalitat Valenciana (SEJJ/2018/034 grant) and the FAU (Emerging Talents Initiative grant #WS16-17\_Nat\_04). Financial support by MINECO through the Excellence Unit María de Maeztu (MDM-2015-0538), Severo Ochoa (SEV-2016-0683) and RETOS (CTQ2014-55178-R) program is acknowledged. M.A.R.-C. thanks MINECO for the concession of a FPU fellowship. We also thank the DFG (DFG-SFB 953 “Synthetic Carbon Allotropes”, Project A1), the Interdisciplinary Center for Molecular Materials (ICMM), and the

Graduate School Molecular Science (GSMS) for financial support. Research at UCM sponsored by Spanish MINECO/FEDER grant MAT2015-066888-C3-3-R and ERC-PoC-2016 grant POLAR-EM. H.-P.S. thanks the European Research Council (ERC) under the European Union's Horizon 2020 research and innovation program for financial support, in the context of an Advanced Investigator Grant granted to him (Grant Agreement No. 693398-ILID). B.S.J.H. and S.S. acknowledge financial support by the DFG within the Cluster of Excellence "Engineering of Advanced Materials" (project EXC 315, Bridge Funding). F.M. acknowledges R. Ransom for very helpful discussions.

#### Author contributions

G.A. and A.L.-P. conceived the research, designed the experiments, analyzed the data, supervised the project, and wrote the manuscript. V.L. and S.W. synthesized the samples. V.L., S.W., and G.A. performed AFM and Raman characterization; M.R.-C. and A.L.-P. performed the XRD experiments and the catalytic and kinetic studies; J.V.-M. contributed with the  $^{31}\text{P}$  MAS-NMR measurements; A.D.-C. contributed with the electrochemical studies. M.V. performed STEM and EELS. F.H. and A.H. supervised the project. B.S.J.H., S.S., H.-P.S., and F.M. performed XPS characterization. All the authors discussed the results and contributed to writing the manuscript.

#### Additional information

**Supplementary Information** accompanies this paper at <https://doi.org/10.1038/s41467-018-08063-3>.

**Competing interests:** The authors declare no competing interests.

**Reprints and permission** information is available online at <http://npg.nature.com/reprintsandpermissions/>

**Journal peer review information:** *Nature Communications* thanks the anonymous reviewers for their contribution to the peer review of this work. Peer reviewer reports are available.

**Publisher's note:** Springer Nature remains neutral with regard to jurisdictional claims in published maps and institutional affiliations.



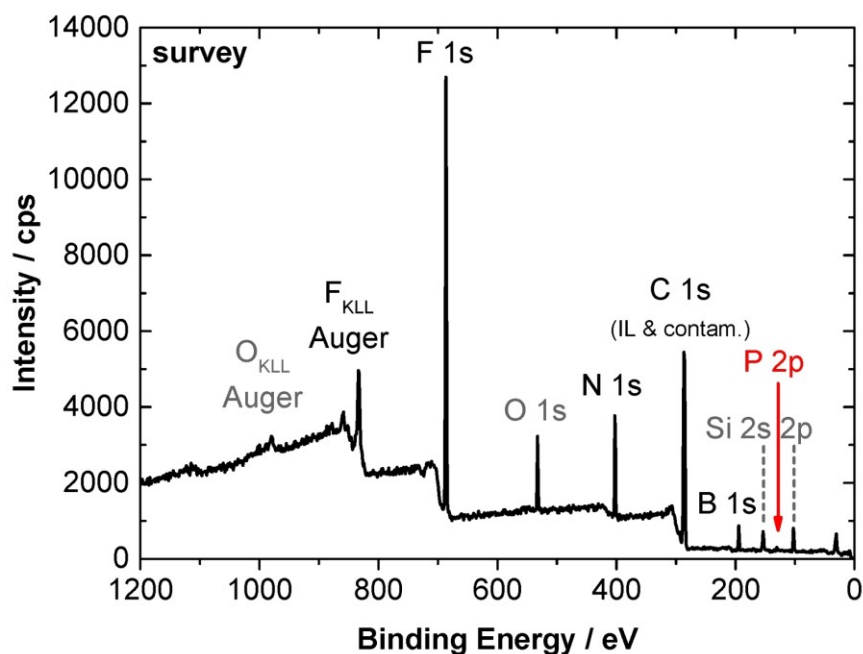
**Open Access** This article is licensed under a Creative Commons Attribution 4.0 International License, which permits use, sharing, adaptation, distribution and reproduction in any medium or format, as long as you give appropriate credit to the original author(s) and the source, provide a link to the Creative Commons license, and indicate if changes were made. The images or other third party material in this article are included in the article's Creative Commons license, unless indicated otherwise in a credit line to the material. If material is not included in the article's Creative Commons license and your intended use is not permitted by statutory regulation or exceeds the permitted use, you will need to obtain permission directly from the copyright holder. To view a copy of this license, visit <http://creativecommons.org/licenses/by/4.0/>.

© The Author(s) 2019

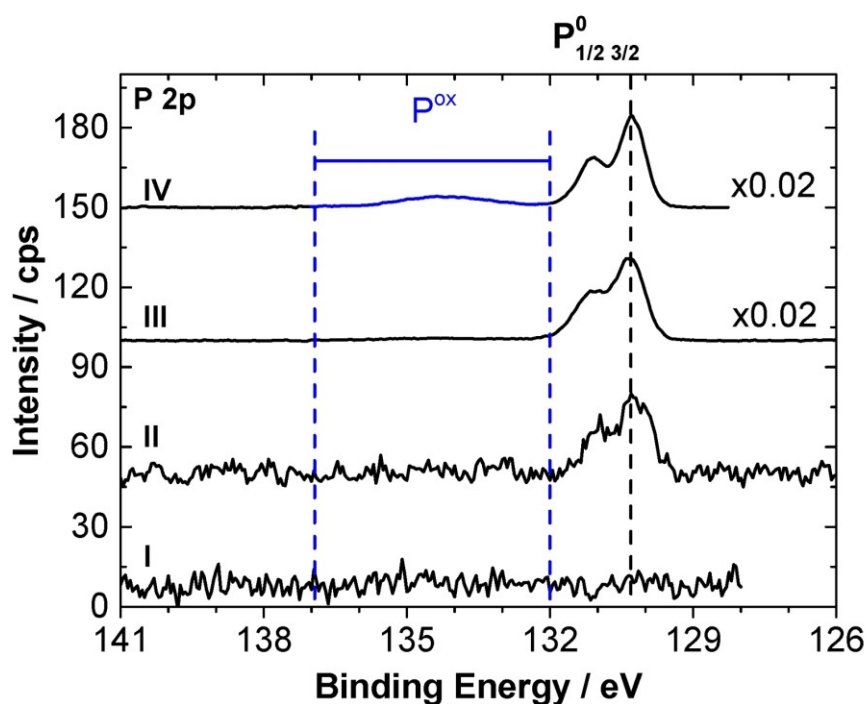
## **Supporting Information**

The complete Supporting Information for this article (60 pages) is available under <https://www.nature.com/articles/s41467-018-08063-3>.

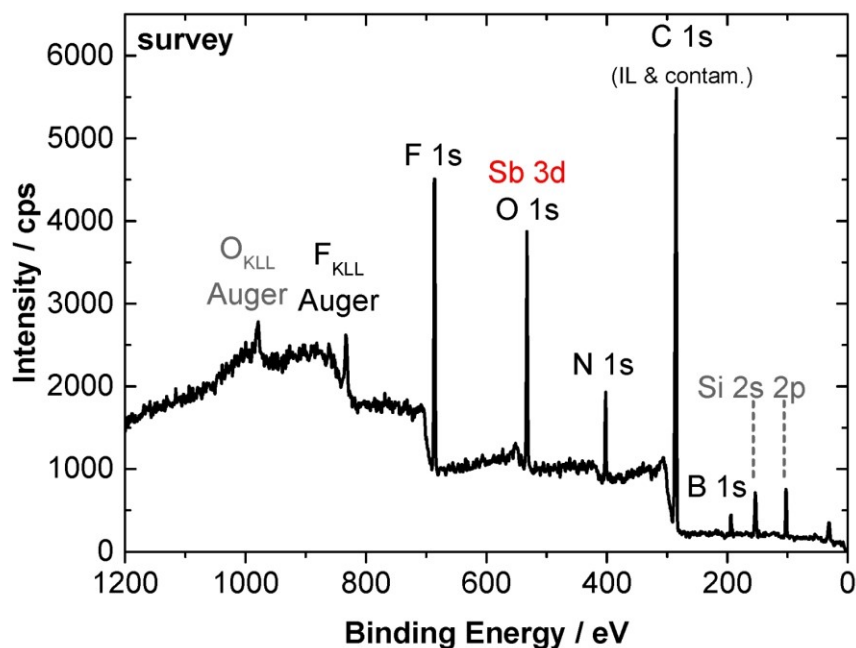
In the following, only the relevant pages for this thesis are shown.



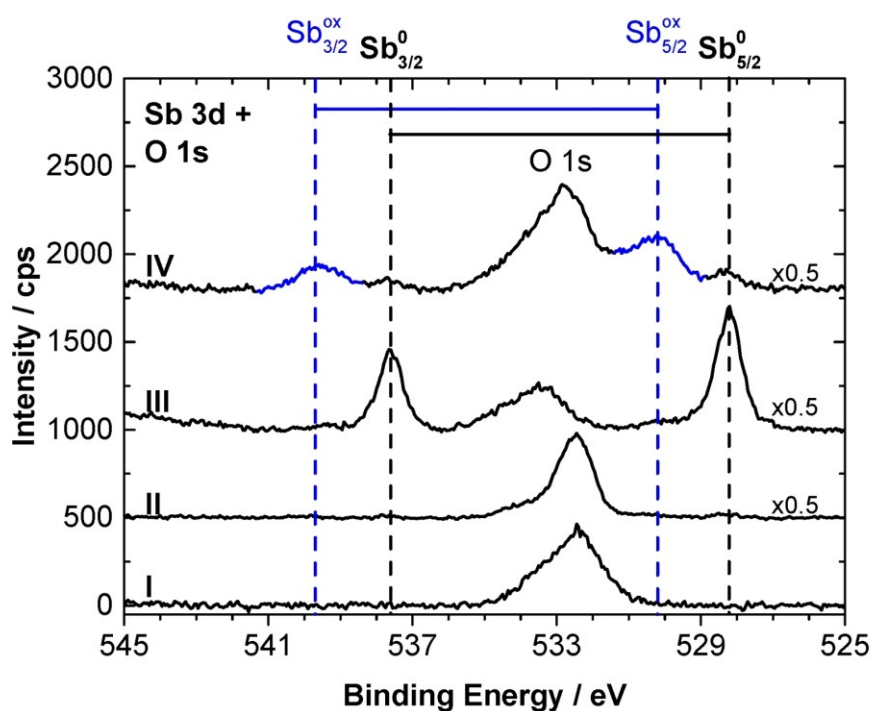
**Supplementary Figure 11.** XPS survey spectrum of FL-BP (Si, O, and C signals originating from an IL contamination are indicated in gray). Source data are provided as a Source Data file.



**Supplementary Figure 12.** XPS P 2p region of the neat bmim-BF<sub>4</sub> IL (I), the highly-concentrated FL-BP suspension (II) showing only P in oxidation state zero at P 2p<sub>3/2</sub> = 130.2 eV (region for oxidized P species is indicated), after removal of most of the IL by heating in UHV (III), and after having exposed the sample subsequently to environmental conditions for a day, showing the presence of a broad oxide P component around 134 eV (IV). Spectra are offset and re-scaled for sake of clarity. Source data are provided as a Source Data file.



**Supplementary Figure 22.** XPS survey spectrum of FL-Sb. Source data are provided as a Source Data file.



**Supplementary Figure 23.** XPS Sb 3d and O 1s region of the neat bmim-BF<sub>4</sub> IL (I) showing oxygen signals from the IL surface contamination layer, of the highly-concentrated FL-Sb suspension (II) showing small signals of non-oxidized (Sb 3d<sub>5/2</sub> at 528.2 eV) and minor contributions from oxidized (530.3 eV) antimony next to the oxygen contamination, after removal of most of the IL by heating in UHV (III), and after submitting the sample to environmental conditions for a day, showing a drastic decrease in Sb(0) and concomitant

## 9.2 Unpublished Results

In the course of this thesis, investigations on several additional ILs have been carried out without being published. This chapter gives an overview of different classes of ILs, cleaning procedures applied and problems during investigation. An overview of the investigated ILs with their physical state at room temperature (RT) and some characteristics are given in Table 9.1.

All data presented in the appendix are depicted without any further data treatment, *i.e.* all binding energies are given as measured without any referencing. Only the 80° emission spectra are scaled up by the respective geometry factor<sup>[97]</sup> for a better visualization of enrichment and depletion effects occurring in the ILs.



Table 9.1: Overview of names, molecular structures and characteristics of supplementary ILs.

Short Name	IUPAC Name	Molecular Structure	Physical State at RT	Synthesized by	Remarks
[C <sub>8</sub> AcIm][Cl]	1-acetyl-3-octylimidazolium chloride		solid	M. Gantman	<i>d</i> ; <i>Si</i> ; no melting point
[C <sub>8</sub> AcIm][PF <sub>6</sub> ]	1-acetyl-3-octylimidazolium hexafluorophosphate		solid	M. Gantman	<i>d</i> ; <i>Si</i> , partly removed by sputtering and dissolving in solvent
[C <sub>8</sub> AcIm][Tf <sub>2</sub> N]	1-acetyl-3-octylimidazolium bis[(trifluoromethyl)sulfonyl]imide		solid	M. Gantman	<i>d</i> ; <i>Si</i>
[C <sub>4</sub> (CO)C <sub>1</sub> Im][Cl]	1-methyl-3-valeroylimidazolium chloride		solid	M. Gantman	<i>d</i> ; <i>Si</i>
[C <sub>4</sub> (CO)C <sub>1</sub> Im][Tf <sub>2</sub> N]	1-methyl-3-valeroylimidazolium bis[(trifluoromethyl)sulfonyl]imide		solid	M. Gantman	<i>d</i> before melting; <i>Si</i>
[C <sub>1</sub> S(PFB)HIm][Tf <sub>2</sub> N]	3-methyl-2-((3,3,4,4,4-pentafluorobutyl)thio)imidazolium bis[(trifluoromethyl)sulfonyl]imide		liquid	G. Partl	clean; not temperature stable; <i>dX</i> in mixture
[Ph <sub>3</sub> PPhOPh][FAP]	(4-phenoxyphenyl)triphenylphosphonium tris(pentafluoroethyl)trifluorophosphate		liquid → solid	N. Taccardi	<i>Si</i> ; <i>dX</i>
[Ph <sub>3</sub> PPhOPh][Tf <sub>2</sub> N]	(4-phenoxyphenyl)triphenylphosphonium bis[(trifluoromethyl)sulfonyl]imide		liquid → solid	N. Taccardi	small <i>Si</i> ; <i>dX</i>

*d*: decomposed IL; measured (stoichiometry does not fit); *dX*: decomposition under X-rays; *Si*: polysiloxane contamination detected

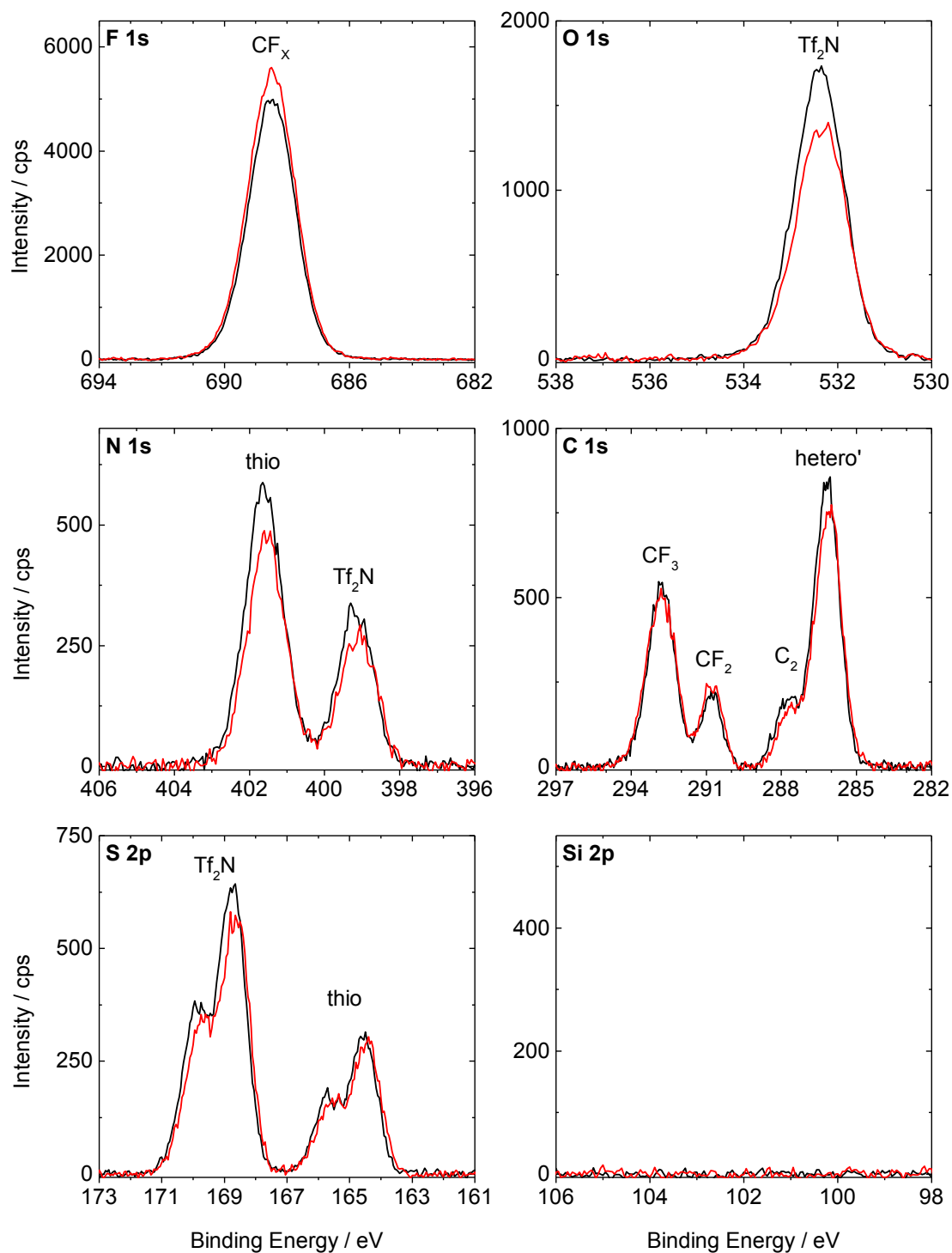
### 9.2.1 (Pentafluorobutyl)thio-Functionalized Ionic Liquid and its Mixture with [C<sub>4</sub>C<sub>1</sub>Im][PF<sub>6</sub>]

[C<sub>1</sub>S(PFB)HIm][Tf<sub>2</sub>N] was synthesized by Dr. Gabriel Partl as a yellow liquid at room temperature. Figure 9.1 shows the ARXP spectra in 0° (black) and 80° (red) emission of this protic IL at 24 °C.

No fitting constraints are applied except for the S 2p spin-orbit-split components (equal FWHM;  $\text{area}(p_{3/2}) = 2 \cdot \text{area}(p_{1/2})$ ; peak separation: 1.21 eV) and in the C 1s spectra the C<sub>hetero</sub> peak is 1.1 times wider than the C<sub>2</sub> peak and both peaks are separated by 1.60 eV.

In 0° emission, one peak is detected in the O 1s spectrum as well as in the F 1s spectrum. The O<sub>Tf<sub>2</sub>N</sub> peak is located at 532.4 eV and the F<sub>CF<sub>x</sub></sub> peak is at 688.5 eV consisting of several components which cannot be resolved with the DASSA setup: CF<sub>2</sub> and CF<sub>3</sub> groups of the fluorinated chain of the [C<sub>1</sub>S(PFB)HIm]<sup>+</sup> cation and the CF<sub>3</sub> groups of the [Tf<sub>2</sub>N]<sup>-</sup> anion. Two components are detected in the N 1s and S 2p spectra. The N<sub>thio</sub> and S<sub>thio</sub> peaks of the [C<sub>1</sub>S(PFB)HIm]<sup>+</sup> cation are located at 401.6 and 165.2 eV. At 399.2 and 169.4 eV, the N<sub>Tf<sub>2</sub>N</sub> and S<sub>Tf<sub>2</sub>N</sub> peaks of the [Tf<sub>2</sub>N]<sup>-</sup> anion are detected. Four peaks are detected in the C 1s spectrum. The C<sub>hetero</sub>, C<sub>2</sub>, C<sub>CF<sub>2</sub></sub> and C<sub>CF<sub>3</sub></sub> peaks are at 286.2, 287.8, 290.8 and 292.8 eV, respectively. Like in the F<sub>CF<sub>x</sub></sub> peak, signals of the CF<sub>3</sub> group of the fluorinated chain of the [C<sub>1</sub>S(PFB)HIm]<sup>+</sup> cation and the CF<sub>3</sub> groups of the [Tf<sub>2</sub>N]<sup>-</sup> anion are overlapping in the C<sub>CF<sub>3</sub></sub> peak. No signal is detected in the Si 2p region confirming a high purity of the IL as polysiloxane from *e.g.* glass ware or septa is a common contamination in ILs.<sup>[47, 139]</sup> The quantitative analysis, given in Table 9.2, shows also a good agreement between the atom numbers in 0° emission and the nominally expected numbers.

In 80° emission (red in Figure 9.1), the O<sub>Tf<sub>2</sub>N</sub>, N<sub>Tf<sub>2</sub>N</sub> and S<sub>Tf<sub>2</sub>N</sub> signals are lower in intensity compared to 0° indicating a depletion of these atoms of the [Tf<sub>2</sub>N]<sup>-</sup> anion whereas the intensity of the C<sub>CF<sub>2</sub></sub>, C<sub>CF<sub>3</sub></sub> and F<sub>CF<sub>x</sub></sub> peaks is the same or even higher in 80° compared to 0° suggesting that the CF<sub>3</sub> groups of the anion are pointing towards the vacuum as well as the fluorinated chain of the [C<sub>1</sub>S(PFB)HIm]<sup>+</sup> cation.



**Figure 9.1:** ARXP spectra of  $[C_1S(PFB)HIm][Tf_2N]$  in  $0^\circ$  (black) and  $80^\circ$  (red) emission recorded at  $24^\circ C$ .

The aim of the measurements of  $[C_1S(PFB)HIm][Tf_2N]$  was to test its suitability as second example of a fluorinated IL in mixtures to perform similar experiments as described in Chapter 4.2.2 for mixtures of  $[PFBMIm][PF_6]$  and  $[C_nC_1Im][PF_6]$ . Measurements at elevated temperature result in a strong decrease of the cation related signals

indicating the decomposition of the  $[C_1S(PFB)HIm]^+$  cation. In addition, a peak broadening of the  $[Tf_2N]^-$  anion signals is detected. Also an influence of the X-rays on the decomposition of the IL cannot be ruled out.

**Table 9.2:** Quantitative analysis of the  $0^\circ$  and  $80^\circ$  XP spectra of  $[C_1S(PFB)HIm][Tf_2N]$  at  $24^\circ C$ .

	F 1s	O 1s	N 1s		C 1s				S 2p	
	CF <sub>x</sub>	Tf <sub>2</sub> N	thio	Tf <sub>2</sub> N	CF <sub>3</sub>	CF <sub>2</sub>	C <sub>2</sub>	hetero'	Tf <sub>2</sub> N	thio
Binding Energy / eV	688.5	532.4	401.6	399.2	292.8	290.8	287.8	286.2	169.4	165.2
ASF	1.00	0.67	0.46	0.46	0.30	0.30	0.30	0.30	0.64	0.64
<i>Nominal</i>	<i>11</i>	<i>4</i>	<i>2</i>	<i>1</i>	<i>3</i>	<i>1</i>	<i>1</i>	<i>5</i>	<i>2</i>	<i>1</i>
$0^\circ$ emission	11.54	4.21	1.97	1.04	3.00	0.89	0.91	4.42	2.07	0.95
$80^\circ$ emission	12.93	3.55	1.64	0.91	3.16	1.01	0.79	4.17	1.91	0.93

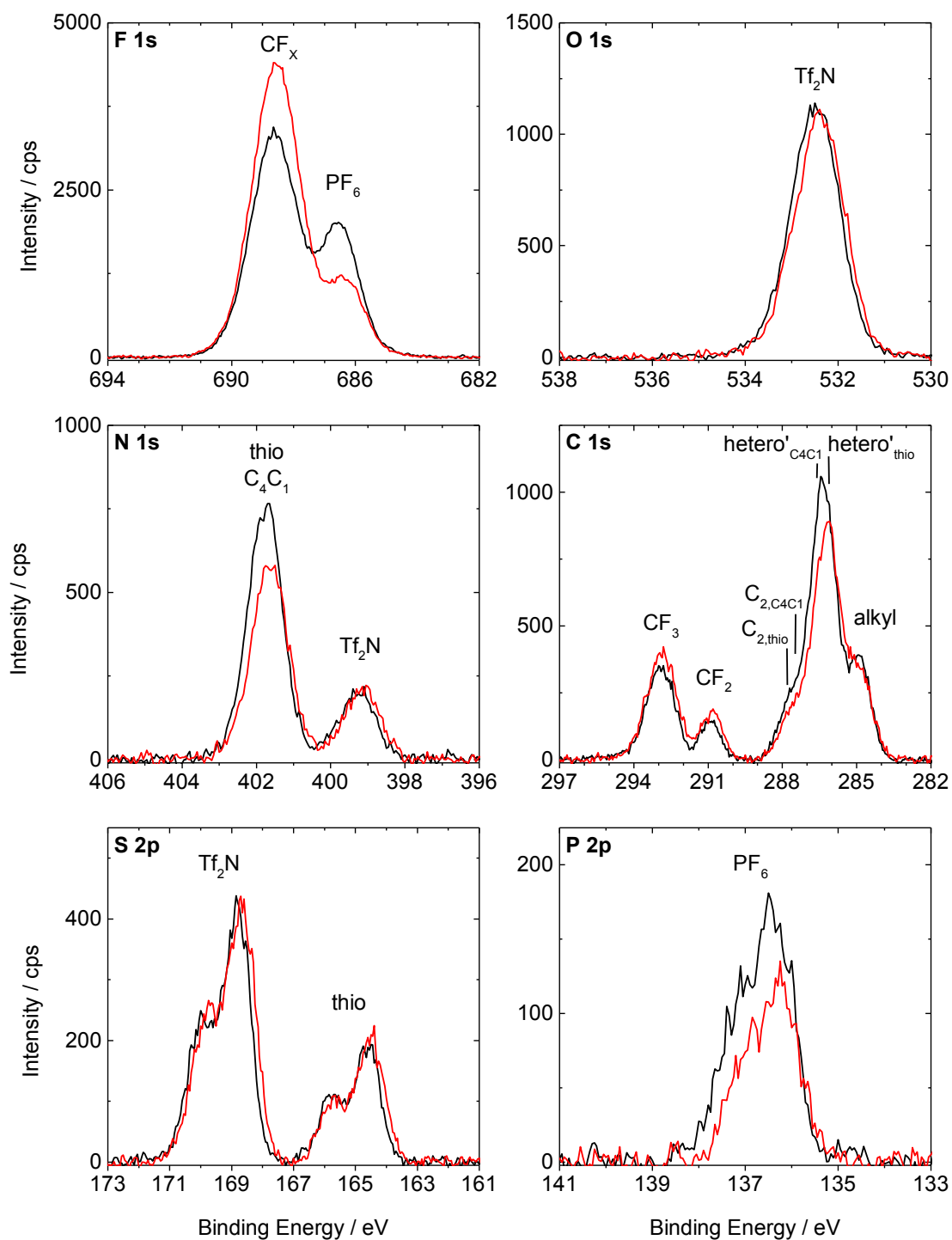
Additionally, an equimolar mixture of  $[C_1S(PFB)HIm][Tf_2N]$  and  $[C_4C_1Im][PF_6]$  was prepared. To ensure proper mixing of both ILs, acetone (Sigma-Aldrich, purity  $\geq 99.5\%$ ) was used as a co-solvent. The solution was spread on a molybdenum sample holder and the solvent acetone evaporated at RT due to the previously described decomposition of the  $[C_1S(PFB)HIm]^+$  cation at higher temperatures.

The ARXP spectra recorded at  $24^\circ C$  are presented in Figure 9.2. In  $0^\circ$  (black) emission, the signals of the  $[PF_6]^-$  anion,  $F_{PF_6}$  and  $P_{PF_6}$ , are at 686.5 and 136.8 eV, respectively. The  $O_{Tf_2N}$ ,  $N_{Tf_2N}$  and  $S_{Tf_2N}$  signals of the other anion are located at 532.5, 399.3 and 169.4 eV, respectively. As mentioned above for neat  $[C_1S(PFB)HIm][Tf_2N]$ , the XP peaks of the  $CF_3$  group of the fluorinated chain in the cation and the  $CF_3$  groups of the  $[Tf_2N]^-$  anion are superimposed ( $F_{CF_x}$  at 688.6 eV and  $C_{CF_3}$  at 292.9 eV). In addition to the  $CF_3$  signal of the  $[C_1S(PFB)HIm]^+$  cation, the  $C_{CF_2}$ ,  $C_{2,thio}$  and  $C_{hetero',thio}$  peaks are located at 290.9, 287.8 and 286.2 eV, respectively, in the C 1s spectrum. The signals of the  $[C_4C_1Im]^+$  cation are at 287.4, 286.5 and 284.9 eV for the  $C_{2,C_4C_1}$ ,  $C_{hetero',C_4C_1}$  and  $C_{alkyl}$ , respectively. Note that as a fit model the constraints for both neat ILs are applied for fitting the C 1s spectrum without any sophisticated optimization. In the N 1s spectrum, the signal of the nitrogen atoms of the imidazolium ring of the  $[C_1S(PFB)HIm]^+$  cation,  $N_{thio}$ , cannot be distinguished from the signal of the nitrogen atoms of the  $[C_4C_1Im]^+$  imidazolium ring,  $N_{C_4C_1}$ , resulting in a combined peak at 401.8 eV. The  $S_{thio}$  peak is located at 165.2 eV. No Si 2p or other XP signals are detected in addition to the expected IL mixture signals confirming that no contaminations are transferred into the mixture during sample

preparation. Within the margin of error, the quantitative analysis (see Table 9.3) in  $0^\circ$  emission fits with the nominal atom ratio.

To get information about the surface enrichment and depletion effects in the equimolar mixture of  $[\text{C}_1\text{S}(\text{PFB})\text{HIm}][\text{Tf}_2\text{N}]$  and  $[\text{C}_4\text{C}_1\text{Im}][\text{PF}_6]$  the  $80^\circ$  (red) spectra are analyzed (see Figure 9.2). The intensity in  $0^\circ$  and  $80^\circ$  emission is roughly the same for the  $\text{O}_{\text{Tf}_2\text{N}}$ ,  $\text{N}_{\text{Tf}_2\text{N}}$  and  $\text{S}_{\text{Tf}_2\text{N}}$  signals of the  $[\text{Tf}_2\text{N}]^-$  anion while the  $\text{F}_{\text{PF}_6}$  and  $\text{P}_{\text{PF}_6}$  peaks of the  $[\text{PF}_6]^-$  anion have a lower intensity in  $80^\circ$  than in  $0^\circ$ , indicating a depletion of the  $[\text{PF}_6]^-$  anion with respect to the  $[\text{Tf}_2\text{N}]^-$  anion as known from literature.<sup>[61, 63, 96]</sup> The  $\text{F}_{\text{CF}_x}$ ,  $\text{C}_{\text{CF}_3}$  and  $\text{C}_{\text{CF}_2}$  intensities are higher in  $80^\circ$  emission indicating a surface enrichment of the fluorinated chain of the  $[\text{C}_1\text{S}(\text{PFB})\text{HIm}]^+$  cation and the  $[\text{Tf}_2\text{N}]^-$  anion. This enrichment is more pronounced in contrast to neat  $[\text{C}_1\text{S}(\text{PFB})\text{HIm}][\text{Tf}_2\text{N}]$ . No changes in intensity are detected for the  $\text{S}_{\text{thio}}$  peak when changing the emission angle. Due to the  $\text{S}_{\text{thio}}$  signal and the intensity decrease of the combined  $\text{N}_{\text{C}_4\text{C}_1}$  and  $\text{N}_{\text{thio}}$  peak from  $80^\circ$  emission to  $0^\circ$  most likely the head group of the  $[\text{C}_4\text{C}_1\text{Im}]^+$  cation is depleted from the surface compared to the surface-enriched head group of the  $[\text{C}_1\text{S}(\text{PFB})\text{HIm}]^+$  cation. In the C 1s region, the signal between 285 and 289 eV has also a lower intensity in  $80^\circ$  but it is hard to say anything about the relative positions of the two head groups with respect to each other. As mentioned, the fitting model preliminary used for the C 1s spectrum does not allow for reliable quantitative ARXPS analysis.

Since neat  $[\text{C}_1\text{S}(\text{PFB})\text{HIm}][\text{Tf}_2\text{N}]$  decomposes at elevated temperature, a cooling experiment starting from RT was performed. The decomposition of the  $[\text{C}_1\text{S}(\text{PFB})\text{HIm}]^+$  cation and a third F 1s species appearing at  $\sim 684.7$  eV are detected. Presumably, the extended X-ray exposure time destroys the mixture due to a limited diffusion of the molecules.



**Figure 9.2:** ARXP spectra of an equimolar mixture of  $[C_1S(PFB)HIm][Tf_2N]$  and  $[C_4C_1Im][PF_6]$  in  $0^\circ$  (black) and  $80^\circ$  (red) emission recorded at  $24^\circ C$ .

**Table 9.3:** Quantitative analysis of the 0° and 80° XP spectra of an equimolar mixture of [C<sub>1</sub>S(PFB)HIm][Tf<sub>2</sub>N] and [C<sub>4</sub>C<sub>1</sub>Im][PF<sub>6</sub>] at 24 °C.

Binding Energy / eV	F 1s		O 1s		N 1s		C 1s						S 2p		P 2p
	CF <sub>x</sub>	PF <sub>6</sub>	Tf <sub>2</sub> N	thio	Tf <sub>2</sub> N	CF <sub>3</sub>	CF <sub>2</sub>	[C <sub>1</sub> S(PFB)HIm] <sup>+</sup> (thio)		[C <sub>4</sub> C <sub>1</sub> Im] <sup>+</sup>		alkyl	Tf <sub>2</sub> N	thio	PF <sub>6</sub>
								C <sub>2</sub>	hetero'	C <sub>2</sub>	hetero'				
ASF	688.6	1.00	532.5	401.8	399.3	292.9	290.9	287.8	286.2	287.4	286.5	284.9	169.4	165.2	136.8
Nominal	11	6	4	4	1	3	1	1	5	1	4	3	2	1	1
0° emission	12.23	5.78	4.32	3.76	1.05	3.23	0.89	0.89	4.66	0.89	3.54	2.72	2.07	0.91	1.07
80° emission	16.32	3.14	4.22	3.07	1.08	3.90	1.18	0.92	3.66	0.92	3.66	2.56	2.19	0.97	0.73

### 9.2.2 Ether-Functionalized Phosphonium Ionic Liquids

[Ph<sub>3</sub>PPhOPh][FAP] and [Ph<sub>3</sub>PPhOPh][Tf<sub>2</sub>N] were synthesized by Dr. Nicola Taccardi as yellow, very viscous liquids (at RT) which crystallized over time becoming white solids.  $T_m$  is  $\sim 75$  °C for [Ph<sub>3</sub>PPhOPh][FAP] and  $\sim 91$  °C for [Ph<sub>3</sub>PPhOPh][Tf<sub>2</sub>N] (both temperatures are deduced from samples heated up in the preparation chamber of the DASSA setup). The samples were measured at 105 °C in their liquid state.

No fitting constraints are applied except for the S 2p and P 2p spin-orbit-split components (equal FWHM;  $\text{area}(p_{3/2}) = 2 \cdot \text{area}(p_{1/2})$ ; peak separation S 2p = 1.21 eV, P 2p = 0.90 eV). For determining the atom numbers in 0° and 80° emission, the C<sub>CF<sub>3</sub></sub> and C<sub>CF<sub>2</sub></sub> peak intensities are linked to the F<sub>CF<sub>x</sub></sub> peak. The remaining shake-up intensity between 288 and 294 eV in the C 1s region is added to the intensity of the C<sub>phenyl</sub> peak. The quantitative analyses are provided in Table 9.4.

**Table 9.4:** Quantitative analysis of the 0° and 80° XP spectra of a) [Ph<sub>3</sub>PPhOPh][FAP] and b) [Ph<sub>3</sub>PPhOPh][Tf<sub>2</sub>N] at 105 °C.

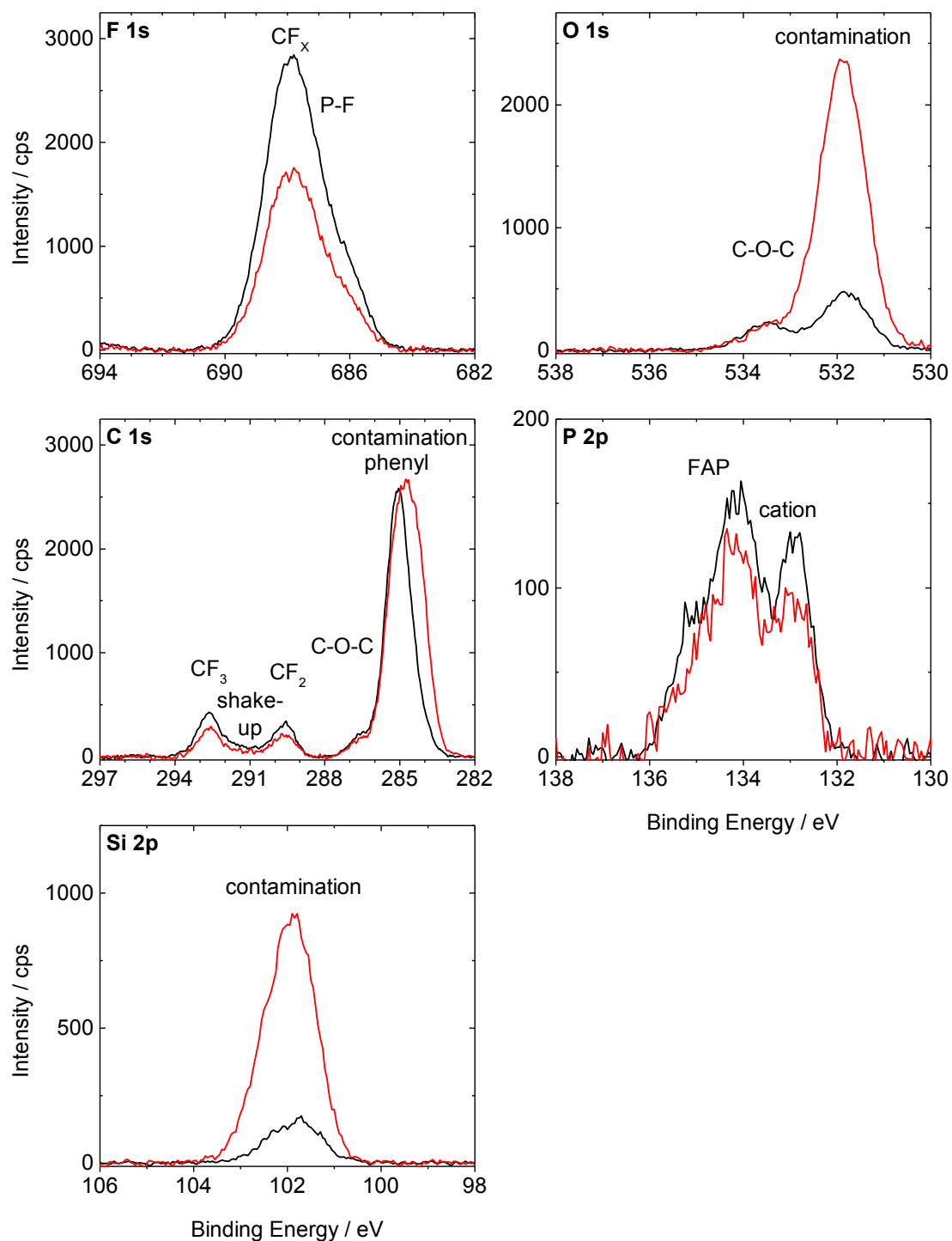
a) [Ph <sub>3</sub> PPhOPh][FAP]	F 1s		O 1s	C 1s				P 2p	
	CF <sub>x</sub>	P-F	C-O-C	CF <sub>3</sub>	CF <sub>2</sub>	C-O-C	contami- nation + phenyl	FAP	cation
Binding Energy / eV	687.9	686.2	533.5	292.7	289.6	286.7	285.0	134.7	133.3
ASF	1.00	1.00	0.67	0.30	0.30	0.30	0.30	0.46	0.46
<i>Nominal</i>	15	3	1	3	3	2	28	1	1
0° emission	14.44	2.81	1.02	2.89	2.89	1.21	29.80	1.02	0.91
80° emission	8.93	1.66	1.08	1.79	1.79	0.63	39.62	0.81	0.70

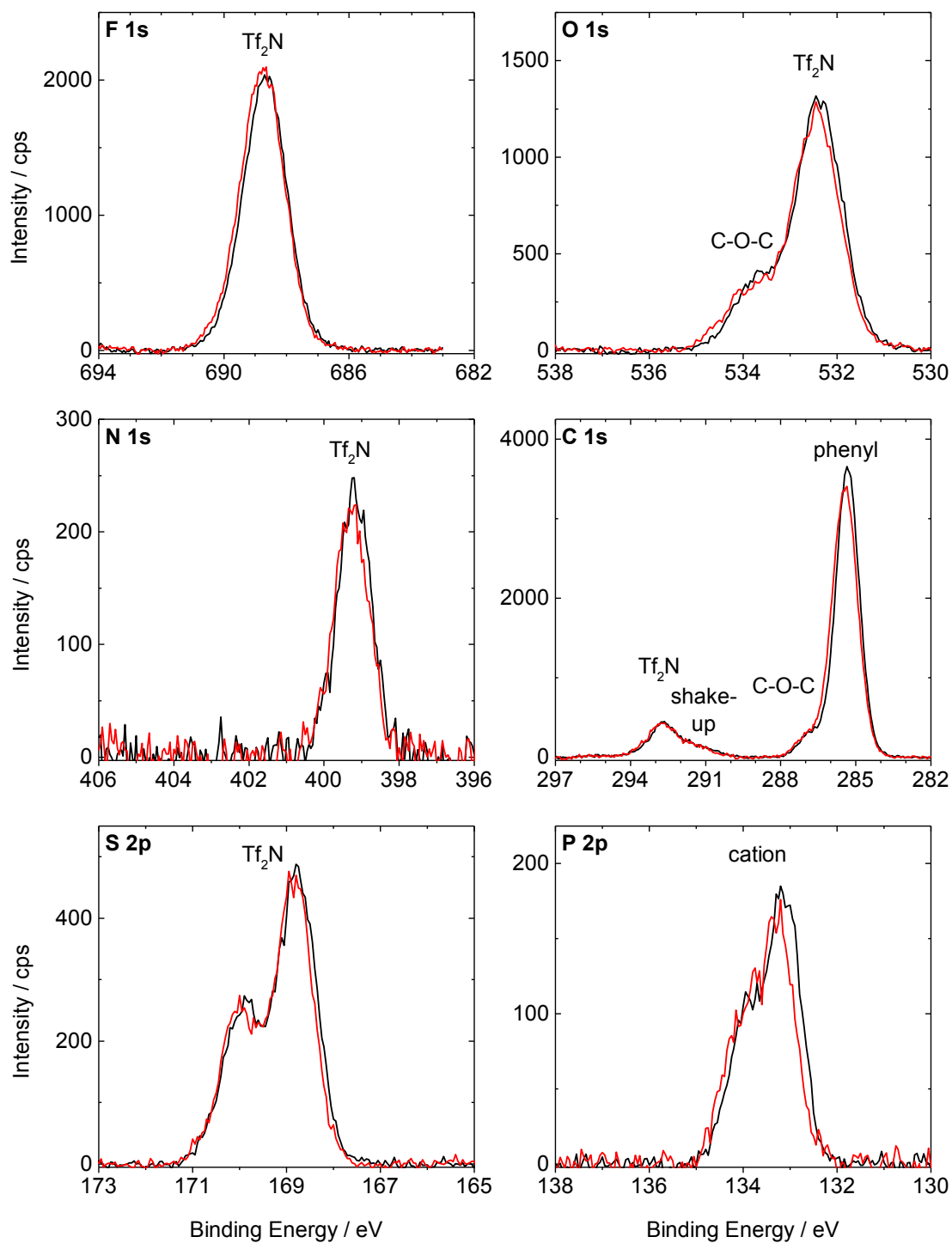
b) [Ph <sub>3</sub> PPhOPh][Tf <sub>2</sub> N]	F 1s	O 1s		N 1s	C 1s			S 2p	P 2p
	Tf <sub>2</sub> N	C-O-C	Tf <sub>2</sub> N	Tf <sub>2</sub> N	Tf <sub>2</sub> N	C-O-C	phenyl	Tf <sub>2</sub> N	cation
Binding Energy / eV	688.7	533.7	532.4	399.2	292.7	286.8	285.3	169.4	133.6
ASF	1.00	0.67	0.67	0.46	0.30	0.30	0.30	0.64	0.46
<i>Nominal</i>	6	1	4	1	2	2	28	2	1
0° emission	6.24	1.11	4.12	1.04	2.08	1.91	27.52	2.05	0.93
80° emission	6.53	1.11	3.95	0.99	2.18	1.78	27.61	1.97	0.87



In general,  $[\text{Ph}_3\text{PPhOPh}][\text{FAP}]$  (see Figure 9.3) has a strong surface active contamination which is presumably polysiloxane whereas for  $[\text{Ph}_3\text{PPhOPh}][\text{Tf}_2\text{N}]$  (see Figure 9.4) only a very small contamination in the Si 2p region (not shown) is observed. A homogeneous distribution of all moieties of  $[\text{Ph}_3\text{PPhOPh}][\text{Tf}_2\text{N}]$  is detected. Both ILs are decomposing under X-rays within a few hours as indicated by peak broadening.



**Figure 9.3:** ARXP spectra of  $[\text{Ph}_3\text{PPhOPh}][\text{FAP}]$  in  $0^\circ$  (black) and  $80^\circ$  (red) emission recorded at  $105^\circ\text{C}$ .



**Figure 9.4:** ARXP spectra of  $[\text{Ph}_3\text{PPhOPh}][\text{Tf}_2\text{N}]$  in  $0^\circ$  (black) and  $80^\circ$  (red) emission recorded at  $105^\circ\text{C}$ .

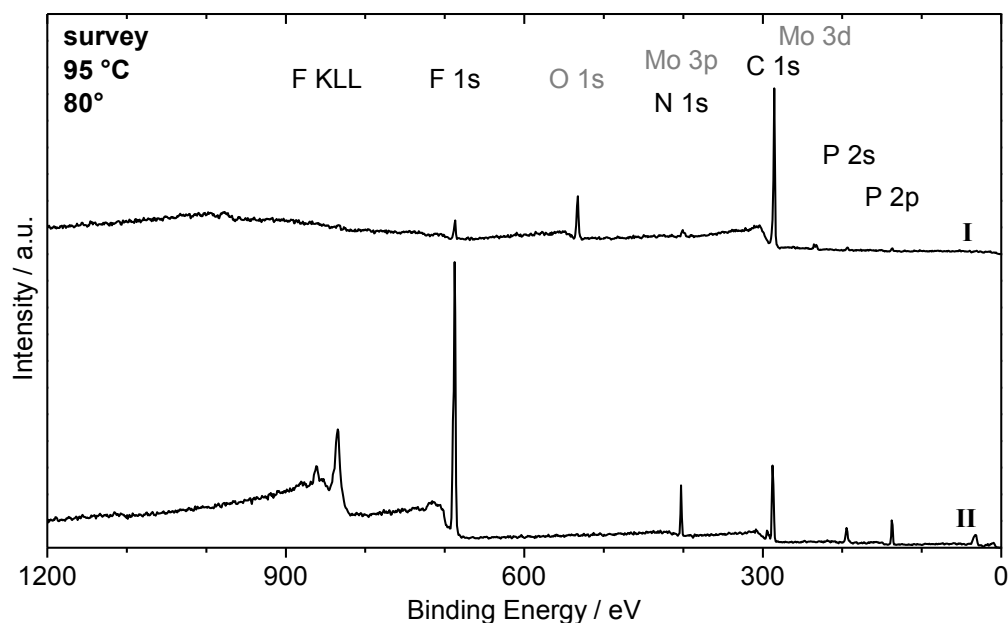
### 9.2.3 Temperature-Dependent Measurements of Mixtures of [PFBMIm][PF<sub>6</sub>] with [C<sub>2</sub>C<sub>1</sub>Im][PF<sub>6</sub>] and [C<sub>8</sub>C<sub>1</sub>Im][PF<sub>6</sub>]

As highlighted in Chapter 4.2.2, temperature-dependent ARXPS measurements of mixtures of [PFBMIm][PF<sub>6</sub>] and [C<sub>2</sub>C<sub>1</sub>Im][PF<sub>6</sub>] or [C<sub>8</sub>C<sub>1</sub>Im][PF<sub>6</sub>] were investigated besides the published measurements of mixtures containing [PFBMIm][PF<sub>6</sub>] and [C<sub>4</sub>C<sub>1</sub>Im][PF<sub>6</sub>].<sup>[137]</sup> For the data of all these mixtures, the published fitting constraints are applied.<sup>[137]</sup>

The ARXP spectra of [C<sub>2</sub>C<sub>1</sub>Im][PF<sub>6</sub>] recorded at 95 °C show the expected peaks in the F 1s, N 1s, C 1s and P 2p regions in 0° and 80° emission. In addition, a polysiloxane contamination is detected in the O 1s and Si 2p spectra as well as a too high C<sub>alkyl</sub> peak in the C 1s region as deduced from the quantitative analysis and the 80° spectrum.

When preparing mixtures of [PFBMIm][PF<sub>6</sub>] and [C<sub>2</sub>C<sub>1</sub>Im][PF<sub>6</sub>] with 10, 25, 50 and 75 mol% [PFBMIm][PF<sub>6</sub>], a cleaning procedure is applied. Both solids are dissolved in acetonitrile. Subsequently, only the lower part of the solution is carefully extracted with a Pasteur pipette, assuming that most of the surface-enriched polysiloxane contamination stays in the remaining topmost 1 to 2 mm of the solution. Unfortunately, this cleaning process has not led to the intended outcome of contamination free samples as illustrated in the 80° survey spectrum of a mixture containing 10 mol% [PFBMIm][PF<sub>6</sub>] in Figure 9.5–I measured at 95 °C. In contrast to the spectrum of neat [C<sub>2</sub>C<sub>1</sub>Im][PF<sub>6</sub>], no Si contamination peak is observed but an oxygen peak as well as a dominating C 1s signal are visible in ARXPS while the IL peaks are very weak. Furthermore, a dewetting of the 10, 25 and 50 mol% [PFBMIm][PF<sub>6</sub>] mixtures on the molybdenum sample holder is visually observed as well as the XP spectra reveal additional Mo signals.

Gentle sputtering with 300 eV Ar<sup>+</sup> ions (~8 μA) for 5 to 15 min improves the wetting on the sample holder for the 10, 25 and 50 mol% [PFBMIm][PF<sub>6</sub>] mixtures. This is attributed to the removal of some contamination on the molybdenum sample holder by sputtering. In Figure 9.5–II, the survey spectrum of the 10 mol% [PFBMIm][PF<sub>6</sub>] mixture after the sputter process indicates not only the improvement of the wetting behavior by the absence of the Mo and O 1s signals but also shows strong IL signals. Note that for the 75 mol% [PFBMIm][PF<sub>6</sub>] mixture no dewetting and no oxygen, silicon and carbon contaminations are observed.



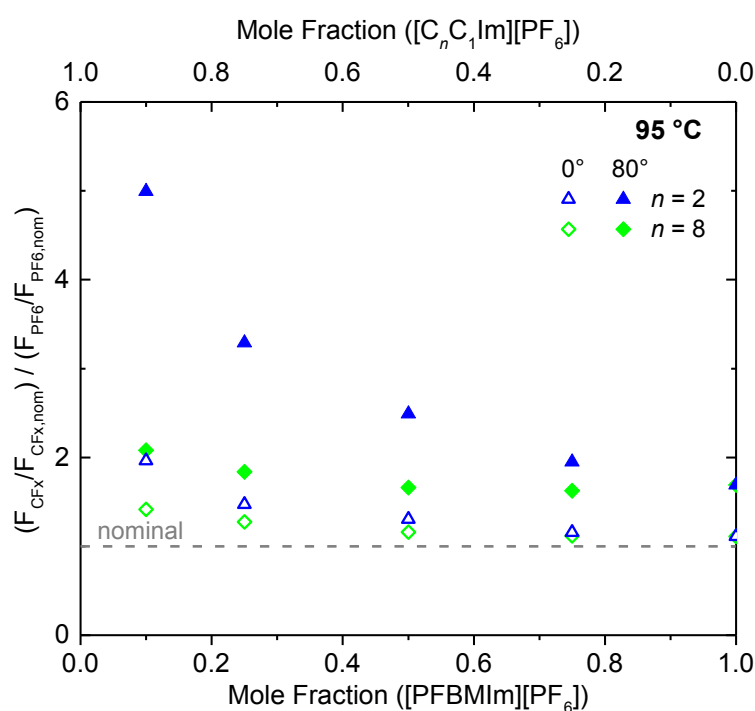
**Figure 9.5:** Survey spectra of a 10 mol% mixture of [PFBMIm][PF<sub>6</sub>] and [C<sub>2</sub>C<sub>1</sub>Im][PF<sub>6</sub>] as prepared (I) and after sputtering (II) recorded at an emission angle of 80°. The sample temperature was 95 °C. The spectra are offset for clarity.

In addition, mixtures of [PFBMIm][PF<sub>6</sub>] and [C<sub>8</sub>C<sub>1</sub>Im][PF<sub>6</sub>] with 10, 25, 50 and 75 mol% [PFBMIm][PF<sub>6</sub>] are prepared using acetonitrile as a co-solvent. No further treatment is necessary because these mixtures fully wet the sample holders and no contamination is detected in the ARXP spectra. For the 10 mol% mixture of [PFBMIm][PF<sub>6</sub>] and [C<sub>8</sub>C<sub>1</sub>Im][PF<sub>6</sub>], an additional FWHM constraint is applied: The  $F_{PF_6}$  peak is 0.76 times wider than the  $F_{CF_x}$  peak due to a dominating  $F_{PF_6}$  peak in the F 1s spectra.

All mixtures are measured at 95 °C and subsequently cooled to lower temperature until peak broadening or shifts are detected indicating the onset of solidification. In general, the same trends, *e.g.* the surface enrichment of the fluorinated chain of the [PFBMIm]<sup>+</sup> cation in contrast to the surface-depleted [PF<sub>6</sub>]<sup>-</sup> anion, are observed as described for the mixtures of [PFBMIm][PF<sub>6</sub>] and [C<sub>4</sub>C<sub>1</sub>Im][PF<sub>6</sub>] in Chapter 4.2.2. This is attributed to the difference in surface tension of the [C<sub>n</sub>C<sub>1</sub>Im][PF<sub>6</sub>] and the [PFBMIm][PF<sub>6</sub>] as it is in accordance with literature that ILs containing fluorinated chains generally possess a lower surface tension compared to their alkylated counterpart<sup>[60, 130, 131]</sup> and the shorter the alkyl chain, the higher is the surface tension of the IL.<sup>[71, 86, 133-135]</sup>

At 95 °C, a more pronounced enrichment of the fluorinated chain of the [PFBMIm]<sup>+</sup> cation relative to the [PF<sub>6</sub>]<sup>-</sup> anion is detected in the F 1s spectrum for both

types of mixtures when decreasing the  $[\text{PFBMIm}][\text{PF}_6]$  content. This is visualized in Figure 9.6 by plotting the normalized ratio of the  $F_{\text{CF}_x}$  and  $F_{\text{PF}_6}$  intensities for the mixtures containing  $[\text{C}_2\text{C}_1\text{Im}][\text{PF}_6]$  (blue triangles) and  $[\text{C}_8\text{C}_1\text{Im}][\text{PF}_6]$  (green diamonds) in  $0^\circ$  (open symbols) and  $80^\circ$  (full symbols) emission. The enrichment of the fluorinated chain of the  $[\text{PFBMIm}]^+$  cation is also detected by the intensity increase of the  $\text{C}_{\text{CF}_3}$  and  $\text{C}_{\text{CF}_2}$  peaks in the C 1s spectrum of the mixtures when comparing the  $0^\circ$  and  $80^\circ$  spectra. Another observation is that in  $80^\circ$  the enrichment is much less pronounced for the mixtures with  $[\text{C}_8\text{C}_1\text{Im}][\text{PF}_6]$  compared to the mixtures containing  $[\text{C}_2\text{C}_1\text{Im}][\text{PF}_6]$  which is attributed to a competing effect of the fluorinated chain and the longer alkyl chain.<sup>[71]</sup> In  $0^\circ$  emission, even the same trend is observed but to a lower extent than in  $80^\circ$ , revealing that below the first 1 to 1.5 nm an enrichment of the fluorinated chain of the  $[\text{PFBMIm}]^+$  cation is detected as observed for other IL systems as well.<sup>[54, 96, 136, 137]</sup>



**Figure 9.6:** Normalized ratio of  $F_{\text{CF}_x}$  and  $F_{\text{PF}_6}$  for mixtures of  $[\text{PFBMIm}][\text{PF}_6]$  and  $[\text{C}_n\text{C}_1\text{Im}][\text{PF}_6]$  with  $n=2$  (blue triangles) and  $8$  (green diamonds) at  $0^\circ$  (open symbols) and  $80^\circ$  (full symbols) emission. The gray dashed line indicates the nominal composition. The sample temperature was  $95^\circ\text{C}$ .

Furthermore, the  $\text{C}_{\text{alkyl}}$  signal in the C 1s spectra of the mixtures of  $[\text{PFBMIm}][\text{PF}_6]$  and  $[\text{C}_8\text{C}_1\text{Im}][\text{PF}_6]$  has a higher intensity in  $80^\circ$  compared to  $0^\circ$  emission showing the surface enrichment of the octyl chain of the  $[\text{C}_8\text{C}_1\text{Im}]^+$  cation besides the enrichment of the fluorinated chain of the  $[\text{PFBMIm}]^+$  cation. This is in contrast to the mixtures containing

[C<sub>2</sub>C<sub>1</sub>Im][PF<sub>6</sub>] and [C<sub>4</sub>C<sub>1</sub>Im][PF<sub>6</sub>] for which no enrichment of the alkyl chain is detected. This observation is in line with MD simulations of Luís *et al.*<sup>[71]</sup> indicating that the surface of mixtures, containing long alkyl chains and shorter fluorinated chains, is dominated by the alkyl chains. This is on expense of the shorter fluorinated chain and the cationic head groups, whereas in the presence of a short alkyl chain the surface is dominated by the fluorinated chain.

For the temperature-dependent measurements, only the 80° emission spectra of the mixtures of [PFBMIm][PF<sub>6</sub>] and [C<sub>2</sub>C<sub>1</sub>Im][PF<sub>6</sub>] or [C<sub>8</sub>C<sub>1</sub>Im][PF<sub>6</sub>] are briefly discussed because the enrichment and depletion effects are more obvious under this emission angle. When decreasing the temperature, the signals of the fluorinated chain, F<sub>CF<sub>x</sub></sub>, C<sub>CF<sub>3</sub></sub> and C<sub>CF<sub>2</sub></sub>, increase in intensity whereas the F<sub>PF<sub>6</sub></sub> peak intensity decreases. In the XP spectra of the mixtures containing [C<sub>8</sub>C<sub>1</sub>Im][PF<sub>6</sub>], the C<sub>alkyl</sub> signal increases as well. Figure 4.6 in Chapter 4.2.2 shows the increase of the normalized intensity ratio of F<sub>CF<sub>x</sub></sub> and F<sub>PF<sub>6</sub></sub> of the mixtures of [PFBMIm][PF<sub>6</sub>] and [C<sub>*n*</sub>C<sub>1</sub>Im][PF<sub>6</sub>] with *n* = 2 (blue triangles), 4 (red squares) and 8 (green diamonds) with decreasing temperature indicating a more pronounced surface enrichment of the fluorinated chain of the [PFBMIm]<sup>+</sup> cation with respect to the [PF<sub>6</sub>]<sup>-</sup> anion relative to the bulk concentration.

In general, the most pronounced surface enrichment of the fluorinated chain of the [PFBMIm]<sup>+</sup> cation is detected for the mixtures containing [PFBMIm][PF<sub>6</sub>] and [C<sub>2</sub>C<sub>1</sub>Im][PF<sub>6</sub>] compared to the mixtures of [PFBMIm][PF<sub>6</sub>] with [C<sub>4</sub>C<sub>1</sub>Im][PF<sub>6</sub>] or [C<sub>8</sub>C<sub>1</sub>Im][PF<sub>6</sub>] and this effect is enhanced when decreasing the temperature.